Design and Control of High-Speed and Large-Range Atomic Force Microscope

by

Iman Soltani Bozchalooi

Submitted to the Department of Mechanical Engineering
in partial fulfillment of the requirements for the degree of

Doctor of Philosophy

at the

MASSACHUSETTS INSTITUTE OF TECHNOLOGY

June 2015

Author .. Signature redacted .....
Department of Mechanical Engineering
May 10, 2015

Certified by..... Signature redacted ..
Kamal Youcef-Toumi
Professor of Mechanical Engineering
Thesis Supervisor

Accepted by ..... Signature redacted
David E. Hardt
Chairman, Department Committee on Graduate Theses

Design and Control of High-Speed and Large-Range Atomic Force Microscope

by

Iman Soltani Bozchalooi

Submitted to the Department of Mechanical Engineering
on May 10, 2015, in partial fulfillment of the
requirements for the degree of
Doctor of Philosophy

Abstract

This thesis presents the design, control and instrumentation of a novel atomic force microscope (AFM). This AFM is capable of high-speed imaging while maintaining large out-of-plane and lateral scan ranges. The primary contributions of this thesis include the design and implementation of a high-speed and large-range AFM; design, implementation and control of a multi-actuated nano-positioner; development of a general direct data-based control design scheme for redundantly actuated nano-positioners; design and implementation of a non-linear amplitude demodulation method for tapping mode imaging; and development of a parameter estimation methodology for piezo actuator hysteresis modeling and compensation.

Atomic force microscopes can provide nano-scale resolution images of sample surface topography in air, vacuum or in liquid. This instrument operates by scanning a micro-mechanical probe on a sample. A measurement of the probe-sample interaction is used to control the AFM scanner and also form a 3D image of the sample surface topography. The mechanical nature and the serial-point-collection bases of operation of this instrument significantly limits its speed and constrains its application to the study of static samples. Unlocking the high-speed performance capability of AFM enables study of dynamic nano-scale processes and opens up the possibility of novel scientific discoveries. Improving the speed performance of AFM however, should not compromise imaging range so that the instrument can accommodate imaging experiments with diverse lateral and out-of-plane scan range requirements. In addition to high-speed and large-range performance, instrument flexibility and ease of use are very important. An AFM should allow samples of different sizes, and provide a simple platform for setting up the imaging experiment.

In this work all the components of the AFM are designed to meet these specifications. A multi-actuated scanner is designed and built that is composed of five nano-positioners with different range and bandwidth characteristics. Through redundant actuation this nano-positioner is capable of operating at high speeds and over large lateral and out-of-plane scan ranges. A general data-based compensator design methodology for the control of redundantly actuated nano-positioners is developed.

In the proposed approach the compensators are obtained directly from the measured scanner actuator response, without any intermediate modeling. This feature makes updating or tuning the associated parameters easier. The flexibility of AFM control is maintained by designing these compensators auxiliary to a PID control unit. It is shown that in this form, a PID controller suffices to meet the needs of high-speed atomic force microscopy. This approach to control design is also used in the thesis to retroactively enhance existing AFMs operating on both flexure-based scanners and piezo-tubes. To improve the positioning accuracy of the scanner we proposed a more accurate parameter estimation scheme for the Maxwell model of hysteresis extended to the full hysteresis loop. Finally, to enable operation of AFMs with probe arrays in tapping mode a non-linear demodulation method based on the Teager Energy Operator is designed and implemented in both analog and digital forms. The main advantage of this technique is simplicity, enabling implementation of hundreds of these operators in digital form on FPGAs (Field Programmable Gate Arrays) or in ASIC (Application-Specific Integrated Circuit) form on AFM probe arrays for parallel sensing.

The developments of this thesis form the bases for the design and implementation of a novel AFM. The implemented instrument is capable of high-speed imaging and simultaneously achieves 6 μm out-of-plane and 120 μm lateral scan ranges making it the largest range high-speed AFM reported to this date. This instrument also features a modular design with a laser spot size of 3.5 μm compatible with small cantilevers, an optical view of the sample and probe for site selection and laser adjustment, a conveniently large (15 mm) waterproof sample stage that accommodates samples with various sizes and a data logging and plotting system with 20 MHz throughput for high resolution image acquisition at high imaging speeds. The designed AFM is used to visualize etching of calcite in a solution of sulfuric acid. Layer-by-layer dissolution along the crystalline lines in a low pH environment is observed in real time and the corresponding dissolution rate is estimated. The designed AFM is also used to visualize in real time the nucleation, growth and striping of copper on gold for the first time.

Thesis Supervisor: Kamal Youcef-Toumi
Title: Professor of Mechanical Engineering

Acknowledgments

Firstly I would like to thank my advisor Professor Kamal Youcef-Toumi for his support and guidance throughout my years at MIT. His insights were invaluable for me in every step of my research work. While ensuring of my path he fully trusted me in important points of my PhD work and gave me the freedom to explore different ideas. This was very important for my professional development. He created a very friendly environment for all of us at the Mechatronics Research Laboratory, making it easier to go through the critical periods and face the challenges. It has been an honor and a true life time opportunity to know him and to work with him.

I would also like to thank my thesis committee members for their time, support and invaluable feedback. I started my MIT course work experience with Prof. Ian Hunter. I was amazed by the depth of his knowledge and his teaching qualities. He taught me so much about instrumentation and measurement technologies, helped me improve my work and motivated me to push myself and achieve higher standards. I cherish every second of my interactions with him. Prof. Kripa Varanasi was always there to help me regardless of how busy he was. I learned so much from him about material sciences and surface engineering. He helped me expand my experience and explore other areas of science otherwise unknown to me. His perspectives in life were invaluable sources of inspiration to me.

I would like to thank KFUPM for their collaboration and financial support. I specially thank Prof. Numan Abu-Dheir for his comments. I would also like to thank National Instruments for their hardware and software support. I especially thank Dr. Jeannie Falcon for her helps. She believed in our AFM research work and took every opportunity to help us with our hardware and software needs. I would also like to thank Joshua Brown, NI field engineer for his time and technical helps.

My lovely labmates created a friendly and pleasant environment at MRL and offered their helps whenever needed. Amith Somanath, Andreas Schuh and Dimitrios Chatzigeorgiou are among the very first group of friends I met at MIT. Having them around was a true blessing. I especially thank my colleague and friend Andrew

Careaga Houck for his helps. He made working on the AFM project a much more pleasant experience. I also thank Dr. Jwaher Alghamdi for her helps on the study of nano-scale processes. I would also like to thank Axel Paugam-Goering, Dalei Wu, Audren Cloitre, You Wu, Bo Jiang and David Donghyun Kim.

I would like to thank Mechanical Engineering Department staff. I especially thank Ms. Leslie Regan. It is difficult to explain how heartwarming it was to have her here in the department. From the very first day of receiving the admission letter all the way to the day of submitting this thesis she was there to help, to share her experiences and to make sure we are all healthy and happy graduate students. I would also like to thank Ms. Catherine Ann Hogan for all her helps during the past few years. I also thank Mr. Pierce Hayward for helping me learn about many manufacturing tools and tricks from lathe to CNC machines, making things look much easier than they actually were.

I would also like to thank Prof. Ming Liang of the University of Ottawa, Canada. I started my exciting journey in scientific research under his supervision. I learned so much from him throughout my years at the University of Ottawa both scientifically and personally. His encouragements and support were and continue to be invaluable for my success and my professional development.

I am indebted to my parents for their unlimited love and support throughout my life. It is needless to say that I wouldn't have been where I am now in my life if it was not for them. I dedicate this work to my mother Prof. Mahvash Oskoui and to the memory of my father Abbas Soltani. I would also like to thank the love of my life, Parisa Emami-Naeini, for her encouragements and support in every step of this thesis work and for making life way more beautiful. I am very fortunate to have her in my life. I would also like to thank my sister, Shabnam Soltani, my brother in-law Alireza Ghaffari and my nephew and niece, Arvin and Lily, for being my family.

To my father, Abbas, and my grandparents, Maliheh and Seyed-Bagher

Contents

List of Figures

List of Tables

Chapter 1

Introduction

The invention of Atomic Force Microscope (AFM) [7], an offspring of the scanning tunneling microscope [8], paved the way for a new era of microscopy where images with sub-diffraction limit resolution could easily be obtained from samples with non-conductive surfaces. The flexility of AFM in imaging various samples in air, vacuum or in liquid has made it a popular instrument for nano-scale characterization and observation. This flexibility opened up doors to many novel scientific discoveries in the fields of biology and material sciences [41, 95, 80].

The mechanical nature and the serial-point-collection bases of operation of AFM limits its speed and introduces uncertainties on the extent of probe sample interactions and the reliability of acquired data. Hence, AFM has been mainly used for the study of static samples that reflect no or minimal variations over time. Enabling high-speed operation of AFM expands the applications of this instrument to the study of dynamic nano-scale processes [31] and opens up the possibility of many new discoveries in science and technology. The main focus of this thesis is to develop techniques that can unlock high-speed performance of AFM and at the same time achieve large lateral and out-of-plane scan ranges. For this purpose we have treated various aspects of AFM operation including control design, mechanical design, and instrumentation. At the heart of the AFM the sample/probe scanner has the most critical role in achieving the speed and range requirements. In addition to the scanner, the AFM control system, optical beam deflection setup, laser detection circuitry,

power amplifiers that drive the scanner, data logging and plotting system and the rest of instrumentation aspects of AFM such as amplitude demodulation unit should all meet stringent requirements. Given the variant operating conditions of AFM, e.g. due to various types of samples, and different imaging modes or imaging environments, these components should also benefit from a certain level of flexibility. Especially, the substantially variant dynamics of AFMs necessitates a flexible and robust control scheme that can maintain satisfactory performance at high imaging speed and on large scan ranges. In this thesis a multi-actuated scanning methodology is devised that leaves virtually no limit on the scanning range while it simultaneously achieves high-speed performance. The proposed control design schemes meet the requirements of high-speed large-range imaging and maintain the flexibility of AFM control to accommodate the variant nature of AFM operation. In addition to speed and range, positioning accuracy is maintained by treating the hysteresis nonlinearity of piezo actuators through a novel Maxwell model parameter estimation scheme. To improve the throughput of atomic force microscopes in tapping mode an amplitude demodulation technique based on the nonlinear Teager Energy Operator (TEO) is proposed and implemented in analog and digital forms. This demodulation scheme is specially suitable for parallel sensing via AFM probe arrays. Based on these fundamental developments a large-range high-speed AFM is designed and implemented. It is then shown that this implementation can be used to study various nano-scale material and electrochemical processes such as dissolution, deposition and stripping.

In the following we give a brief overview of AFM operation, discuss the root causes of its limitations and review the relevant prior art. This section also gives a summary of the material presented in this thesis and lists its main contributions.

1.1 Background

Atomic force microscope operates by scanning a micro-mechanical probe relative to the sample. It uses the probe-sample interaction measurements to form a 3D image of the surface topography. In one mode of imaging referred to as contact mode

the probe is continuously in contact with the sample. The deflection of the probe is measured and regulated in a feedback control loop to minimize the tip-sample interaction forces. The lateral (x,y) and vertical (z) position of the sample/probe are collected and plotted in the form of a topography image. It is common to plot the deflection (error) of the probe in a separate image to capture surface features that AFM control is unable to track. There are other imaging modes, such as dynamic modes, that aim to minimize the effects of probe lateral forces on the sample. In dynamic mode, the AFM micro-cantilever is excited to vibrate at or near its resonance frequency [39]. The interaction of the vibrating cantilever with the sample surface affects the amplitude, phase or frequency of vibrations [15]. In two variations of this imaging mode, probe vibration amplitude or frequency are utilized as the feedback parameter, referred to as amplitude modulated (AM) or frequency modulated (FM) imaging modes, respectively [125, 2]. Figure 1-1 schematically illustrates the principle of operation of an AFM in contact mode.

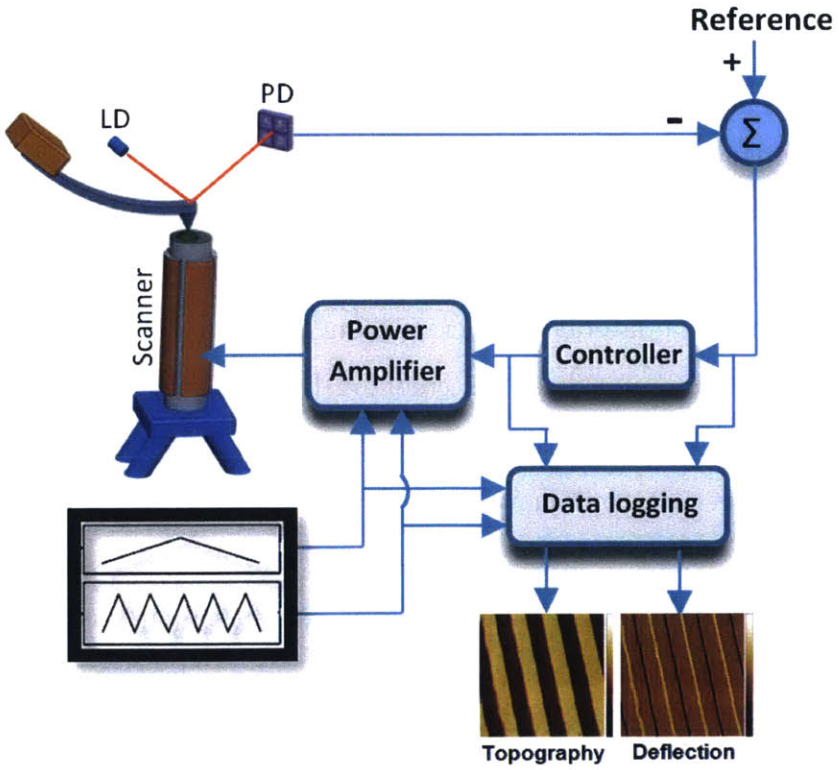

Figure 1-1: Schematics of AFM operation in contact mode based on an optical beam deflection detection setup.

1.1.1 Speed Limitation of Atomic Force Microscopes

The rate at which atomic force microscopes can capture images is very limited. In the following we discuss various components of AFM and their contribution to its speed limitation.

One major bottleneck is the scanner speed. Scanner is responsible for the lateral and out-of-plane motion of the sample or the probe. Like any mechanical system, the AFM scanner has a limited bandwidth and may demonstrate complex dynamic behavior at high frequencies. The frequency content of the command signal that drive the out-of-plane scanner actuator is dependent on the surface topography features and the probe speed. As the probe speed increases the sample surface topography features introduce higher frequency disturbances to the AFM probe. Assuming that the AFM controller is fast enough to respond to such disturbances, the out-of-plane actuator of the scanner experiences higher frequency excitations. As the frequency content of such disturbances approach the frequency ranges where AFM scanner demonstrate strong dynamics such as resonances the scanner behavior deviates from the expected. The dynamic response of the scanner usually appear as shadows and ripples in the acquired AFM images and may ultimately destabilize the AFM control. The first out-of-plane resonance of conventional AFM scanners (piezo tubes) can be around 5-7 kHz. Figure 1-2a shows an example AFM image that is smeared by out-of-plane dynamics. Similarly, for lateral scanner motion high-speed excitation can lead to image artifacts. In AFM imaging it is common for the lateral scanning motion to follow a triangular raster scan pattern. The command signal in this case is a periodic triangular wave. This pattern is shown in Figure 1-1 for both slow and fast scan axes. For high-speed imaging the frequency of the triangular wave is increased. As such, the higher harmonics of the scan command may excite the high frequency dynamics of the scanner and affect the quality of captured images. The first lateral resonance of conventional AFM scanners (piezo tubes) can be around 1 kHz. An example of the artifacts appearing on the AFM images due to the lateral scanner dynamics is shown in Figure 1-2b. As the scan speed increases these artifacts strengthen to a point that

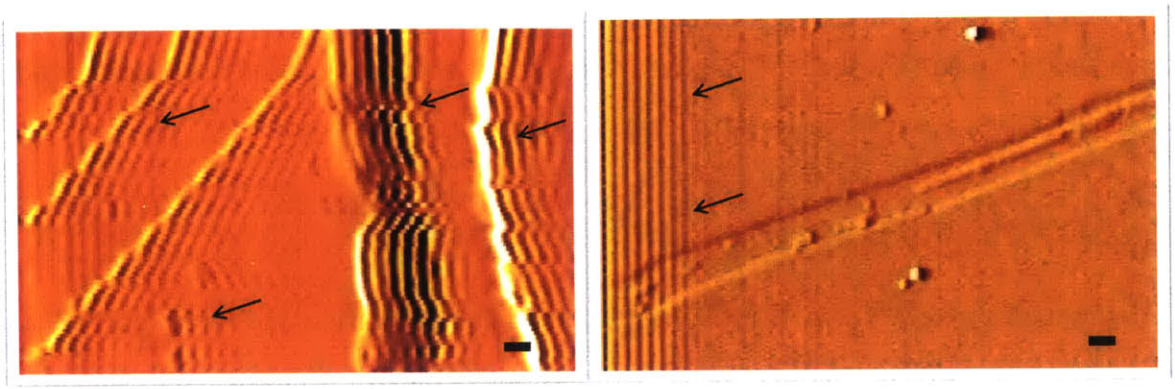

(a) (b)

Figure 1-2: Example effect of a) out-of-plane and, b) lateral scanner dynamics on a topography image of a freshly cleaved and sanded mica sample. Scale bars are 500 nm.

they fully undermine the applicability of the acquired images.

Probe is another important component of the AFM that may adversely affect its speed performance. Micro-cantilevers that are soft and large usually have very slow dynamics (low resonance frequency). As the imaging speed increases such probes can easily loose contact with the surface and disrupt imaging. One should ensure that the disturbances introduced to the probe by the sample surface topography do not excite cantilever dynamics. Although probes that have a larger spring constant may perform better in terms of speed, they apply larger forces to the sample and hence may damage the tip or the sample. Smaller AFM probes usually benefit from faster dynamics and potentially maintain a relatively small spring constant. In tapping mode, the Q factor of the probe also plays a crucial role in determining the maximum imaging speed. High Q-factor cantilevers have a slow response to sample surface topography changes and hence can significantly limit imaging speed.

The instrumentation and signal processing aspects of the AFM can also limit the scanning speed. For high-speed imaging the laser detection (photodiode) circuitry, and the power-amplifiers that drive the scanner actuators should be able to operate at high frequencies. Signal conditioning components such as the amplitude or frequency demodulation units (in dynamic mode) should also meet this criteria. Most importantly AFM controller should be able to regulate a minimal interaction force between

the sample and the probe to avoid probe/sample damage at high-speed. To maintain a reasonable image resolution, the data throughput requirements of the logging and plotting system also increases significantly at high imaging speeds.

1.1.2 Why high speed?

The main advantage of the AFM is its sub-nanometer resolution and its functionality in various imaging environments e.g. vacuum, air or liquid. Conventional scanning electron microscopes (SEM) may achieve nano-meter resolution but they operate only in vacuum and on conductive surfaces. These requirements limit the application of electron microscopy. Environmental SEM (ESEM) [25] aims to expand the application of the method to insulating or even wet samples. In this approach differential vacuum pumping maintains a vacuum pressure near the electron gun and allows higher pressures of up to 10 torr [28] near the sample. Although presenting a significant improvement relative to the conventional SEMs, ESEMs are still very limited on the type of samples that they can image. The relatively low sample pressure requires its operation at low temperatures (near freezing point) to avoid drying of wet samples. Furthermore, this microscopy technique can only provide topography information and hence for samples that are immersed in liquid it can only visualize the top surface of the liquid [9]. Transmission electron microcopy (TEM) techniques also require high vacuum. Environmental TEMs (ETEM) relax this requirement but suffer from similar limitations as those of ESEMs with the exception that they can be used to observe samples immersed in liquid [9] if the thickness of the liquid layer and sample combined is less than a few microns [51]. Aside from the imaging environment and resolution, one should note that bombarding the sample with a high intensity electron beam can also easily damage the sample [28, 9, 13] which even further limits the use of all electron microscopy techniques.

Given the resolution and flexibility of AFM, and the fundamental limitations of competing microscopy techniques such as ESEM and ETEM, AFM has become the instrument of choice in many biological or material science applications [107, 54, 86, 110]. By improving the speed performance of AFM, one can extend its application

to the study of dynamic nano-scale processes. Such an instrument can be used for real-time study of various material processes such as dissolution [96], deposition [110], polymer melting and crystallization [91], and phase transition in ferroelectric material [53]. It can also be used to study biological processes such as cellular events [109], or protein/biomolecule dynamics [16, 3, 57]. High-speed atomic force microcopy is also useful in high-speed nanofabrication [23], and for wideband nano-mechanical characterization of materials [87]. The research potentials brought about through high-speed atomic force microscopy technology have been the motivation behind several research efforts in this direction. In the following we review the various approaches taken during the past few years to improve the speed of AFMs.

1.2 Prior Art

To enable high speed performance of AFMs, all the bottlenecks of the instrument should be identified and treated. A great portion of earlier research efforts focus only on one selected aspect of AFM operation. In these research approaches, the improved aspect is commonly implemented and evaluated on an existing commercial AFM. In another category, limited to very few efforts, a full design of the AFM for high-speed operation is presented. The research results reported by both groups of researchers are reviewed in the following based on the addressed AFM operation aspect.

1.2.1 Lateral Scan Pattern

As explained in section 1.1.1 triangular raster scan pattern (Fig. 1-3a) is commonly used to move the sample or probe in the lateral directions. At high speed, the sharp turnarounds of this pattern excites the scanner dynamics. One approach to improve the AFM scan speed is to use other scan patterns that avoid such sharp turnarounds. Spiral scan pattern (please see Fig. 1-3b) [71, 74] in both constant linear velocity and constant angular velocity have been implemented on conventional AFMs, demonstrating improved scan speed. Two other examples are cycloid [122] and Lissajous [5] scan patterns shown in Figs. 1-3c and d, respectively. The triangular

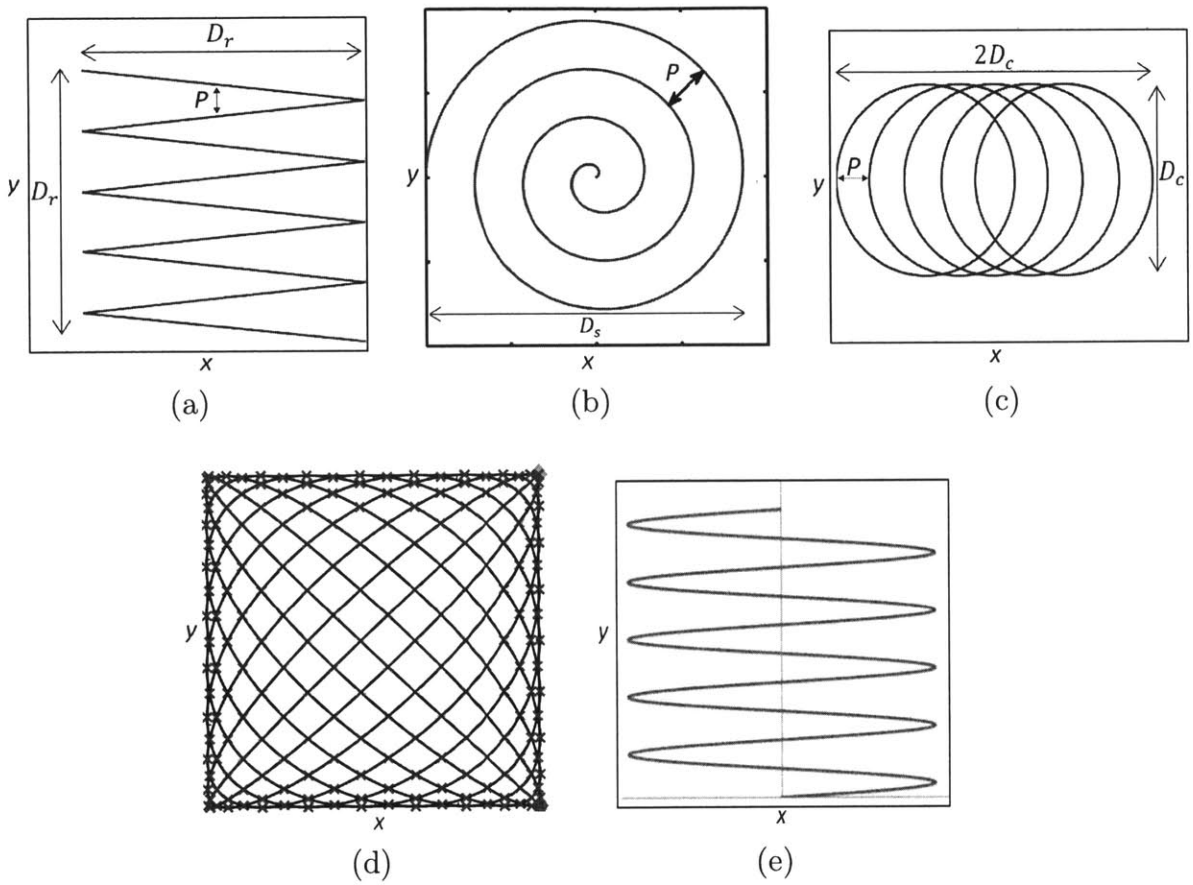

Figure 1-3: a) Triangular raster, b) Spiral [71], c) cycloid [122], d)Lissajous [5] and e) sinusoidal raster [20] scan patterns

raster scan pattern has also been replaced by a sinusoidal raster scan [20] as shown in Fig. 1-3e.

1.2.2 Lateral Scan Control

Through various control techniques researchers have tackled the nonlinearities as well as dynamic behavior of the lateral AFM scanners. The open-loop control arrangement of Fig. 1-4a is one common implementation scheme [64]. When position sensors are available, feedback control [24, 72] can be applied as shown in Fig. 1-4b. Fig. 1-4c shows an arrangement where a combination of feedforward and feedback control in the form of a 2DOF scheme is used for lateral scan [22, 111, 126]. The nonlinearities of AFM scanner such as creep and hysteresis are specially treated in applications

where positioning precision is of great concern. This is achieved by incorporating an inverse model of nonlinearities (denoted by H^{-1} in the figures) in the control system [85, 106]. Lateral scanner dynamics is only problematic at high scan speeds and hence is compensated when imaging speed is to be improved. An effective approach is to form an inverse of the scanner dynamics. The applied model inversion approach should ensure of the stability of the resulting system especially for scanners with non-minimum phase behavior [127]. Given the properness of scanner dynamics the adopted model inversion technique should also ensure of system roll-off at high frequencies to avoid saturation and noise amplification [22].

Unlike out-of-plane scan where the unknown sample surface topography-features determine the positioning command, the lateral scan pattern is known apriori. The availability of this information makes it possible to utilize noncausal feedforward controllers [67]. Non-causal controllers are in general easier to implement and outperform their causal counterparts in terms of system phase response. Periodicity is another important characteristic of the lateral scan motion in imaging applications. This feature opens up the possibility of utilizing inversion-based iterative control techniques (IIC) [22, 67]. In these methodologies the controller parameters can be adaptively updated from one actuation cycle to the next. This feature is valuable in atomic force microscopy where scanner dynamics can change considerably from one imaging experiment to another.

In addition to the inversion based control, modifications to the actuator drive circuitry have proven effective in improving the scanner precision and speed. Active damping techniques have been utilized to reduce the effect of scanner resonances at high speeds [72, 59]. Application of charge amplifiers instead of voltage amplifiers to drive the piezo actuators of the scanner can reduce the effect of hysteresis nonlinearity and improve scanner positioning precision [33].

1.2.3 Out-of-Plane Tracking Control

The requirements of out-of-plane tracking motion of the AFM scanner are more stringent than those of the lateral scan motion when it comes to high speed imaging. The

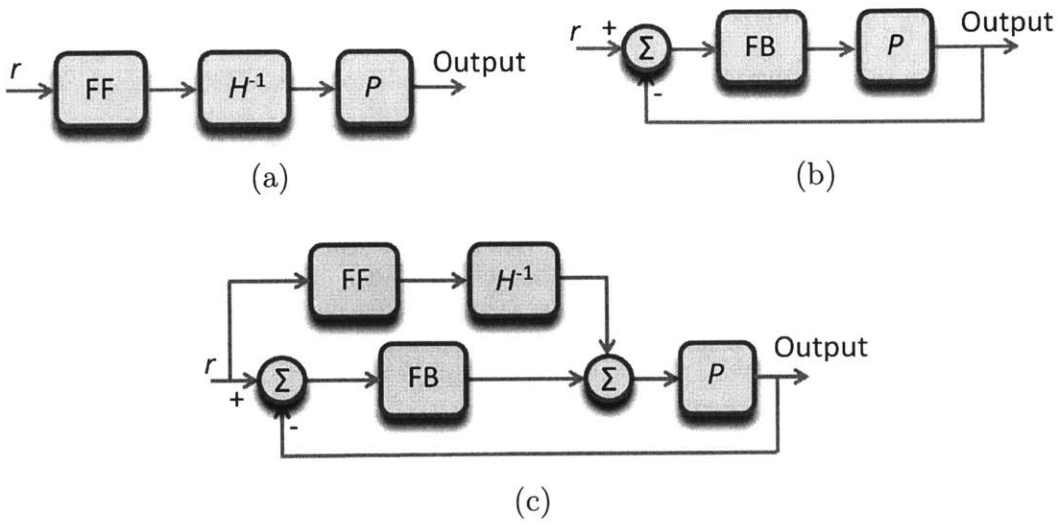

Figure 1-4: Control for lateral scanning motion: a) open-loop control, b) closed-loop control, and c) two degree of freedom combined feed-forward and feedback control. Nonlinearity compensation is denoted by H^{-1}.

inability of AFM scanner to maintain a minimal interaction force between the sample and the probe leads to tip or sample damage. It is important to note that the aim of high speed AFM is to observe nano-scale processes. Such processes are invariably very sensitive to the smallest external disturbances. It is very important to keep the AFM operation as noninvasive as possible by ensuring that the finest sample features are properly tracked and the tip/sample force is well regulated. As such, the out-of-plane closed loop control is one of the most important components of an atomic force microscope. The commonly used control strategy in AFMs is proportional-integral-derivative (PID). Although there have been some efforts to replace the PID unit with optimal and robust control schemes [1, 102, 99], it has remained popular due to its adjustable parameters and hence adaptability to various imaging tasks. Assuming that the sample profile does not change significantly from one scan line to the next, a two degree of freedom, combined feedforward and feedback control scheme has also been proposed for AFM control [98] where the last recorded scan line drives the feedforward control. Active damping techniques have also been used to restrain the dominant out-of-plane scanner resonance and hence extend the AFM tracking bandwidth [58].

Regardless of the adopted control strategy, the tracking performance is limited by the mechanical bandwidth of the out-of-plane positioner. To improve tracking beyond the available bandwidth of AFM scanner, researchers have adopted dual actuation schemes [101, 35, 61, 108, 50, 75, 30, 36, 32, 120, 60, 55]. In this approach the tracking responsibility is divided between two actuators where one is slow and large range and the other fast and short range. Earlier work on dual actuation can be divided into two main categories. In one, self-actuated AFM probes are used in combination with external piezos [108, 50]. In the second category [101, 35, 59, 75], two external piezo actuators are used on independent substrates to avoid dynamic coupling where one actuator moves the sample and the other moves the probe. To control these actuators some researchers [108, 75] have applied separate controllers in a nested feedback loop, with each loop controlling a single actuator, and others used optimal control schemes to divide the tracking task between the two positioners [101, 60].

1.2.4 Scanner Design

Conventional atomic force microscopes operate on tube scanners [19]. In this design a single piezo tube with inner or outer metal coating is sectioned into 4 quadrants. Actuation of paired X or Y quadrants leads to the bending of the tube in the lateral direction (Fig. 1-5). When actuated all together, the same quadrants are capable of providing z extension, although in some designs an independent piezo ring is responsible for out-of-plane (z) motion [124]. Piezo tubes are very simple in design and usually operate over relatively large ranges. However, they are not suitable for high-speed operation due to their relatively low-frequency dynamics in both lateral and out-of-plane directions.

A part of research on high-speed atomic force microscopy focuses on the design of faster scanners. These efforts are mainly geared towards the development of flexure-based nano-positioners that operate on piezo stack actuators. Generally flexure mechanisms can be designed to effectuate a mechanical amplification of the actuator range [121]. In such designs a normal piezo stack actuator may generate hundreds of microns of travel range although at a reduced speed. The objective for the design of such flex-

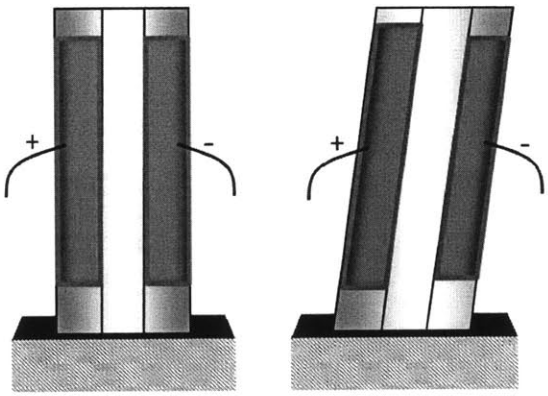

Figure 1-5: Principle of operation of piezo tubes.

ure mechanisms is then to maximize the travel range with a minimal compromise on the positioning bandwidth. Most of the flexure-based high-speed scanners designed so far, only kinematically constrain the positioning stage and pre-load the incorporated piezo stack actuators without introducing any mechanical amplification. Preloading the piezo stacks can in fact be very helpful to reduce the piezo load-dependence and vulnerability to tensile stress. Depending on the stiffness of the preloading structure it can reduce the travel range. As such, in these designs the scanner positioning range is smaller than that of the utilized piezo actuators reaching a few microns (~10um), while achieving several kilohertz (~10 kHz) bandwidth [12, 3, 4, 123, 117, 100].

Figures 1-6 (a) to (d) show a few examples of flexure designs for high speed imaging. In all the designs, the Z positioner is stacked on the X-Y stage. The lateral positioning can be based on either parallel [100] or serial [4, 117] kinematics. Scanner designs with serial kinematics can do a better job in terms of decoupling the lateral X, Y axes.

1.2.5 AFM Probes

The mechanical bandwidth of the AFM micro-cantilever directly influences the imaging speed of the instrument. For AFM probes with similar size, larger spring constant (stiffer probes) naturally leads to higher resonance frequency and hence better performance at high imaging speeds. However, for larger spring constant the force sen-

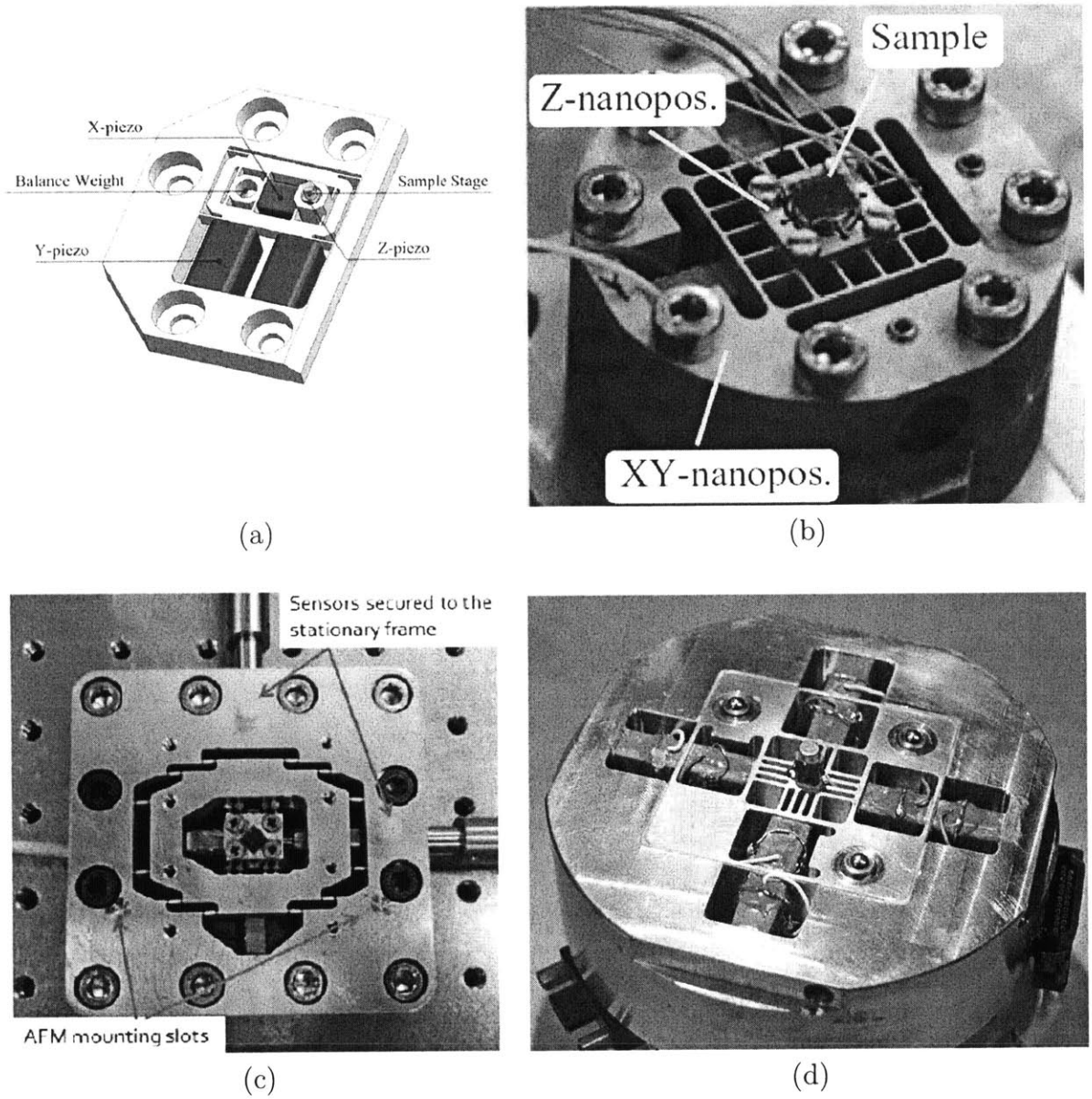

(a) (b)

(c) (d)

Figure 1-6: Examples of high-speed flexure-based scanner designs: a) Ando et. al [4], b) Yong et. al [123], c)Wadikhaye et. al [117] and d) Schitter et. al [100]

sitivity decreases and the tip-sample interaction force increases, potentially leading to probe or sample damage. As mentioned earlier, the main purpose of high-speed imaging is to non-invasively observe delicate nanoscale processes. As such, minimizing the tip-sample forces goes a long way in maintaining the reliability of the captured images.

By reducing the size of AFM probes one can increase their mechanical bandwidth and simultaneously achieve a reasonably small spring constant [119, 90]. Several research efforts have focused on the development and application of small AFM probes [46, 17, 116, 118, 66]. Figure 1-7a shows a side by side view of the newer generation of small AFM probes suited for high-speed imaging in comparison to their larger conventional counterparts [112]. The length, width and thickness of commonly used conventional AFM probes are usually around 100 $\mu m, 30\mu$ m and 1μm, respectively. These values for small AFM probes can be as small as $10\mu m, 2\mu$ m and 100 nm, respectively.

Another approach to increasing AFM imaging throughput is to use multiple probes in parallel. This requires application of an array of AFM probes instead of a single probe. In this form individual AFM probes need to be self-actuated so they can follow their corresponding sample surface topography. The probes also need to be able to provide independent readings of the cantilever deflection which requires incorporated sensing. Very few research efforts took this route by making self-sensed and/or self-actuated probe arrays [56]. Figure 1-7b shows an array of 25 self-sensed and self-actuated probes. The actuation mechanism is usually based on piezoelectric coating of the micro-cantilever [56] although other approaches such as bimorph actuation has also been deployed [14]. Self-sensing is based on either the piezoelectric [104] or piezoresistive coatings [114]. One impediment towards vast application of this technique is the requirement of independent control and signal processing for individual probes. This is specially challenging in tapping mode where amplitude or frequency demodulation of the individual probe vibration signals is additionally needed.

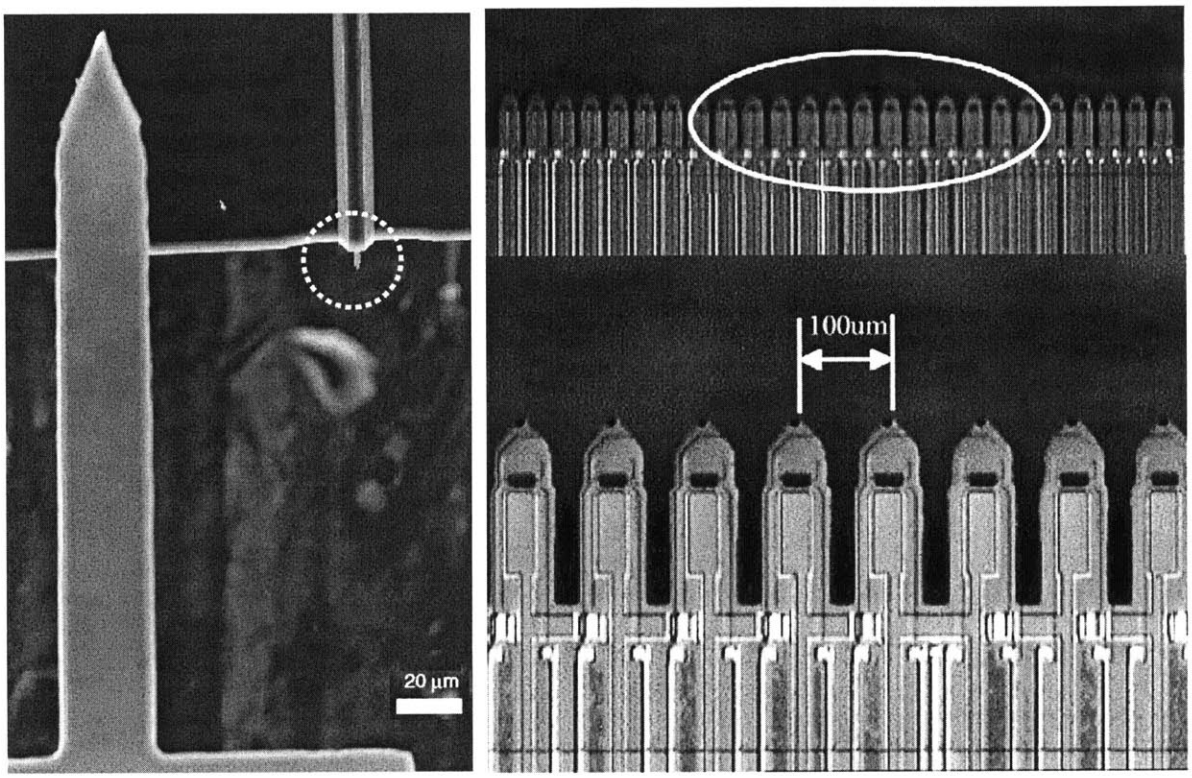

(a) (b)

Figure 1-7: a) A side by side comparison between the large conventional and the newer generation of small AFM probes [112], and b) an array of micro-fabricated self-sensed and self-actuated AFM probes. [56]

1.2.6 Optical Beam Deflection Setup

Upon reducing the size of AFM probe for faster dynamic performance, the optical beam deflection setup should also be improved. Conventional AFM probes are considerably wider and longer than their high-speed counterparts and hence can accommodate a large laser spot size ($\sim 30\ \mu$m). For small cantilevers however, the laser spot size should be reduced to a few microns to avoid leakage of incident laser beam. Laser leakage reduces the intensity of the laser reflected off the AFM probe and increases the parasitic reflections from the sample and other AFM surfaces. These effects are detrimental to the signal to noise/intereference ratio of the measured deflection signal.

Research efforts in the past have addressed the required changes in the optical setup of AFMs operating on small cantilevers [115, 37]. These designs usually have a more compact arrangement and utilize higher quality optical components with minimal abberations, a well collimated laser source and a focusing lens with higher numerical aperture [38]. One such approach is based on co-axial laser measurement where the laser beam reflected off the cantilever beam is collected through the focusing lens. This arrangement allows for the application of higher numerical aperture lenses with smaller working distance [115, 112].

1.2.7 Instrumentation

As the mechanical bandwidth of the probe is boosted, the associated instrumentations i.e. the photodiode circuitry should also be improved for a wider measurement bandwidth. This makes the system more vulnerable to high frequency noise and interferences. As such, it is important to minimize the effect of various noise sources. Specially the effect of laser diode instabilities e.g. mode hopping needs special attention. This problem similarly faced in videodisc players has been mitigated through RF modulation of laser source drive [88]. This approach has also been undertaken to reduce the optical feedback noises in AFMs [38, 37].

In addition to the laser drive and detection, other instrumentation components of AFM such as scanner drivers have been investigated. In [34] the limiting aspects of

a piezo driver are identified and a wide-band dual-amplifier is presented. To reduce the piezo hysteresis nonlinearity on AFM imaging performance, high-speed charge amplifiers have also been designed [33].

1.3 Thesis Overview

The main focus of this thesis work is to develop control, positioning and instrumentation methodologies that enable high-speed and large-range atomic force microscopy. The result of the developments in this thesis is a novel atomic force microscope capable of high-speed imaging and featuring large out-of-plane and lateral scan ranges. In addition to technical advantages, this instrument benefits from a modular and easy-to-use design, it is compatible with small cantilevers, features an optical view to the sample and probe for site selection and laser adjustment, and has a large sealed sample stage suitable for imaging in air or in liquid. In the following we give a brief overview of the main contributions and the development path adopted in this thesis work.

1.3.1 Lateral and Out-of-Plane Scan Motion

The thesis starts by an evaluation of the possible scan arrangements i.e. probe-scan vs sample-scan in section 2.1. The smaller carried mass in the sample-scan arrangement (see Fig. 2-1) and the associated potential for high-speed performance leads us to adopt this design. We then take a closer look at candidate scan patterns (Fig. 1-3). Following a qualitative/quantitative comparison in section 2.2 (Tables 2.1 and 2.2) we propose to use a raster scan pattern with position triggered sampling (Fig. 2-3). It is discussed that in this form one can benefit from the constant linear speed and the zero-scan-angle property of triangular raster scan up to a certain frequency. At very high scan frequencies ($f_{\text{scan}} > f_b/7$, f_b is the available lateral mechanical bandwidth) where the higher harmonics of the scan pattern fall beyond the mechanical bandwidth of the scanner (Fig. 2-4), the triangular raster scan pattern is smoothed on the turnarounds and in the limit approaches a sinusoidal pattern instead. This leads to variations of

the sample lateral velocity. However, due to the position triggered sampling strategy the variations of lateral instantaneous speed is seamlessly accepted by the AFM. In this form one can use the full mechanical bandwidth of the scanner. An evaluation of possible actuation mechanisms follows in section 2.3. In this section we aim to ensure that the actuation methodology best suitable for our AFM design is selected. Through quantitative/qualitative comparison between two major candidates namely piezo-actuators and lorentz force actuators we show that piezo actuators are better equipped to tackle the challenges of high-speed large-range AFM imaging.

1.3.2 AFM Control

Following the determination of scan arrangement, scan pattern and actuation mechanism we study the peculiar requirements of AFM control in section 3.1. The variability of AFM dynamics is highlighted in this section calling for a control methodology that can be easily tuned/updated. It is argued that PID controllers as have widely been used in AFMs meet the flexibility requirements very well. In section 3.2 we evaluate the conditions under which a PID controller suffices to meet the performance requirements of high-speed large-range out-of-plane tracking. Understanding these requirements helps us design control schemes that ensure of the optimal performance of the PID unit. This is done in section 3.3 where additional controllers, auxiliary to a PID unit, are designed (Fig. 3-1). The design of these auxiliary controllers is kept as simple as possible for easy update. A novel data-based control design strategy is proposed that solely relies on the measured response of the scanner to a wideband excitation signal and does not require any models of the scanner behavior. The data-based control design strategy is proposed in a general form for multi-input single-output actuators. This is to accommodate redundantly actuated scanners.

A similar data-based compensator design strategy also suitable for redundantly actuated scanners is proposed for lateral scan control. However, for the lateral scan, the possibility of non-causal control design and implementation is exploited (Fig. 3-7). In the proposed form the designed compensators are decomposed into non-causal and causal portions. The non-causal portion can tackle more critical aspects of control

task, mostly limited in a causal implementation, such as phase matching, hysteresis compensation and/or frequency assignment. The causal portion on the other hand takes care of the requirements critical to closed-loop implementation such as scanner dynamics. This arrangement makes us able to meet the positioning accuracy and speed requirements of lateral slow and fast scan directions, respectively.

1.3.3 Nano-Positioning with Redundant Actuation

In chapter 4 the proposed data-based compensator design scheme is used to control two fundamentally different redundantly actuated AFM scanners (Figs. 4-7 and 4-27). In one design a counterbalancing piezo actuator is incorporated into the AFM scanner to suppress the excited out-of-plane dynamics (Fig. 4-5). The principle of operation and the limitations of this technique is discussed in detail in section 4.2.1. It is shown that under non-ideal circumstances not only the counterbalancing is unable to suppress the excited vibrations it may in fact increase their intensity, leading to an inferior AFM performance (Fig. 4-15-left). To tackle these limitations we propose to shape the command signal that drives the counterbalancing piezo in section 4.2.2. A compensator is formed using the data-based design approach. The method is tested on an atomic force microscope and the resulting improvements are demonstrated experimentally in section 4.2.3.

The proposed data-based compensator design scheme is then adopted to the control of a retroactively enhanced piezo-tube scanner in section 4.3. This section starts by presenting a simplified model of a cascaded series of multiple actuators. The dynamic coupling phenomenon is discussed and the necessity for dynamics compensation is highlighted. A high-speed flexure cap (Fig. 4-27) is designed, built and incorporated into the conventional tube scanner. The out-of-plane motion of the resulting multi-actuated positioner is provided by the combined operation of the slow/large-range piezo tube and the fast/short-range flexure cap. In this form the large-range of the tube and the high speed of the flexure cap are used to achieve large-range high-speed positioning performance. The role of the compensators is to divide the positioning responsibility between the actuators and simultaneously compensate for

their coupled dynamics. The effect of this approach on imaging performance is experimentally evaluated on a conventional atomic force microscope. It is shown that this technique can improve the tracking bandwidth performance of the AFM by more than an order of magnitude. The most valuable aspect of the method is that the improvement in bandwidth comes without any compromise on the tracking range of the AFM. These are demonstrated on the imaging performance of the AFM in contact and tapping modes, in air and in liquid (Figs. 4-33, 4-34 and 4-35).

Finally the multi-actuation methodology is extended to the lateral positioning of a general scanner. The proposed control structure (Fig. 4-36) includes a non-causal frequency division step based on Fourier decomposition that divides the positioning responsibility between different lateral actuators. Several optimal delay units are also included in the control to ensure the response of each actuator is in phase with that of the largest-range actuator of the scanner. This is necessary to ensure of constructive superposition of individual actuator responses and to avoid distortion of overall lateral positioning. The proposed structure also features a closed loop control scheme that ensures of positioning precision.

The results reported in section 4.3 show us the great potential of the multi-actuation methodology to enable high-speed large-range AFM imaging. These capabilities are partially unlocked by retroactively enhancing a conventional AFM. To fully explore the method we continue by designing and implementing a multi-actuated nano-positioner composed of several fast/short-range and slow/large-range actuators in chapter 5. The lateral and out-of-plane multi-actuation control schemes proposed earlier are implemented on this custom-made AFM scanner.

1.3.4 Design and Control of a Multi-Actuated High-Speed and Large-Range Nano-Positioner

To enable effective design of our multi-actuated nano-positioner we start by taking a closer look at the dynamic model of a cascaded series of multiple actuators. In section 5.1 we analytically demonstrate that by reducing the mass carried by the

faster actuator or increasing the mass carried by the slower actuator in a two actuator setup one can lessen the intensity of the dynamic coupling. This observation can be used to properly distribute the masses in the design of the multi-actuated scanner. The designed scanner is shown in Fig. 5-1. It is composed of 5 nano-positioners: 1) A high-speed (100 kHz) short-range (1 μm) flexure cap for out-of-plane positioning, 2) a short-range (10 μm) and high-speed (7 kHz) shear piezo for fast lateral motion, 3) A relatively slow and large-range (6 μm) flexure-diaphragm designed for large-range out-of-plane tracking, 4) a slow (140 Hz) and large-range (120 μm) scanner aligned along the fast lateral scan axis and 5) another slow and large-range (120 μm) lateral positioner aligned along the slow lateral scan axis. The design of the flexure components of the scanner are explained in detail in section 5.2 (Fig. 5-2). Following the design, the control schemes proposed in sections 4.3.3 and 4.3.5 are implemented to drive the out-of-plane and fast lateral scanner positioners. The dynamic performances of the scanner with and without the application of proposed control are demonstrated in Figs. 5-4 and 5-7.

The control of slow lateral positioner that is responsible for frame-up frame-down motion disregards dynamics compensation and puts further emphasis on the positioning precision 5.5. This is to ensure that the consecutively acquired AFM images match well so that they can be compiled into a video. The control is composed of a feedforward nonlinear hysteresis compensator based on the Maxwell model and a PID feedback controller that utilizes the position measurement output of a capacitive sensor (Fig. 5-15). The Maxwell model of hysteresis is intuitive, easy to implement and does not require model inversion. These features make it an attractive modeling choice. However, the conventional Maxwell model parameter estimation fully relies on the validity of the corresponding physical basis. With this assumption only the initial rise portion of piezo displacement in response to a ramp input (i.e. origin to first maximum) is needed to solve a set of linear equations and find the unknown parameters of the model. This however, leads to modeling error. To improve the estimation accuracy we modified the estimation step such that it can utilize the full hysteresis loop. In this form, instead of solving a set of linear equations, the pa-

rameter vector is obtained in the least mean square error sense using the positioning measurements in response to a periodic triangular command. In the identification step one can excite the piezo for as many cycles as needed and use the whole length of measured data to make a more reliable estimate of model parameters. This approach showed very effective in compensating for the hysteresis of lateral slow axis positioner when applied in isolation (Fig. 5-16) and also as part of a 2DOF nonlinear feedforward-feedback scheme (Fig. 5-17).

1.3.5 Amplitude Demodulation Based on Teager Energy Operator

A fundamental limitation in tapping mode imaging is rooted in the relatively slow dynamics of a vibrating probe. Micro-mechanical cantilevers are often minimally damped leading to high Q-factor oscillations at resonance. The higher the Q-factor the slower the prob reaction to topography changes on the sample. An approach with great potential to compensate for this limitation is to use parallel sensing with probe arrays (Fig. 1-7b). However, this approach also requires an array of processing units that extract instantaneous amplitude of vibration of individual probes. As such, a computationally inexpensive amplitude demodulation scheme that can be implemented in array form accommodating hundreds of its replicates with minimal cost can be very valuable. Chapter 6 presents one such processing methodology. It is based on the nonlinear Teager Energy Operator (TEO). Sections 6.2.1 and 6.2.2 discuss the continuous-time and discrete-time versions of this operator, respectively. It is analytically shown that both continuous and discrete time forms of TEO are capable of extracting the instantaneous amplitude of the deflection signal measured from an oscillating probe.

Sections 6.3 and 6.4 discusses digital and analog hardware implementations of TEO, respectively. To reduce the effect of quantization noise without any compromise on the control loop rate, the digital form of TEO is generalized (Eq. (6.11)) to accommodate arbitrary delays in-between the input samples. For the analog im-

plementation the destructive effect of phase-lag associated with the non-ideality of differentiators are discussed. This limitation is treated through phase compensation (Fig. 6-6). It is then proven that phase compensated version of TEO is in essence equivalent to an implementation with ideal differentiators but operating on a lowpassed version of the input signal (Fig. 6-6). Both the analog and digital implementations of TEO are tested on synthetic amplitude modulated signals (Fig. 6-9). This demodulation technique is also tested on the imaging performance of an atomic force microscope (Fig. 6-10).

1.3.6 MIT Large-Range High-Speed AFM Design

The developments presented in chapters 2 to 6 are used as the bases for the design and implementation of a high-speed large-range atomic force microscope. Details of the design are given in chapter 7. This instrument utilizes the multi-actuated nano-positioner discussed in chapter 5, and the control schemes proposed in section 4.3. The optical beam deflection detection system is based on co-axial laser measurement and provides an optical view to the sample and probe for sample site selection and laser adjustment. Figures 7-1, 7-2 and 7-3 illustrate the design of this AFM setup. A description on the design of photodiode and piezo drive circuitry are given in section 7.1.2. The implemented AFM setup is used to study nano-scale processes in real-time. First etching of calcite in a diluted solution of sulfuric acid is visualized in real-time where layer by layer removal of calcite is captured. In another set of experiments, the electrochemical process of deposition and striping of copper on gold is visualized for the first time.

1.3.7 Fixed-Point Implementation of IIR Filters on FPGA Targets

All the control schemes proposed in this thesis are implemented on FPGA platforms. Details on the fixed point implementation of these controllers on FPGA is discussed in appendix (A). Given the lack of a unified learning package on the topic, this appendix

is written with a tutorial theme so that it can be used in isolation from the rest of the thesis by researchers, students and engineers in the field.

Chapter 2

Lateral and Out-of-plane Scan Motion

In this chapter we take a close look at the lateral and out-of-plane motions of the AFM scanner. We start by discussing possible arrangements for relative displacement of sample and probe and their potential for high-speed performance. We also discuss the lateral scan patterns and the available actuation mechanisms. Our proposed scan arrangement, scan pattern and actuation methodology are presented based on these analysis and discussions.

2.1 Sample-Scan vs Probe-Scan

The relative motion of the probe with respect to the sample can be achieved by moving the probe, the sample or both. AFMs that operate by scanning the sample along the three X, Y, Z directions with respect to a stationary probe are referred to as sample-scan. The design of these AFMs can be potentially simpler as in this form the optical beam deflection setup is stationary. This arrangement is shown in Fig. 2-1a.

In contrast, probe-scan atomic force microscopes have a stationary sample stage and a moving probe (see Fig. 2-1b). The probe-scan AFMs can accommodate large samples. They can also be combined with an inverted optical microscope (Fig. 2-1b) potentially leading to more information about the sample. The view of the inverted microscope to the sample and the probe also makes it easier to functionalize the tip

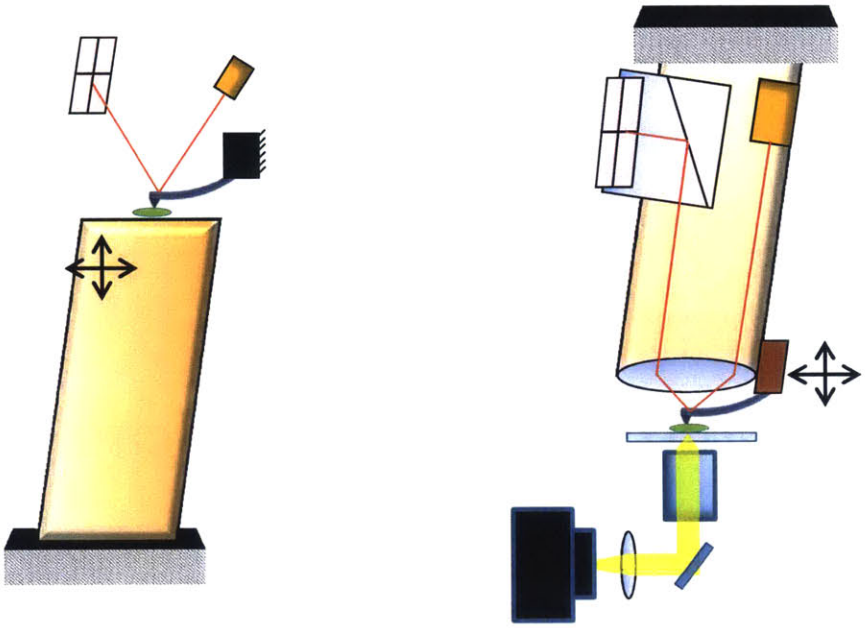

(a) (b)

Figure 2-1: AFM sample/probe scan arrangements: a) sample-Scan, and b) probe-Scan combined with inverted optical microscopy.

e.g. for biomolecule detection, force spectroscopy, etc. Furthermore, in this form it is possible to combine atomic force microscopy with other optical microscopy techniques such as fluorescent microscopy, confocal microscopy, etc [65]. Such a multi-functional instrument has the potential for some interesting research work such as studying the mechanotransduction characteristics of cells [18]. However, in probe-scan AFMs, for the laser beam to properly track the probe, some of the optical components of the system need to be moved along with the probe. As the optical beam deflection (OBD) setup is usually bulky and contains relatively heavy optical components, it is in general more challenging to adopt a probe-scan AFM design for high-speed imaging. Here we select a sample-scan arrangement for our AFM design. All the statements in the rest of this thesis work are made in reference to a sample-scan AFM arrangement. Although, most of the techniques developed here can be easily extended to probe-scan designs.

2.2 Selection of Scan Pattern

As explained in section 1.2.1 a simple approach to improving the scanning speed of an AFM is to use scan patterns that feature smooth path curves. This is to avoid excitation of scanner dynamics at high speeds. However, for the selection of suitable scan pattern one should also take into account other characteristics directly associated with the probe/sample interactions, namely probe instantaneous speed and scan angle.

Triangular raster scan pattern constitutes sharp turnarounds which limit scan frequency, but it has certain advantages. One advantage of the raster pattern is the associated constant scan angle. It is customary to measure the scan angle with respect to the cantilever longitudinal axis. A scan direction that is aligned with the probe longitudinal axis has a zero scan angle (see Fig. 2-2a). With zero scan angle the sample surface topography is almost fully reflected in the probe deflection (cantilever bending) and can be picked up by the photodiode differential measurements. This is not the case for a non-zero scan angle where surface topography can also lead to the torsion of the probe (see Fig. 2-2b). The extreme case correspond to a scan angle of 90 degrees where the effect of topography on probe torsion is maximal. At this angle the frictional forces between the probe tip and the sample, also contribute to the rotation of the probe. One might be able to infer certain information about the frictional properties of the sample when scanning the sample at 90 degrees scan angle. As such, in conventional atomic force microscopy, zero scan-angle is reserved for topography tracking and 90 degrees scan-angle is applied for the study of sample surface frictional properties (friction force microcopy (FFM)). One can easily switch between the two modes by exchanging the fast and slow scan axes when using raster pattern. In all the non-raster scan patterns e.g. cycloidal, spiral and Lissajous the scan angle is continuously changing (see Fig. 1-3). This limitation should be kept in mind when comparing various scan patterns.

Another important advantage of the triangular raster pattern is the associated constant velocity of the sample. For a given sample surface spatial frequency content,

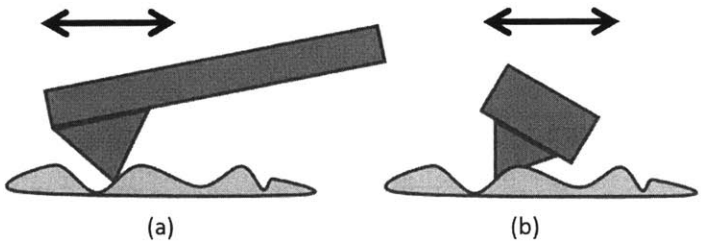

Figure 2-2: Scan Angle: a) scan direction matches the longitudinal axis of the cantilever (zero scan angle), and b) scan direction is perpendicular to the longitudinal axis of the cantilever (90 degrees scan angle).

faster relative probe-sample speed corresponds to higher frequency content of the disturbances to the probe. As the out-of-plane tracking bandwidth of the AFM scanner is finite, for a given sample spatial frequency content there is a maximal sample speed beyond which AFM is unable to properly regulate the tip-sample interaction forces. As such, for a given out-of-plane tracking bandwidth, the fastest coverage of the scan area is achieved when the sample is moved at this maximal speed at all times i.e. at a constant linear velocity. Furthermore, variable scan speed leads to inhomogeneity in the distribution of deflection error and may make parameter tuning and image interpretation more difficult. Another consequence of variable linear speed is image distortion at a constant sampling rate. For a given sampling rate and assuming a constant instantaneous scan velocity, a unform sampling of the AFM image is obtained. However, variable velocity leads to variations in the density of acquired image data-points and image distortion. In addition to the above two advantages (constant velocity and zero-scan-angle), the raster scan pattern (both sinusoidal or triangular) makes data logging and image formation straightforward. Every block of data captured synchronous with a scan line during raster scan imaging, matches a single row of the N by M image matrix. In other words, the location of the captured data points in the corresponding N by M image matrix approximately matches the cartesian coordinates of the pixel in the image plane. As such, every matrix of acquired data can be directly plotted or saved as a captured image. This does not apply to cycloid, spiral or Lissajous patterns. For these scan patterns one needs to find the nearest cartesian coordinates (e.g. in terms of Euclidean distance) associated with

every captured data point in order to form an image [74].

Given the above discussion, in the following we make a comparison between various scan patterns listed in section 1.2.1. Based on the comparison results the scanning strategy to be adopted in this thesis for high-speed atomic force microscopy is then described.

The imaging speed associated with each scan pattern, expressed as sweep-rate (unit area/sec), is listed in Table 2.1. To make a fair comparison, the sweep-rate calculations are made for images with similar scan pitch, p. A smaller pitch value leads to a better image resolution. The pitch value for each scan pattern is denoted in Figs. 1-3a to c (pitch and image dimensions are defined similarly for raster and sinusoidal patterns). The comparison is based on images with approximately equal area, hence we assume D_s=$2D_r/\sqrt{\pi}$ and D_c=$D_r/\sqrt{1+\pi/4}$. A periodic triangular command signal is composed of infinite Fourier components. Here we assume that at least 7 harmonics of the scan frequency are needed to maintain the authenticity of the raster scan pattern. It is also assumed that the dynamics of the scanner (e.g. resonances) are well compensated as proposed in many of the prior research works [22], leading to a relatively flat frequency response for the lateral scanner. The mechanical bandwidth of the compensated scanner is denoted by f_B. The comparison includes spiral (constant angular velocity), cycloid, triangular-raster and sinusoidal-raster scan patterns. Lissajous pattern includes many self-intersections (revisit of already visited sample sites) and spiral with constant linear velocity encounters the dynamic limitations of the scanner when approaching the center of the spiral pattern [73]. Hence, these two patterns are not included in the comparison. Table 2.1 also shows if each scan pattern meets or violates the constant instantaneous velocity and zero scan angle characteristics. Table 2.2 lists the sweep rates, normalized with respect to that of the triangular-raster scan pattern denoted by S_n. The maximal instantaneous probe speed normalized with respect to that of the triangular-raster pattern, denoted by v_n is also listed in this table. A larger S_n is apparently preferred. A v_n value that is close to S_n is reflective of the effectiveness of the scanning pattern in achieving higher scan speed without significantly increasing the maximal instantaneous speed of the

	Triangular Raster	Sinusoidal Raster	Cycloid	Spiral
Sweep rate	$\frac{2PD_rf_B}{7}$	$2PD_rf_B$	$\left(1+\frac{\pi}{4}\right)D_cPf_B$	$\frac{\pi D_sf_BP}{2}$
Max tip speed	$\frac{2D_rf_B}{7}$	πD_rf_B	πD_cf_B	πD_sf_B
Constant tip speed	✓	×	✓	×
Zero Scan Angle	✓	✓	×	×

Table 2.1: Sweep rate and maximum tip speed for various scan patterns. The listed equations for cycloid and spiral patterns are derived for parallel kinematic scanners. For serial kinematic scanners, equations for cycloid and spiral patterns include a correction factor of $\sim 1/\sqrt{(2)}$. P, D_c and D_r are defined in Fig. 1-3. Equations are derived for equal area coverage leading to $D_s{=}2D_r/\sqrt{\pi}, D_c{=}D_r/\sqrt{1+\pi/4}$.

	Triangular Raster	Sinusoidal Raster	Cycloid	Spiral
Normalized sweep rate (S_n)	1	7	4.67 (3.3)	6.2 (4.38)
Normalized max tip speed (v_n)	1	10.99	8.22 (5.81)	12.4 (8.76)
$\mu_n = v_n/S_n$	1	1.57	1.76	2.03

Table 2.2: Sweep rate and maximum tip speed, normalized with respect to those of the triangular raster scan pattern. The ratio of normalized sweep rate to normalized maximum tip speed denoted by μ is a measure of the effectiveness of the scan pattern. A value of μ close to unity is preferred. Listed values are for parallel kinematic scanners. Approximate values for serial kinematic scanners are listed inside brackets.

probe. To demonstrate this feature in a more clear fashion another index $\mu = v_n/S_n$, is listed in Table 2.2. A μ value closer to 1 is preferred. It is also important to note that in the analysis it is assumed that the mechanical bandwidth, f_B, is similar for X and Y directions of the lateral scanner. This assumption can usually be applied to parallel kinematic scanners such as piezo tubes. In serial kinematic scanners where one scan axis is stacked on top of another, the maximum available bandwidth corresponds to that of the slower direction. One can roughly assume equal masses for the X and Y scanners. With this assumption the available mechanical bandwidth is approximately limited to $1/\sqrt{2}f_B$. The values listed inside the brackets in Table 2.2 take into account this limitation of serial kinematic scanners. For either of the raster scan strategies (e.g. triangular or sinusoidal) one of the scan axes is driven significantly faster than the other and hence this limitation does not apply.

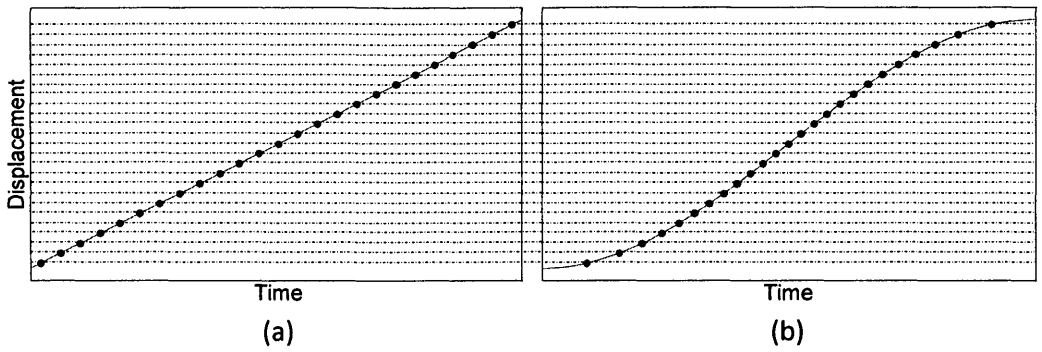

Figure 2-3: Position triggered sampling for a) a ramp, and b) a half cycle sinusoidal wave. For a given sampling position, the sampling rate associated with the ramp command is constant. For a sinusoidal pattern, position triggered sampling leads to a variable sampling time.

Of the listed patterns, triangular-raster scan is the only scanning pattern that meets both the constant linear velocity and constant scan angle criteria. As such, for scan frequencies where $f_{\text{scan}} < f_B/7$ it is rational to use a triangular-raster pattern. For $f_{\text{scan}} > f_B/7$ a different pattern should be adopted. As observed from Table 2.2 the largest increase in the scanning speed is associated with the sinusoidal-raster scan pattern. Interestingly the smallest μ value also belongs to this scanning strategy. Another advantage of sinusoidal-raster pattern is the associated zero scan angle. As explained earlier this feature is important from the perspective of the accuracy of surface topography measurements. Sinusoidal raster also benefits from the same advantages of the triangular raster in terms of simplicity in data-logging and plotting. The only downside of this scanning method is the associated variable scan speed. The image distortion problem associated with constant sampling rate can be removed by implementing the image acquisition based on position triggered sampling (rather than a time triggered sampling). In this form triangular-raster scan and sinusoidal-raster scan patterns can both be adopted under the same image acquisition platform. Figures 2-3a and b show the position triggered sampling strategy for triangular and sinusoidal raster patterns, respectively. In this form the captured data points are associated with the same physical locations on the sample surface for triangular, sinusoidal as well as any intermediate (smoothed) raster patterns.

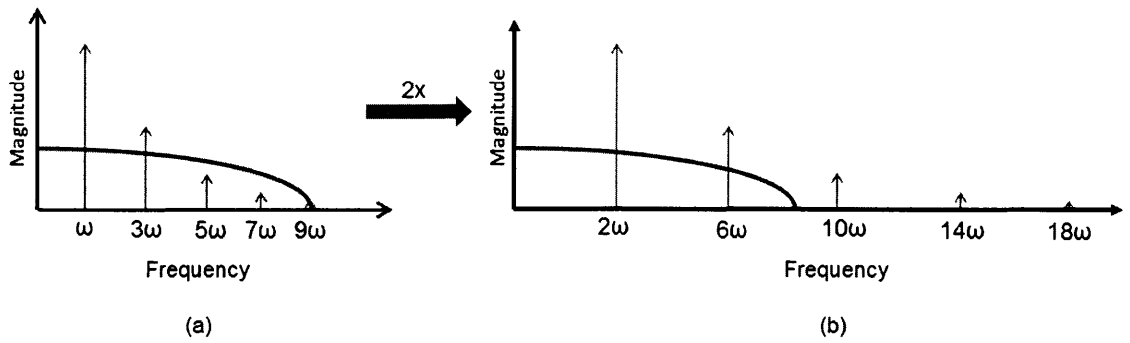

Figure 2-4: Illustration of the frequency response of a lateral scanner with compensated dynamics. a) the scanner bandwidth accommodates the first 7 harmonics of the fundamental scan frequency f_{scan}, and b) when the scan frequency is doubled, only the first few harmonics of the new fundamental frequency ($2f_{\text{scan}}$) fall within the mechanical bandwidth. This leads to the smoothing of turnaround points.

Based on the above discussions we propose a scan strategy for high-speed AFM imaging that is intermediate to the triangular-raster scan and the sinusoidal-raster patterns as described in the following:

Triangular-to-Sinusoidal raster scan pattern with position triggered image sampling: In this form for lower scan frequencies ($f_{\text{scan}} < f_B/7$) a raster scan with the desired triangular pattern is achieved. As the scan frequency increases beyond $f_B/7$, higher harmonics of the triangular pattern fall outside the available mechanical bandwidth of the scanner (see Fig. 2-4) and hence the turnaround extremities of the pattern are smoothed to form a pattern intermediate to triangular and sinusoidal. This smoothing compromises the constant linear speed of the sample. However, by incorporating position triggered image data acquisition the variable instantaneous scan speed does not distort the captured image. In the limit when the mechanical bandwidth of the scanner only accommodates the fundamental harmonic of the scan frequency and misses all the higher harmonics, the scanner follows a sinusoidal pattern and μ reaches its upper limit of 1.57 as listed in Table 2.2.

2.3 Actuation Mechanism

In this subsection we take a closer look at the available actuation mechanisms. An actuation methodology that potentially leads to a faster scan rate and at the same time achieves a larger scan range is preferred and will be adopted in this thesis for the design of a large-range high-speed AFM. There are a few research works that compare various actuation methodologies [128, 6, 47, 48]. As reported, piezoelectric and magnetostrictive actuators are the top two actuation techniques in terms of speed and force density. Both techniques can achieve several microns of range at several kilohertz bandwidths [6] and hence are very good candidates for high-speed large-range atomic force microscopy. By incorporating these actuators into flexure bearings with mechanical amplifications, the actuation range can be increased significantly at the expense of actuation bandwidth. An example of a large-range nano-positioner operating on a piezoelectric actuator is P-629 made by Physik Instrumente (PI) that reportedly can achieve 1800 μm range with 110 Hz loaded resonance (120 g load). On the other end of the speed/range spectrum a PL022.30 piezo stack actuator made by PI has 2.2 μm range at an unloaded resonance of $\sim$ 300 kHz. Compared to piezoelectric actuators, electrostatic actuators achieve larger ranges while maintaining a wider bandwidth, however, they are very limited in terms of generated forces (in the order of 0.001 Newtons [47]). In atomic force microscopy the carried masses are not insignificant, hence requiring relatively large dynamic forces (in the order of hundreds of Newtons). As such, electrostatic actuators are not suitable for high-speed positioning.

Electromagnetic actuators on the other hand have shown great potential in nano-positioning applications [63, 21]. Both moving magnet and moving coil arrangements have been used for this purpose. In [21] a moving-magnet micro-fabricated electromagnetic actuator achieves $\pm$2.7 μm range and $\sim$2 kHz first resonance. Another example of a micro-fabricated electromagnetic nano-positioner is reported in [42], featuring 10 μm travel range and 1 kHz resonance. According to the various design examples reported in the literature, Lorentz force nano-positioners are inferior in

terms of speed and generated forces in comparison to piezoelectric or magnetostrictive actuators. However, when scan range is a concern, these actuators have virtually no limit e.g. for the magnetically levitated positioners [113]. This feature makes it tempting to further explore the possibility of using Lorentz force actuation for high-speed large-range nano-positioning. In the following we aim to understand whether a Lorentz force nano-positioner can reach or surpass the specifications offered by magnetostrictive or piezoelectric actuators. This is done by quantifying the improvements necessary in the highest-performance electromagnetic positioners reported so far in order to meet these specifications. This is done through first order analysis, based on the micro-fabricated Lorentz force design reported in [42].

The force generated by an electromagnetic actuator can be written as [42]:
$F = JBpA_{coil}t_{coil}$
where J is the coil current density (A/m^2), A_{coil} is the cross sectional area of the coil (m^2), t_{coil} is the width of the coil wiring (m), B is the magnetic field in Tesla (T) and p is the packing ratio.

For a second order mechanical system with mass m, exposed to the force F, and displacement δ we have:
$k = F/\delta$ and $f_{res} = \frac{1}{2\pi}\sqrt{k/m}$
where k is the spring constant (N/m) and f_{res} is the associated resonance frequency (Hz). So we can write:

$$f_{res} \approx \frac{1}{2\pi}\sqrt{\frac{JBpA_{coil}t_{coil}}{m\delta}} \tag{2.1}$$

The parameters reported in [42] are: m = 0.01g, δ = 10μm, A_{coil}=3.5 mm^2, B=0.2 T, t_{coil} = 30μm, p=0.75, and J=250e-6 A/m^2. Substituting these values in Eq. (2.1) results in an approximate resonance frequency of 1 kHz as reported in [42]. We aim to improve this design so that the resulting actuator has a 2 μm range and 100 kHz bandwidth for a 0.25 g load, specifications that can be easily met by a piezoactuator such as PL022.30 made by PI. Certain parameters of the Lorentz force actuator design reported in [42] such as current density and packing ratio are left

unchanged as they are perceived to be close to their achievable upper bounds. The coil thickness is also kept unchanged. The remaining design parameters are B and A_{coil}. Substituting the new specifications in Eq. (2.1) it is possible to show that the $B \times A_{coil}$ for the new actuator should be increased by a factor of 5e4. In a similar fashion the spring constant of the new Lorentz force actuator should be increased by a factor of 2.5e5. As one may observe the expected increase in $B \times A_{coil}$ and stiffness,k, values go significantly beyond those achievable by optimizing the design. In practice 1 Tesla is considered to be associated with a relatively strong magnetic field. In a similar fashion, actuator stiffness can only be marginally improved e.g. by the changing the material (Aluminium: 70 GPa, Diamond: 1220 GPa). One should also note that in this design an increase in the coil area, A_{coil}, is tantamount to increasing the moving stage mass by the same proportions, which in return leads to a lower resonance. As such, one can conclude that the specifications of the piezo and magnetostrictive actuators fall well beyond the reach of their electromagnetic counterparts.

An important drawback of magnetostrictive actuators is their corresponding magnetic field. The electromagnetic aspect of both the magnetostrictive and Lorentz force actuators makes them impractical in certain modes of AFM imaging such as magnetic force microscopy (MFM) where the magnetic properties of the sample surface is imaged. Magnetic fields may also affect the behavior of certain nano-scale processes that may be studied with a high-speed AFM e.g. electrochemical processes such as deposition. As such, piezo-actuation is selected and will be used in the design of an atomic force microscope in this thesis.

2.4 Chapter Summary

This chapter starts by discussing two different scan arrangements where in one probe is stationary and sample moves (sample-scan) and in the other sample is fixed and probe moves (probe-scan). The limitations and advantages of each technique is presented. The sample-scan arrangement is then selected due to its potential for high-speed

operation.

In this chapter we also take a close look at various scan patterns namely triangular raster, cycloid, spiral, and sinusoidal raster. Following qualitative and quantitative analysis of each, we propose a scan pattern intermediate to triangular and sinusoidal raster scan. This strategy is selected to achieve maximal scan speed, zero scan-angle and constant instantaneous scan speed. In the proposed approach a triangular raster pattern is adopted at lower scan frequencies when $f_{\text{scan}} < f_B/7$. In this case zero scan-angle and constant speed requirements are both met. As the scan frequency goes beyond this limit ($>f_B/7$) the scan pattern is smoothed on turnarounds naturally due to the limited mechanical bandwidth of the scanner. This leads to variable scan speed. In the limit when the scanner can only accommodate the fundamental scan harmonic, the scanner follows a sinusoidal raster pattern. To avoid image distortion due to the variable instantaneous scan speed a position triggered image acquisition strategy is adopted.

We finally discuss the actuation methodology. A qualitative/quantitative comparison between two potential actuation means namely piezo and Lorentz-force actuation is presented. It is shown that the specifications of the piezo actuators fall well beyond the capabilities of Lorentz-force actuators. As such, piezo actuation is adopted for the design of our high-speed large-range atomic force microscope discussed in the later chapters.

Chapter 3

AFM Control

In this chapter we take a closer look at the requirements of lateral and out-of-plane AFM scanner control. Based on these requirements the control strategy and the control design approaches are presented.

3.1 Requirements of AFM Control

There are certain characteristics of atomic force microscope operation that make its control requirements rather peculiar especially at high imaging speeds. Firstly the main objective of AFM out-of-plane control is not only to regulate the probe-sample interaction forces but also to form an estimate of sample surface topography. In conventional atomic force microscopes it is customary to assume that the out-of-plane scanner does not reflect considerable dynamics. With this assumption, the control input to the scanner can be collected as an estimate of the surface topography. This assumption may not hold true at high imaging speeds where scanner dynamics cannot be overlooked. In this case the complexity of the controllers need to be increased for optimal performance. As a result, the raw controller output cannot be taken as proportional to surface topography. This constraint only applies to out-of-plane control. Another important aspect of AFM operation that should be taken into account for control design is its variable dynamics. The dynamics variations may be caused by the changes of the sample, sample stage and mounting mechanism from

one imaging experiment to another. Changes in the sample mass or that of the sample substrate can affect AFM dynamics. Different sample substrates e.g. glass, metal, etc even the means that fix the sample to the substrate and the substrate to the scanner stage e.g. glue, magnet, wax, etc can affect the dynamics. The AFM cantilever is commonly changed in each imaging experiment to meet the associated requirements. For some imaging applications softer cantilevers may be more suitable (e.g. biological samples) and others may accommodate stiffer probes (e.g. silicon wafers). The resonances associated with various types of probes can range from a few kilohertz to a few megahertz. The imaging mode and imaging environment are also important factors in AFM dynamics performance. In tapping mode imaging the dynamics of the probe is mostly governed by its Q factor or in other words the damping properties of the probe/environment. When operated in air in tapping mode, the Q factor of AFM probes can be quite high (e.g. 300$\sim$400) leading to very slow probe response to sample surface topography changes. The same probe when utilized in tapping mode in a liquid environment features much faster dynamics due to the increased damping properties of the environment. Out-of-plane dynamics of the AFM is most affected by these variations, making the control design for high-speed operation challenging. As such, the main focus of this chapter is on the development of robust and flexible control methodologies for high-speed out-of-plane tracking. Lateral AFM dynamics is mainly affected by the mass variations of the sample and the substrate and hence the corresponding control is not as demanding. Many of the results obtained for out-of-plane control can be utilized in lateral positioning with some modifications as discussed later in this chapter.

The variable dynamics of AFM call for flexible control strategies that can be easily tuned or updated. Since the invention of AFM proportional-integral-derivative (PID) control has been its indispensable component. Due to simplicity and easy adaptation to dynamics variations, PID controllers continue to be the control method of choice for out-of-plane tracking in state-of-the-art AFMs. As a PID controller is unable to tackle complex out-of-plane plant dynamics, AFM user needs to force a roll-off at frequencies lower than the dominant dynamics of the system. In this case, only the

lower frequency ranges where AFM demonstrates a flat frequency response is utilized. This makes things simple as the controller output can then be reliably recorded as an estimate of the surface topography. However, from the perspective of high-speed imaging this is not an acceptable strategy. In the following we take a close look at the PID controllers and the conditions under which they can operate sufficiently to meet the requirements of high-speed atomic force microscopy. Based on these requirements we then propose a complementary control strategy that benefits from the flexibility of a PID controller and at the same time ensures of its effective performance in high-speed imaging applications. This is followed by our proposed lateral control strategy.

3.2 Conditions for the Sufficiency of PID Control for Out-of-Plane Tracking in High-Speed AFM

Figure 3-1a shows the topography tracking control loop in an atomic force microscope. In this figure, C^{v} is an arbitrary controller, P^{v} is the AFM plant reflecting the out-of-plane dynamics, and δ denotes the disturbance input to the probe associated with sample surface topography. The superscript v denotes out-of-plane (vertical) direction. Let us assume a simple structure for the plant, P^{v}, represented as:

$$P^{\mathrm{v}}(\tau_c, n) = P_I = \frac{\alpha}{(1+\tau_c s)^n} \tag{3.1}$$

where s is the Laplace variable, n determines the roll-off slope and $\omega_c = 1/\tau_c$ is the cut-off frequency. This ideal AFM plant, $P^{\mathrm{v}} = P_I$, has a flat frequency response over the pass-band followed by a roll-off at ω_c. The ideal closed loop performance of AFM is obtained when the corresponding complementary sensitivity function, T, demonstrates a minimal phase lag and a maximal bandwidth. This is achieved when T reflects a first order behavior with a cut-off frequency matching that of the system bandwidth, ω_c, i.e.:

$$T(s) = \frac{C^{\mathrm{v}}(s)P^{\mathrm{v}}(s)}{1 + C^{\mathrm{v}}(s)P^{\mathrm{v}}(s)} = \frac{1}{1+\tau_c s} \tag{3.2}$$

Substituting for P^{v} (from Eq. (3.1)) in Eq. (3.2) we can solve for the required control, C^{v}. We have:

$$C^{\mathrm{v}} = \frac{1}{\tau_c s} + \frac{a_1}{\tau_c} + \frac{a_1}{\tau_c} s + \frac{a_1}{\tau_c} s^2 + \ldots$$

For n=1, $C^{\mathrm{v}} = \frac{1}{\tau_c s} + \frac{a_1}{\tau_c}$, is a PI controller, and for, n=2, $C^{\mathrm{v}} = \frac{1}{\tau_c s} + \frac{a_1}{\tau_c} + \frac{a_1}{\tau_c} s$, a PID controller. In a similar fashion for $n = 3$, C^{v} is a PIDD controller and so on. In other words, assuming a steeper roll-off for the AFM plant (larger n), we require a higher order derivative action on the photodiode measurement. These consecutive differentiations aim to compensate for the plant phase lag by reducing the roll-off to a first order. Although the phase lead associated with a single differentiation may result in improvements in the closed loop bandwidth, beyond that, it only amplifies the actuator and measurement noises. As such, when the AFM plant demonstrates a frequency response resembling that of Eq. (3.1), a PID controller is sufficient for effective topography tracking at high speed. The main feature of this ideal plant is a flat frequency response with no dynamics on the passband. Ideally for the best performance of the PID controller we need $n \leq 2$. Higher order roll-off requires higher order differentiation which is usually avoided in practice due to noise amplification. In the following we utilize this observation to ensure that a PID controller is capable of operating optimally even for complex out-of-plane AFM dynamics.

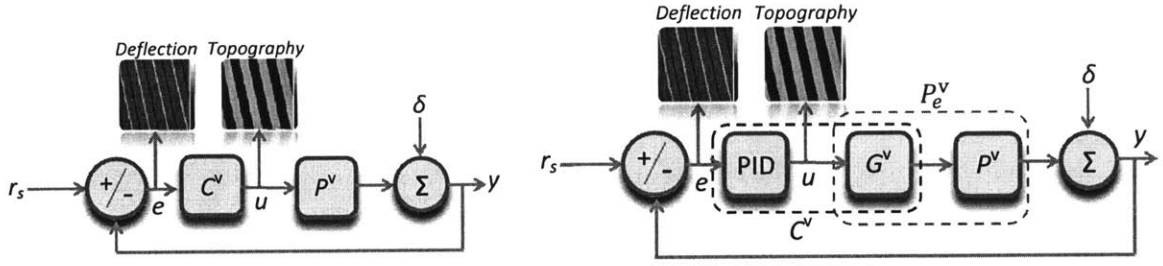

(a) (b)

Figure 3-1: a) AFM topography tracking control loop, and b) proposed auxiliary control arrangement. The auxiliary control G^{v} ensures that the behavior of the equivalent plant, P_e^{v}, resembles that of Eq. (3.1). This guarantees effective performance of the PID unit at high imaging speeds. See section 3.2.

3.3 Data-Based Auxiliary Out-of-Plane Control Design

To benefit from the advantages of PID control even for complex plant dynamics, we propose to design controllers that are complementary to a PID unit. The objective of auxiliary control is to ensure that the conditions required for the effective performance of the PID unit is met. The proposed control arrangement for topography tracking is illustrated in Fig. 3-1b. As shown in this figure, the general controller C^{v} of Fig. 3-1a is decomposed into a PID control unit cascaded with an auxiliary control, G^{v}. The effective control, C^{v}, composed of G^{v} and the PID unit can be arbitrarily complex to deal with challenging dynamics of the plant. At the same time the PID portion of the control can be tuned by the AFM user to meet the requirements of the given imaging task.

One may also think of the cascade of the auxiliary control, G^{v} and the plant, P^{v}, as a modified equivalent plant, P_e^{v}. As discussed in section 3.2 for effective performance of the PID control at high speed, P_e^{v} should reflect a maximally flat frequency response represented by Eq. (3.1). As a result, to enable high-speed performance of the AFM, the objective for the design of the auxiliary control, G^{v}, is to ensure that the behavior of the equivalent plant, P_e^{v}, can be expressed by Eq. (3.1). Hereafter, the auxiliary controllers are referred to as compensators to distinguish them from the PID controller. Although the equivalent plant, P_e^{v} is a single-input single-output (SISO) system, in general G^{v} and P^{v} can be single-input multi-output (SIMO) and multi-input single-output (MISO) systems, respectively. This generalized form also includes over-actuated scanners (redundant actuation) composed of several components that can cooperate to effectuate the overall positioning. Given the desired behavior of P_e^{v}, expressed by Eq. (3.1), the compensator design problem can be formulated as shown in Fig. 3-2a. In this form compensator parameters are obtained by reducing the discrepancies between the responses of equivalent and ideal plants. In Fig. 3-2b the compensator G^{v} and the plant P^{v} are represented in their general SIMO and MISO forms, respectively.

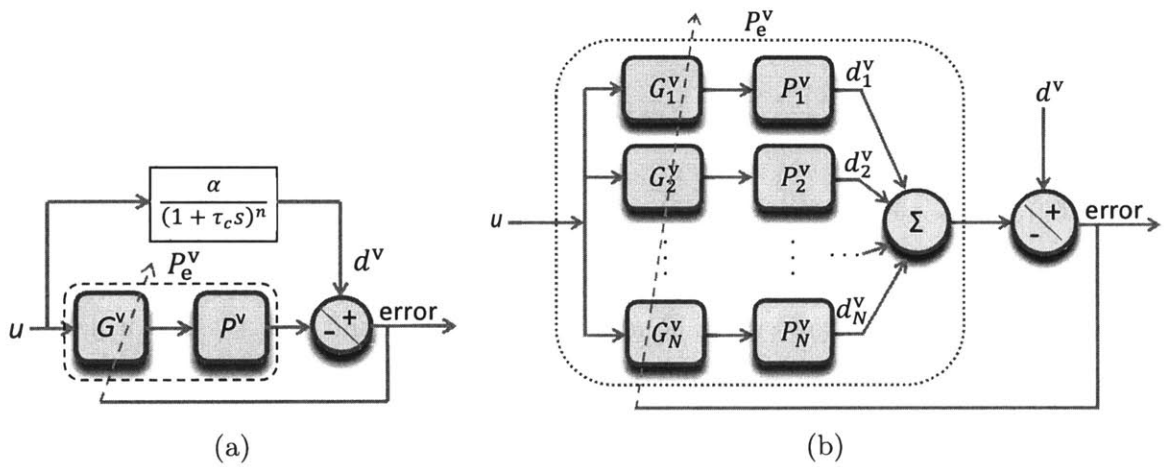

Figure 3-2: a) Design of the auxiliary compensator is expressed in terms of the desired behavior of the equivalent plant P_e^{v}, b) the compensator G^{v} and the plant P^{v} are represented in their general SIMO and MISO forms, respectively

In Fig. 3-2b the sequence of the plants, P_n^{v} and compensators, G_n^{v} can be changed as shown in Fig. 3-3a. Let us now assume that the input dataset, $\mathbf{U_n} = \mathbf{U} = \{u(m), m = 1, \ldots, M\}$ (Fig. 3-3a), to the equivalent plant is a known wide-band excitation such as a random binary sequence (RBS). The plant components can be replaced with their response datasets, $\mathbf{R_n^v} = \{r_n^{\mathrm{v}}(m), m = 1, \ldots, M\}$ (Fig. 3-3a), to the common wide-band excitation input, $\mathbf{U_n}$, as shown in Fig. 3-3b. In this form the compensator design can be interpreted as a MISO system identification problem. For an ideal set of compensators, $\tilde{G}_n^{\mathrm{v}}, n = 1, \ldots, N$, we have, $e \simeq 0$, or:

$$d^{\mathrm{v}} \simeq d_1^{\mathrm{v}} + d_2^{\mathrm{v}} + \ldots + d_N^{\mathrm{v}} \tag{3.3}$$

where d^{v} is the desired response of the equivalent plant P_e^{v}, and d_n^{v} is the desired response of the compensator, G_n^{v}, $n = 1, \ldots, N$ such that Eq. (3.3) holds. In the absence of any constraints this problem has infinite solutions. Each solution set, $\tilde{G}_n^{\mathrm{v}}, n = 1, \ldots, N$, corresponds to a unique set of desired compensator response set, $d_n^{\mathrm{v}}, n = 1, \ldots, n = N$ (see Fig. 3-3b). In practice, not all solutions are acceptable. To limit the solution set we need to utilize certain information about the expected behavior of individual plant components, P_n^{v}, e.g. available bandwidth.

Let us for now assume that our knowledge of the system can help us limit the

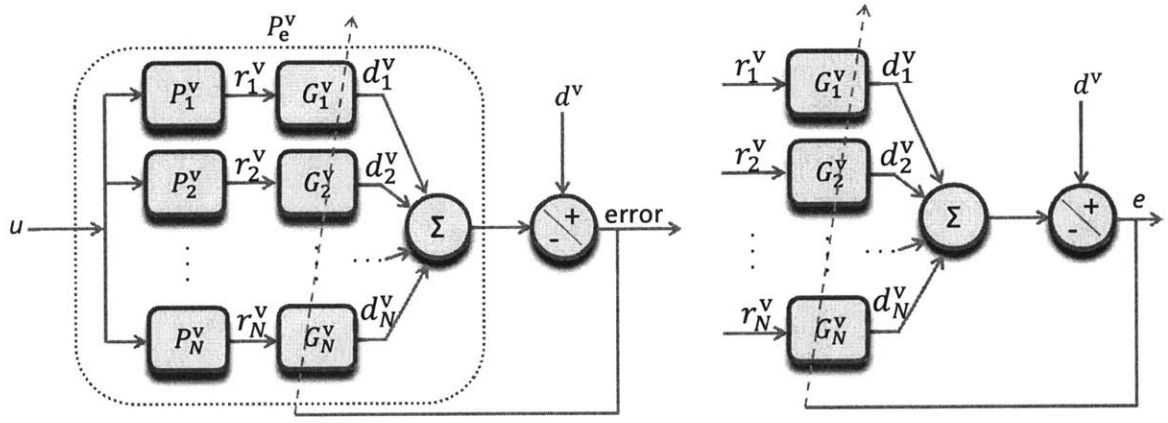

Figure 3-3: a) The sequence of compensator and plant units in Fig. 3-2b are changed, b) the plants units can be replaced with their responses, r_n^v, to a wideband excitation signal, u.

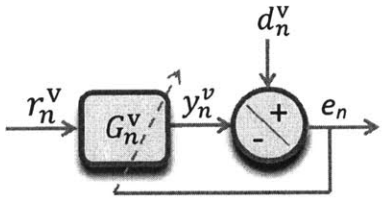

Figure 3-4: Solving for individual compensators: Upon the availability of r_n^v and d_n^v, the unknown parameters of the compensator G_n^v can be obtained by minimizing the error output, e_n.

result to a single solution and uniquely construct the datasets, $\mathbf{D_n^v} = \{d_n^v(m), m = 1, \ldots, M\}$, corresponding to the individual compensator units G_n^v. Given Eq. (3.3) one needs access to $N-1$ out of the N desired datasets, $D_n^v, n = 1, \ldots, N$. Upon the availability of D_n^v, the unknown parameters of the compensator, G_n^v, can be obtained by minimizing the output error (deviation from the desired behavior) as shown in Fig. 3-4.

The control structure for G_n^v is represented by an IIR filter:

$$G_n^v = \frac{b_{n,0} + b_{n,1}z^{-1} + \cdots + b_{n,j}z^{-j}}{1 - a_{n,1}z^{-1} - \cdots - a_{n,i}z^{-i}}$$

where $b_{n,0\ldots j}$ and $a_{n,1\ldots i}$ denote the numerator and denominator coefficients respectively, and z^{-k} is a delay of order k. For the n^{th} compensation unit we can write:

$$\tilde{\mathbf{\Theta}}_{\mathbf{n}} = \text{argmin} E(\mathbf{\Theta}_{\mathbf{n}}) \tag{3.4}$$

where $\mathbf{\Theta}_{\mathbf{n}} = \{b_{n,0}, b_{n,1}, \ldots, b_{n,j}, a_{n,1}, a_{n,2}, \ldots, a_{n,i}\}$ is a vector containing the unknown parameters of compensator G_n^{v}, and

$$E(\mathbf{\Theta}_{\mathbf{n}}) = (\mathbf{D}_{\mathbf{n}}^{\mathrm{v}} - \mathbf{Y}_{\mathbf{n}}^{\mathrm{v}}(\mathbf{\Theta}_{\mathbf{n}}))(\mathbf{D}_{\mathbf{n}}^{\mathrm{v}} - \mathbf{Y}_{\mathbf{n}}^{\mathrm{v}}(\mathbf{\Theta}_{\mathbf{n}}))^T = \sum_{m=1}^{M} [d_n^{\mathrm{v}}(m) - y_n^{\mathrm{v}}(m, \mathbf{\Theta}_{\mathbf{n}})]^2 \tag{3.5}$$

is the error energy with respect to a discrete set of desired response samples, $\mathbf{D}_{\mathbf{n}}^{\mathrm{v}}$. In Eq. (3.5), $\mathbf{Y}_{\mathbf{n}}^{\mathrm{v}}(\mathbf{\Theta}_{\mathbf{n}}) = \{y_n^{\mathrm{v}}(m, \mathbf{\Theta}_{\mathbf{n}}), m = 1, \ldots, M\}$, contains the discrete-time samples associated with the compensator response, i.e.

$$y_n^{\mathrm{v}}(\mathbf{\Theta}_{\mathbf{n}}) = h_n^{\mathrm{v}} * r_n^{\mathrm{v}} \tag{3.6}$$

where asterisk denotes convolution and h_n^{v} represents the impulse response associated with $G_n^{\mathrm{v}}(\mathbf{\Theta}_{\mathbf{n}})$. The optimization problem of Eq. (3.4) is well studied, convex, and with a guaranteed solution for linear systems [70]. Furthermore, the stability of the resulting unit can be warranted per virtue of minimization of the error energy [70]. The proposed approach simplifies the design step as it removes a need for any intermediate modeling and directly leads to a discrete domain compensator ready for hardware implementation (see Appendix A). Due to the simplicity of this design approach, control parameters can be easily updated as needed. For this purpose one needs access to the datasets $\mathbf{R}_{\mathbf{n}}^{\mathrm{v}}$ and $\mathbf{D}_{\mathbf{n}}^{\mathrm{v}}$. $\mathbf{R}_{\mathbf{n}}^{\mathrm{v}}$ can be acquired by exciting the n^{th} component of the out-of-plane AFM positioner using $\mathbf{U}_{\mathbf{n}} = \mathbf{U}$ (see Fig. 3-3a), a wideband excitation signal. The desired response dataset, $\mathbf{D}_{\mathbf{n}}^{\mathrm{v}}$, should be formed separately. The step of forming the desired response, $\mathbf{D}_{\mathbf{n}}^{\mathrm{v}}$, for each compensation unit depends on the AFM scanner design and will be discussed in detail in chapter 4.

3.3.1 Influence of Non-Linearity and Measurement Noise on Data-Based Control Design

In this subsection we study the effect of noise and nonlinearities on the performance of controllers designed directly based on the proposed data-based technique. We drop the superscript v and the subscript n as the following analysis are general to the data-based control design methodology. Let us take a closer look at a single pair of (G, P) as shown in Fig. 3-5a. The objective of compensator design is to ensure that the response of cascaded (G, P) system matches the desired response d. The desired response d is a filtered version of the input u using the desired filter F (Fig. 3-5a). This is a model matching problem where the compensator G should be designed such that GP-cascade matches the desired model F in some sense (e.g. H_2 norm). In model-based approach to control design this process starts with identifying the model P. Compensators are then designed based on the modelled plant [45]. To model the plant, it is excited with a wideband excitation signal, u, and its response, r, is measured. A model is then fitted to the measured input/output data either in time or frequency domains. The reliability of the fitted model at different frequency ranges can be expressed by the magnitude squared coherence (MSC), ρ_{ur}, of (u, r) data pair:

$$\rho_{ur}(\Omega) = \frac{|\phi_{ur}(\Omega)|^2}{\phi_{uu}(\Omega)\phi_{rr}(\Omega)} \tag{3.7}$$

where ϕ_{ur} is the cross power spectral density, and ϕ_{uu}, ϕ_{rr} are the power spectral densities for u and r. ρ_{ur} is a function of frequency, between 0 and 1, and reflects the relation between the excitation input and the measured response. At frequencies where $\rho_{ur} << 1$, either the linearity assumption between the excitation and measurement does not hold and/or the measured signal is corrupted by noise. As such, one should ensure that the frequency ranges with low MSC are given a lower emphasis for system identification. Otherwise, the identified model will be erroneous around these frequencies. Such modelling errors will be inherited by the designed model based controllers.

As proposed in section 3.3, by rearranging the order of the plant, P and com-

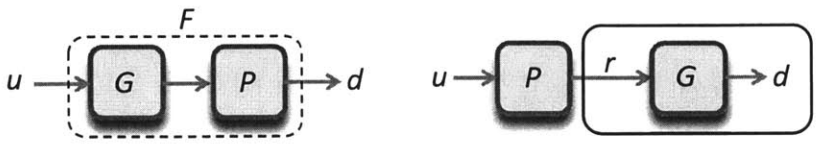

(a) (b)

Figure 3-5: a) Model matching interpretation of the design problem for a plant-compensator pair, b) proposed data-based compensator design scheme based on (r,d) pair of data.

pensator G (see Fig. 3-5b) one may directly start the compensator design step in an exactly similar process as that of a model identification but using the data pairs (r, d) instead. As in this form the plant modeling step is eliminated we need to evaluate how measurement noise and system nonlinearities affect the quality of the resulting compensators. For the cross power spectrum of the signals r and d we can write:

$$\phi_{rd}(\Omega) = \sum_{k=-\infty}^{\infty} \Gamma_{rd}(k) e^{-j\Omega\ k} \tag{3.8}$$

where Γ_{rd} is the cross correlation between the signals r and d given as:

$$\Gamma_{rd}(k) = E\{r(n+k)d(n)\} \tag{3.9}$$

On the other hand for d we can write:

$$d(n) = \sum_{m=-\infty}^{\infty} f(m)u(n-m) \tag{3.10}$$

where f is the discrete-time impulse response associated with the desired plant F (see

Fig. 3-5a). Substituting Eq. (3.10) into Eq. (3.9) we have:

$$\begin{aligned}\Gamma_{rd}(k) &= E\{\sum_{m=-\infty}^{\infty} f(m)u(n-m)r(n+k)\} \\ &= \sum_{m=-\infty}^{\infty} f(m)E\{u(n-m)r(n+k)\} \\ &= \sum_{m=-\infty}^{\infty} f(m)\Gamma_{ur}(k+m)\end{aligned} \tag{3.11}$$

We substitute Eq. (3.11) into Eq. (3.8). Now we can write:

$$\begin{aligned}\phi_{rd}(\Omega) &= \sum_{k=-\infty}^{\infty}\sum_{m=-\infty}^{\infty} f(m)\Gamma_{ur}(k+m)e^{-j\Omega\ k} \\ &= \sum_{q=-\infty}^{\infty}\sum_{m=-\infty}^{\infty} f(m)\Gamma_{ur}(q)e^{-j\Omega\ (q-m)} \\ &= \sum_{q=-\infty}^{\infty} f(m)e^{-j\Omega\ q}\sum_{m=-\infty}^{\infty}\Gamma_{ur}(q)e^{j\Omega\ m)} \\ &= \phi_{ur}(\Omega)F(-\Omega)\end{aligned} \tag{3.12}$$

where $q = k + m$. In a similar fashion one can show that:

$$\phi_{dd}(\Omega) = \phi_{uu}(\Omega)|F(\Omega)|^2 \tag{3.13}$$

From Eqs. (3.12) and (3.13), for the magnitude squared coherence of (d, r) data pair, we can write:

$$\rho_{dr}(\Omega) \quad = \frac{|\phi_{dr}(\Omega)|^2}{\phi_{dd}(\Omega)\phi_{rr}(\Omega)} = \frac{|\phi_{ur}(\Omega)F(-\Omega)|^2}{\phi_{uu}(\Omega)\phi_{rr}(\Omega)|F(\Omega)|^2} \tag{3.14}$$

From Eqs. (3.7) and (3.14) we have:

$$\rho_{dr}(\Omega) = \rho_{ur}(\Omega) \tag{3.15}$$

The proof for continuous-time case can be given in a very similar fashion. According to Eq. (3.15) noise and nonlinearities affect the accuracy of the compensators derived through the proposed data-based design scheme in the same way as they may compro-

mise the accuracy of the identified plant models in a model-based design approach. As such the same care given to identifying the plant model, P, in a model-based control design approach should be given to the direct data-based compensator design step as proposed in Fig. 3-4. To improve compensator design accuracy the frequency ranges where actuator response is corrupted (low MSC) should be given a smaller weight in the calculation of the error energy in the control design step. This is further discussed in the following subsection.

3.3.2 Frequency Domain Interpretation and the Weighting Function

As proposed by Eqs. (3.4) and (3.5), the compensator parameters are obtained by minimizing the output error energy with respect to the desired response of the compensator in the time-domain. Although, the error energy of Eq. (3.5) is presented in discrete-time, the optimization step of Eq. (3.4) can be implemented based on either a discrete-time or a continuous-time version of the compensator G. In this work since all the designed controllers will be implemented on FPGA platforms, the compensators are derived directly in discrete domain (see appendix A). This is another advantage of the proposed control design scheme as it evades a redundant continuous-to-discrete transformation step e.g. based on bilinear transformation, etc. All such transformation techniques lead to discrete-time domain filters that deviate from the originally designed continuous-time controller specially at higher frequencies.

When the error is defined based on the time-response of the compensator G (Eq. (3.5)), in the optimization step (Eq. (3.4)) one does not have direct control on the weighting given to various frequency ranges. A frequency domain equivalent of Eq. (3.5) can be written as:

$$E(\boldsymbol{\Theta}) = \sum_{m=1}^{M} |\frac{D(2\pi\ m/M)}{R(2\pi\ m/M)} - G(2\pi\ m/M, \boldsymbol{\Theta}_{\mathbf{n}})|^2 |R(2\pi\ m/M)|^2 \tag{3.16}$$

where $R(2\pi\ m/M)$ and $D(2\pi\ m/M)$ denote the Fourier domain representations of the datasets $\mathbf{R} = \{r(m), m = 1, \ldots, M\}$ and $\mathbf{D} = \{d(m), m = 1, \ldots, M\}$ (see Fig. 3-5b), at discrete frequency $\Omega = 2\pi\ m/M$. Similar to previous subsection here we drop the superscript v and the subscript n for generality.

As observed from Eq. (3.16) the emphasis given to various frequency components is determined by the spectral energy of r i.e. $|R(\Omega)|$. $|R(\Omega)|$ is a natural and often suitable weighting selection. This is because the SNR of the measured AFM dynamic response is usually lower on frequency ranges where $|R(\Omega)|$ is small (assuming a white background noise). To modify the weighting, one can filter both of the signals, r, and d, using a filter V i.e. $R'(\Omega) = R(\Omega)V(\Omega)$, and $D'(\Omega) = D(\Omega)V(\Omega)$. This modifies the incorporated frequency weighting function to $R'(\Omega) = R(\Omega)V(\Omega)$ [70]. One can also implement the optimization directly in the frequency domain and replace $|R(\Omega)|$ by any weighting function that best reflects the reliability of the measured signal in the frequency domain.

3.4 Lateral Scan Control

Due to certain characteristics of AFM lateral scan, its control requirements are different from those of the out-of-plane direction. Unlike the out-of-plane topography tracking where the unknown disturbances to the probe necessitate closed-loop control, the lateral scan motion does not experience any external disturbances and hence, the corresponding control can be implemented in open loop. Closed loop control may optionally be used in the lateral direction to enhance positioning accuracy by compensating for actuator nonlinearities such as creep and hysteresis. More importantly due to the apriori knowledge about the scan pattern, lateral control can be at least partially designed in a non-causal form. This may simplify the design as it is not limited by the phase and magnitude response constraints similar to those of the causal implementation.

The control strategies proposed for fast and slow lateral scan axis are shown in Figs. 3-6 and 3-7, respectively. The adopted control approach for the slow scan

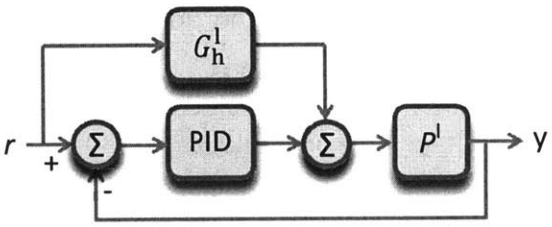

Figure 3-6: Proposed control structure for slow lateral scan axis. A non-causal feedforward, G_h^l, is combined with a PID feedback controller for increased precision.

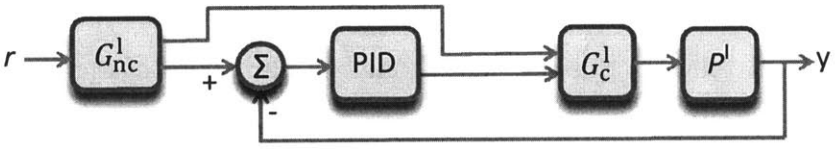

Figure 3-7: Proposed control structure for fast lateral scan axis. It is a combination of non-causal unit, G_{nc}^l, a causal unit, G_c^l, and a PID feedback controller.

axis emphasizes positioning precision and fully disregards scanner dynamics. This is because the slow scan frequency corresponds to the imaging frame rate and hence, even in very high speed applications is limited to a few hertz. On the other hand, as the captured frames may need to be compiled into a video, it is important to ensure that the consecutive frames are perfectly aligned. For this purpose creep and hysteresis effects should be fully treated. In the proposed 2DOF structure of Fig. 3-6, a feedforward non-causal and non-linear controller, G_h^l, tackles the scanner hysteresis. Any remaining positioning errors are removed by the closed-loop portion of the control operating on a PID. The control strategy proposed for the fast scan axis takes into account the effect of dynamics excitation at high-speed. This is done by a causal compensation unit denoted by G_c^l. Positioning precision along the fast scan axis is boosted in closed-loop. The feedforward unit G_{nc}^l takes control responsibilities that mostly benefit from a non-causal implementation. Examples of such control tasks are frequency assignment and phase matching for multi-actuated scanners. These will be discussed in more detail in section 4.3.5. An advantage of the structure of Fig. 3-7 is the possibility of conversion to an open loop implementation. This can be done by setting the PID parameters to zero. Unlike closed-loop case, one can

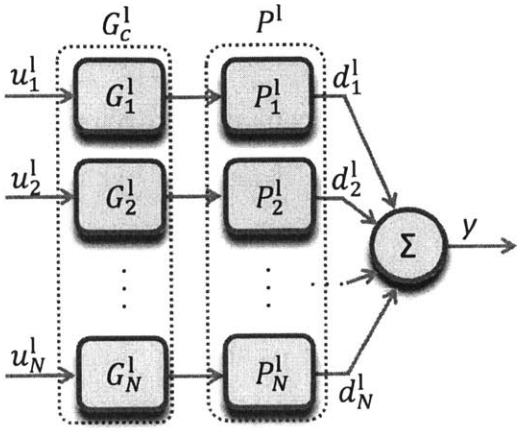

Figure 3-8: The cascade of causal control and the lateral scanner plant in general form. To design the individual compensator units, G_n^{l}, based on the proposed data-based scheme (see Fig. 3-4) one needs access to the desired responses, d_n^{l}.

utilize the full mechanical bandwidth of the lateral scanner positioners in an open-loop implementation to achieve faster scanning.

Figure 3-8 shows the expanded version of the causal controller, $G_{\mathrm{c}}^{\mathrm{l}}$, and the corresponding plant components, P_n^{l}, for a redundantly actuated scanner. One can utilize the same data-based control design scheme proposed in section 3.3 to find the unknown parameters of G_n^{l}. A description of the steps of forming the desired data-sets, d_n^{l}, also the design of the non-causal unit $G_{\mathrm{nc}}^{\mathrm{l}}$ is postponed to section 4.3.5 where more details about the proposed structure of the AFM scanner is given.

3.5 Chapter Summary

This chapter starts by summarizing the requirements and challenges associated with AFM control. The variable dynamics of AFM, mainly influencing the out-of-plane tracking, is presented as the most challenging aspect of AFM control. These variations call for a very flexible control scheme that can easily adapt to the requirements of the given imaging experiment. As a PID controller meets the flexibility requirement very well it has been an indispensable part of AFM. However, it lacks the ability to meet the performance requirements of high-speed imaging in the presence of complex dynamics.

To maintain the flexibility offered by PID controllers and simultaneously ensure of their optimal performance at high-speed we propose a control scheme that acts auxiliary to the PID unit. The auxiliary control unit, referred to as the compensator, ensures that the AFM dynamics reflect a lowpass behavior with a flat frequency response on the pass-band. It is shown that in this form a PID suffices for high-speed AFM operation.

A data-based approach to the design of the compensator unit is presented. In the proposed design approach the unknown parameters of the compensator unit are estimated directly from the AFM response to a wideband excitation. This approach avoids any intermediate AFM modeling and is very simple to implement. The method is proposed in a general form for a multi-input single-output (MISO) AFM plant. This is to enable the application of the technique for redundantly actuated AFM scanners.

The effect of measurement noises and nonlinearities on the estimation of compensator parameters is then discussed. It is proven analytically that the noise and nonlinearities influence the proposed data-based compensator design scheme in the same way as they may compromise the accuracy of the identified plant models in a model-based design approach. As such the same care given to identifying AFM dynamic model in a model-based control design should be given to the proposed direct data-based compensator design approach.

This chapter also presents a frequency domain interpretation of the proposed control design methodology. It is discussed that the control design can be improved by emphasizing frequency ranges of the measured AFM response that reflect a higher signal-to-noise ratio. This is done by either filtering the measured AFM response in the time domain or directly selecting a suitable weighting function in the frequency domain.

Finally this chapter discusses lateral scan control. Two different control strategies are proposed for the fast and slow lateral scan axes. To control the slow lateral scan the positioning precision is emphasized through a 2DOF feedforward-feedback scheme. A feedforward non-causal and nonlinear control compensates for the actuator hysteresis. The remaining positioning error is then tackled by a PID controller.

The proposed control for fast lateral positioning emphasizes the scanner dynamics to maximize the scan speed. The proposed strategy is composed of a causal implementation which acts as part of a closed-loop control in combination with a PID unit. A separate feedforward controller takes responsibilities that mostly benefit from a non-causal implementation e.g. frequency assignment and phase matching for redundantly actuated scanners.

Chapter 4

Nano-Positioning with Redundant Actuation

4.1 Introduction

At the heart of the AFM, the sample scanner plays a crucial role in setting the performance limits of this instruments. Redundant actuation presents a great potential for improving the scanner performance in achieving high-speed and large-range AFM imaging. The extra actuators can be used in two fundamentally different schemes. In one approach the additional actuators work along with the fundamental piezo to position the sample. In other words, positioning responsibility is divided between multiple actuators. This method is referred to as *multi-actuation.* In another approach, only the fundamental actuator is responsible for positioning the sample and the extra actuators aim to actively suppress the dynamics excited in the system. The latter technique is commonly referred to as *counter-balancing* [58, 3] or *active vibration suppression.*

In the following sections we take a close look at both techniques. The limitations of the counter-balancing method are discussed and control means to tackle these limitations are presented. The controller design for improved vibration suppression in counterbalancing approach is presented according to the data-based technique proposed in chapter 3. This approach is applied to retroactively enhance the

performance of an existing flexure based AFM scanner that accommodates a counterbalancing piezo actuator. In this chapter we also propose a general multi-actuation scheme. In the proposed approach multiple actuators are cascaded in series to form a single multi-component nano-positioner featuring high-speed and large-range. The dynamic coupling between different actuators are treated using independent compensators. This approach is useful in any positioning application that simultaneously requires high-speed and large-range performance. The proposed methodology, implemented for out-of-plane topography tracking is then used to retroactively enhance the performance of a conventional AFM operating on a piezo tube. This scheme is also extended to lateral positioning. The developments and experimental observations made in this chapter form the basis for the design and implementation of a high-speed large-range multi-actuated nano-positioner in chapter 5.

4.2 Counterbalancing for Active Vibration Suppression

As explained in chapter 1 a major boost in the scanning bandwidth has been realized through improving the mechanical design of the AFM nano-positioner. In flexure based designs, independent piezo stack actuators move the sample in the x, y and z directions. An example is schematically illustrated in Fig. 4-1. As observed in [3], in these scanner designs the structural dynamics in the z direction occur at a lower frequency compared to the resonance of the z piezo stack itself. Consequently, further improvements in the imaging bandwidth could be obtained by compensating for such dynamics. A simple approach to suppress the structural vibrations is to use a counterbalancing piezo-actuator [58, 3]. As shown in Fig. 4-2, in this approach, an additional piezo actuator is installed on the opposite side of the z-piezo platform, actuated by the same control signal as that driving the z-piezo. The role of the additional piezo actuator (hereafter referred to as counter-z or cz piezo) is to counteract the momentum transferred to the base (where the z piezo is mounted, see Fig. 4-2)

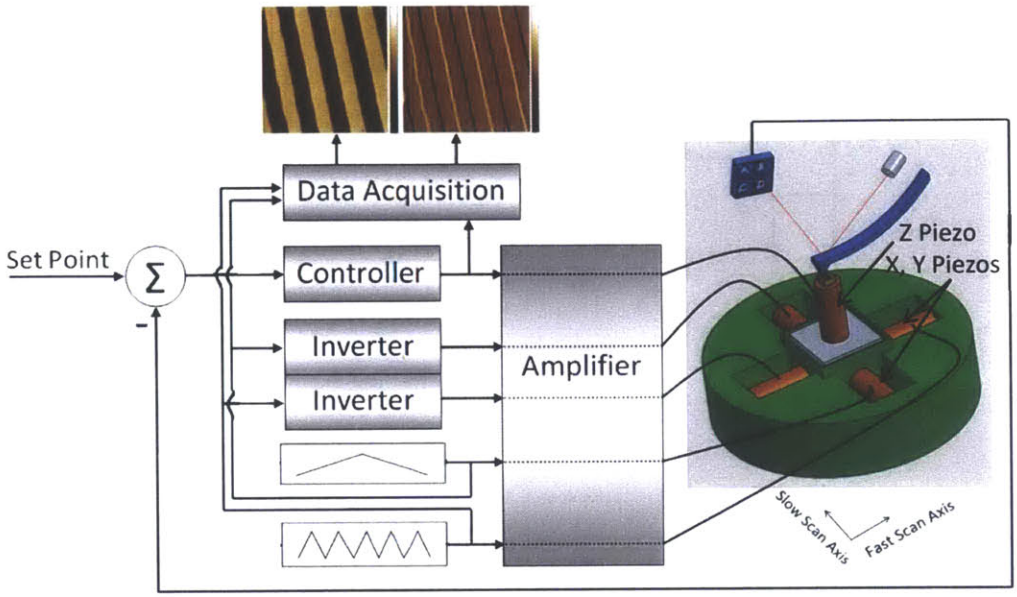

Figure 4-1: AFM operation based on a rigid scanner driven by piezo stack actuators.

by the z piezo and hence keep the structure stationary.

Although, the counterbalancing technique leads to some improvements in the dynamic performance of AFM, it also suffers from some limitations. As will be demonstrated in the following section, the counterbalancing scheme can only tackle the fundamental mode of structural dynamics. This approach is not only unable to compensate for the higher order dynamics e.g. associated with the z-piezo, but also intensifies the corresponding vibrations, potentially leading to the deterioration of imaging performance. Furthermore, the differences between the mechanical properties of the z and the counter-z piezos e.g. damping, spring constant, carried masses, etc limit the effectiveness of the technique even in suppressing the fundamental mode of structural vibrations. This is especially important as it is not practical to update the mass carried by the cz piezo in accord with the variations of the sample and the sample stage on every imaging experiment.

In the following we propose a technique that compensates for these limitations. In the proposed methodology, the signal driving the cz piezo is not the same as the one driving the z piezo. The cz actuation signal is obtained by filtering the AFM controller output via a linear filter, hereafter referred to as Counter Actuation (CA)

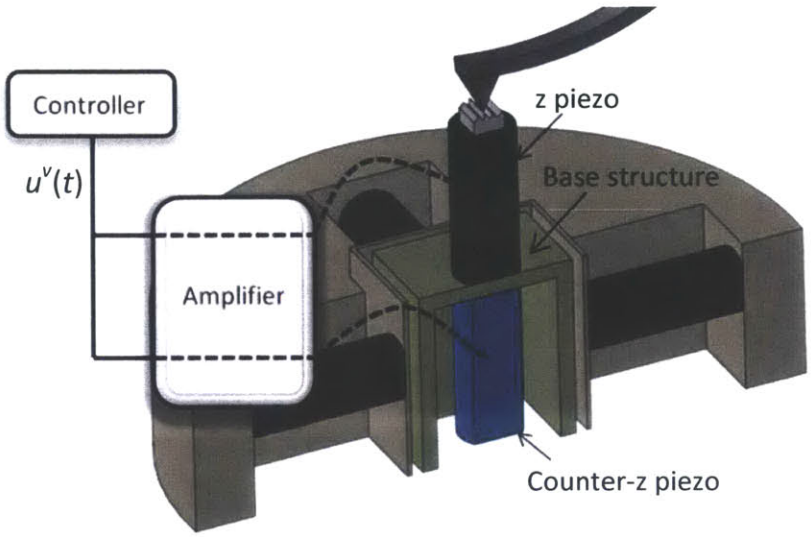

Figure 4-2: A section view of the scanner of Fig. 4-1 demonstrating the conventional counterbalancing methodology.

compensator. The CA compensator parameters are estimated based on the direct data-based design scheme proposed in section 3.3. Before going into the details of compensator design, in the following we study the principle of operation and the limitations of counter-balancing technique.

4.2.1 Conventional Counterbalancing: Principle of Operation and Limitations

As shown in Fig. 4-2, in the conventional counterbalancing technique both the z and counter-z (cz) piezos are driven by the AFM controller output, $u^{\text{v}}(t)$. A block diagram representation of Fig. 4-2 is shown in Fig. 4-3a, where P_{z} and P_{cz} represent the transfer functions from the voltage excitation of z and cz piezos to the displacement response on top of the z piezo, respectively. Figure 4-3b demonstrates a 3 DOF model of the counterbalancing mechanism where (m_b, m_z, and m_{cz}), (k_b, k_z, and k_{cz}), and (c_b, c_z, and c_{cz}), represent the equivalent point masses, spring and damping constants of the base structure, z piezo and the counter-z piezo (cz piezo), respectively. To give a heuristic explanation on the operation and the limitations of the counter balancing technique we evaluate three transfer functions, a) $Q_z(s)$ from $f_z(t)$ to $x(t) = x_z(t)$, b)

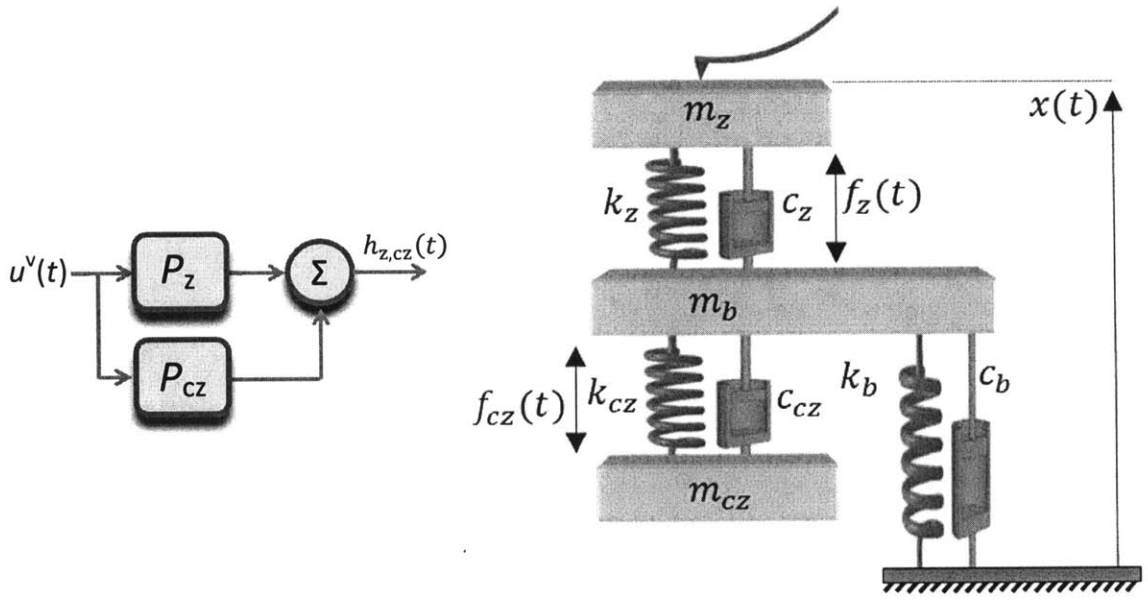

(a) (b)

Figure 4-3: a) Block diagram corresponding to the conventional counterbalancing method, and b) a 3 DOF model of the counterbalancing scheme showing the z piezo, counter-z piezo and the base structure where both piezos are mounted.

$Q_{cz}(s)$ from $f_{cz}(t)$ to $x(t) = x_{cz}(t)$, and c) $Q_{z,cz}(s)$ corresponding to the simultaneous actuation of z and cz piezos i.e. from $f_z(t) = f_{cz}(t) = f(t)$ to $x(t) = x_{(z,cz)}(t)$. The subscripts denote the excited piezo (e.g. z, cz or both). We have:

$$Q_z(s) = \frac{N_z(s, m_{cz}, m_b, c_{cz}, c_b, k_{cz}, k_z)}{D(s, m_z, m_{cz}, m_b, c_z, c_{cz}, c_b, k_z, k_{cz}, k_b)}, \tag{4.1}$$

where $N_z(s) = [m_b s^2 + (c_b + c_{cz})s + (k_b + k_{cz})](m_{cz}s^2 + c_{cz}s + k_{cz}) - (c_{cz}s + k_{cz})^2$, and, $D(s) = (m_z s^2 + c_z s + k_z)[m_b s^2 + (c_{cz} + c_z + c_b)s + (k_{cz} + k_z + k_b)](m_{cz}s^2 + c_{cz}s + k_{cz}) - (c_{cz}s + k_{cz})^2(m_z s^2 + c_z s + k_z) - (c_z s + k_z)^2(m_{cz}s^2 + c_{cz}s + k_{cz})$.

Figure 4-4a shows the Bode plots associated with Q_z (blue, solid line), Q_{cz} (green, dotted line) and, $Q_{z,\,cz}$ (red, dashed line) for tentative values of dynamic properties, $m_b = 6g, m_{cz} = m_z = 2g, k_b = 2.5e7N/m, k_z = k_{cz} = 1e8N/m$, $\xi_b = 0.03$, and $\xi_z = \xi_{cz} = 0.06$, where ξ denotes the damping ratio. As shown in this figure Q_z features three pairs of complex poles, at 8 kHz, 35 kHz and 46 kHz, and two pairs

of complex zeros at 9 kHz and 41 kHz. The characteristics of the poles and zeros respectively at 8 kHz and 9 kHz are mainly ruled by the total mass ($m_b + m_z + m_{cz}$) and the base structural properties. The pair of complex poles at 35 kHz is associated with the dynamics of the z piezo and the pairs of zeros and poles respectively at 41 kHz and 46 kHz are associated with the addition of the counter-z piezo to the opposite side of the base.

For the case where the counter-z piezo is actuated by the same signal as that driving the z-piezo, the transfer function, $Q_{z,cz}(s)$, from the actuation force, $f_z(t) = f_{cz}(t) = f(t)$, to the response of the z piezo, $x(t) = x_{z,cz}(t)$, can be written as:

$$Q_{z,cz}(s) = \frac{N_{z,cz}(s, m_{cz}, m_b, c_z, c_{cz}, c_b, k_z, k_{cz}, k_z)}{D(s, m_z, m_{cz}, m_b, c_z, c_{cz}, c_b, k_z, k_{cz}, k_b)}, \tag{4.2}$$

where $N_{z,cz}(s) = [m_b s^2 + (c_b + c_{cz})s + (k_b + k_{cz})](m_{cz}s^2 + c_{cz}s + k_{cz}) - (c_{cz}s + k_{cz})^2 + m_{cz}s^2(c_z s + k_z)$. As noted above (Eqs. (4.1) and (4.2)), both the transfer functions Q_z and $Q_{z,cz}$ have a similar denominator, $D(s)$. In other words, actuation of the counter-z piezo does not affect the location of the poles. Furthermore, the numerator of both Q_z and $Q_{z,cz}$ are independent of the mass carried by the z piezo i.e. locations of the zeros are not affected by the mass of the z-piezo. The operation of the conventional counterbalancing technique can be explained based on the above mentioned properties and the Bode plots of Fig. 4-4. For the case where the dynamic properties of the z and the cz piezos are similar (balanced case), the simultaneous actuation of the cz piezo moves the two pairs of zeros to match the pairs of poles at 8 kHz and 46 kHz, cancelling both pairs (Fig. 4-4a, red). Now consider a second case where the equivalent point mass of the z piezo is deviated from that of cz piezo (unbalanced case). According to the above, although changing the z piezo mass shifts the poles of $Q_{z,cz}$ away from their original locations, the zeros of $Q_{z,cz}$ remain intact. As such, the pole-zero cancellation does not take place and hence counterbalancing loses effectiveness (Fig. 4-4b, red). Though interpreting the effect of deviating the spring constant and the damping characteristics of the z piezo from those of the cz piezo is not as straightforward, a similar argument applies. To demonstrate the effect of mass unbalance, the mass

of the z piezo is deviated from that of the cz piezo, $m'_z = 2m_z = 4$g. Considering the small weight of the piezo stack actuators used in high speed rigid scanners, the sample and sample stage masses are comparable to the z piezo mass. Hence, the given deviation is realistic. The Bode plots associated with the unbalanced case corresponding to Q_z, Q_{cz} and $Q_{z,cz}$ (solid blue, dotted green and dashed red lines respectively) are shown in Fig. 4-4b.

Another limitation of the counterbalancing approach is the intensification of the vibrations associated with the z-piezo dynamics. This is true even when the dynamic propertied of the z and cz piezos are exactly similar. This phenomenon can be observed from the Bode plot of $Q_{z,cz}$ in both Figs. 4-4a and 4-4b (red dashed line) where the magnitude of the peak associated with the poles at 35 kHz (corresponding to the z-piezo dynamics) is increased. As evident from these Bode plots, on a frequency range bounded by the zeros of Q_z, Q_{cz} is in phase with Q_z. As such, on this frequency range the dynamics induced by the actuation of z and cz piezos are superposed constructively leading to the intensification of the corresponding vibrations. It is important to note that this phenomenon takes place even in the balanced case. Now consider a more realistic case where a perfect match between the mechanical properties of the z and cz piezos is practically very difficult. In this case, the counterbalancing technique is not only unable to properly suppress the base structural vibrations, it also intensifies the dynamics associated with the z piezo. In such cases, excitation of the cz piezo may even lead to an inferior performance of the AFM.

4.2.2 Improved Counterbalancing: Control Design

To tackle the limitations of counterbalancing technique, the arrangement of Fig. 4-5 is proposed. In the proposed form the signal driving the CZ piezo is shaped through a counter actuation (CA) compensator denoted in the figure by G_{CA}. The role of G_{CA} is to compensate for the adverse effect of the unbalance between the mechanical properties of the z and cz piezos in suppressing the base structural vibrations. Furthermore, the proposed compensator effectuates the suppression of the dynamics associated with the z piezo actuator which are otherwise intensified in the conven-

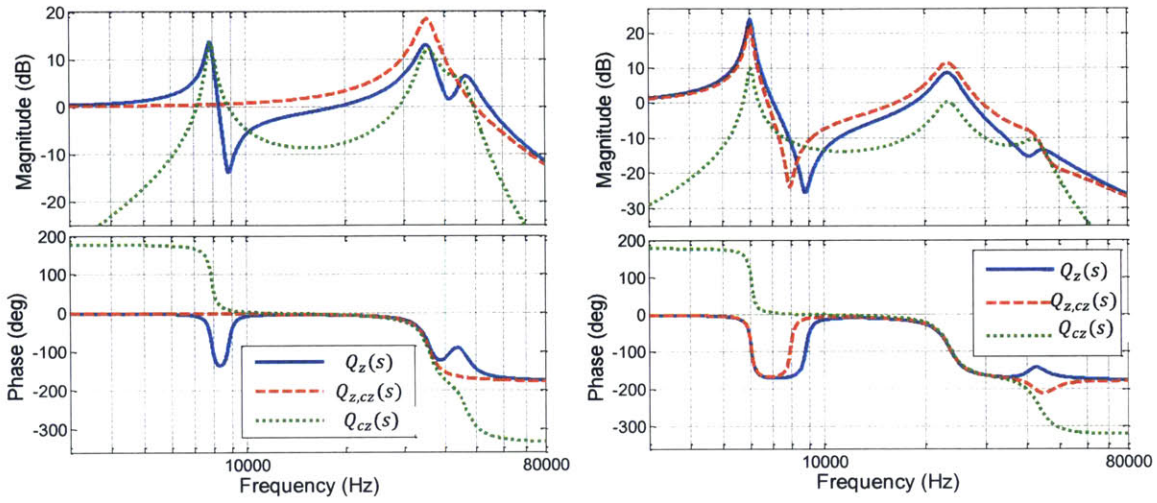

(a) (b)

Figure 4-4: Bode plot of the transfer functions Q_{z}(solid blue line), $Q_{\mathrm{z,cz}}$ (red dashed line) and Q_{cz} (green dotted line), corresponding to two cases where a) the dynamic properties of the z and cz piezos perfectly match, and b) the dynamic properties of the z piezo are deviated from those of the cz piezo.

tional counterbalancing scheme.

The block diagram associated with the proposed arrangement of Fig. 4-5 is demonstrated in Fig. 4-6 where the AFM controller is assumed to be a PID. Referring back to the discussions of chapter 3 the design objective for the CA compensator, G_{CA}, is to ensure that the behavior of the equivalent plant, P_e, enclosed by the dotted line in Fig. 4-6, resembles that represented by Eq. (3.1). A comparison between the block diagrams of Fig. 4-6 and Fig. 3-2b reveals that $P_1^{\mathrm{v}} = P_z$, $P_2^{\mathrm{v}} = P_{\mathrm{cz}}$, $G_1^{\mathrm{v}} = 1$, and $G_2^{\mathrm{v}} = G_{\mathrm{CA}}$. d_1^{v}, d_2^{v} and d^{v} represent the desired responses of the z, cz and the combined z-cz system, respectively.

To implement the control design scheme proposed in section 3.3 we need access to two of the three desired datasets d_1^{v}, d_2^{v} and d^{v}. Since the control signal driving the z piezo is left intact in the arrangement of Fig. 4-6, i.e. $G_1^{\mathrm{v}} = 1$, the desired response of the z piezo is in fact the same as its natural response to a wideband excitation signal u^{v}, so we have:

$$d_1^{\mathrm{v}} = h_z * u^{\mathrm{v}}$$

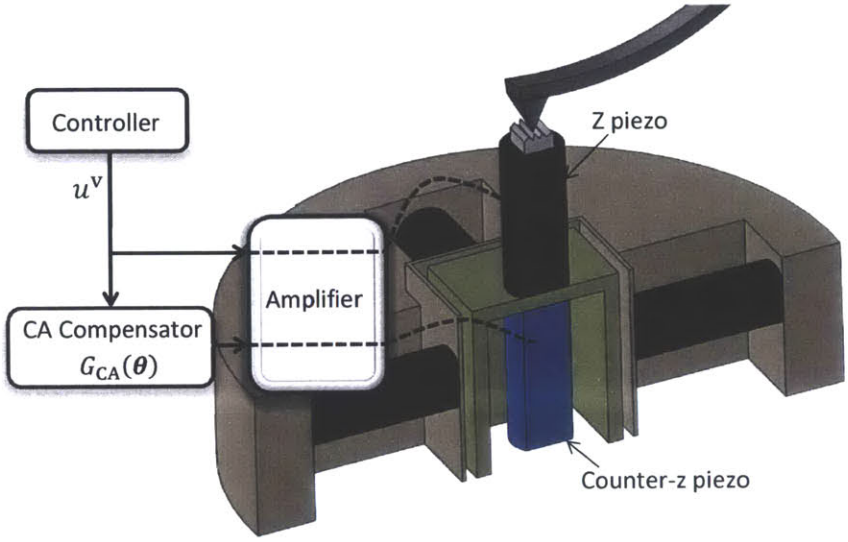

Figure 4-5: Schematics of the proposed counter actuation based on CA compensator, G_{CA}. $\boldsymbol{\Theta}$ is the unknown parameter vector associated with the CA compensator.

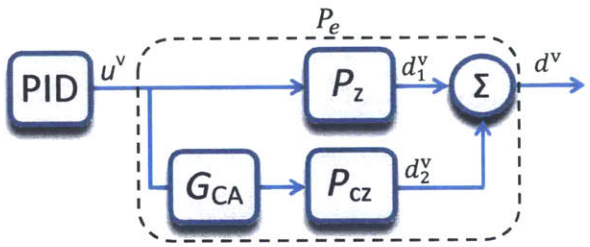

Figure 4-6: A block diagram of the proposed modified counterbalancing scheme.

where h_z is the impulse response associated with the z piezo and u^v is the PID controller output which for the design of G_{CA} can be replaced by a wideband excitation signal.

As discussed in section 3.2 the desired behavior of the overall system composed of the z, cz piezos and the G_{CA} is given by Eq. (3.1). In order to form the overall desired response, d^v, we first need to find the cutoff frequency τ_c, the DC gain α and the roll-off order n (see Eq. (3.1)). These parameters can be obtained by fitting an ideal plant model to the frequency response of the z piezo:

$$(\tilde{\tau}_c, \tilde{n}, \tilde{\alpha}) = \text{argmin}_{(\alpha,\tau_c,n)} \int_0^{+\infty} |W(\omega)^2||P_l(\alpha, \tau_c, n, \omega) - P_z(\omega)|\, d\omega \qquad (4.3)$$

where P_l is the ideal plant behavior given in Eq. (3.1), $P_z(\omega)$ is the frequency response

function associated with the z piezo, and $W(\omega)$ is a weighting function chosen to emphasize the high SNR portions of the z piezo frequency response. For discrete-time implementation the ideal plant P_{I} can be converted to discrete time. The main feature of the ideal plant model (Eq. (3.1)) is its lowpass behavior i.e. featuring a flat frequency response over the passband followed by a roll-off at higher frequencies. As such, one can also replace the ideal plant in the fitting of Eq. (4.3) by a scaled lowpass filter. A Butterworth lowpass has a maximally flat frequency response on the passband and hence is a very good candidate. The scale, order and the cut-off frequency of the lowpass filter can be obtained through a similar optimization step (Eq. (4.3)). Upon estimating the parameters of the ideal plant, P_{I}, the desired response, d^{v} can be obtained as:

$$d^{\mathrm{v}} = h_{\mathrm{I}} * u^{\mathrm{v}}$$

where h_{I} is the impulse response associated with the fitted ideal plant, $P_{\mathrm{I}}(\tilde{\alpha}, \tilde{\tau}_c, \tilde{n})$ model and u^{v} is the excitation signal. With the availability of the desired responses d_1^{v} and d^{v} one can solve for the desired response d_2^{v} using Eq. (3.3). We have:

$$d_2^{\mathrm{v}} = d^{\mathrm{v}} - d_1^{\mathrm{v}}.$$

The unknown parameter vector $\boldsymbol{\Theta}$ of the CA compensator, $G_{\mathrm{CA}}(\boldsymbol{\Theta})$ can then be found as proposed in section 3.3 (Fig. 3-4 and Eqs. (3.4), (3.5) and (3.6)).

4.2.3 Improved Counterbalancing: Case Study

In this subsection we evaluate the effectiveness of the proposed method via experimentations on a flexure based scanner equipped with a counter-z piezo. This evaluation is in terms of dynamic performance behavior of the scanner and the imaging capability of a commercial AFM that operates on this scanner.

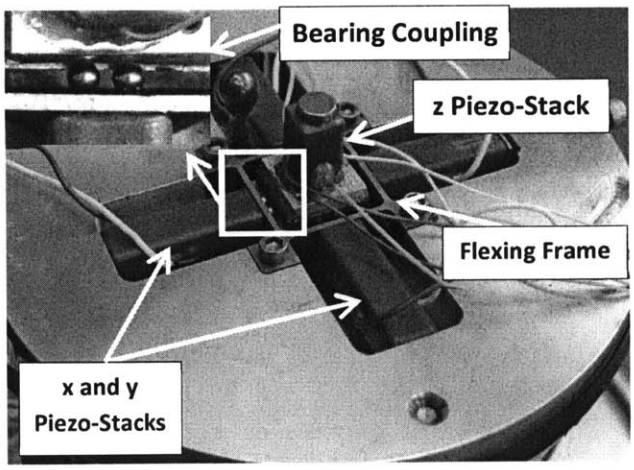

Figure 4-7: The AFM scanner used in the experiments [10] which utilizes a counter-z piezo for vibration suppression.

Experimental setup

The scanner used in this research is described in [10] and is shown in Fig. 4-7. The counter z piezo is directly underneath the z piezo platform. In the experiments, a micro-cantilever, model TM300-A from SensaProbes, with 300 kHz resonance frequency is brought in contact with a mica sample. The cantilever deflection is the only measured signal, hence eliminating the need for any additional sensors. This characteristic of the proposed technique makes it quite versatile and easy to implement on the existing AFM scanners that are equipped with a counter-z piezo. To observe the effectiveness of the proposed scheme, in the following experiments the dynamic unbalance between the z and the counter piezos is increased by using a sample substrate with 1 g mass.

CA compensator design

The z and counter-z piezos are excited independently with a wideband binary sequence excitation voltage, u^{v}. The displacement responses of z and cz piezo (r_1^{v} and r_2^{v}, respectively) are captured through the probe deflection signal at 250 kHz sampling rate. The empirical transfer function estimate (ETFE) associated with the measured data, r_1^{v} and r_2^{v} and excitation signal u^{v}, are plotted in Figs. 4-8 and 4-9, respectively. The associated magnitude squared coherence (MSC) plots are shown in Figs. 4-10a

and 4-10b. These data are then used to estimate a 10^{th} order compensator as discussed in section 4.2.2. The designed compensator is implemented on a NI PXI-7851R FPGA in transposed, direct-form II, second order sections format (see appendix A). The Bode plot of the designed CA compensator is illustrated in Fig. 4-11.

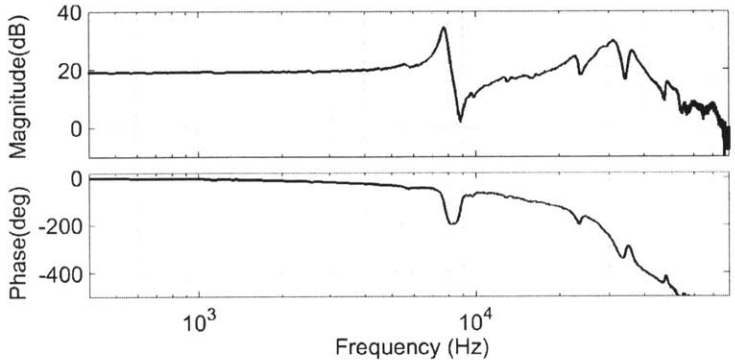

Figure 4-8: Empirical transfer function estimate for the z piezo.

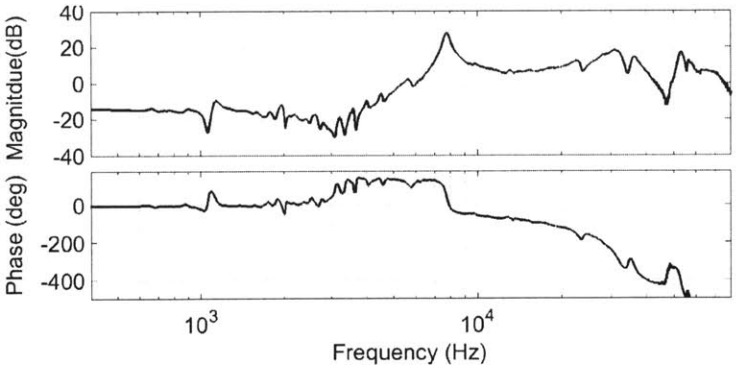

Figure 4-9: Empirical transfer function estimate for the cz piezo.

Dynamic performance

To assess the performance of the compensator, the z piezo is excited by step inputs and the deflection signal is measured for two separate cases as shown in Figs. 4-12a and 4-12b. Figure 4-12a shows the difference in performance between the conventional counterbalancing method in blue (solid line) and no-balancing in black (dotted line). The figure shows that there are two dominant modes of vibration as also observed in the ETFE of Fig. 4-8. One mode is at 31 kHz, rooted in the z piezo dynamics, and the other at 7.7 kHz which is related to the base structural dynamics. The response

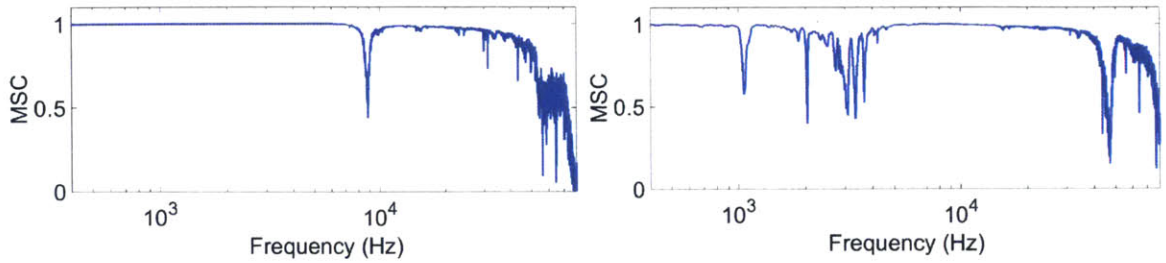

(a) (b)

Figure 4-10: Magnitude squared coherence plot (MSC) associated with the frequency response of a) z, and b) cz piezos of Figs. 4-8 and 4-9.

with no balancing, in black (dotted line), shows the worst performance. As shown in Fig. 4-12a (blue, solid line), with the application of counterbalancing although there is a slight reduction in the level of vibrations associated with the lower frequency mode (base structural dynamics), the higher frequency mode (z piezo dynamics) of oscillations are intensified. Figure 4-12b shows in red (solid line), the response corresponding to the case where the CA compensator is applied. A significant decrease in the level of vibrations is observed. This improvement in performance is attributed to the cancellation of the vibrations associated with the base (7.7 kHz) as well as significant reduction in the z piezo dynamics (31 kHz).

Figure 4-13 presents the empirical transfer function estimates associated with the cases described in Fig. 4-12. One can observe that the conventional counter balancing approach, in blue (dashed line), reduces slightly the peaks associated with the low frequency resonance and anti-resonance. However, the higher frequency modes are intensified. These behaviors of the conventional counter balancing approach were predicted in section 4.2.1. The same figure shows a significant improvement in performance due to the CA compensator, in red (solid line). Figure 4-14 shows the magnitude squared coherence associated with the frequency response of the scanner when both z and cz piezos are active.

Imaging performance

The performance of the proposed method is evaluated by using the AFM to image several samples of freshly cleaved and sanded mica. Figure 4-15 shows a typical

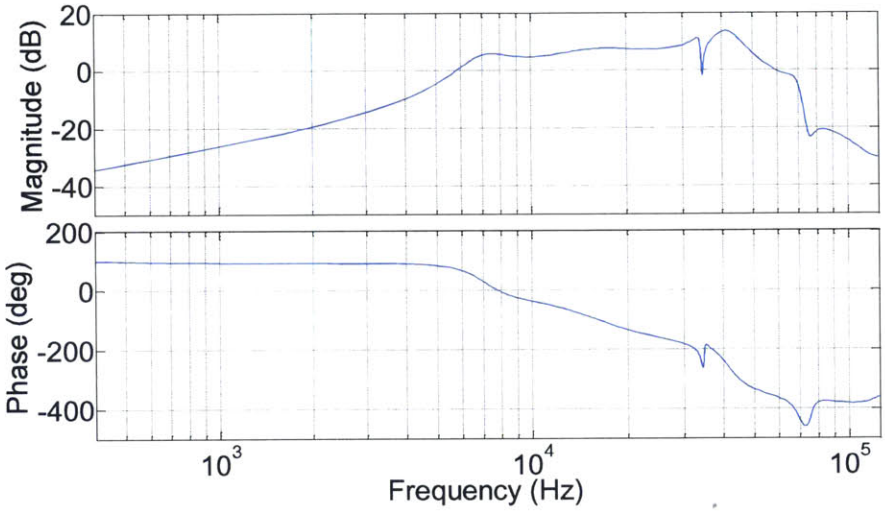

Figure 4-11: Bode plot of the designed CA compensator.

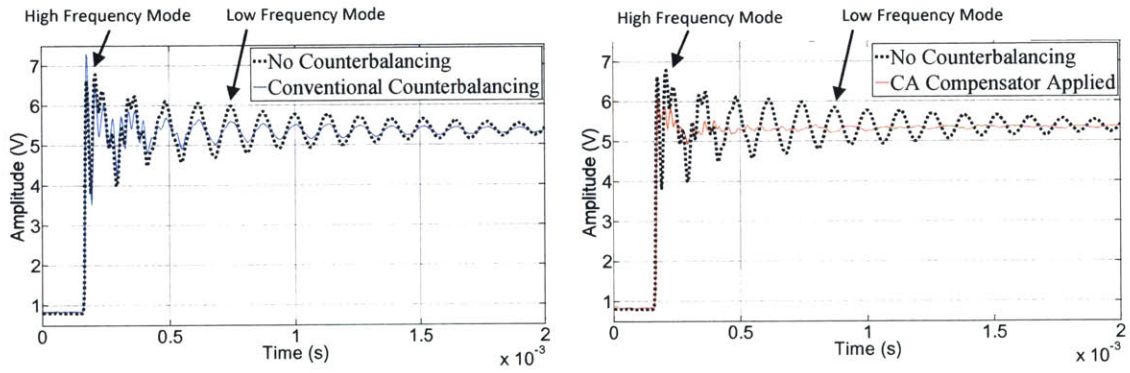

(a) (b)

Figure 4-12: Deflection signal in response to an step signal actuating the z piezo, (a) black, dotted line: no counter-balancing is used; blue, solid line: the cz piezo is driven by the same signal as that driving the z piezo, and (b) black, dotted line: no counter-balancing is used; red, solid line: the CA compensator is applied.

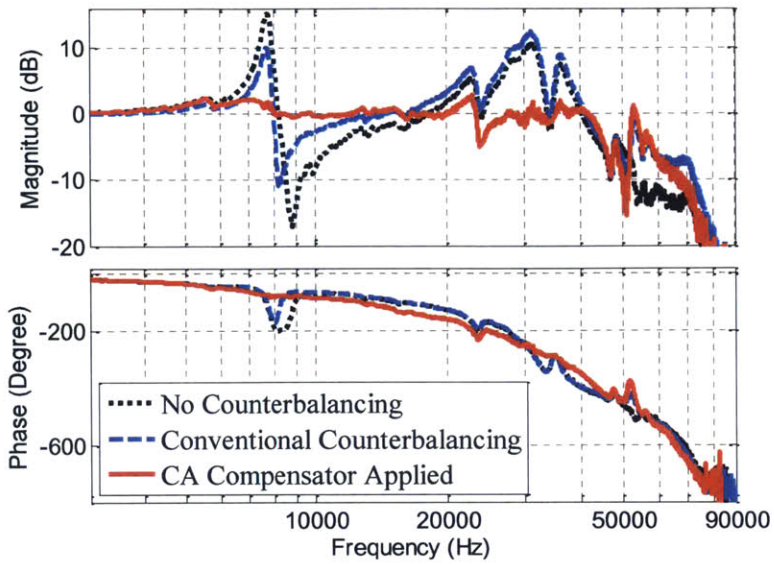

Figure 4-13: Empirical transfer function estimates associated with the three cases represented in Fig. 4-12, black dotted line: the cz piezo is not active, blue dashed line: the cz piezo is driven by the same signal as that driving the z piezo (conventional counterbalancing), red solid line: the CA compensator is applied.

result of the topography and the deflection images taken at 60 Hz scan rate when the conventional counterbalancing (left) and the designed CA compensator (right) are applied. One can see from Fig. 4-15 (right) that with the application of the CA compensator the shadows and ripples appearing in the left-side, error and height images, are completely removed, significantly improving the quality of the images.

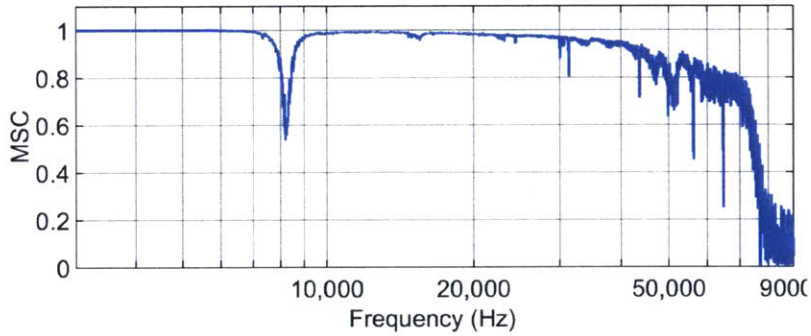

Figure 4-14: Magnitude squared coherence associated with the frequency response of the scanner when both z and cz piezos are actuated.

In this section we illustrated that by proper actuation of the counter-z piezo one can compensate for the limitations of conventional counterbalancing scheme. This

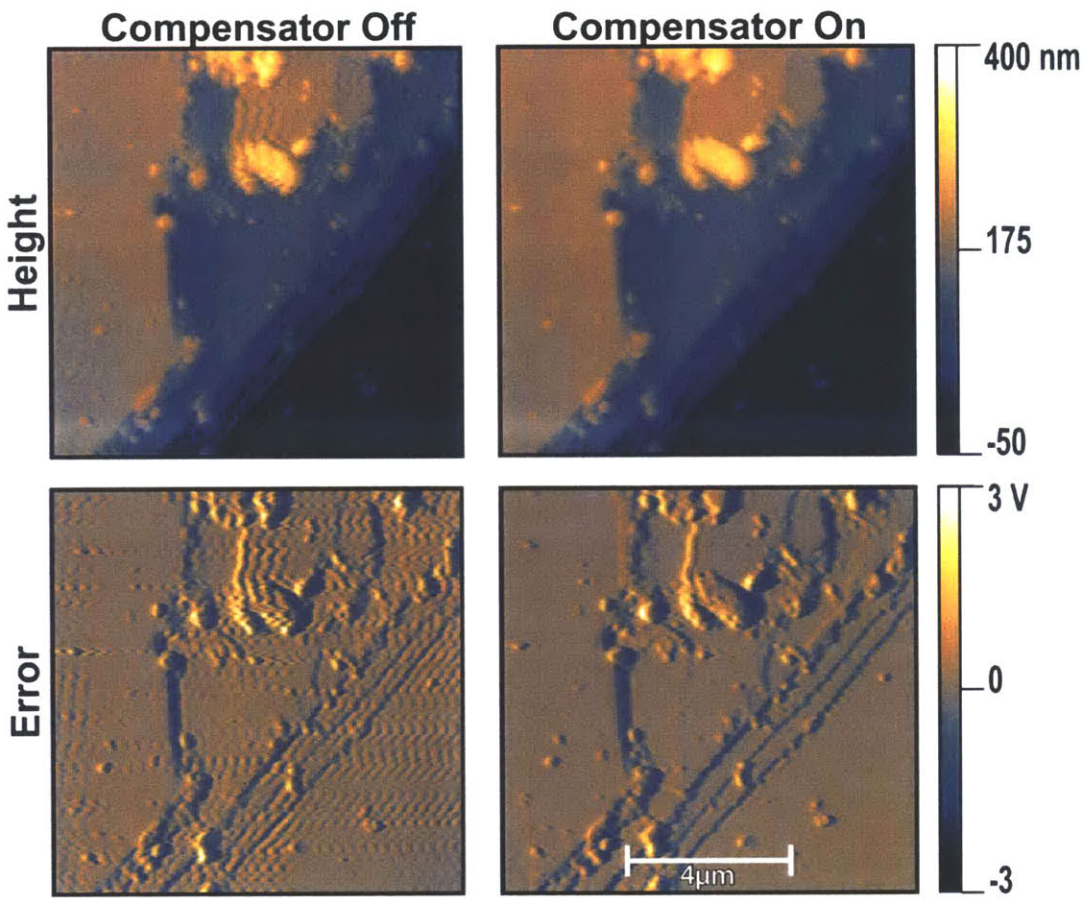

Figure 4-15: Topography (top) and deflection (bottom) AFM images, taken from freshly cleaved and sanded mica at 60 Hz scan rate with conventional counterbalancing technique (left), and CA compensator applied (right), for similar PID gains.

was achieved by shaping the AFM controller output via a counter actuation (CA) compensator. The compensator parameters were estimated using the data-based control design scheme proposed in section 3.3.

4.3 Multi-Actuation for High-Speed and Large-Range Atomic Force Microscopy

To achieve higher scan speeds one needs to use faster actuators. As actuators with wider mechanical bandwidth have a shorter range, achieving high-speed positioning is in general accompanied by a compromise on the scan range. In a different form of

redundant actuation, hereafter referred to as multi-actuation, several actuators with different range and bandwidth specifications cooperate to simultaneously achieve the speed and range requirements. Unlike the counterbalancing scheme where the extra actuator is used to suppress the vibrations excited in the system, in multi-actuation each actuator directly contributes to the overall positioning of the sample. In this section a general multi-actuation scheme is proposed that is applicable to any nano-positioning task requiring high-speed and large-range performance. In the proposed scheme multiple actuators are cascaded in series. The larger actuators are responsible for the large-range/slow positioning of the sample and the smaller actuators take care of the short range/fast motions. Effective operation of such a multi-component nano-positioner requires control schemes that properly divide the positioning responsibility between the actuators and simultaneously compensate for their coupled dynamics. This is elaborated in the following subsections.

4.3.1 The notion of multi-actuation

The advantage of utilizing multiple actuators in atomic force microscopy is rooted in the fact that, for both lateral and out-of-plane motion of the scanner, the travel range requirements are less stringent at higher frequencies. The bandwidth requirements of the out-of-plane motion is dictated by the spatial frequency content of the sample surface topography, which commonly contains low amplitude/high spatial frequency and large amplitude/low spatial frequency features. Figure 4-16 schematically illustrates an example of sample surface topographic features usually observed in practice. As shown in this figure, larger amplitude features occur at low transition rates (low spatial frequency content). A typical and practically important large range/low spatial frequency feature corresponds to the sample tilt. This is likewise illustrated in Fig. 4-16. For a sample with length $L = 20\mu$m slanted at $\alpha = 14°$, the height difference between the two endpoints of the sample is approximately $H_1 \approx 5\mu$m which is considered relatively large for out-of-plane positioning. As these low-spatial frequency features lead to low frequency disturbances to the cantilever, a slow actuator can easily handle them at high imaging speeds. On the contrary, the small ampli-

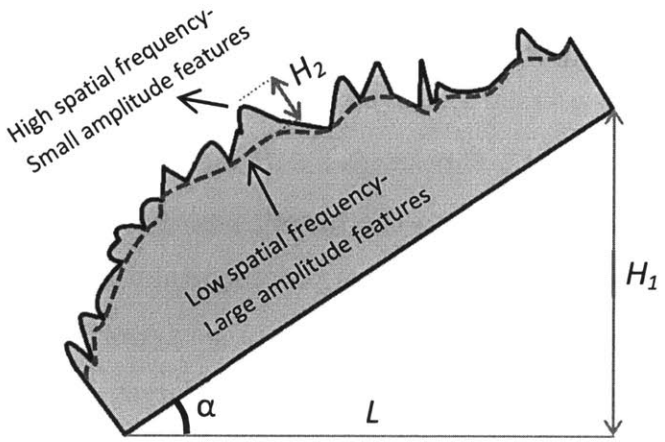

Figure 4-16: Schematics of topographic features reflecting high spatial frequency-small amplitude and low spatial frequency-large amplitude components. H_1 and H_2 represent the maximum height variations respectively for low and high spatial frequency features.

tude/high spatial frequency topographic features of the sample surface at high scan rates translate to high frequency disturbances with tens of kilohertz bandwidth. For an AFM operating solely on a large-range (and hence slow) nano-positioner, the user is forced to settle with very slow scan speed to translate the high spatial frequency features of the sample to low temporal frequency disturbances to the cantilever. On the other hand, an AFM solely equipped with a high-speed (and hence short-range) nano-positioner suffers from many constraints regarding the variety of imaging experiments that can be accommodated. Given the nature of the problem, application of multiple actuators seems to be an effective solution. In this approach one needs to divide the responsibilities between multiple actuators over the frequency domain so that smaller and faster actuators take care of high frequency/low amplitude topographic features, while the larger and consequently slower actuators follow the large scale/low frequency topographic features of the sample such as tilt.

A slightly different argument applies to the lateral positioning. It can be shown that the high frequency components of the triangular raster command input to the lateral scan actuators are localized near the turnaround points which constitute a small portion of the scanning range. Equations (4.4) and (4.5) give the Fourier series

representation of a periodic triangular raster command signal with period $2L$.

$$f(t) = \sum_{n=1}^{\infty} b_n \mathrm{Sin}(\frac{n\pi\ t}{L}) \tag{4.4}$$

where b_n is given as:

$$b_n = \frac{8}{\pi^2 n^2} \begin{cases} 1 & n \text{ odd} \\ (-1)^{\frac{n-1}{2}} & n \text{ even} \end{cases} \tag{4.5}$$

Let us divide this signal into two separate components, as given below:

$$f(t) = f_1(t) + f_2(t) = \frac{8}{\pi^2}\mathrm{Sin}(\frac{\pi\ t}{L}) + \sum_{n=2}^{\infty} b_n \mathrm{Sin}(\frac{n\pi\ t}{L}) \tag{4.6}$$

The first component, $f_1(t)$, only includes the first or fundamental harmonic of scanning frequency, and the second component, $f_2(t)$, includes all the higher harmonics. These signal components are illustrated in Fig. 4-17 for a triangular wave of unity amplitude and a period of 1 s (blue). The first component, $f_1(t)$, and the second component, $f_2(t)$, are superimposed on the same plot in red and black, respectively. In this plot, $f_2(t)$ includes the first 1000 harmonics of the summation of Eq. (4.6). As shown in this figure, the peak amplitude associated with the fundamental harmonic is 0.81. The peak amplitude for the second signal component, $f_2(t)$, composed of all the higher harmonics of the periodic triangular wave is 0.19. In other words, in triangular raster scanning 81 percent of the scan range is accommodated by the first harmonic of the series, with all the higher harmonics forming the remaining 19 percent.

The above discussions imply that for both lateral and out-of-plane motion of the scanner high-speed and large-range nano-positioning is possible if one combines slower and larger-range actuators with those of wider mechanical bandwidth and shorter range.

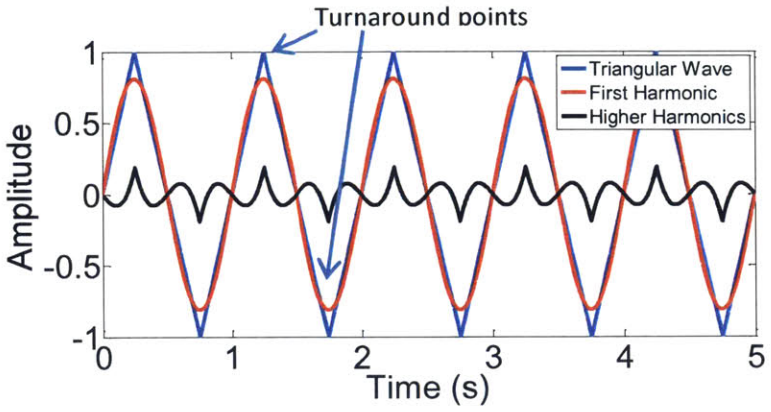

Figure 4-17: Decomposition of a triangular wave into two components, $f_1(t)$ and $f_2(t)$ per Eqs. (4.4), (4.5) and (4.6).

4.3.2 Dynamic Coupling

In one form of multi-actuation, several actuators are cascaded in series, sorted from the largest (slowest) to smallest (fastest). Figure 4-18 schematically demonstrate this arrangement for a series of N actuators where each actuator is represented as a 2^{nd} order system with an incorporated actuation force. In this arrangement all the scanner components can be enclosed into a single package. Although this is practically appealing, it leads to dynamic coupling and thus makes the control task more complex.

Before addressing the control design for a multi-component scanner let us take a closer look at the dynamic coupling effect. Figure 4-19a illustrates a second order model of a single isolated actuator, with the corresponding transfer function given as:

$$\frac{x_1(s)}{F_1(s)} = \frac{1}{m_1 s^2 + c_1 s + k_1} \tag{4.7}$$

Fig. 4-19b shows a cascaded series of two actuators with the corresponding transfer functions given below:

$$\frac{x_2(s)}{F_1(s)} = \frac{c_2 s + k_2}{(m_1 s^2 + c_1 s + k_1)(m_2 s^2 + c_2 s + k_2) + m_2 s^2 (c_2 s + k_2)} \tag{4.8}$$

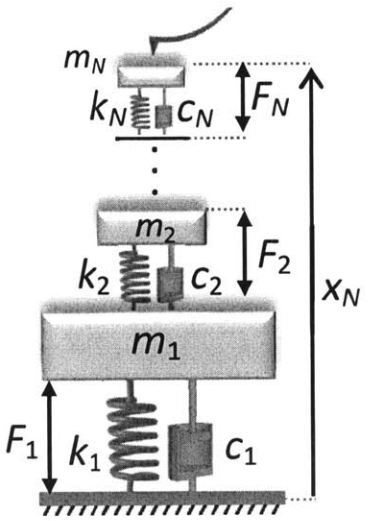

Figure 4-18: Schematics of a cascaded series of N actuators, each modelled as a 2nd order system.

$$\frac{x_2(s)}{F_2(s)} = \frac{m_1 s^2 + c_1 s + k_1}{(m_1 s^2 + c_1 s + k_1)(m_2 s^2 + c_2 s + k_2) + m_2 s^2 (c_2 s + k_2)} \tag{4.9}$$

It is assumed that the additional actuator is always smaller (shorter range) i.e. with smaller mass ($m_2 < m_1$), higher stiffness ($k_2 > k_1$) and lower damping ($c_2 < c_1$) in line with the characteristics of the actuators encountered in practice. We assign tentative values to the mass, stiffness and damping of actuator #1 (Fig. 4-19b) as $m_1 = 6e-3$ kg, $\zeta_1 = \frac{c_1}{2\sqrt{m_1 k_1}} = 0.03$, and $k_1 = 2.5e07$ N/m. The extra actuator (#2 in Fig. 4-19b) is assumed to have a quarter of the range of actuator #1. The corresponding parameters are set as $m_2 = m_1/4$, $c_2 = c_1/4$, and, $k_2 = 4k_1$. The Bode plots for the transfer functions associated with Eqs. (4.8) and (4.9) are shown in Figs. 4-20a and 4-20b (blue solid line), respectively. In these plots, the red dashed lines reflect the behavior of the individual actuators (Eq. (4.7)) when excited in isolation (i.e. when mounted on a ground structure similar to Fig. 4-19a). As expected from the additional term, $m_2 s^2 (c_2 s + k_2)$, in the denominator of both transfer functions (Eqs. (4.8) and (4.9)), the poles are shifted with respect to those of the individual actuators. This shift for the first actuator is towards lower

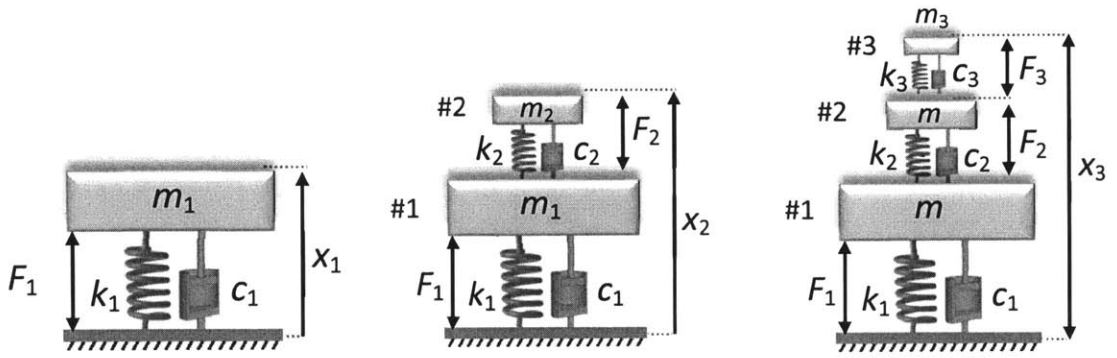

(a) (b) (c)

Figure 4-19: a) A second order model of a single actuator, b) a cascaded series of two actuators, and c) a cascaded series of three actuators. The mass, spring constant and damping of each actuator is denoted by m_i, k_i, and c_i, respectively. The actuation force is represented by F_i.

frequencies and for the faster actuator towards the higher frequencies. It is observed from Fig. 4-20a that the excitation of the slower actuator also excites the dynamics of the faster actuator. However, the dynamics of the faster actuator falls beyond the mechanical bandwidth of the slow actuator and hence can be overlooked in the frequency response of the slower actuator. As such (from Fig. 4-20a), the dynamic response of the larger actuator (#1) remains almost the same (except for a reduction in the bandwidth due to the added mass). In a similar fashion, upon driving the faster actuator (actuator #2), it also excites (Fig. 4-20b) the dynamics associated with the slower actuator (actuator #1). In this case the effect of dynamic coupling appears on the passband of the fast actuator and is hence problematic. A pair of complex conjugate zeros exactly matching the original poles of the slow/large-range actuator extends the bandwidth of the system all the way to the natural mechanical bandwidth of the faster actuator (see Fig. 4-20b and Eq. (4.9)). As a result, although the faster actuator features its original mechanical bandwidth, it also demonstrates some additional in-band dynamics caused by the dynamic coupling with the slower actuator.

We repeat the analysis for the case of three cascaded actuators as shown in Fig. 4-19c. The third actuator is set to have a range of one fourth of the second actuator.

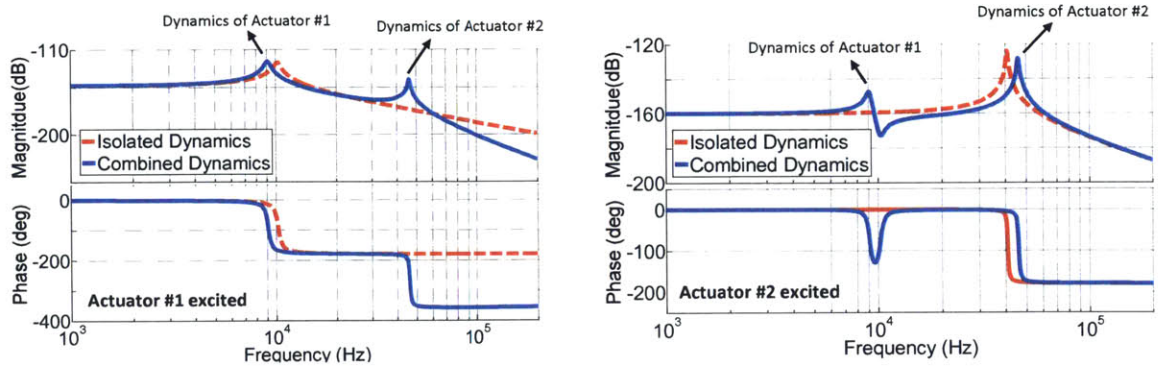

(a) (b)

Figure 4-20: Bode plot associated with the transfer functions of a) Eq. (4.8), and b) Eq. (4.9) (blue solid line). Red dashed line in both parts (a) and (b) corresponds to the bode plot of the isolated actuators (respectively for actuator #1 and #2 of Fig. 4-19b.

As is also observed from the Bode plots of Figs. 4-21(a), (b) and (c), excitation of each actuator also excites the dynamics associated with all the other actuators. However, such dynamics are of importance only if they belong to a slower actuator as in such cases they fall within the bandwidth of the excited actuator.

4.3.3 Out-of-Plane Multi-Actuation: Control Design

As discussed in chapter 3 the proposed out-of-plane control consists of a PID controller and one or more auxiliary compensation units that aim to achieve a maximally flat frequency response for the equivalent AFM plant, P_e^{v} (see Fig. 3-1b). The out-of-plane control arrangement for a multi-actuated scanner is shown in Fig. 4-22 where the actuators are sorted from the slowest/largest-range, P_1^{v} to fastest/shortest-range, P_N^{v}. The design of the compensators, G_n^{v}, $n = 1, \ldots, N$ where N is the number of actuators, can be converted to the design problem of Figs. 3-3 and 3-4. Referring to these figures the datasets $r_1^{\mathrm{v}}, \ldots, r_N^{\mathrm{v}}$ can be acquired by measuring the response of individual actuators to a common, wideband excitation signal, u^{v}. To implement the proposed design scheme of Fig. 3-4 we also need access to the desired datasets, d_n^{v}. Given Eq. (3.3) and upon the availability of the overall desired response of the equivalent AFM scanner, d^{v}, in the out-of-plane direction, we need access to $N-1$

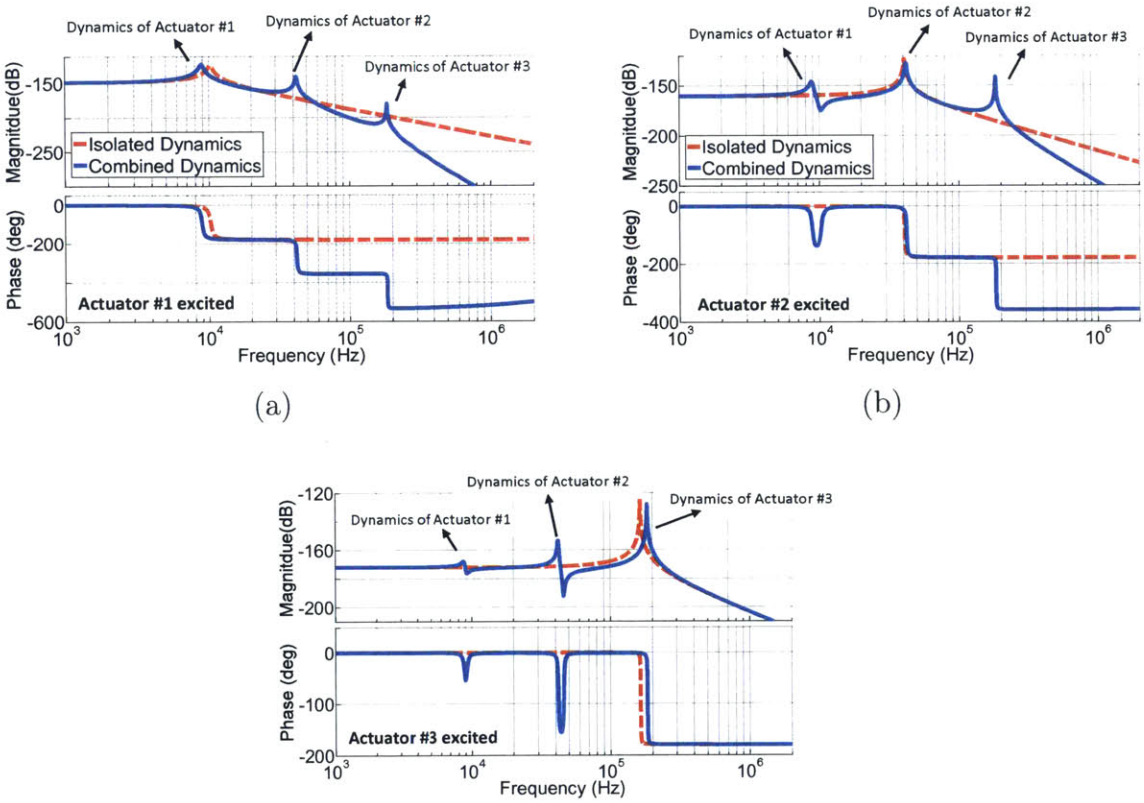

Figure 4-21: Bode plots associated with the three DOF system of Fig. 4-19c, with transfer functions of a) F_1 to X_3, b) F_2 to X_3, and c) F_3 to X_3, (blue solid lines), red dashed lines correspond to each actuator excited in isolation.

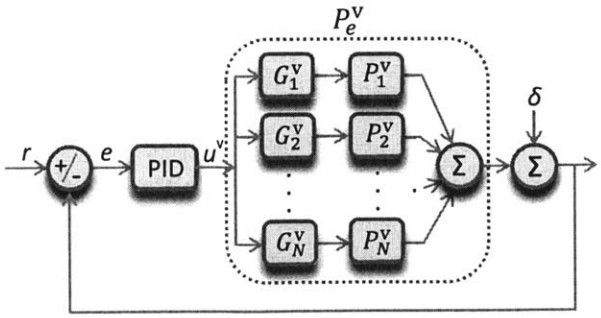

Figure 4-22: The proposed out-of-plane control arrangement for a multi-actuated AFM scanner: control units, G_n, in series with the actuators compensate for their excited dynamics and divide the tracking responsibilities between the actuators.

out of the N desired responses, d_n^v, $n = 1, \ldots, N$.

To find d^v we need to find the unknown parameters of the ideal plant P_I (Eq. (3.1)). The parameters of the ideal plant, (τ_c, α, n) , can be obtained by fitting the model of Eq. (3.1) to the fastest out-of-plane actuator of the scanner, P_N^v:

$$(\tilde{\alpha}, \tilde{\tau_c}, \tilde{n}) = \text{argmin}_{(\alpha,\tau_c,n)} \int_0^{+\infty} |W(\omega)^2||P_I(\alpha, \tau_c, n, \omega) - P_N^v(\omega)|\, d\omega \tag{4.10}$$

where P_I is the ideal plant behavior given in Eq. (3.1), $P_N^v(\omega)$ is the frequency response function associated with the fastest actuator of the scanner, and $W(\omega)$ is a weighting function chosen to emphasize the high SNR frequency ranges of P_N^v dynamics. For discrete-time implementation the ideal plant P_I can be converted to discrete-time or as discussed in section 4.2.2 be replaced by a discrete-time low-pass filter. As mentioned before, a Butterworth lowpass is maximally flat on the passband and hence, is a suitable lowpass structure candidate. Upon estimating the parameters of the ideal plant, P_I, the desired response, d^v can be obtained as:

$$d^v = h_I * u^v \tag{4.11}$$

where h_I is the impulse response associated with the fitted ideal plant (Eq. (4.10)), and u^v is a wideband excitation signal such as a random binary sequence.

Let us now assume that the operating frequency range to be assigned to each

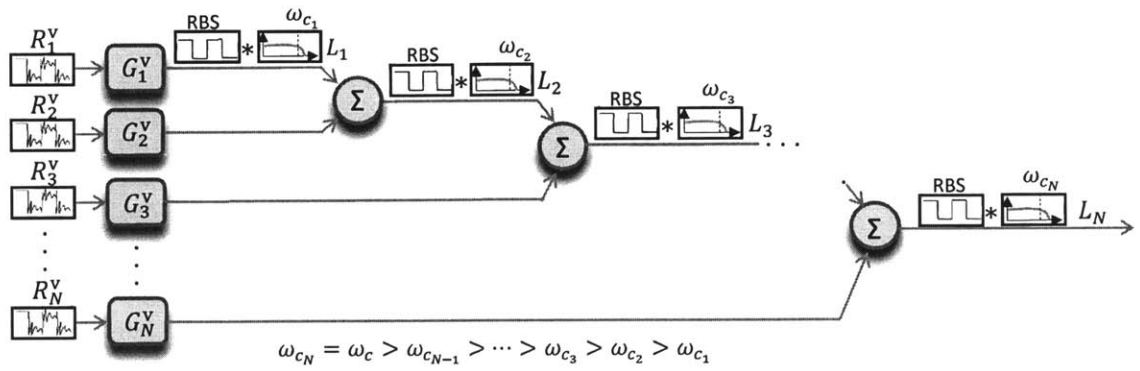

Figure 4-23: With the addition of each actuator the cumulative bandwidth is extended up to the mechanical cut off frequency of that actuator.

actuator is known apriori i.e. $0 - \omega_{c_1}$ for P_1^v, $\omega_{c_1} - \omega_{c_2}$ for P_2^v, and so on. Upon the addition of a faster actuator, the mechanical bandwidth of the combined system extends to the maximum drive frequency assigned to that actuator e.g. upon the addition of P_2^v to P_1^v, the mechanical bandwidth of the equivalent system changes from ω_{c_1} to ω_{c_2}, and so on. This is shown in Fig. 4-23, where the behavior of the n^{th} stage composed of the actuators $[P_1^v, \ldots, P_n^v]$ is represented by a lowpass filter, L_n with cut-off frequency of ω_{c_n}, $\omega_{c_n} < \omega_{c_{n+1}}$. Note that for the last stage $L_N = P_1$. Starting from the first actuator (slowest and largest range), the desired response,d_1^v, is a lowpassed version of the wideband excitation input, u^v, i.e.

$$d_1^v = k_1^v * u^v \tag{4.12}$$

where k_1^v is the impulse response associated with the lowpass filter, L_1, with a cutoff frequency of ω_{c_1}. Upon the availability of d_1^v, $G_1^v = \tilde{G}_1^v$ can be obtained per Eqs. (3.4) and (3.5). This is schematically illustrated in Fig. 4-24a. Following the design of G_1^v, the desired response, d_2^v, of the second actuator, P_2^v, can be obtained. From Fig. 4-23, we know that the desired response of the first two actuators combined is a lowpassed version of the excitation input, u^v. Hence, we can write:

$$d_2^v + \tilde{h}_1^v * r_1^v = k_2^v * u^v \Rightarrow d_2^v = k_2^v * u^v - \tilde{h}_1^v * r_1^v \tag{4.13}$$

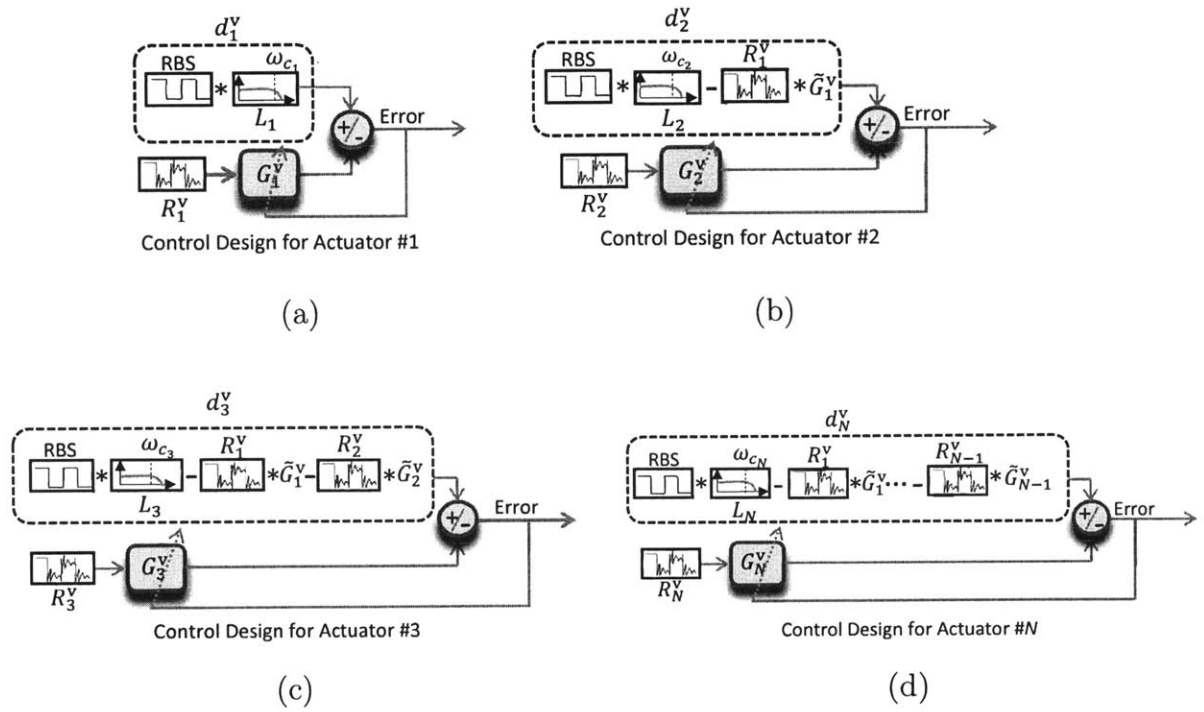

Figure 4-24: Sequential design of control units a) G_1^{v}, b) G_2^{v}, c) G_3^{v}, d) G_N^{v}. ω_{c_n} represents the desired bandwidth of the n^{th} piezo actuator.

where $\tilde{h}_1^{\mathrm{v}}$ is the impulse response associated with the designed compensator $\tilde{G}_1^{\mathrm{v}}$, k_2^{v} is the impulse response corresponding to the second stage lowpass filter, L_2, with a cutoff frequency of ω_{c_2}. r_n^{v} is the response of P_n^{v} to the excitation input u^{v} (see Fig. 3-3). As before, upon the availability of d_2^{v}, $G_2^{\mathrm{v}} = \tilde{G}_2^{\mathrm{v}}$ can be obtained using Eqs. (3.4),(3.5) and (3.6). The design of the second compensator is schematically shown in Fig. 4-24b. The design of the third compensator is similarly shown in Fig. 4-24c. For the last compensator we utilize the overall desired response d^{v} to find d_N^{v} i.e. using Eq. (3.3). We have: $d_N^{\mathrm{v}} = d^{\mathrm{v}} - d_1^{\mathrm{v}} - d_2^{\mathrm{v}} - \ldots\ d_{N-1}^{\mathrm{v}}$. We have:

$$d^{\mathrm{v}} = k_N * u^{\mathrm{v}}$$

where $k_N = h_I$ (Eq. (4.11)) is the impulse response associated with $L_N = P_I$. The last design stage is shown in Fig. 4-24d.

Summary of the Compensator Design Steps for Multi-Actuated Scanners

The design of compensators, G_n^{v}, for a multi-actuated scanner can be summarized in the following steps:

1) Excite the individual actuators with a wide band random binary sequence (RBS) to obtain the responses, $\mathbf{R_n^v} = \{r_n^{\mathrm{v}}(m), m = 1, \ldots, M\}$.

2) Form desired response datasets based on Fig. 4-24, starting from the slowest actuator:

$$d_n^{\mathrm{v}} = k_n^{\mathrm{v}} * u^{\mathrm{v}} - \sum_{j=1}^{n-1} \tilde{h}_j^{\mathrm{v}} * r_k^{\mathrm{v}} \tag{4.14}$$

where k_n^{v} is the impulse response associated with the n^{th} stage lowpass filter, L_n, and $\tilde{h}_j$ is the impulse response associated with the designed compensator $\tilde{G}_j, j < n$.

3) Find the control parameters for stage n using Eqs. (3.4),(3.5) and (3.6) for a given set of actuator response data, $\mathbf{R_n^v}$, and the desired response dataset, $\mathbf{D_n^v} = \{d_n^{\mathrm{v}}(m), m = 1, \ldots, M\}$, .

4) Repeat steps 1 to 3 for all compensator units G_n^{v}, $n = 1, \ldots, N$.

Stage Lowpass Filters: Selection of cut-off frequency and order

Now we discuss the selection of order and cut-off frequency for the stage lowpass filters (L_n for $n = 1, \ldots, N-1$) in Figs. 4-23 and 4-24. Here we assume a Butterworth structure for the stage lowpass filters. Although, the following arguments apply to any other structure. From earlier discussions (see Fig. 4-24) we know that upon a successful design of $G_{n+1}^{\mathrm{v}} = \tilde{G}_{n+1}^{\mathrm{v}}$ we can write:

$$L_n + \tilde{G}_{n+1}^{\mathrm{v}} P_{n+1}^{\mathrm{v}} \approx L_{n+1} \tag{4.15}$$

where L_{n+1} is the lowpass associated with the $(n+1)^{\mathrm{th}}$ stage. Let us now define the transition frequency, ω_t (Fig. 4-25), as the frequency where the magnitudes of the first two parts of the left-hand side of Eq. (4.15) are equal, i.e.

$$a = |L_n(\omega_t)| = |\tilde{G}_{n+1}^{\mathrm{v}}(\omega_t) P_{n+1}^{\mathrm{v}}(\omega_t)| \leq 1.$$

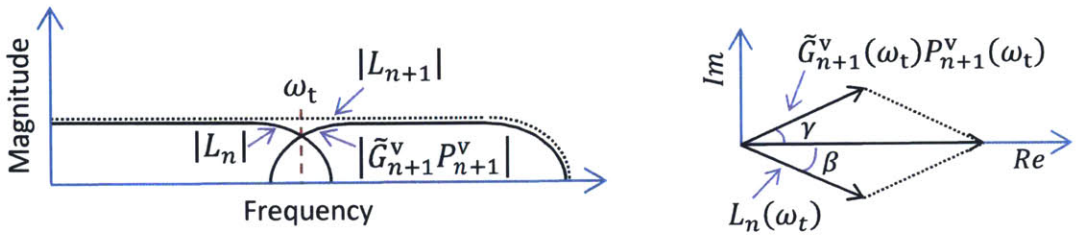

(a) (b)

Figure 4-25: a) Magnitude responses (Eq. (4.15)) and the transition frequency, ω_t, where $a = |L_n(\omega_t)| = |\tilde{G}^{v}_{n+1}(\omega_t)P^{v}_{n+1}(\omega_t)|$, and b) summation in vector form, $\gamma = \angle(\tilde{G}^{v}_{n+1}(\omega_t)P^{v}_{n+1}(\omega_t))$, and $\beta = -\angle(L_n(\omega_t))$.

where for simplicity we assumed that the DC gain of L_n is normalized to 1. Figure 4-25a schematically illustrates the magnitude responses of $|L_n|$, $|\tilde{G}^{v}_{n+1}P^{v}_{n+1}|$ and $|L_{n+1}|$. This figure also shows the transition frequency, ω_t. Eq. (4.15) can be represented in vector form as shown in Fig. 4-25b. From Figs. 4-25a and 4-25b assuming a unity DC gain for L_n and L_{n+1} we can write:

$$a\cos\gamma + a\cos\beta = 1 \tag{4.16}$$

$$a\sin\gamma - a\sin\beta = 0 \tag{4.17}$$

From Eqs. (4.16) and (4.17) we have: $\gamma = \beta$ and $a = \frac{1}{2\cos\gamma}$. So $1/2 < a < 1$ and $\gamma = \beta \leq \pi/3$. Figure 4-26 shows a plot of gain versus phase lag at the transition frequency in red (where $a = \frac{1}{2\cos\gamma}$). On the same figure the phase-magnitude response for Butterworth filters with different orders are superimposed. The intersections of the red and blue curves show the solutions to Eqs. (4.16) and (4.17) for various Butterworth orders. According to this figure for filter orders $q_n \geq 3$ the transition frequency resides at $\gamma = \beta \approx \pi/3$ where the filter magnitude response is $a \approx 1$ (both actuators are fully active). For higher order stage lowpass filters, the transition frequency is shifted towards lower frequencies. Increasing the lowpass order ensures that the slow actuators fully deactivate at high frequencies, but introduces additional

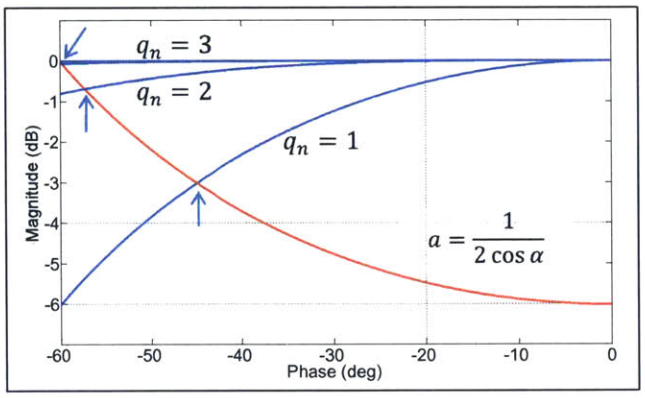

Figure 4-26: Red: gain versus phase lag at the transition frequency $a = \frac{1}{2\cos\gamma}$, blue: phase-magnitude plot for Butterworth lowpass filters. Intersection points denote the solutions for Eqs. (4.16) and (4.17) for a given stage lowpass.

phase lag and results in an opposing effort of the two actuator. To balance these effects we propose to use $q_n = 3$ for all stage lowpass filters (when using a Butterworth lowpass structure), L_n, $n < N$.

In the above argument we inherently assumed that the slower actuator does not introduce a large phase lag at the transition frequency, ω_t. To ensure that this assumption holds a rule of thumb is to select the transition frequency such that $\angle P_n^{\text{v}}(\omega_t) < 20°$. For a 3rd order Butterworth lowpass the frequency at which a $\pi/3$ phase lag occurs resides near $\omega_{c_n}/2$, where ω_{c_n} is the corresponding cut-off frequency. As such, the cutoff frequency for the stage lowpass, L_n, can be calculated from the selected transition frequency as $\omega_{c_n} = 2\omega_t$.

The following summarizes the steps of forming the stage low-pass filters, L_n:

1) Select the transition frequency, $\omega_t, n < N$, for the n^{th} nano-positioner, P_n^{v}, such that $|\angle P_n^{\text{v}}(\omega_t)| < 20°$.

2) Form L_n, $n < N$, the n^{th} stage low-pass, as a 3rd order Butterworth filter with a cut-off frequency of $\omega_{c_n} = 2\omega_t$.

3) For the last stage low-pass filter, $L_N = P_I$ (see Eq. (4.10)).

4.3.4 Out-of-Plane Multi-Actuation: Case Study

In this section the dynamic performance and the imaging capability of a conventional AFM that is retroactively enhanced through the proposed multi-actuation scheme is investigated. For this purpose a high-speed short-range nano-positioner is incorporated into the conventional tube scanner of this instrument as detailed in the following.

Experimental Setup

The proposed multi-actuation methodology is implemented on a Bruker AS-130NM tube scanner with a lateral range of 125 μm and an out of plane range of 5 μm. A small (2 mm $\times$ 2 mm $\times$ 2 mm) piezo stack, model PL022.30 from Physik Instrumente (PI) is used as a high speed additional actuator to improve the imaging speed of a Bruker Multi-Mode atomic force microscope. The high speed actuator is enclosed in an aluminum flexure cap in order to preload the piezo stack and protect the high voltage electrical connections when operating in fluid (Fig. 4-27). The flexure cap is composed of a top aluminum diaphragm (1 mm thick), and a lower pressure screw. The piezo stack actuator is glued to the top diaphragm and then pre-loaded from the bottom by the pressure screw. Figure 4-27a, illustrates the tube scanner and the additional stack actuator assembly mounted on top. The effective range of the piezo stack assembly is $\sim$1 μm. This actuator is driven by a custom made power amplifier (TechProject) with a bandwidth of 100 kHz. For the experiments the PID controller, as well as the designed units, $\tilde{G}_1^{\mathrm{v}}$ and $\tilde{G}_2^{\mathrm{v}}$, are implemented on a NI FlexRio FPGA platform. A separate compensator, implemented on a NI PXI-7851R FPGA module, is used to tackle the cross axis coupling rooted in the lateral piezo tube dynamics. This compensator can be designed based on the proposed multi-actuation control design methodology implemented for a single actuator (Fig. 4-24a). A schematic of the experimental setup is illustrated in Fig. 4-27b.

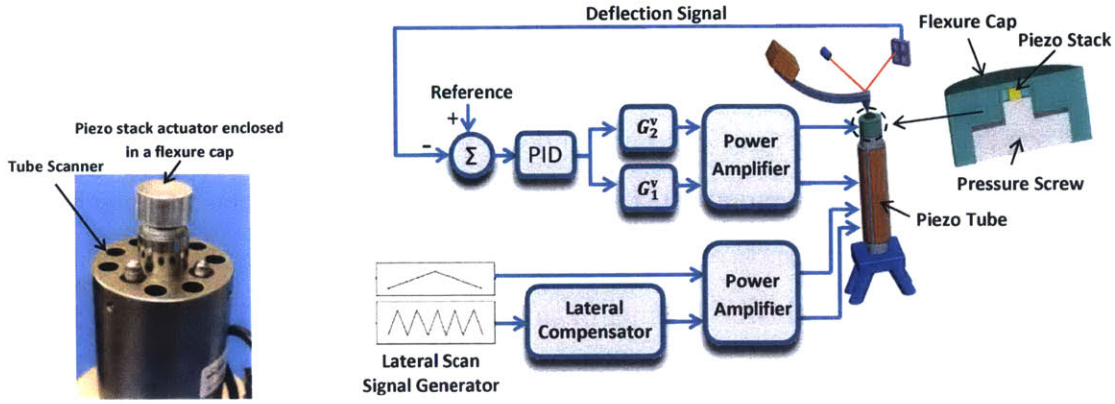

(a) (b)

Figure 4-27: a) AS-130NM tube scanner and the additional high-speed actuator mounted on top, and b) schematics of the experimental setup.

Design of G_1^v and G_2^v

The two units, G_1^v and G_2^v are designed to divide the responsibilities and compensate for the actuator dynamics. To measure the dynamic behavior of the individual actuators a rigid edge of a sample is brought in contact with the cantilever. As the sample and probe are in contact a wideband random binary sequence excites the tube and the stack independently while the two response datasets, $\mathbf{R_1^v}$ and $\mathbf{R_2^v}$, are respectively measured. The 1st and 2nd stage lowpass structures (L_1 and L_2) are selected as Butterworth with cut-off frequencies of $\omega_{c_1} = 1.5$ kHz and $\omega_{c_2} = 87$ kHz, respectively. The gain of L_1, α_1, matches the DC gain of the tube scanner, P_1^v. As discussed in this section, the order of L_1, $q_1 = 3$ and the cut-off frequency $\omega_{c_1} = 2\omega_t$ where ω_t is selected such that $\angle P_1^v(\omega_t) < 20°$. The gain, α_2, order, q_2, and cutoff frequency, ω_{c_2} of the Butterworth lowpass associated with L_2 is obtained by fitting its frequency response to that of the second (fastest) actuator, in a similar fashion as proposed by Eq. (4.10). We have:

$$\begin{aligned}(\tilde{\alpha_2}, \tilde{q_2}, \tilde{\omega}_{c_2}) &= \text{argmin}_{\alpha_2, q_2, \omega_{c_2}} \\ &= \sum_{m=1}^{M} |\frac{R_2^v(2\pi\ m/M)}{U^v(2\pi\ m/M)} - \alpha_2 B(2\pi\ m/M, q_2, \omega_{c_2})|^2 |W(2\pi\ m/M)|^2\end{aligned} \tag{4.18}$$

where $U^{\mathrm{v}}(\Omega)$ is the frequency domain representation of the wide band excitation,$\mathbf{U}^{\mathrm{v}} = \{u^{\mathrm{v}}(m), m = 1, \ldots, M\}$, B is a unity gain Butterworth lowpass filter, with cutoff frequency ω_{c_2}, and order q_2. The weighting function is selected as $|W(2\pi\ m/M)|^2 = |R_2^{\mathrm{v}}(2\pi\ m/M)|^2$ to emphasize high SNR frequency bands. We have:

$$L_2 = \tilde{\alpha}_2 B(2\pi\ m/M, \tilde{q}_2, \tilde{\omega}_{c_2})$$

Given L_1, L_2, $\mathbf{R}_1^{\mathrm{v}}$ and $\mathbf{R}_2^{\mathrm{v}}$, the parameters of G_1^{v} and G_2^{v} are found according to the schematics of Figs. 4-24a and 4-24b and Eqs. (4.14), (3.4),(3.5) and (3.6). MATLAB system identification toolbox is used to find the compensator parameters for a given pair of datasets $(\mathbf{D}_{\mathbf{n}}^{\mathrm{v}}, \mathbf{R}_{\mathbf{n}}^{\mathrm{v}})$.

Dynamic Performance

To assess the effectiveness of the method, we investigate the open-loop and closed loop dynamic behavior of the actuators. The black curve in Fig. 4-28 illustrates the open-loop dynamics of the tube, demonstrating a strong resonance at 6.2 kHz. The dynamic response of the stack actuator is superimposed on the same figure in red. As expected the stack actuator excites the dynamics of the tube (denoted by yellow dotted circles). It also demonstrates a strong resonance near 75 kHz.

The bode plot of the designed compensators, $\tilde{G}_1^{\mathrm{v}}$ (4^{th} order) and $\tilde{G}_2^{\mathrm{v}}$ (12^{th} order) are illustrated in Fig. 4-30. The control unit, $\tilde{G}_1^{\mathrm{v}}$, compensates for the strong tube resonance and acts as a lowpass filter. The second controller, $\tilde{G}_2^{\mathrm{v}}$, gradually assigns actuation responsibility to the piezo stack and compensates for the associated dynamics on the passband. The frequency response of the combined multi-actuated setup is shown in Fig. 4-28 (blue). A flat frequency response is achieved and the effective bandwidth of the multi-actuated setup is extended to 87 kHz (3dB cut-off), reflecting more than an order of magnitude improvement compared to that of the tube actuator alone. The magnitude squared coherence plots associated with the frequency responses of Fig. 4-28 are given in Fig. 4-29.

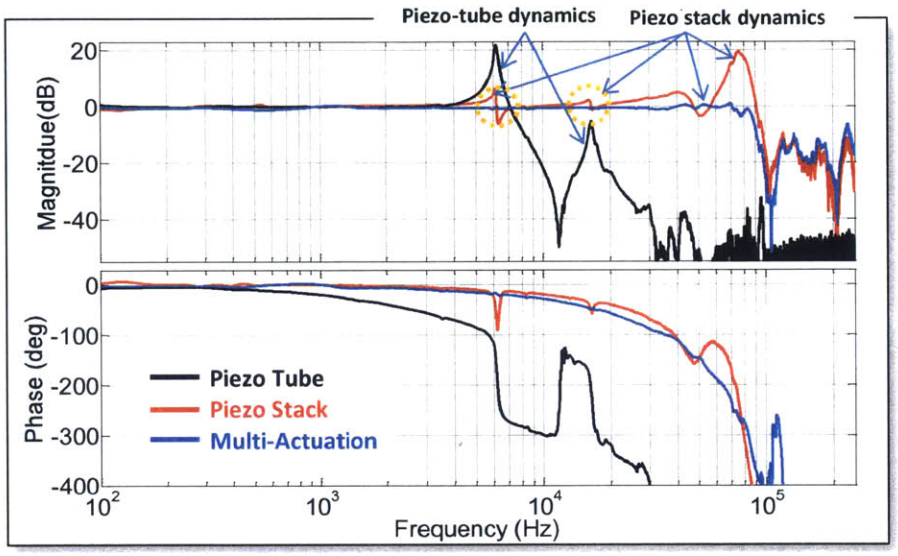

Figure 4-28: Empirical transfer function plots for the piezo tube (black), piezo stack (red) and the combined and compensated multi-actuated setup (blue). The frequency ranges denoted by yellow circles correspond to coupling between the dynamics of the piezo tube and the piezo stack.

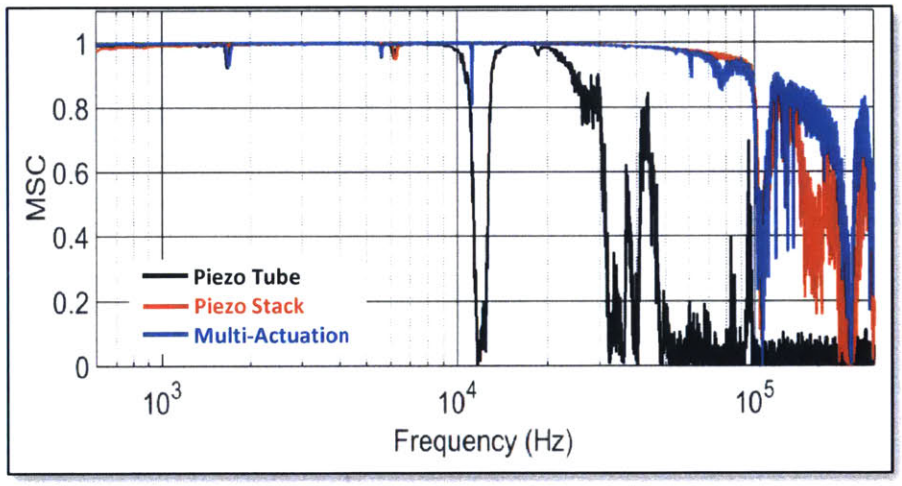

Figure 4-29: Magnitude squared coherence associated with the frequency response plots of Fig. 4-28.

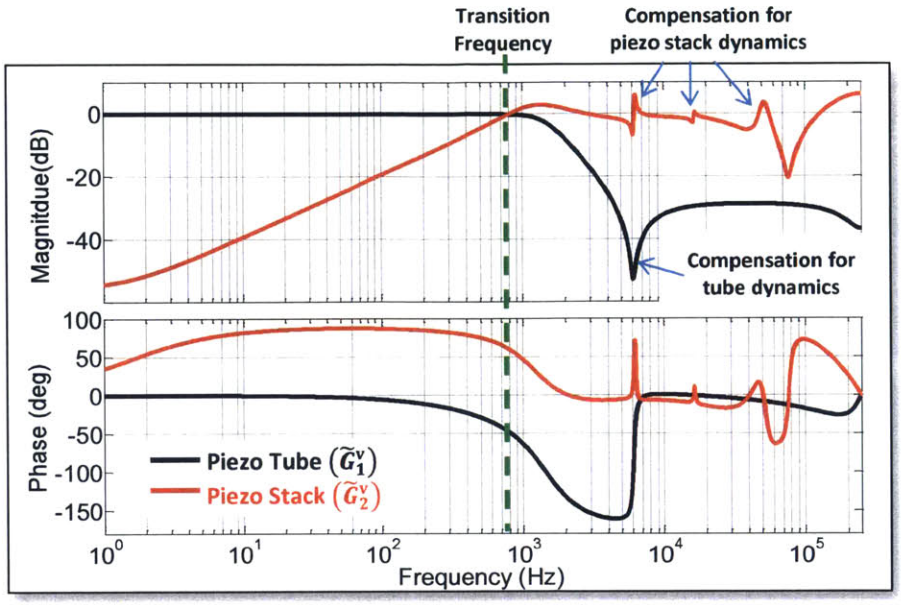

Figure 4-30: Bode plots of the designed control units for the piezo tube, $\tilde{G}_1^v$, (black), and piezo stack, $\tilde{G}_2^v$, (red).

To better observe the improvement in topography tracking, the closed-loop behavior of the system is evaluated when 1) the piezo tube is used alone, 2) the piezo stack is used alone and 3) the two actuators are combined via the designed controllers $\tilde{G}_1^v$ and $\tilde{G}_2^v$. For this purpose a probe is brought in contact with a rigid sample. Then a wideband excitation signal is injected into the loop as a variable reference set point, r_s (see Fig. 3-1). The PID gains are then gradually increased until the loop shows signs of instability. Figure 4-31 illustrate the closed loop behavior of the AFM system for the three cases mentioned above in black, red and blue, respectively. For case (1) the closed loop system shows strong oscillations at 5.6 kHz. This frequency is slightly higher for case (2) where strong oscillations appear at 5.9 kHz. For the multi-actuated system the closed loop bandwidth is extended to 60 kHz. A close up view of the multi-actuated closed loop frequency response near the strong dynamics of the piezo tube demonstrates some dynamic residuals. This is rooted in the controller errors and slight nonlinearities in the system. The magnitude squared coherence plots associated with the frequency responses of Fig. 4-31 are given in Fig. 4-32.

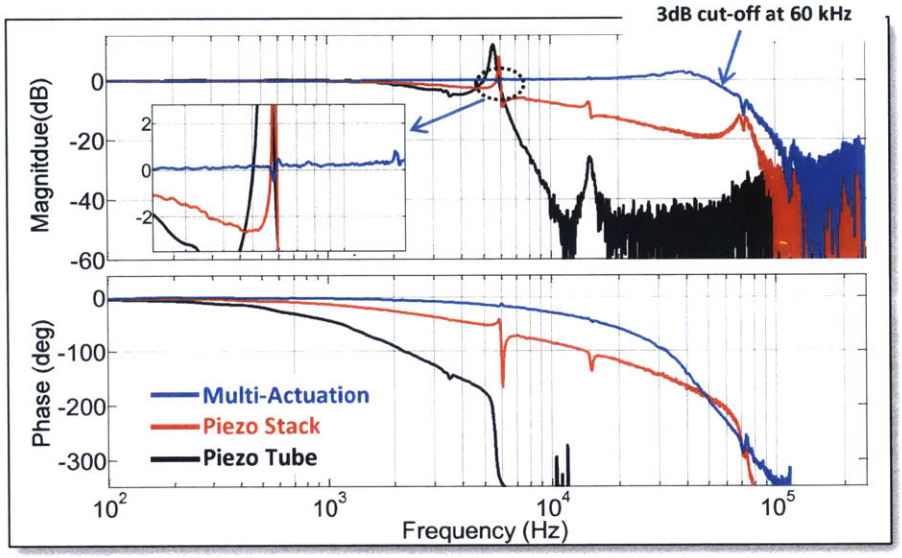

Figure 4-31: Closed loop behavior of the system for the actuation of piezo tube (black), piezo stack (red) and multi-actuation setup (blue).

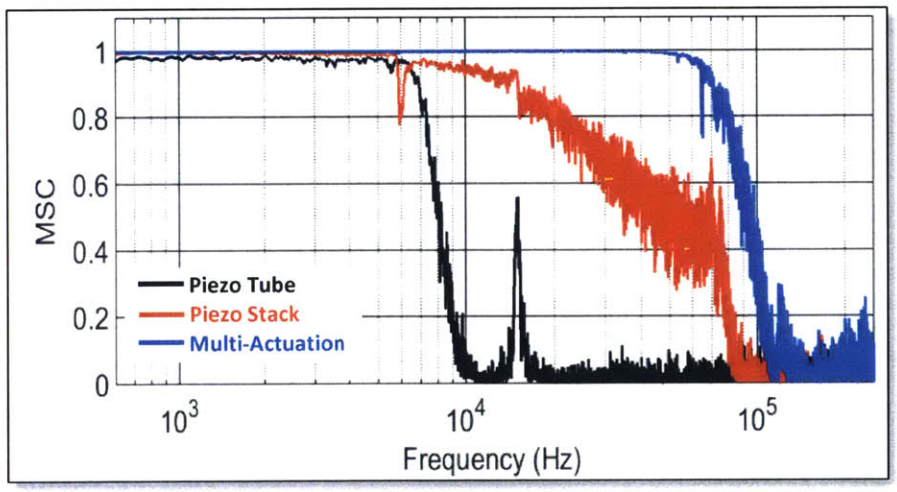

Figure 4-32: Magnitude squared coherence associated with frequency response plots of Fig. 4-31.

Imaging Performance

The imaging performance of the multi-actuated setup is evaluated in contact and tapping modes, in air and in liquid. First, a standard 3 μm-pitch square calibration grating is imaged in contact mode in air. The grating was placed on a fully flat surface to ensure that the required tracking range could be provided by the piezo stack alone. This is to observe the influence of dynamic coupling on imaging performance. The fast scan direction is chosen perpendicular to the grating edges to introduce the highest possible disturbance bandwidth to the probe. At 3.3 mm/s tip speed the AFM probe is subject to periodic square wave disturbances with a period of $T = 0.9$ ms.

Figure 4-33 shows AFM images and image section views when the isolated tube, isolated stack and the multi-actuation methodology are used. When either the piezo tube or the stack actuator is used in isolation, the AFM is only able to react to the first few harmonics of the fundamental frequency of the disturbance input. This results in severely smoothed response of the AFM actuator, inaccurate topography estimation and large probe-sample interaction forces. This is better observed form section views of the acquired deflection images plotted in Fig. 4-33(d) (black and red curves). Although the mechanical bandwidth of the stack actuator can accommodate high frequency components, the dynamic coupling with the piezo tube inhibits its closed loop operation beyond the tube resonance. This observation is also in line with the measured closed loop response of Fig. 4-31 (red). Given the 60 kHz closed loop bandwidth for the multi-actuation method, the AFM is able to react to the first 54 Fourier components of the disturbance. This leads to more accurate topography estimation and significantly reduced probe deflection as observed in Fig. 4-33(c) and the blue curve in Fig. 4-33(d).

Next, a sample of collagen fibrils extracted from rat tail is imaged [94]. The curved surface of this sample can introduce large tilt type height variations. The individual fibrils show 67 nm periodic banding patterns which introduce high frequency disturbances to the AFM probe when scanned at high speed. This sample provides a good platform to test the large range and high bandwidth of the multi-actuated

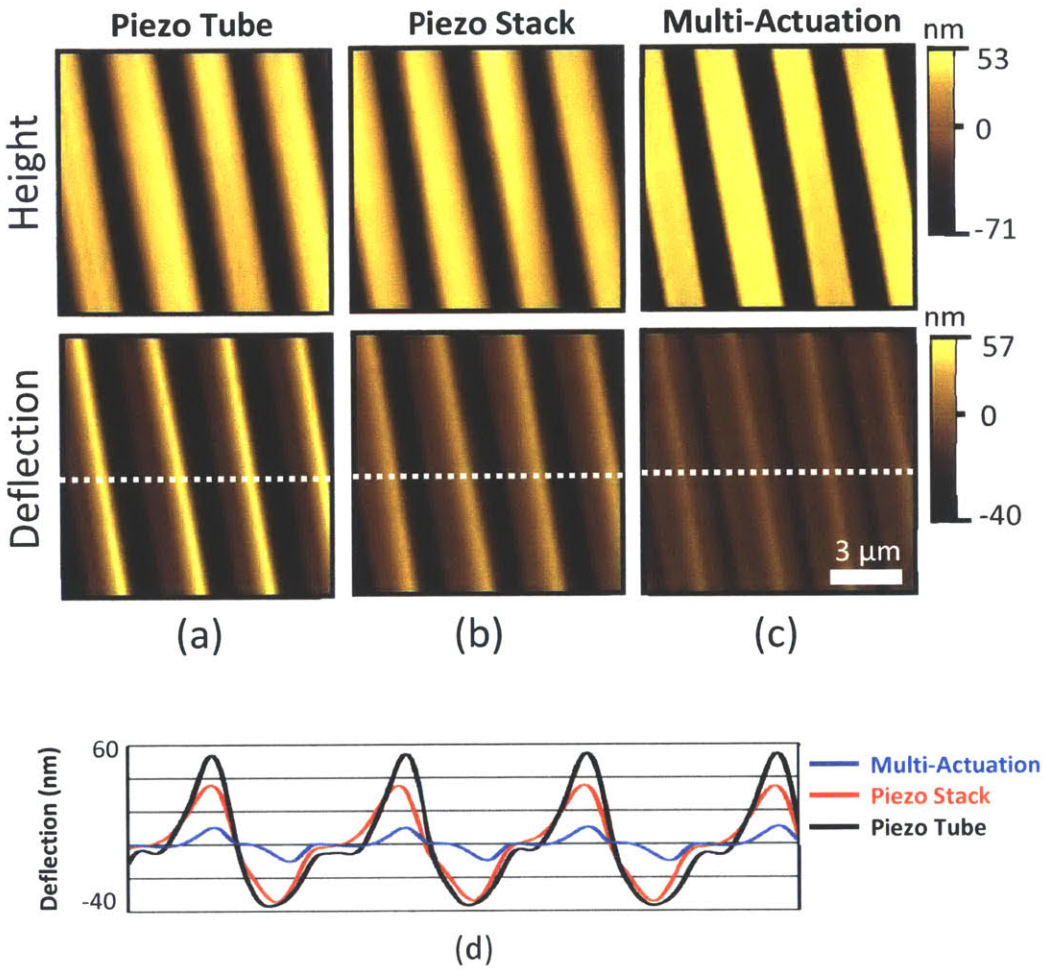

Figure 4-33: AFM Imaging of a 3 μm pitch calibration grating at 3.3 mm/s tip speed (97.7 lines/sec), perpendicular to the grating edges, using a) the tube actuator, b) the stack actuator and c) the proposed multi-actuated setup, d) a section (horizontal white dotted line) view of the deflection error images for the three cases presented in parts (a), (b) and (c) (Images are 11 μm cutout of 16.6 μm images, taken on retrace).

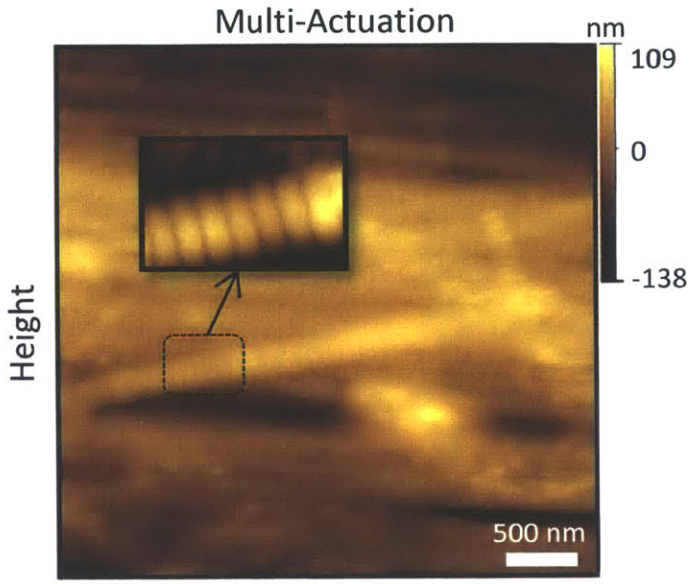

Figure 4-34: Retrace height image of collagen fibril extracted from rat tail, taken at 977 μm/s tip speed (97.7 lines/sec), in contact mode in air using the multi-actuated setup (image is a 3.7 μm cutout of a 5 μm image)

setup. Figure 4-34 presents the height image (with 1st order plane fit) of collagen fibrils obtained using the multi-actuation setup at 977 μm/s tip speed. At this speed, when moving in a direction perpendicular to the 67 nm banding pattern, the tip experiences periodic disturbances with a fundamental frequency of 15 kHz. This frequency falls well beyond the closed-loop bandwidth of the AFM when operated on the conventional tube.

The last imaging experiment is conducted in liquid, in tapping mode on a sample of freshly cleaved and sanded mica to demonstrate the effect of improved z-bandwidth in reducing the parachuting artifacts. Parachuting occurs in tapping mode when the probe loses contact with the sample on a falling edge at high imaging speed. In this period the amplitude error remains small and hence delays landing. This effect is observed in Fig. 4-35(a), appearing as shadows on the left side of the scratch edge. Since AFM control is open-loop during parachuting, increasing the PID gains results in faster landing without inducing instability. However, large PID gains can destabilize the loop upon landing. The image of Fig. 4-35(b) is taken using the

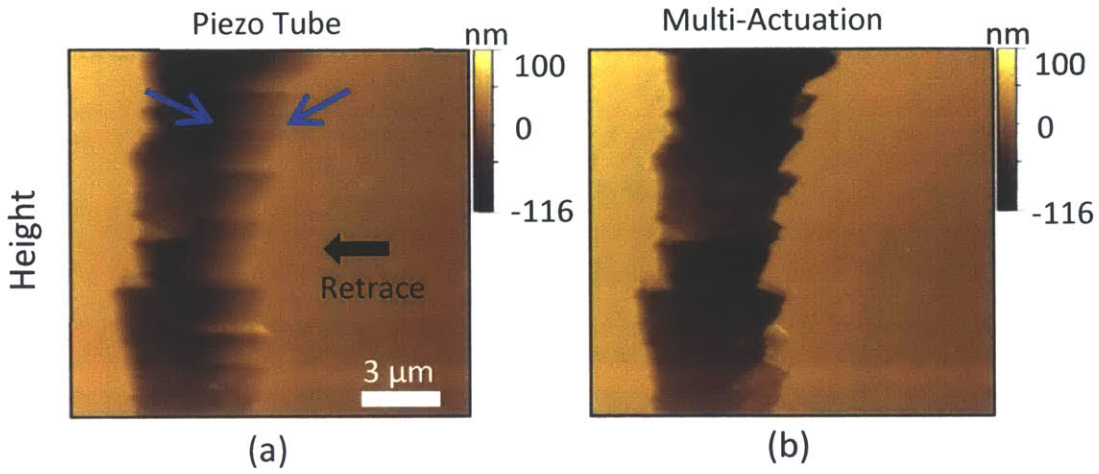

Figure 4-35: a) Retrace height image of freshly cleaved and sanded mica in tapping mode in liquid (120 kHz cantilever resonance frequency in liquid) acquired at 293 μm/sec tip speed (9.77 lines/sec), using conventional tube scanner alone, and c) using the multi-actuation setup.

multi-actuated setup. The edges of the scratch line are well defined in this image.

In this section we illustrated that through the proposed multi-actuation scheme the speed of conventional AFMs can be enhanced without fundamental changes in their design, operation or control. Given the number of conventional atomic force microscopes currently operational in research labs around the world, and the high cost of their replacement, a low-cost retroactive enhancement technique can be valuable. The proposed multi-actuation methodology proves to be one such technique. The proposed form of multi-actuation, reported here for the first time, enables the combination of several actuators to form a single multi-component actuator with large-range and high-speed performance.

4.3.5 Lateral Multi-Actuation: Control Design

As discussed in section 4.3.1 the lateral positioning of the sample can also benefit from the multi-actuation concept. In this approach, faster and naturally shorter range actuators are driven by the higher harmonics of the triangular raster scan pattern while the larger amplitude, lower harmonics of the pattern are fed to the slower but

larger range actuators. The proposed control scheme for the fast lateral positioning, discussed in section 3.4, is a combination of causal and non-causal components as shown in Fig. 3-7. This control scheme adopted to the multi-actuation methodology is presented in Fig. 4-36. Each of the SISO G_n^{l} compensators is coupled with one lateral actuator of the scanner, P_n^{l}, to compensate for the associated dynamics. A Fourier decomposition unit, denoted by *FD* in the block diagram, reflects a non-causal processing of the reference, r_s, and divides the tracking responsibility between various actuators. The signal component, u_n^{l}, assigned to actuator, P_n^{l} actuator is selected to fall within the mechanical bandwidth of that actuator. Handling of the frequency division by the non-causal Fourier decomposition unit makes the control design much simpler. As such, unlike the causal case, even the slowest actuator can potentially be driven over its full mechanical bandwidth. The role of the causal compensators G_n^{l} is to ensure that the dynamics of individual actuators and their corresponding couplings are well compensated. Please note that in the arrangement of Fig. 4-36 it is only necessary for G_N^{l} to be causal. The other compensator units G_n^{l} $(n < N)$ can have a noncausal form. Here we design all the G_n^{l} units in a causal form. As such, the design of each of the compensator units, G_n^{l}, can be done independently based on the proposed scheme of Fig. 3-4. The desired behavior of each actuator can be represented by a lowpass filter, L_n. Similar to Eq. (4.18) the parameters of this lowpass can be obtained as:

$$\begin{aligned}(\tilde{\alpha_n}, \tilde{q_n}, \tilde{\omega_{c_n}}) &= \mathrm{argmin}_{\alpha_n, q_n, \omega_{c_n}} \\ &= \sum_{m=1}^{M} |\frac{R_n^{\mathrm{l}}(2\pi\ m/M)}{U_n^{\mathrm{l}}(2\pi\ m/M)} - \alpha_n B_n(2\pi\ m/M, q_n, \omega_{c_n})|^2 |W(2\pi\ m/M)|^2\end{aligned} \tag{4.19}$$

where as before B_n is a unity gain lowpass filter (e.g. a Butterworth filter), with cutoff frequency ω_{cn}, and order q_n. The weighting function is selected such that $|W(2\pi\ m/M)|^2 = |R_n^{\mathrm{l}}(2\pi\ m/M)|^2$. Then we have:

$$L_n = \tilde{\alpha}_2 B(2\pi\ m/M, \tilde{q}_n, \tilde{\omega}_{c_n})$$

The desired response, d_n^{l} can then be obtained as:

$$d_n^{\mathrm{l}} = k_n * u^{\mathrm{l}}$$

where k_n is the impulse response associated with L_n and u^{l} is a wideband excitation signal.

As noted from Fig. 4-36, only the fastest actuator of the scanner is included in the closed loop portion of the control scheme. In this approach it is inherently assumed that a very small positioning range is required to tackle the tracking error left out by the feedforward portion of the proposed control.

It is also important to ensure that the lateral piezo actuators move in phase. When this condition is met the actuators move constructively to form a triangular pattern. Naturally faster actuators lead the slower ones in phase. To compensate for this phase mismatch one can introduce synthetic phase lag along the command line of faster actuators so that their phase responses match that of the slowest actuator, P_1^{l}. This is done by using digital delays. The proper delay values, $v_n (n = 2, , N-1)$ are found by minimizing the error between the phase responses of P_n^{l} and P_1^{l}:

$$\tilde{v}_n = \mathrm{argmin} F(v_n) \tag{4.20}$$

and

$$F(v_n) = \sum_{i=1}^{I} [f_1(\omega_i) - f_n(\omega_i, v_n)]^2 \tag{4.21}$$

where $f_n(\omega_i, v_n)$ is the phase response of the n^{th} compensated and v_n sample delayed actuator at frequency ω_i. The frequency range $\omega_i (i = 1, \ldots, I)$ covers the passband of P_1^{l}.

The lateral multi-actuated method described in this subsection will be evaluated experimentally on a custom-made multi-component scanner. The presentation of the experimental results are postponed to the next chapter where the detailed design of this scanner is given.

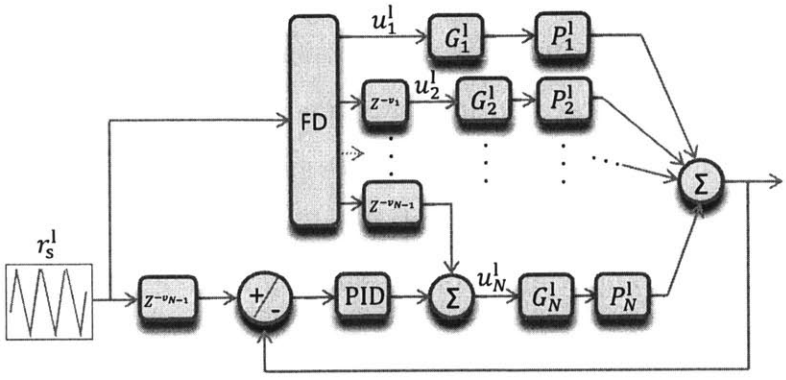

Figure 4-36: Control arrangement for the lateral motion of a multi-actuated scanner. This design is based on the proposed arrangement of Fig. 3-7.

4.4 Chapter Summary

In this chapter the control design approach developed in chapter 3 is adopted to the control of redundantly actuated scanners. Two fundamentally different redundant actuation techniques namely the *counter-balancing* and the *multi-actuation* are discussed.

First the principle of operation and the limitations of counter-balancing approach are presented. It is shown that counter-balancing operates based on pole-zero cancellation which is disrupted for slight mismatch between the mechanical properties of z and counter-z piezos. It is also shown that even in ideal circumstances where the mechanical properties of the two piezos match perfectly, the counterbalancing approach leads to an intensification of z piezo dynamics. To tackle these limitations a control strategy is proposed where the signal driving the counter piezo is properly shaped via a compensator. The design of the compensator was implemented based on the data-based approach proposed in chapter 3. The method is then experimentally evaluated on an existing flexure-based scanner with an incorporated counter-balancing piezo.

The latter part of this chapter presents the multi-actuation approach. The notion of multi-actuation and the reasons for its applicability in AFM imaging is discussed. We start by elaborating on the out-of-plane control design for a multi-actuated system. The design steps are given in detail based on the general data-based methodology

presented in chapter 3. The capabilities of out-of-plane multi-actuation is then show cased on a conventional AFM operating on a modified tube scanner. A fast, short-range nano-positioner is incorporated into the tube scanner to enable its high-speed operation while benefitting from its large scan range. The AFM imaging results corroborate the effectiveness of the method. Finally we discuss the multi-actuation methodology for the lateral positioning of the sample. The adopted control approach is based on the strategy proposed in section 3.4 but tailored to a multi-actuated setup. The experimental evaluation of the technique is postponed to chapter 5 where the details of the design and implementation of a multi-component scanner is presented.

According to the results of this chapter, multi-actuation has a great potential to improve the lateral and out-of-plane positioning bandwidth of the AFM scanners. This methodology does not suffer from the limitations of counterbalancing scheme, it is relatively easy to implement and provides the possibility to simultaneously achieve large-range and high-speed nano-positioning. To fully explore the capabilities of this approach, in the next chapter, we design and implement a multi-actuated nano-positioner composed of several fast/short-range and slow/large-range actuators. The lateral and out-of-plane multi-actuation control schemes proposed here will be implemented on this nano-positioner and later used for high-speed and large-range AFM imaging in chapter 7.

Chapter 5

Design and Control of a Multi-Actuated High-Speed and Large-Range Nano-Positioner

As demonstrated in previous chapter, given the short-range positioning requirements of AFM at high frequencies, one can achieve both large-range and high-speed AFM imaging by combining faster/shorter-range and slower/larger-range actuators in the form of a multi-actuated positioner. In this chapter we discuss the design and implementation of a multi-actuated AFM scanner that benefits from this concept in both lateral and out-of-plane scan directions.

5.1 Arrangement of Multi-Actuated Scanner Components

Before going into the details of the scanner design we take a closer look at the modeling results of section 4.3.2 to better understand the proper arrangement of the actuators for best scanner performance. As discussed before, in a cascaded series of multiple actuators, there is a dynamic coupling between the fast and slow actuators. Part of the responsibility of the compensators proposed in section 4.3 is to tackle these

dynamics. However, this may not be always possible in practice. In certain cases when the coupled zeros are lightly damped, compensation requires very large gains. This may lead to command signal saturation and improper operation of the scanner.

A closer look at the transfer function of Eq. (4.9) reveals that the distance between the in-band pairs of complex conjugate poles and zeros associated with the dynamic coupling is dependent on the ratio of the masses of the two actuators. For $\lambda = \frac{m_2}{m_1} << 1$, the denominator, $D(s)$ of Eq. (4.9) can be written as $D(s) \approx (m_1 s^2 + c_1 s + k_1)(m_2 s^2 + c_2 s + k_2)$. Hence, a pair of complex conjugate poles of this transfer function perfectly match the pair of complex conjugate zeros of the system and the simplified transfer function can be written as:

$$\frac{x_2(s)}{F_2(s)} \approx \frac{1}{(m_2 s^2 + c_2 s + k_2)} \tag{5.1}$$

In this case, the effect of dynamic coupling is fully removed and the fast actuator shows a 2nd order behavior. This implies that by reducing the mass carried by the faster actuator or increasing the mass carried by the slower actuator one can decrease the intensity of the dynamic coupling. This observation can be used to properly distribute the masses in a multi-actuated scanner as discussed in the next section.

5.2 Multi-Actuated Scanner Design

A schematic illustration of the proposed design for a multi-actuated scanner is shown in Fig. 5-1a. The implemented scanner is shown in Fig. 5-1b. The scanner is composed of five independent positioners, 2 for out-of-plane Z motion, 2 for lateral (fast raster scan) X motion, and 1 for lateral (frame up/down) Y positioning. For both of the out-of-plane nano-positioners, a piezo-stack actuator is pre-loaded in between a pressure screw and a flexure diaphragm as shown in Figs. 5-2a and d. In addition to pre-loading, the flexure cap protects the high voltage electrical connections of the piezos when operating in liquid. Both out-of-plane flexure diaphragms are made in house from 6061 aluminium alloy. The out-of-plane motion is achieved as the piezo-

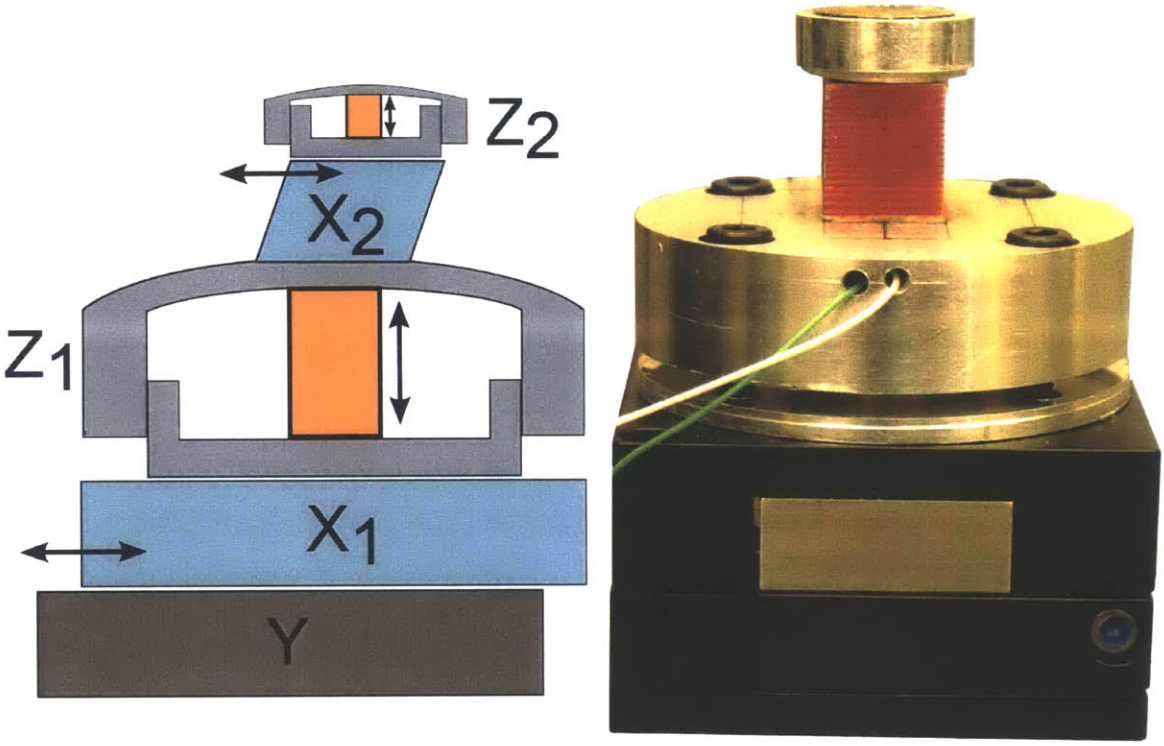

(a) (b)

Figure 5-1: a) Schematics of the proposed multi-actuated scanner design, and b) A picture of the implemented multi-actuated scanner.

stack expands and deforms the aluminum diaphragm. The range and bandwidth of each out-of-plane positioner is affected by the diameter and thickness of the flexure diaphragm.

The Z_2 positioner is designed to achieve a wide mechanical bandwidth at a relatively short range ($\sim$1 μm). The outer diameter of the cap and the flexure diaphragm are 15.2 mm and 11.9 mm, respectively. In this design a piezo stack actuator (2 mm$\times$2 mm$\times$2 mm, Physik Instrumente, PL022.30) is glued on both ends to the 0.5 mm thick diaphragm as well as the pressure screw as shown in Fig. 5-2b using instant adhesive (Loctite 401). In this form the center of the diaphragm is constrained, hence, maximizing the out-of-plane bandwidth. The first vibration mode of the Z_2 diaphragm is shown in Fig. 5-2c, associated with a 112 kHz resonance. The weight of the Z_2 cap is approximately 2 grams.

The Z_2 cap is the most important component of the scanner in terms of required positioning bandwidth. As shown in Fig. 5-1 this positioner is placed on top of the scanner and only carries the sample mass. To minimize the effect of dynamic coupling, as discussed in section 5.1, the rest of the scanner components are distributed in a Z-X alternating fashion. The Z_2 cap is carried by a short-range (10 μm) and high-speed shear piezo (10 mm$\times$10 mm$\times$12 mm shear piezo stack, Physik Instrumente, P-141.10) for fast lateral actuation, hereafter referred to as X_2. The X_2-Z_2 assembly is accommodated by a large-range (6 μm) and slow out-of-plane flexure diaphragm referred to as Z_1.

The large-range out-of-plane flexure cap, Z_1, is driven by a 5 mm$\times$5 mm$\times$9 mm piezo stack (Physik Instrumente, P-885.11) and features a large aspect ratio (diameter, 42 mm, height, 10.25 mm) to minimize the effect of lateral structural dynamics. The thickness of the diaphragm and its diameter are 0.6 mm and 19.1 mm, respectively. The Z_1 piezo stack actuator is permanently fixed only on one end to the flexure diaphragm as shown in Figs. 5-2e using Loctite 401 to enable disassembly of the scanner. Figure 5-2f demonstrates the first out-of-plane vibration mode-shape of Z_1 diaphragm at 6.7 kHz. The torsional vibration mode-shape of the Z_1 diaphragm, corresponding to the schematics of Fig. 5-2g, at 5.6 kHz, is shown in Fig. 5-2h. This mode of vibration is of importance to the lateral positioning capability of the scanner and limits the lateral scan bandwidth of the shear piezo.

The $Z_2 - X_2 - Z_1$ assembly is mounted on a large-range (120 μm) X positioner (hereafter referred to X_1) aligned with X_2 and mounted on a slow and large-range (120 μm) Y positioner (Physik Instrumente, P-611.20). To reduce the effect of out-of-plane dynamics of the stacked X_1-Y positioner, the setup is passively damped by filling the gap between the X_1 and Y flexures with polyurethane film (Sorbothane) with a durometer hardness of 60 OO and thickness of 1.5 mm. The serial arrangement of the lateral positioners ensures a kinematically decoupled response. The slowest actuator Y is aligned with the slowest lateral scan direction and performs the frame up/down positioning. The X_1 and X_2 actuators work together to move the sample along the fast raster scan axis. Similarly the Z_1 and Z_2 cooperate to achieve a large-range and

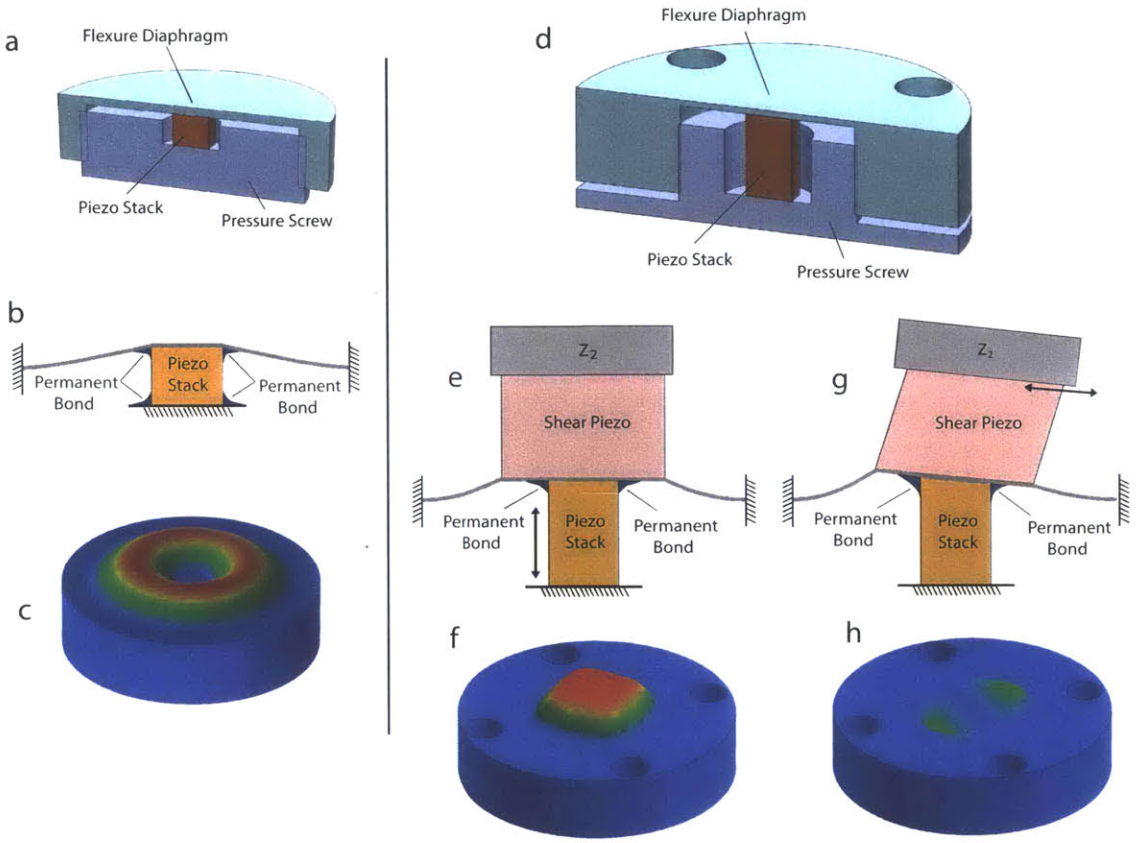

Figure 5-2: a) A section view of the high-speed/short-rage out-of-plane flexure cap, Z_2, b) assembly and out-of-plane flexing schematics of Z_2, c) first mode of vibration of the Z_2 flexure diaphragm, d) a section view of the slow/large-range out-of-plane flexure cap, Z_1, e) assembly and out-of-plane flexing schematics of Z_1, f) first out-of-plane mode of vibration of the Z_1 flexure diaphragm, g) schematics of the torsional flexing of the Z_1 diaphragm induced by the shear piezo motion, and h) first torsional mode of vibration of Z_1 flexure diaphragm.

high-speed out-of-plane performance.

The simplified distribution of masses in the proposed Z-X alternating arrangement is shown in Fig. 5-3. In this figure each of the positioners are represented by two lumped upper and lower masses denoted by the superscripts U and L, respectively. We can write:

$$\begin{aligned} m_2^{\mathrm{Z}} &= m_{\mathrm{s}} + m_{\mathrm{Z}_2}^{\mathrm{U}} \\ m_1^{\mathrm{Z}} &= m_{\mathrm{Z}_2}^{\mathrm{L}} + m_{\mathrm{X}_2}^{\mathrm{U}} + m_{\mathrm{X}_2}^{\mathrm{L}} + m_{\mathrm{Z}_1}^{\mathrm{U}} \end{aligned} \tag{5.2}$$

where, m_s is the sample mass. m_1^{Z} and m_2^{Z} are associated with a 2DOF representation of the $\mathrm{Z_1}$- $\mathrm{Z_2}$ positioner and reflect the m_1 and m_2 masses of the 2DOF actuator of Fig. 4-19b, respectively. According to Eq. (5.2) from the perspective of the fast out-of-plane scanner, $\mathrm{Z_2}$, the mass of the fast lateral scanner, $m_{\mathrm{X_2}} = m_{\mathrm{X_2}}^{\mathrm{U}} + m_{\mathrm{X_2}}^{\mathrm{L}}$, is seen as part of the mass of the slower out-of-plane scanner, $\mathrm{Z_1}$. This leads to a smaller $\frac{m_2^{\mathrm{Z}}}{m_1^{\mathrm{Z}}}$ ratio which as discussed in section 5.1 reduces the influence of dynamic coupling on the pass-band of $\mathrm{Z_2}$. This same argument applies to the fast lateral positioning. We have:

$$\begin{aligned} m_2^{\mathrm{X}} &= m_{\mathrm{s}} + m_{\mathrm{Z_2}}^{\mathrm{U}} + m_{\mathrm{Z_2}}^{\mathrm{L}} + m_{\mathrm{X_2}}^{\mathrm{U}} \\ m_1^{\mathrm{X}} &= m_{\mathrm{X_2}}^{\mathrm{L}} + m_{\mathrm{Z_1}}^{\mathrm{U}} + m_{\mathrm{Z_1}}^{\mathrm{L}} + m_{\mathrm{X_1}}^{\mathrm{U}} \end{aligned} \tag{5.3}$$

where m_1^{X} and m_2^{X} again reflect the point masses associated with a 2DOF representation of multi-actuated X positioning (see Fig. 4-19b). According to Eq. (5.3) from the perspective of $\mathrm{X_2}$, the mass of $\mathrm{Z_1}$ is seen as part of the mass of $\mathrm{X_1}$. Again for a smaller $\frac{m_2^{\mathrm{X}}}{m_1^{\mathrm{X}}}$ ratio, the intensity of the dynamic coupling between $\mathrm{X_1}$ and $\mathrm{X_2}$ is reduced. This does not remove the need for dynamic compensation but makes the compensation task rather easier.

5.3 Control Setup for Out-of-Plane and Fast Lateral Scan Axes

Two independent FPGA platforms are used to drive the lateral and out-of-plane actuators. The out-of-plane actuators are driven by a National Instruments (NI) PXIe-7966R FlexRIO module coupled with a NI 5781 baseband transceiver. The PID controller is implemented at 25 MHz clock rate on the same FPGA hardware. Two compensators $\tilde{G}_1^{\mathrm{v}}$ and $\tilde{G}_2^{\mathrm{v}}$ cascade the PID unit to divide the tracking responsibilities between $\mathrm{Z_1}$ and $\mathrm{Z_2}$ and also compensate for their coupled dynamics as proposed in Fig. 4-22. The three lateral actuators are driven by a NI PXI-7851 FPGA module. Fourier decomposition and shaping of the fast raster scan command signals via $\tilde{G}_1^{\mathrm{l}}$

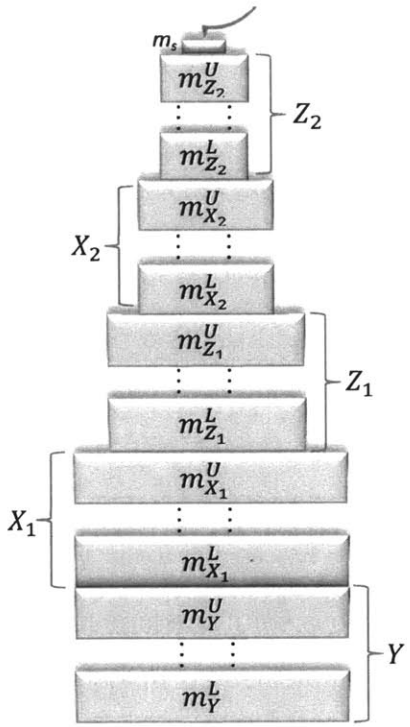

Figure 5-3: A simplified distribution of masses in the multi-actuated scanner of Fig. 5-1. The mass of each actuator is represented by an upper and lower point mass denoted by the U and L superscripts.

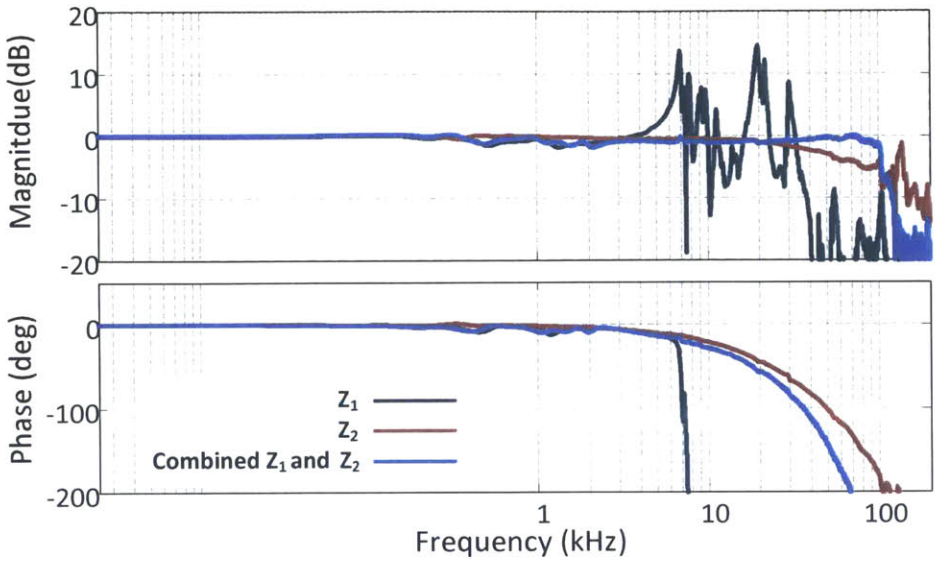

Figure 5-4: Frequency responses of the Z_1, Z_2 and combined Z_1 and Z_2 actuators.

and $\tilde{G}_2^1$ (as proposed in Fig. 4-36) are done on a host NI PXIe-8135 with 2.3 GHz core controller. The control for lateral multi-actuation is implemented in open-loop i.e. when the PID gains in Fig. 4-36 are set to zero.

5.4 Scanner Dynamic Performance

The dynamic performance of various scanner components are measured using a custom-made dynamic signal analyzer implemented in LabVIEW on a NI USB-6251 DAQ device. The analyzer excites the scanner with a random binary sequence and measures the response. The empirical transfer function estimate of each actuator is then formed in MATLAB. The network analyzer can also generate raster scan patterns with incorporated Fourier decomposition, signal shaping, and delay according to Fig. 4-36, in order to evaluate the combined performance of the lateral actuators.

5.4.1 Out-of-Plane

To measure the frequency responses associated with Z_1 and Z_2, the designed scanner of Fig. 5-1 is first incorporated into a custom made atomic force microscope (described in chapter 7). An AFM probe with fast dynamics is then brought in contact

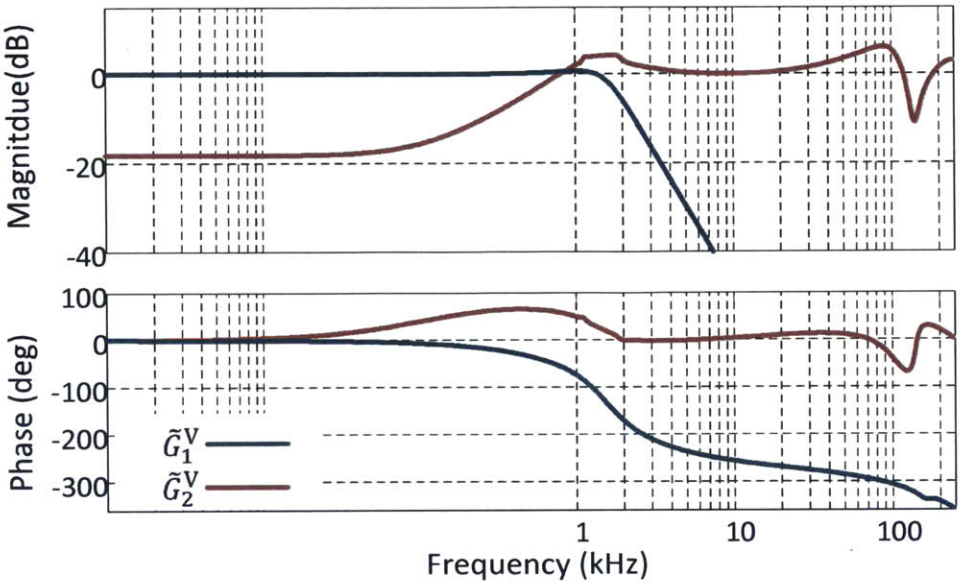

Figure 5-5: Frequency responses of the designed compensators $\tilde{G}_1^{\mathrm{V}}$ and $\tilde{G}_2^{\mathrm{V}}$.

with the sample. While the probe and sample are engaged, each of the Z_1 and Z_2 actuators is excited by a wideband random binary sequence and the cantilever deflection is simultaneously acquired. Figure 5-4 demonstrates the open-loop frequency response of the slow/large-range out-of-plane actuator, Z_1. This actuator has a strong resonance near 7 kHz, as expected from the finite element analysis results (Fig. 5-2f). The frequency response of the fast/short-range actuator, Z_2, is demonstrated on the same figure. Figure 5-5 demonstrates the frequency response of the compensators G_1^{v} and G_2^{v} designed based on the methodology presented in section 4.3.3. $\tilde{G}_1^{\mathrm{v}}$ (4^{th} order) demonstrates a lowpass behavior, assigning 0-1.5 kHz to Z_1. This frequency range handles tracking of the sample tilt and low spatial frequency surface features with 6 μm range. $\tilde{G}_2^{\mathrm{v}}$ (10^{th} order) shows a high-pass behavior, complementary to $\tilde{G}_1^{\mathrm{v}}$, to assign higher frequency tracking to the faster out-of-plane positioner. This compensator also tackles the higher frequency dynamics of the flexure cap to achieve a maximally flat frequency response over the passband 0-100 kHz. The coupled dynamics of Z_1 and Z_2 appearing on the pass-band of Z_2 is minimal and does not require treatment by the $\tilde{G}_2^{\mathrm{v}}$ compensator. This is owing to the arrangement of the masses in the multi-actuated scanner and the large mass ($\sim$ 9 g) of the shear piezo which leads to a small

$\frac{m_2^Z}{m_1^Z}$ ratio. The frequency response of the combined $Z_1 - Z_2$ system is superimposed on Fig. 5-4 in blue. Due to the accumulated phase lag, partly contributed by the analog to digital, digital to analog converters and the power amplifiers, the achieved closed-loop bandwidth is limited to ~62 kHz. The magnitude squared coherence plots associated with the frequency responses of Fig. 5-4 are shown in Fig. 5-6.

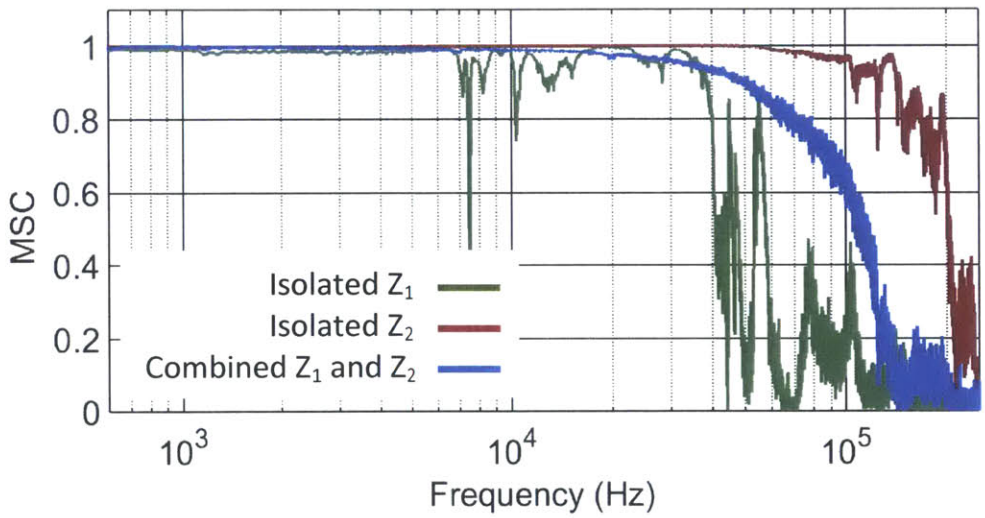

Figure 5-6: Magnitude squared coherence plots associated with the frequency responses of Fig. 5-4.

5.4.2 Lateral

A laser interferometer (SIOS SP-S 120) is used to measure the dynamic response of the lateral actuators. Figure 5-7 shows the frequency responses of the uncompensated X_1 and X_2 lateral positioners. The compensators $\tilde{G}_1^l$ (6^{th} order) and $\tilde{G}_2^l$ (8th order) are implemented at 5 kHz and 50 kHz, respectively. The shaped command signals are up-sampled to 800 kHz to maximize the lateral positioning resolution of the AFM at high speeds. The frequency responses of the designed compensators, $\tilde{G}_1^l$ and $\tilde{G}_2^l$, are given in Fig. 5-8. The compensated frequency responses are superimposed on the plot of Fig. 5-7 for X_1 and X_2, reflecting a mechanical bandwidth of 140 Hz and 7 kHz, respectively. The phase response of the compensated X_2 leads the phase

response of the compensated X_1. As such, X_2 is artificially delayed to avoid phase distortion in the combined response of the two actuators. Here an optimal delay of 239 samples at 50 kHz compensation frequency, obtained using Eqs. (4.20) and (4.21), is incorporated into the X_2 command line. Figure 5-7 also demonstrates the phase response of the delayed and compensated X_2 actuator (dashed light brown line). With the incorporation of the delay, the phase responses of the two actuators X_1 and X_2 match well over the pass-band of X_1. The magnitude squared coherence plots for the frequency responses of Fig. 5-7 are shown in Fig. 5-9. Figure 5-10 shows the combined displacement response of the two actuators at 100 Hz scan rate and for a 30 μm scan range in blue. The triangular pattern is preserved in the combined response of the multi-actuated setup. At this frequency the X_1 component of the scanner can only respond to the first harmonic of the scan command. The higher harmonics of the raster scan pattern are fed to the short-range/high-speed shear piezo (X_2). The isolated response of the individual actuators X_1 and X_2 measured with the laser interferometer are superimposed on the same plot. As expected, the isolated response of the slow and large-range actuator is smoothed significantly on turnarounds. It is noted that a major portion of the 30 μm scan range is covered by this actuator. X_2 provides the sharp turnarounds with approximately 6 μm travel range to complement X_1.

5.5 Two Degree of Freedom Control for Frame-up/down Motion

The speed performance of the slow lateral scan axis is not critical to high-speed AFM imaging. The slow lateral scanner is responsible for frame-up/down motion and hence, even at high-speed imaging application experiences very low frequency excitations. For example, for an imaging rate of 20 frames/sec the slow lateral positioner is driven at 10 Hz. As a result, dynamics compensation is not a concern for this scan axis. Accuracy however is very critical for video compilation as the slightest mismatch

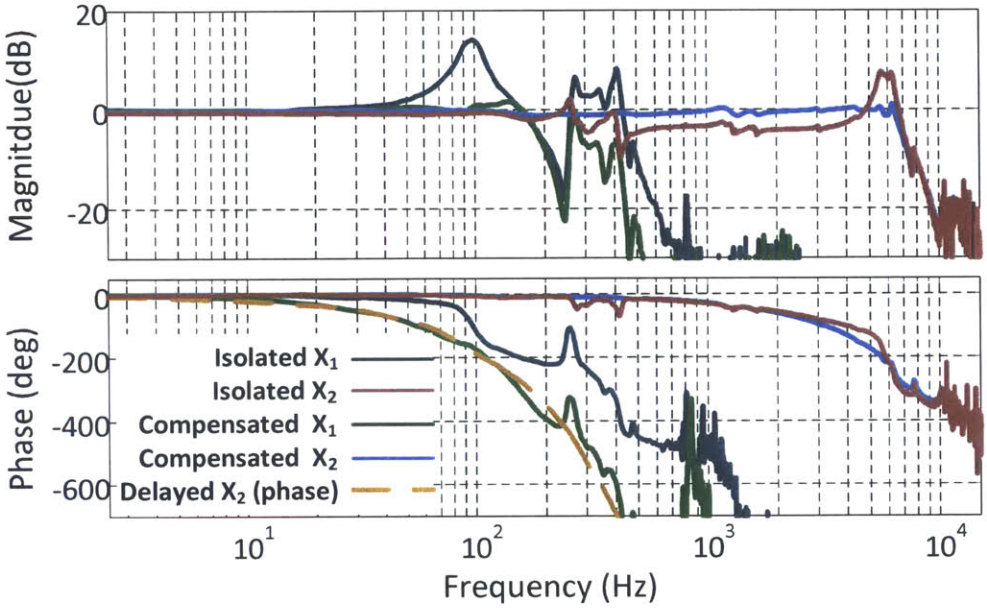

Figure 5-7: Frequency responses of the uncompensated X_1, uncompensated X_2, compensated X_1 and compensated X_2 positioners.

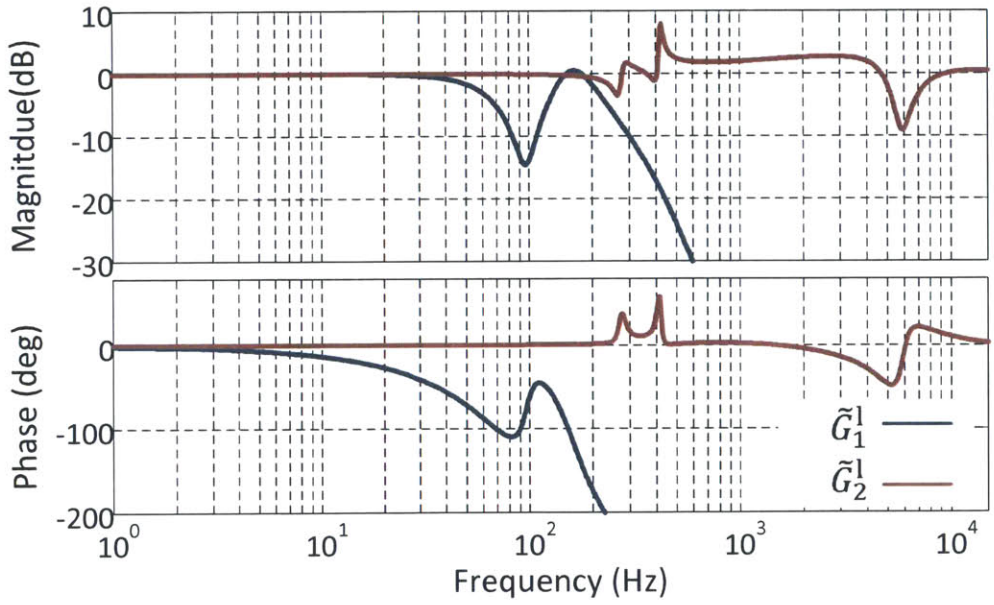

Figure 5-8: Frequency response of the designed compensators $\tilde{G}_1^1$ and $\tilde{G}_2^1$.

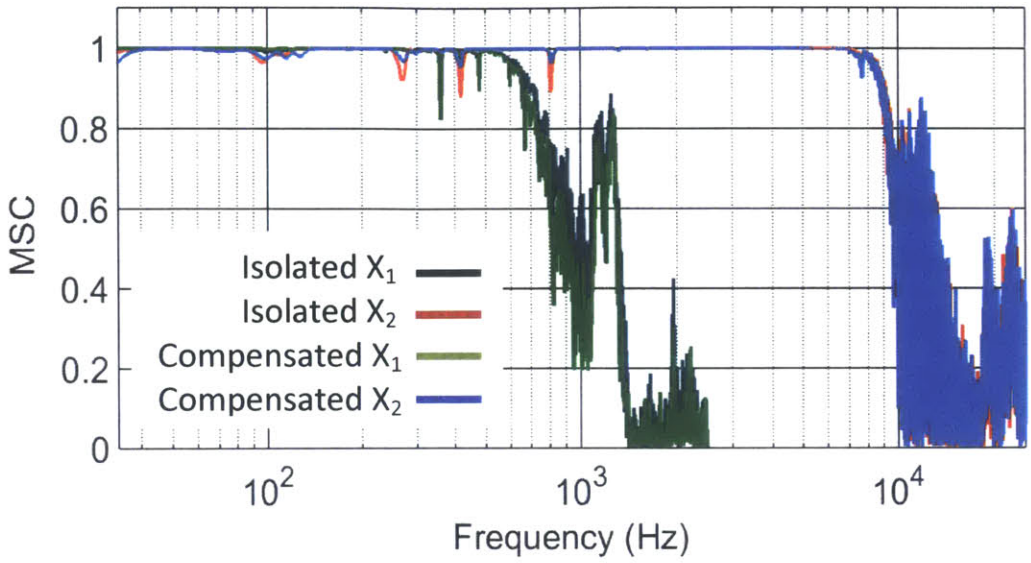

Figure 5-9: Magnitude squared coherence plots associated with the frequency responses of Fig. 5-7.

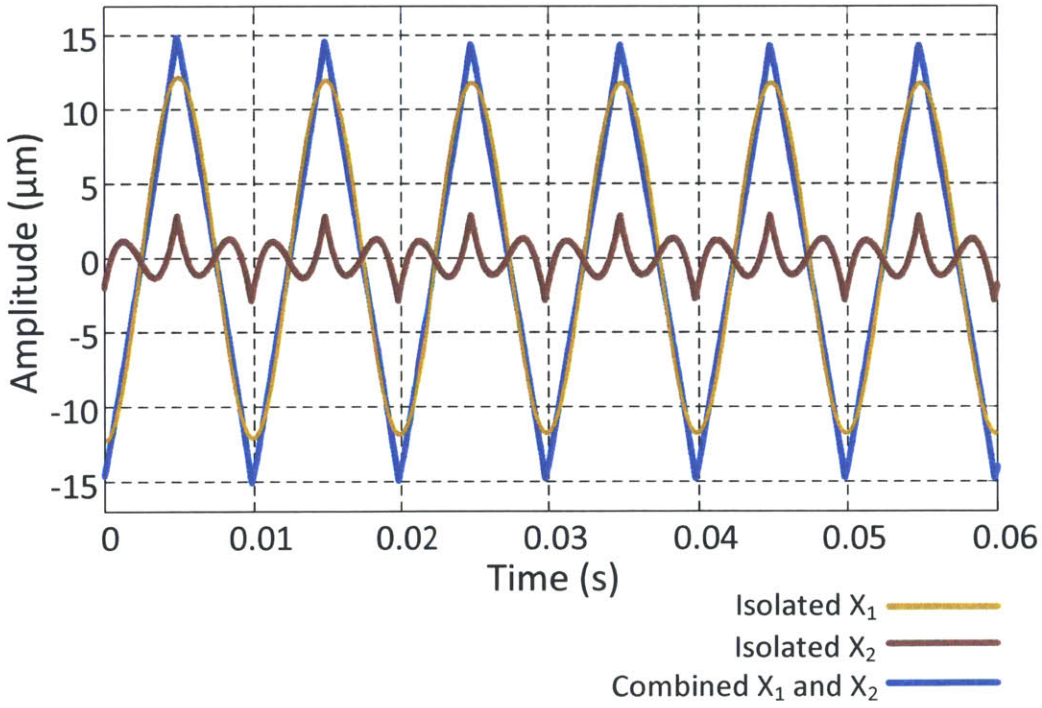

Figure 5-10: Combined and isolated displacement responses of the lateral multi-component scanner to a 100 Hz, triangular command signal.

between the consecutive frames would appear as jitter in the video. The 2DOF control structure of Fig. 3-6, proposed in section 3.4, will be implemented here for the slow scan axis of the designed nano-positioner. The feedforward controller, $G_{\mathrm{h}}^{\mathrm{l}}$, of Fig. 3-6 is noncausal and nonlinear, designed to compensate for the Y piezo hysteresis. In the following we discuss the nonlinear modeling of hysteresis, estimation of the associated parameters and the implementation of the corresponding compensator.

5.5.1 Improved Parameter Estimation for a Maxwell Model of Hysteresis

An intuitive approach to implement a nonlinear model of hysteresis is proposed in [44, 43]. In this approach the hysteretic behavior of a piezo actuator is represented by a number of pure energy storage elements (e.g. springs) and rate-independent dissipation elements (e.g. Coulomb friction element). This scheme originally proposed by James Maxwell in the mid 1800 is shown in Fig. 5-11 [44] where hysteresis is modeled by a combination of several massless elasto-slide elements. To model the hysteresis in a piezo actuator driven by a voltage command input, the input force to the elasto-elements in the Maxwell model can be replaced by the input voltage. As the number of elasto-slide elements increases the accuracy of the fitted model improves. Unlike the nonlinear compensation schemes based on other hysteresis modeling approaches such as Preisach model [40], a nonlinear compensator based on the Maxwell model does not require an inverse calculation and the associated parameters can be easily identified.

The Maxwell model parameter estimation method proposed in [44] is demonstrated in Fig. 5-12. In this approach the origin-to-max portion of the hysteresis curve is divided into M equal intervals. For the slope of each piece, s_m, we can write:

$$s_m = \sum_{n=m}^{M} k_n \tag{5.4}$$

where k_n is the spring constant associated with the n^{th} massless elasto-slide element.

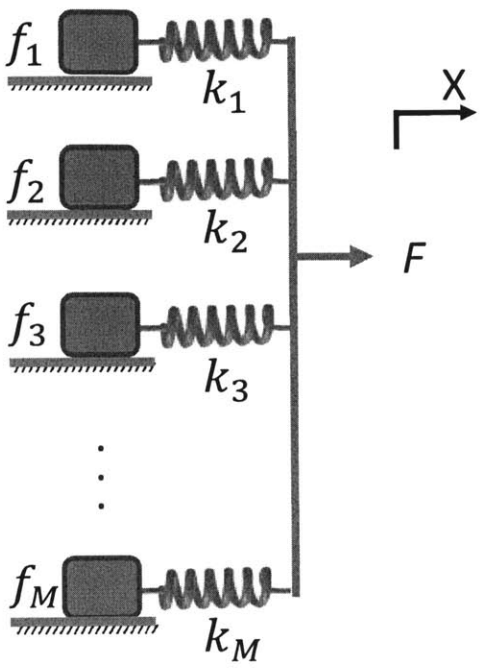

Figure 5-11: A Maxwell model of hysteresis: a combination of several massless elasto-slide elements.

In matrix form this equation can be written as:

$$\mathbf{S} = \mathbf{AK} \tag{5.5}$$

where $\mathbf{S} = [s_m, m = 1, \ldots, M]$, $\mathbf{K} = [k_m, m = 1, \ldots, M]$ and,

$$\mathbf{A} = \begin{bmatrix} 1 & 1 & \ldots & 1 \\ 0 & 1 & \ldots & 1 \\ 0 & 0 & \ldots & 1 \\ & & \ldots & \end{bmatrix}.$$

As such, to find the unknown parameters of the model i.e. vector $\mathbf{K}$ one can solve the set of M linear equations represented in Eq. (5.5) as:

$$\mathbf{K} = \mathbf{A}^{-1}\mathbf{S} \tag{5.6}$$

Using the above equation for large number of elements, the piece-wise linear behavior

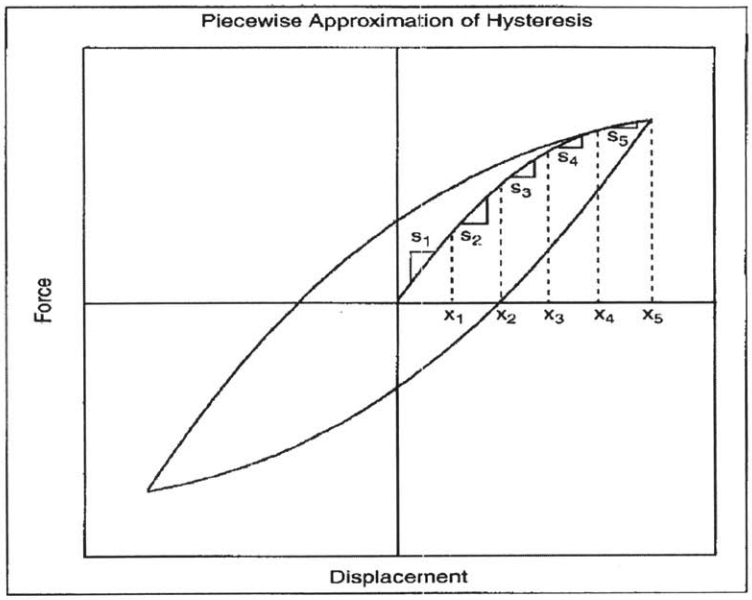

Figure 5-12: The parameters of the Maxwell model can be estimated using the origin-to-max portion of the hysteresis curve [44].

of the origin-to-max portion of the Hyteresis curve can be perfectly matched. The estimated parameters of the Maxwell model can then be used to simulate the behavior of the piezo for the rest of the hysteresis cycle.

This approach to nonlinear model parameter estimation is not optimal. In practice, for system identification one can capture several number of full periods of piezo displacement response data. However, only the initial portion of the measured response (i.e. origin-to-max) is utilized for parameter estimation. This increases the sensitivity of the model parameter estimation to noises, deviations of the piezo hysteresis behavior from the assumed elasto-slide physical model and other errors in the initial portion of the measured response. This drawback can be ameliorated by utilizing all the measured displacement data-points in the parameter estimation step. This increases the modeling accuracy and robustness to noises and outliers in the data.

Let us take a closer look at a single elasto-slide element where the moving direction of the massless box is reversed. This is shown in Fig. 5-13. To reverse the direction of a massless box, the extension of the spring should be brought back to zero (Fig. 5-13 part (a) to part (b)) and then extended up to Δ in the reverse direction (Fig. 5-13 part (b) to part (c)). As such, beyond the origin-to-max portion of the hysteresis curve, the

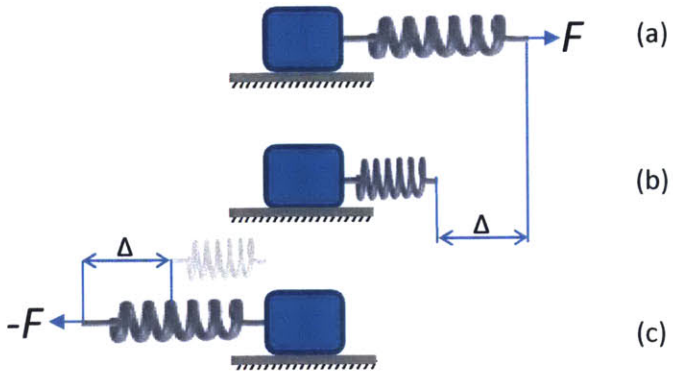

Figure 5-13: The required displacement to reactivate (induce sliding) an elasto-slide element in the reverse direction is 2Δ.

piece-wise force-distance slopes are repeated over a 2Δ displacement interval. This is shown in Fig. 5-14 for a hysteresis loop simulated on arbitrary range/voltage values. Starting from the maximum point of the hysteresis loop in the reverse direction, the slope of the force-displacement curve matches the slope of the first portion of the origin-to-max curve i.e. $s_6 = s_1$. This is because right after the displacement direction changes, all the massless boxes stop sliding (are deactivated) and hence the resulting force-distance slope returns to its initial value. Reactivation of the softest spring element requires 2δ displacement at which point the slope changes to $s_7 = s_2$. In a similar fashion upon 4δ displacement with respect to the maximum the slope changes to $s_8 = s_3$ and so on. As such, when extended to the full period of the hysteresis loop we have:

$$s_m = \begin{cases} \sum_{n=m}^{M} k_n & m \leq M \\ s_j & m > M, j = m \bmod M \end{cases} \tag{5.7}$$

where M is the number of linear pieces assumed for the origin-to-max portion of hysteresis curve. We also have:

$$\mathbf{S}' = \mathbf{A}'\mathbf{K} \tag{5.8}$$

where $\mathbf{S}' = [s_m, m = 1, \ldots, LM]$, L is the number of times the two extrema of

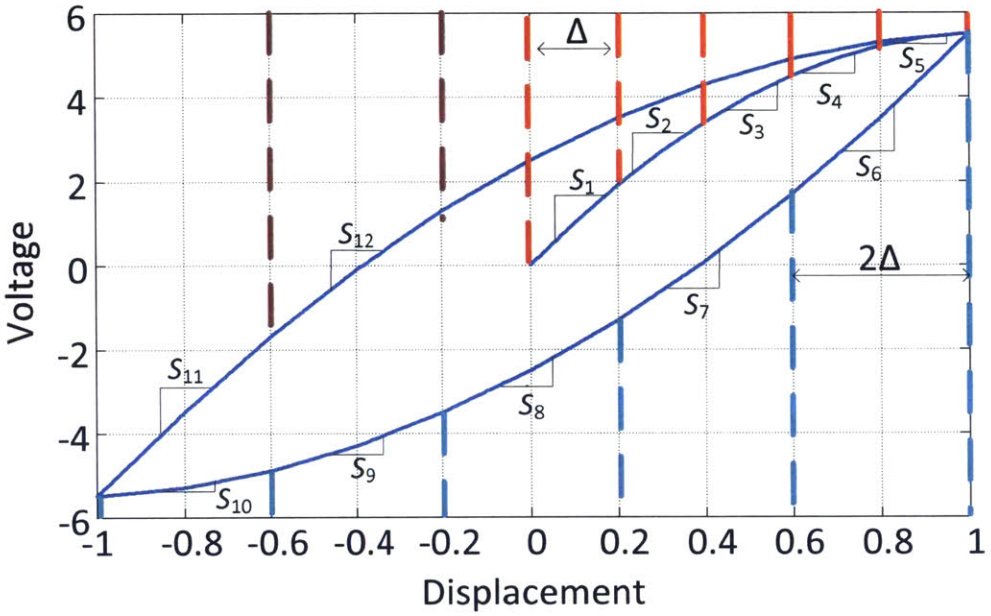

Figure 5-14: Extension of Maxwell parameter estimation to full hysteresis loop.

hysteresis loop are met, as before $\mathbf{K} = [k_m, m = 1, \ldots, M]$ and,

$$\mathbf{A}' = \begin{bmatrix} A \\ A \\ \vdots \\ A \end{bmatrix}.$$

In A', A is replicated L times. Unlike in Eq. (5.5) where matrix A is square, in the above equation, A' has LM rows and M columns. M is the number of elasto-slide elements and L is the number of times the extrema of the hysteresis curve are met (origin is not counted as an extremum). In this form the number of available equations is L times the number of unknowns. As such, the model identification can be implemented in a least mean-square error sense. We can write:

$$\mathbf{K} = \mathbf{A}'^{+}\mathbf{S}' \tag{5.9}$$

where the superscript $+$ denotes the Moore-Penrose pseudoinverse operation [92].

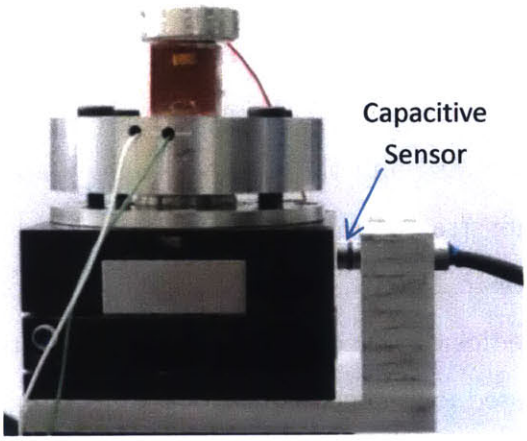

Figure 5-15: A capacitive sensor is incorporated into the multi-actuated scanner to measure the positioning response along the Y axis.

5.5.2 Performance

To identify the non-linear Maxwell model according to the methodology described above, the Y positioner of the multi-actuated scanner presented in section 5.2 is driven by a 1 Hz triangular wave. The peak to peak amplitude of excitation is set to different values and the identification step is repeated for each case. The resulting Maxwell model was then implemented in Labview to compensate for the hysteresis effect of Y piezo actuator. The feedforward hysteresis compensation operates in conjunction with a PID unit as was proposed in Fig. 3-6. The closed loop portion of control uses position measurements from a capacitive sensor (Microsense-8810 operating on a 2823 probe) incorporated into the multi-actuated scanner as shown in Fig. 5-15. Measurements from the same sensor was used to identify the Maxwell model parameters.

Figure 5-16a shows the open loop uncompensated response of the scanner to a triangular command signal when the nonlinear compensation unit is deactivated (set to unity gain). This figure also demonstrates the desired, 50 μm peak-to-peak, response of the scanner. As one can see the hysteresis effect leads to relatively large positioning error ($\sim 17\mu m$ maximum error). Figure 5-16b shows an overlap of the desired and measured Y axis response upon the implementation of the nonlinear feedforward compensation unit. The residual positioning error in this case is shown in Fig. 5-16c.

Over a 50 μm commanded displacement, this figure shows a peak displacement error of 670 nm. This residual error is then tackled by the closed loop controller.

Figure 5-17a shows the desired and the measured response of the scanner when both the nonlinear-feedforward and the feedback control schemes are applied. The positioning error is demonstrated in Fig. 5-17b. The closed loop controller reduces the peak positioning error to 230 nm for the given 50 μm displacement range. Figure 5-17c shows both the feedforward and feedback control efforts for the 2DOF control implementation. The closed loop controller is contributing minimally, mostly around the turnaround extremities. This is indicative of the effective performance and the accuracy of the proposed nonlinear/noncausal feedforward compensation scheme.

5.6 Chapter Summary

In this chapter we present the design of a multi-actuated scanner. First the dynamic model of a multi degree of freedom scanner is evaluated to find the proper distribution of masses. This is to minimize the effect of dynamic coupling. The implemented scanner is composed of 5 nano-positioners, 2 for out-of-plane (Z), 2 for fast lateral (X) and 1 for slow lateral (Y) positioning. The control techniques proposed in section 4.3 for out-of-plane and lateral multi-actuation are implemented on this scanner. To improve the positioning precision of the scanner in the slow lateral Y direction a non-linear feedforward compensator based on the Maxwell model is used. Unlike the conventional approach where only the initial rise portion of the hysteresis loop is used for Maxwell parameter estimation, in the proposed approach the full hysteresis loop is utilized. This enables application of all the measured piezo displacement data-points to achieve a more effective compensation of piezo hysteresis. The details of experimental setup is given and the performances of the scanner along X, Y, and Z axis are presented.

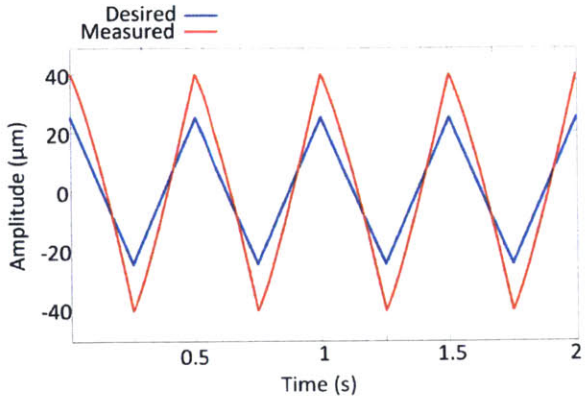

(a)

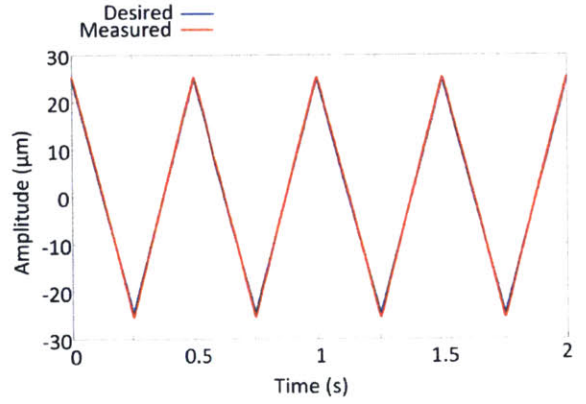

(b)

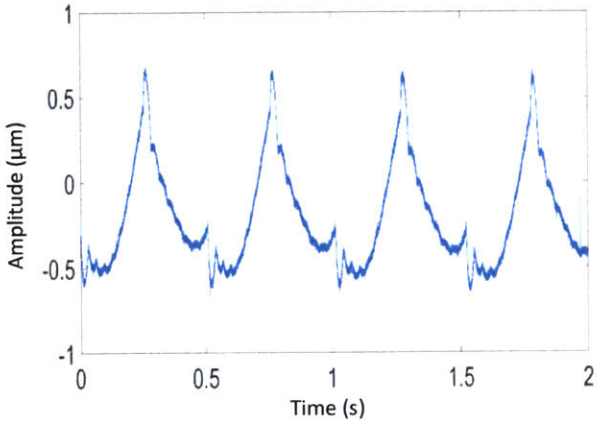

(c)

Figure 5-16: a) Desired and measured response of the Y positioner with both the feedback and feedforward controllers inactive, b) desired and measured response of the Y positioner with the activation of the feedforward nonlinear compensator implemented based on the fitted Maxwell model, and c) residual error associated with the response shown in part (b).

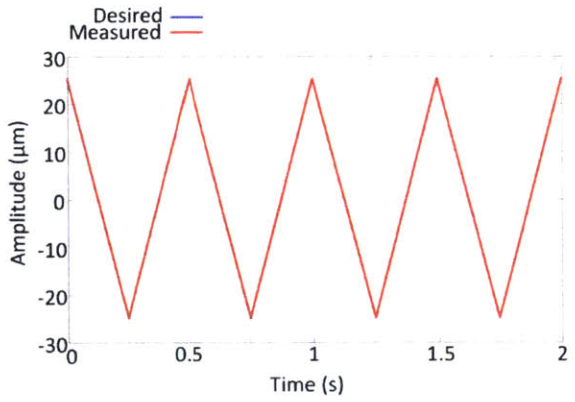

(a)

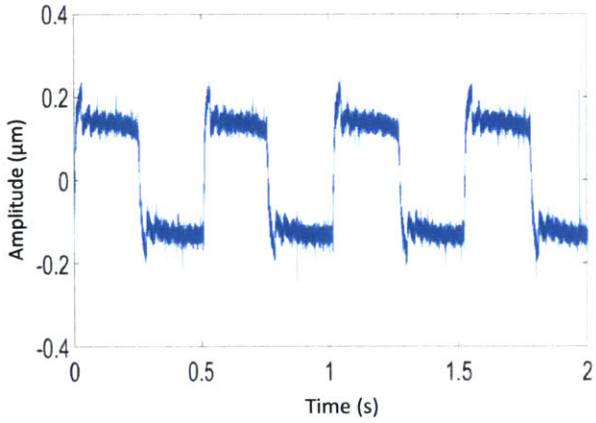

(b)

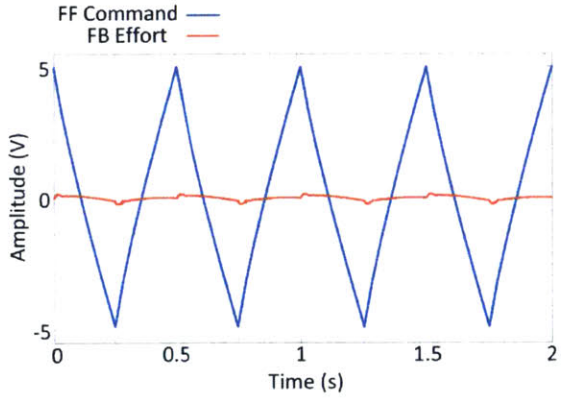

(c)

Figure 5-17: a) Desired and measured response of the Y positioner when a 2DOF nonlinear feedforward+feedback is utilized, b) residual positioning error associated with the plot of part (a), and c) feedforward and feedback control efforts.

Chapter 6

Amplitude Demodulation Based on Teager Energy Operator

6.1 Introduction

Dynamic mode has proven to be a less invasive imaging technique and hence a better choice for delicate samples such as biological specimen. Specially at high-imaging speeds the intermittent interaction between the probe and the sample can reduce the possibility of sample damage or disruption of the studied nano-scale process.

In one mode the amplitude of vibration of the probe is regulated during imaging (referred to as amplitude modulated AFM or AM-AFM). AM-AFM imaging requires an amplitude demodulation (ADM) step in the feedback loop. Conventionally a lock-in amplifier is used in AFM for this purpose. In a lock-in amplifier the measured deflection signal is mixed with a sine and a cosine of the same frequency exciting the probe. The output of each mixer includes a double frequency component. As such, a lowpass filtering step is necessary to recover the demodulated signal. Due to the fact that the peak to peak amplitude of the double frequency interference is similar to that of the modulation component of interest, the applied lowpass filters are commonly very aggressive. The phase lag introduced by this lowpass filtering step adds up directly to the overall cumulative delay of the AFM feedback control loop and can potentially limit the imaging bandwidth.

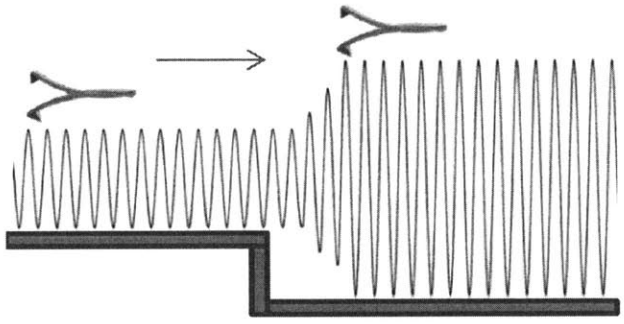

Figure 6-1: Gradual response of the probe vibration amplitude to the topography changes. Probe's response is slower for higher Q factors.

Another important limitation of tapping mode imaging is associated with the slow response of the probe vibration amplitude to the features of the surface topography. This is shown in Fig. 6-1 where due to slow amplitude response on a topography step-down, the probe loses contact with the sample surface (sometimes referred to as parachuting in the AFM literature). This behavior is related to the Q factor of the probe vibration and becomes more sever as the AFM tip speed increases. For lower Q factor (higher damping) the response time of the vibrating probe to surface topography is shorter. Hence, when imaging in a liquid the speed performance is superior due to the additional damping introduced by the viscous surrounding environment. It is also worth noting that although decreasing the Q factor may improve imaging speed it reduces the measurement sensitivity.

Although the imaging speed in terms of maximal tip velocity may be constrained by the above mentioned limitations, the imaging throughput can still be improved via parallel sensing. This was discussed briefly in section 1.2.5. However, this approach has received very limited attention by the industry and researchers, mainly due to the practical limitations associated with its implementation cost. For the example of Fig. 1-7b with an array of 25 self-sensed and self-actuated probes one needs a similar number of independent feedback controllers for amplitude regulation, and lock-in amplifiers for amplitude demodulation.

In this chapter we aim to provide a simpler substitute for the amplitude demodulation unit of the AFM such that it can be easily implemented in large numbers

with very low cost. Such a technique can move us one step closer to an affordable atomic force microscopy platform operating on parallel sensing. For this purpose we investigate an amplitude demodulation scheme based on the nonlinear Teager Energy Operator (TEO) [93, 78, 76], and examine the possibility of applying it for tapping mode AFM imaging. We start by describing the mathematics of TEO and move on to the details associated with its digital and analog implementations. Through AFM imaging experiments it is shown in this chapter that the method can be a simple substitute for lock-in amplifiers and potentially be used for parallel sensing applications involving probe arrays.

6.2 Teager Energy Operator (TEO)

6.2.1 Continuous-Time TEO

The Teager Energy Operator applied on a continuous signal, $x(t)$, can be written as [77]:

$$\Psi_c(x(t)) = (\frac{dx(t)}{dt})^2 - x(t)(\frac{d^2x(t)}{dt^2}) \tag{6.1}$$

Applying this operator,$\Psi_c()$, to a general signal in the form of $x(t) = a(t)b(t)$ leads to [52]:

$$\Psi_c(x(t)) = a^2(t)\Psi_c(b(t)) + b^2(t)\Psi_c(a(t)) \tag{6.2}$$

Let us now consider a case where $a(t)$ is a general time varying function and $b(t) = \cos(\phi(t))$, where $\phi(t) = \omega_c t$, and ω_c is a constant i.e. $\ddot{\phi}(t) = 0$. We have:

$$\Psi_c(\cos(\phi(t)) = \dot{\phi}^2(t) + \frac{1}{2}\ddot{\phi}(t)\sin 2\phi(t) \tag{6.3}$$

Using Eqs. (6.2), (6.3) and the fact that $\ddot{\phi}(t) = 0$ we get:

$$\Psi_c(x(t)) = a^2(t)\omega_c^2 + \cos^2(\omega_c t)\Psi_c(a(t)) \approx a^2(t)\omega_c^2 \tag{6.4}$$

Equation (6.4) holds when:

$$\cos^2(\omega_c t)\Psi_c(a(t)) \ll a^2(t)\omega_c^2 \tag{6.5}$$

As such, in AM-AFM, $\sqrt{\Psi_c(x(t))}$ extracts the modulations in the cantilever vibration amplitude if the above inequality holds for the measured probe deflection signal. In the following we evaluate the validity of inequality (6.5) for probe deflection signals measured in AM-AFM imaging mode.

As the amplitude of vibration in tapping mode varies about a pre-defined set-point, the deflection measurment resembles a double-sideband-with-carrier (DSB-WC) signal with a relatively small modulation depth. For a single harmonic modulation such a signal can be written as:

$$x(t) = [1 + a_m \cos(\omega_m t)]b\cos(\omega_c t + \theta) \tag{6.6}$$

where ω_c is the carrier frequency, b the carrier amplitude, ω_m is the modulation frequency and a_m is the modulation depth. Applying the Teager Energy Operator to the signal of Eq. (6.6), one obtains:

$$\Psi_c(x(t)) = (1 + a_m \cos\omega_m t)^2 b^2 \omega_c^2 + a_m \omega_m^2 (\cos\omega_c t)^2 (a_m + \cos\omega_m t) b^2 \tag{6.7}$$

It is reasonable to assume that $\omega_m < \omega_c$ i.e. frequency of modulations associated with sample surface topography is smaller than the tapping frequency. We can also assume that $a_m \ll 1$, i.e. the AFM feedback control can prevent the tapping amplitude to depart too far from the amplitude setpoint. With these assumptions the second term in Eq. (6.7) can be ignored, and we have:

$$\Psi_c(x(t)) \approx (1 + a_m \cos\omega_m t)^2 b^2 \omega_c^2 \tag{6.8}$$

According to Eq. (6.8), TEO can be used to demodulate AM-AFM deflection signals. A block diagram of this operator is given in Fig. 6-2.

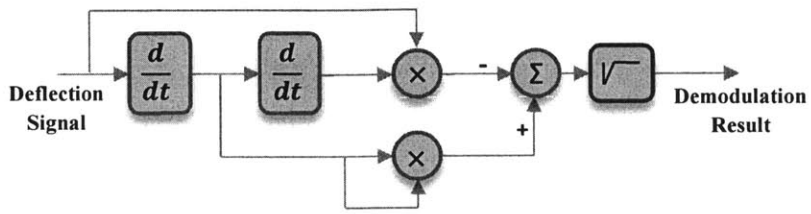

Figure 6-2: Block diagram of the demodulation scheme based on continuous-time Teager Energy Operator.

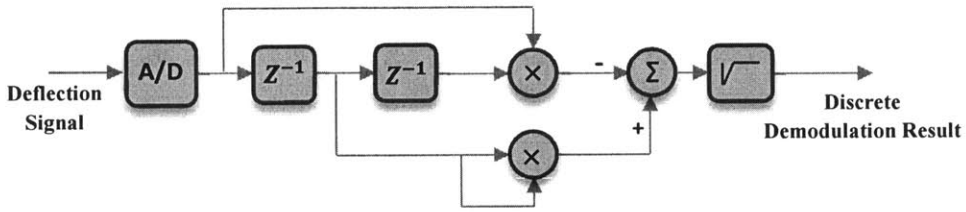

Figure 6-3: Block diagram of the demodulation scheme based on causal discrete-time Teager Energy Operator.

6.2.2 Discrete-Time TEO

A discrete-time version of Eq. (6.1) can be derived as [77]:

$$\Psi_d(x(n)) = x^2(n) - x(n-1)x(n+1) \tag{6.9}$$

Following a proof similar to that presented for the continuous-time case, it can be shown that for an amplitude modulated signal $x(n) = (1 + a_m \cos(\Omega_a n))b\cos(\Omega_c n + \theta)$ with small modulation depth, $a_m \ll 1$, and a maximum modulation frequency, $\Omega_a < \Omega_c$ the following approximation holds [77]:

$$\Psi_d(x(n)) \approx (1 + a_m \cos(\Omega_a n))^2 b^2 \sin^2(\Omega_c) \tag{6.10}$$

According to Eq. (6.10), similar to the continuous-time case, the discrete-time version of the TEO can be used for amplitude demodulation in tapping mode AFM imaging. Figure 6-3 illustrates the block diagram of a causal version of the discrete-time TEO.

The simplicity of the Teager Energy Operator in discrete form as presented in

Eq. (6.9) is very attractive. It requires two multiplications and a subtraction step. The availability of low cost, high-speed and powerful computing platforms such as FPGAs, makes implementation of this technique for parallel sensing feasible. Given the low computation cost of the method, a single FPGA platform can accommodate hundreds of this operator for parallel processing. Nowadays most AFMs are equipped with FPGAs for control and processing purposes. In the following sections we take a closer look at both digital and analog implementations of TEO for AFM imaging in tapping mode.

6.3 Digital Implementation

For digital form of Teager energy operator, the only implementation intricacy corresponds to the proper management of the numerical errors associated with the finite precision hardware arithmetic. At high sampling rates the subtraction result of Eq. (6.9) is very close to zero at all times. This is because the consecutively sampled datapoints $x(n-1), x(n)$,and $x(n+1)$ are almost identical. This makes the demodulation result vulnerable to the noises associated with the finite precision arithmetic, and can significantly reduce the corresponding signal to quantization noise ratio. Reduction of the sampling rate improves the situation but may adversely affect the control performance of the atomic force microscope.

To mitigate this limitation, one needs to decouple the control loop rate from the effective sampling rate associated with the TEO processor. This can be done by generalizing the discrete form of TEO according to:

$$\bar{\Psi}_d(x(n)) = x^2(n) - x(n-M)x(n+M) \tag{6.11}$$

where a delay of order M replaces the unit delay of Eq. (6.9). For $M > 1$ the signal to quantization noise ratio is increased while the throughput of the operator and hence control bandwidth of the AFM is maintained intact. The proper M value is dependent on the level of quantization noises and should be larger for higher quantization noise

intensity. The following heuristic equation can be used to select the value of M for a given data acquisition rate, f_s and probe resonance frequency, f_r:

$$M = \lfloor \frac{f_s}{P f_r} \rfloor \tag{6.12}$$

where P is an integer on the range $[10, \ldots, 20]$. This ensures that the effective sampling rate observed by the TEO processing unit is always 10 to 20 times the cantilever resonance frequency.

As explained earlier the computational simplicity of digital implementation of TEO makes it very attractive for parallel processing of the signals measured from probe arrays. However, the analog form can also be valuable when digital processing is not available. The analog form of the TEO can also be implemented in ASIC form on the cantilever chips to make the next generation of tapping probes with incorporated demodulation units. The analog implementation of TEO is discussed in the following section.

6.4 Analog Implementation

According to Eq. (6.1) an analog circuit realization of the TEO includes two derivative operations. An ideal differentiator is not realizable in practice. As such a band-limited differentiation should be used. One such circuit is illustrated in Fig. 6-4a. The transfer function from input voltage, v_{in}, to the output voltage, v_{out}, of the differentiator of Fig. 6-4 can be written as:

$$H_{\text{diff}}(s) = -\frac{R_2 C_1 s}{(1 + R_1 C_1 s)(1 + R_2 C_2 s)} \tag{6.13}$$

The magnitude and phase response plots associated with $H_{\text{diff}}(s)$ for $R_1 C_1 = R_2 C_2 = 2\pi$ Mrad/s, are shown in Fig. 6-4b. A non-ideal version of the analog TEO implemented based on the differentiator of Fig. 6-4 is illustrated in Fig. 6-5. In this form the non-ideal nature of the differentiation step adversely affects the TEO performance. As shown in Fig. 6-4b the magnitude response of a non-ideal differentiator

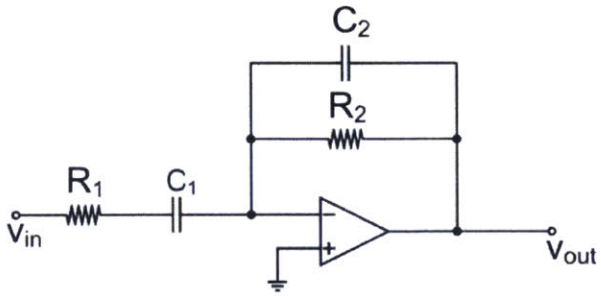

(a)

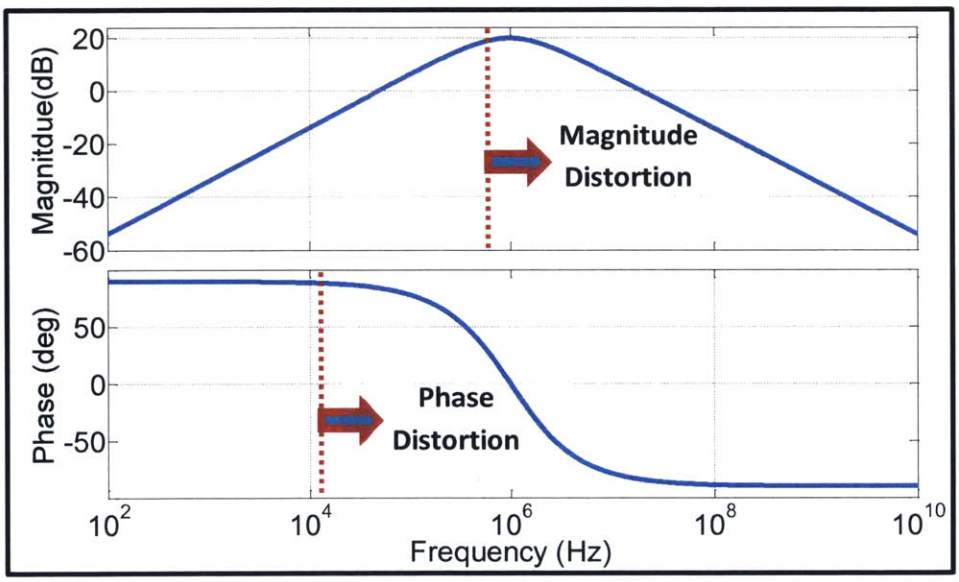

(b)

Figure 6-4: a) A realizable band-limited differentiator, and b) amplitude and phase response of the non-ideal differentiator block of part (a) with 1 MHz bandwidth.

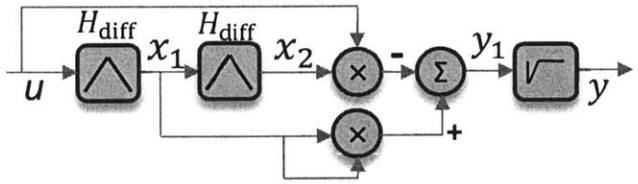

Figure 6-5: A block diagram of analog TEO based on non-ideal differentiators.

follows a linear increase for the most part of the differentiation bandwidth. However, the deviation from 90° phase lead starts at frequencies much lower than the pole frequency of 2π Mrad/s in Fig. 6-4b. Ideally on the analog TEO implementation (see Fig. 6-5), x_1 and x_2 should lead the input signal by 90° and 180°, respectively for the TEO to operate as predicted by Eq. (6.1). However, due to the phase lag associated with the introduced extra poles i.e. $\frac{1}{R_1C_1}$ and $\frac{1}{R_2C_2}$ of the realizable differentiators this is not the case for the implementation of Fig. 6-5. These phase errors lead to distortions in the TEO output especially for wide-band modulation signals.

We remove the above limitation by introducing similar phase deviations as those imposed on the differentiated signals to other signal components of the TEO formulation. Let us start with the signal component having the largest phase deviation, i.e. the double differentiated, x_2. For this signal we can write:

$$X_2(s) = \frac{(R_2C_1s)^2}{(1+R_1C_1s)^2(1+R_2C_2s)^2}U(s) \tag{6.14}$$

where $U(s)$ and $X_2(s)$ are the Laplace transforms of $u(t)$ and $x_2(t)$, respectively. To compensate for the phase deviation affecting $x_2(t)$ one can modify the block diagram of Fig. 6-5 according to Fig. 6-6. As shown in this figure, phase compensation units, $H_{\text{PC}}(s) = \frac{1}{(1+R_1C_1s)(1+R_2C_2s)}$, are incorporated into the block diagram to adjust the phase of the signal components $x_1(t)$ and $u(t)$. This ensures that x_1' leads u' by 90°, and similarly x_2 leads x_1' by 90° and hence, guarantees an accurate demodulation result at the output of the TEO circuit over the entire bandwidth of the non-ideal differentiator. A phase compensation unit, $H_{\text{PC}}(s)$, can be formed by cascading two analog lowpass filters with an architecture shown in Fig. 6-7 and poles matching

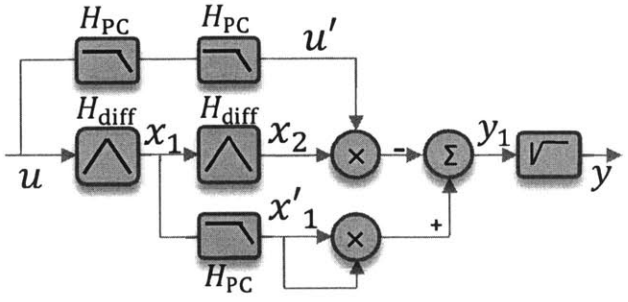

Figure 6-6: A block diagram of phase compensated analog TEO operating on non-ideal differentiators.

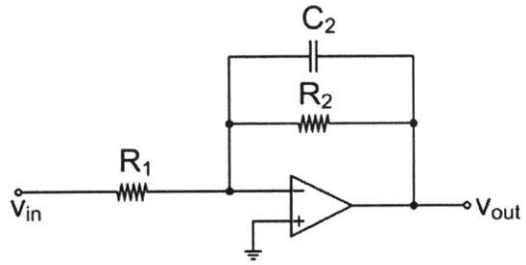

Figure 6-7: An analog lowpass architecture. A cascade of two lowpass filters forms the phase compensation unit, $H_{\mathrm{PC}}(s)$.

those of the non-ideal differentiators.

For the analog implementation of the phase compensated TEO presented in Fig. 6-6, we can write:

$$y_1(t) = [L^{-1}(H_{\mathrm{diff}}H_{\mathrm{PC}}U(s))]^2 - [L^{-1}(H_{\mathrm{diff}}^2U(s)) \times L^{-1}(H_{\mathrm{PC}}^2U(s))] \tag{6.15}$$

where L^{-1} denotes the inverse Laplace transform. We have:

$$H_{\mathrm{diff}}H_{\mathrm{PC}} = -\frac{R_2C_1s}{(1+R_1C_1s)^2(1+R_2C_2s)^2} = -H_{\mathrm{LP}}R_2C_1s \tag{6.16}$$

$$H_{diff}^2 = \frac{(R_2C_1s)^2}{(1+R_1C_1s)^2(1+R_2C_2s)^2} = H_{\mathrm{LP}}(R_2C_1s)^2 \tag{6.17}$$

where $H_{\mathrm{LP}} = H_{\mathrm{PC}}^2$ is a 4^{th} order lowpass. Using Eqs. (6.16), and (6.17), Eq. (6.15)

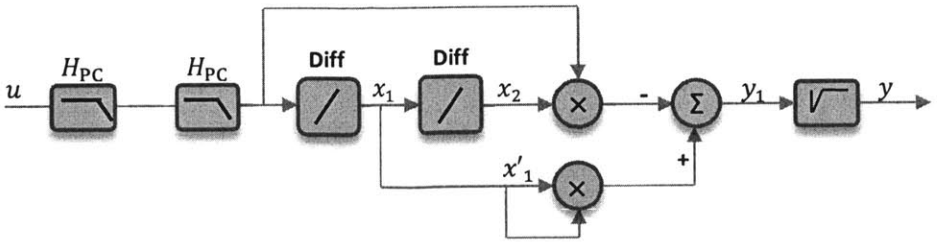

Figure 6-8: Equivalent of the phase compensated analog TEO of Fig. 6-6.

can be written as:

$$y_1(t) = (R_2C_1)^2([L^{-1}sH_{\mathrm{LP}}U(s)]^2 - [L^{-1}s^2H_{\mathrm{LP}}U(s) \times L^{-1}H_{\mathrm{LP}}U(s)]) \tag{6.18}$$

Noting that $U'(s) = H_{\mathrm{LP}}U(s)$ corresponds to a lowpassed version of the input signal u, Eq. (6.18) can be written in the following form:

$$y_1(t) = k^2[(\frac{d}{dt}u'(t))^2 - u'(t) \times \frac{d^2}{dt^2}u'(t)] \tag{6.19}$$

where $k = R_2C_1$. In the above equation we used the fact that $L^{-1}(sU'(s)) = \frac{d}{dt}u'(t)$ and $L^{-1}[s^2U'(s)] = \frac{d^2}{dt^2}u'(t)$. As one can observe from Eq. (6.19) for the phase compensated TEO, in fact an ideal TEO given by Eq. (6.1), is operating on a 4^{th} order lowpass filtered version of the input signal u. Hence, as long as the signal components of interest fall within the bandwidth of this lowpass filter, any distortion of the demodulation result is avoided.

6.5 Experimental Evaluation and Imaging Results Based on TEO Demodulation

6.5.1 Digital Platform

The digital version of the TEO is implemented according to Eq. (6.11) on a National Instruments (NI) Flexrio PXI-7954R FPGA module. The cantilever deflection signal is sampled at 100 MHz, down-sampled with a factor of 16 and then processed. The

main reason for the down-sampling step is to meet the processing time requirement of the FPGA. The implementation allows for real-time update of the generalized delay M.

6.5.2 Analog Platform

The proposed phase compensated analog TEO architecture was successfully tested on a single channel implementation featuring 600 kHz bandwidth. To enable application of the method for AFM probes with a diverse range of resonance frequencies a second prototype with multiple channels each featuring a different bandwidth was later made in collaboration with the University of Ulm. The latter implementation, used in the following experiments, can be used for probe resonances ranging from 10 kHz to 800 kHz. In this implementation four sets of resistors, [R_1=634 Ω,R_2 = 3.16 kΩ], [R_1=316 Ω,R_2=1.58 kΩ], [R_1=160 Ω,R_2=806 Ω], and [R_1=80.6 Ω,R_2=402 Ω] (see Figs. 6-4a, 6-6 and 6-7) are used for the phase compensated TEO circuit. Each set of resistors corresponds to a different roll-off frequency of the differentiation, H_{diff}, and phase compensation, H_{PC}, units. By switching between the different sets the TEO demodulation bandwidth can be adjusted for various AFM cantilever choices. Capacitors C_1 and C_2 are 1 nF and 200 pF, respectively.

6.5.3 Frequency Response

Figure 6-9 illustrates the open-loop frequency response of the analog and digital TEO implementations. Three carrier signals of 64 kHz, 128 kHz and 256 kHz were amplitude modulated over a wide frequency range with 5% modulation depth. As shown in this figure, both analog and digital TEO implementations reflect a flat frequency response almost up to the carrier frequencies denoted by vertical red lines. Such a wide demodulation bandwidth is rooted in the instantaneous nature of the Teager Energy Operator. This also demonstrates TEO's potential for high-speed imaging applications where the demodulation speed is a bottleneck of the AFM feedback loop.

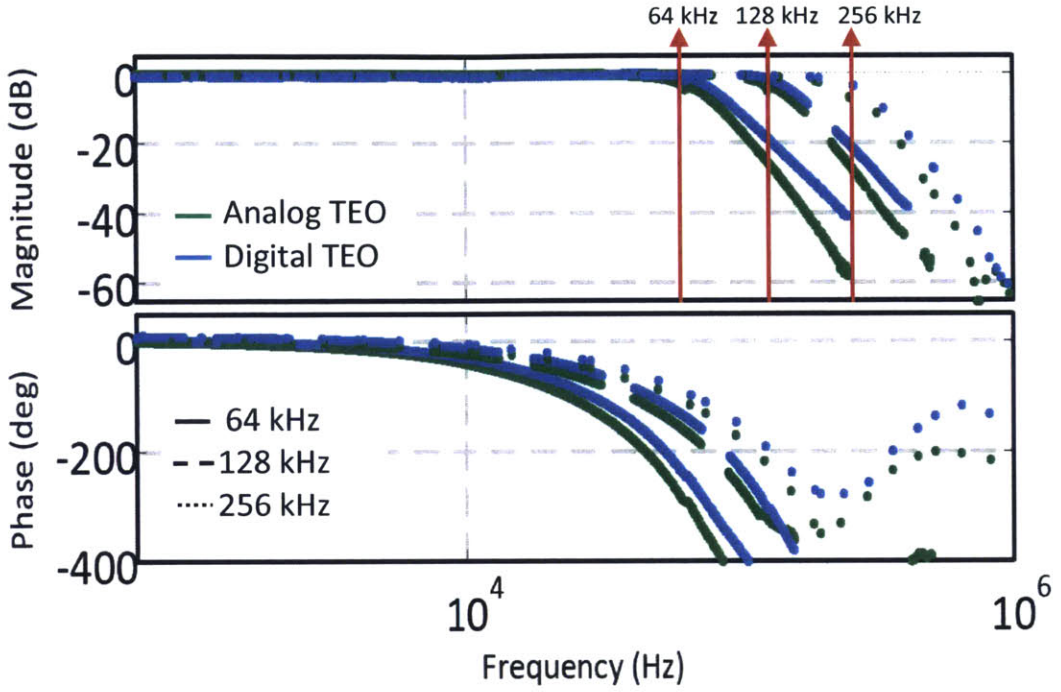

Figure 6-9: Demodulation frequency response of the Analog TEO (green), and Digital TEO (blue) implementations for three carrier frequencies of 64 kHz (solid), 128 kHz(dashed) and 256 kHz (dotted).

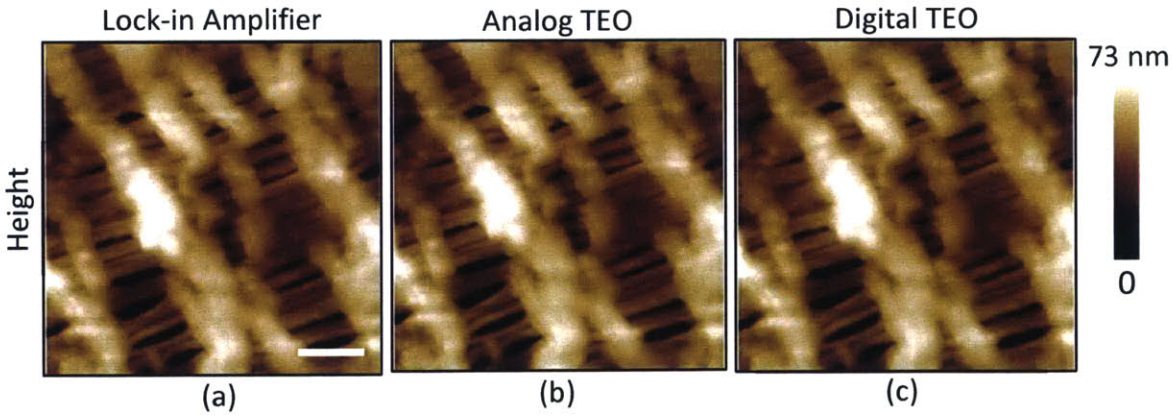

Figure 6-10: AFM images of Celgard taken in tapping mode in air at 1 Hz scan rate when the applied amplitude demodulation scheme is based on a) lock-in amplification, b) analog implementation of TEO, and c) digital implementation of TEO (images recorded on re-trace).

6.5.4 Imaging Performance

The method is then evaluated on the imaging performance of a Bruker Multi-Mode atomic force microscope operating in tapping mode. Figure 6-10 illustrates AFM images of a sample of microporous isotactic polypropylene (iPP) separator membrane (Celgard). The iPP membrane reflects fibrillar and lamellar structures [103]. The nano-fibrils are covered by several bent lamellae aligned perpendicular to the fibrils. The AFM images of Fig. 6-10 are taken in tapping mode in air, using three amplitude demodulation schemes, that is Lock-in amplification, analog TEO and Digital TEO for Figs. 6-10(a), (b) and (c) respectively. The imaging result demonstrates the applicability of the proposed TEO based demodulation for AFM imaging in tapping mode.

6.6 Chapter Summary

In this chapter an amplitude demodulation method based on the Teager energy Operator (TEO) is proposed. The main advantage of the method is its simplicity specially in the discrete-time form. This feature of TEO demodulation makes it suitable for parallel sensing applications. The digital and analog implementations of TEO are discussed in detail.

For digital implementation discrete-time TEO is generalized. In the generalized version the control loop rate and the effective TEO sampling rate are decoupled. This enables high control loop rate and maintains an acceptable signal to quantization noise ratio in the presence of finite precision digital arithmetic.

Effective analog implementation also requires certain provisions. The differentiation components of the TEO can not be implemented in ideal form. The phase lag associated with non-ideal differentiators can adversely affect the demodulation performance of TEO. To tackle this limitation, additional phase compensation was incorporated into the analog circuitry. It is proven that the performance of the phase compensated TEO is equivalent to the performance of an ideal TEO based on ideal differentiators processing a low-passed version of the input signal. As such, as long as

the input signal falls within the pass-band of the equivalent low-pass any distortion of the demodulation result is avoided.

Finally, the digital and analog implementations of TEO are evaluated experimentally. The amplitude demodulation performance of the TEO on synthetic signals and the AFM imaging results demonstrate the applicability of the method in AM-AFM imaging.

Chapter 7

MIT High-Speed and Large-Range AFM

In earlier chapters of this work different aspects of AFM operation were discussed and certain developments were presented. The potentials of the proposed methodologies in improving AFM performance were demonstrated by retroactively enhancing existing AFMs. However, as discussed in chapter 1, to enable true high-speed, large-range atomic force microscopy all the components of the AFM including the scanner, photodiode circuitry, piezo-drivers, optical beam deflection setup, cantilever, data logging and plotting, control units, etc should meet stringent requirement. Here we build upon our developments presented in earlier chapters and design and implement a novel AFM (referred to as MIT-AFM) with all its components set to meet the requirements of high-speed and large-range imaging.

7.1 Description of the MIT-AFM Components

In the following subsections various components of the MIT-AFM setup are described. The MIT-AFM assembly is shown in Fig. 7-1. All the optical components as well as the photodiode circuitry are accommodated in (1). The group (1) of components are mounted on the XYZ positioner (2) to enable moving the laser focusing lens in the lateral and out-of-plane directions. This is used for locating/adjusting the laser spot

on the back of the cantilever. The assembled group of components (1) and (2) along with the cantilever holder (3) are mounted on the upper supporting deck (4). The groups of components (1), (2), (3) and (4) are connected to a lower base plate (5) via the structural columns (6). The base plate also accommodates an XYZ positioner (7). The AFM scanner (8) is mounted on the XYZ positioner (7). The stepper motor (9) is connected to the Z axis of the XYZ positioner (7) to move the sample in the vertical direction for engagement. The XY degrees of freedom of the positioner (7) are used to move the sample manually in the lateral direction for coarse site selection. Fig. 7-2 shows the AFM setup. The scanner used in this AFM and the corresponding control schemes are the same as those described in chapter 5. The rest of the components are further described in the following.

7.1.1 Optical Beam Deflection Setup

A polarizing beam-splitter with a wavelength range of 420-680 nm (48-999, Edmund), a dichroic shortpass mirror with a transmission wavelength of 400-580 nm (69-192 Edmund) and a $\lambda/4$ plate (wavelength 670 nm, 46-552 Edmund) guide the laser and provide an optical view to the sample/probe for site selection and laser adjustment as shown in Fig. 7-3. A separate beam splitter (50:50 BSW10R-Thorlabs) coaxially illuminates the sample for optical view through a Cannon-EOS-SL1 camera. The laser diode (670 nm, 5 mW, VPSL-0670-005-X-5-B, BlueSky Research) is aligned with a collimation tube (LT110P-B, Thorlabs) accommodating an aspheric lens with a focal length of $f = 6.24$ mm to form a 2.4 mm collimated laser beam. The laser driver is RF-modulated to reduce laser optical feedback noise as discussed in [38]. An L Plan 20X SLWD Nikon objective lens focuses the laser to a 3.5 μm spot compatible with small cantilevers. As discussed in section 1.2.5 small cantilevers feature faster dynamics and maintain a small spring constant making them suitable for high-speed imaging of delicate nano-scale processes.

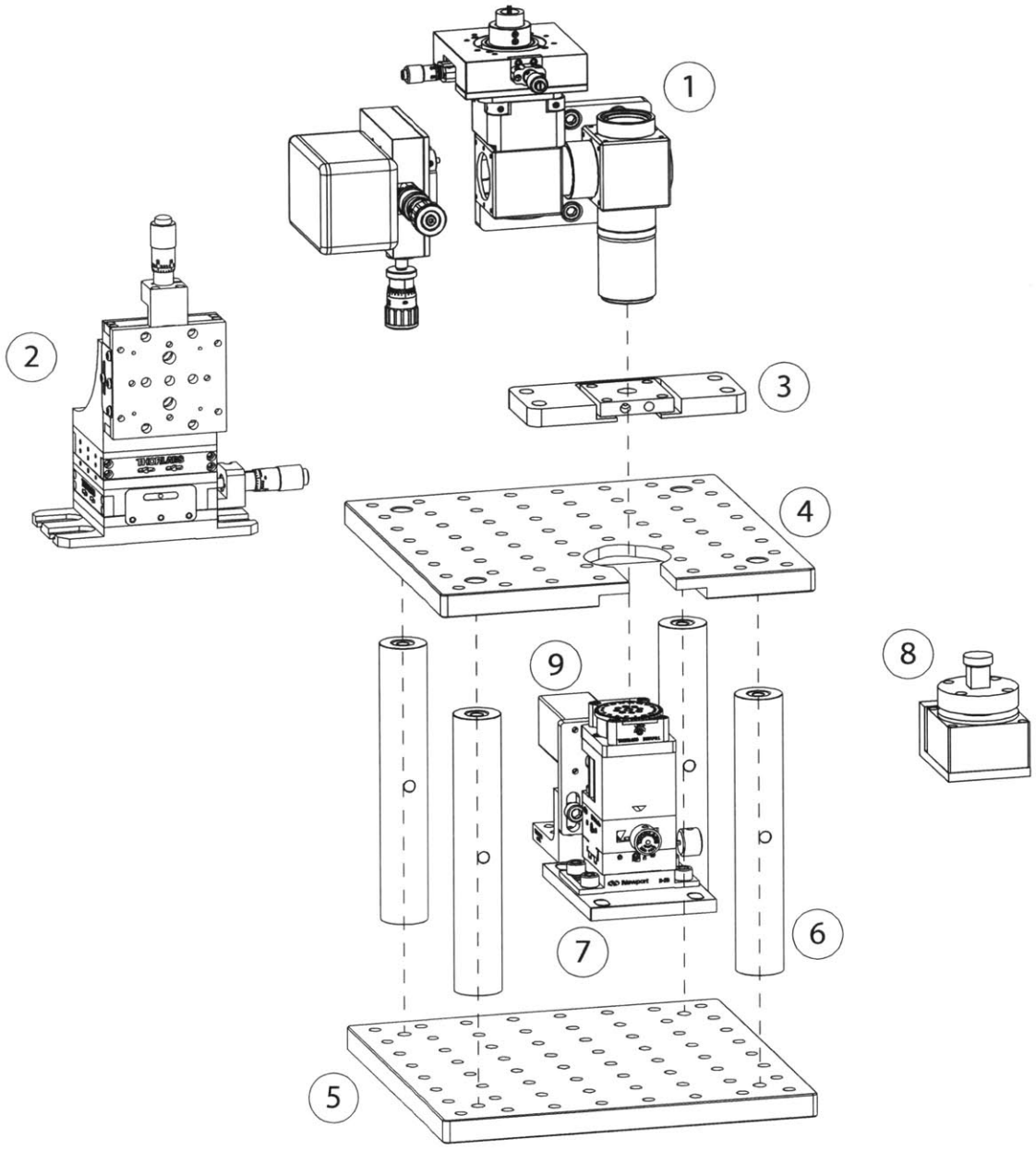

Figure 7-1: MIT-AFM assembly.

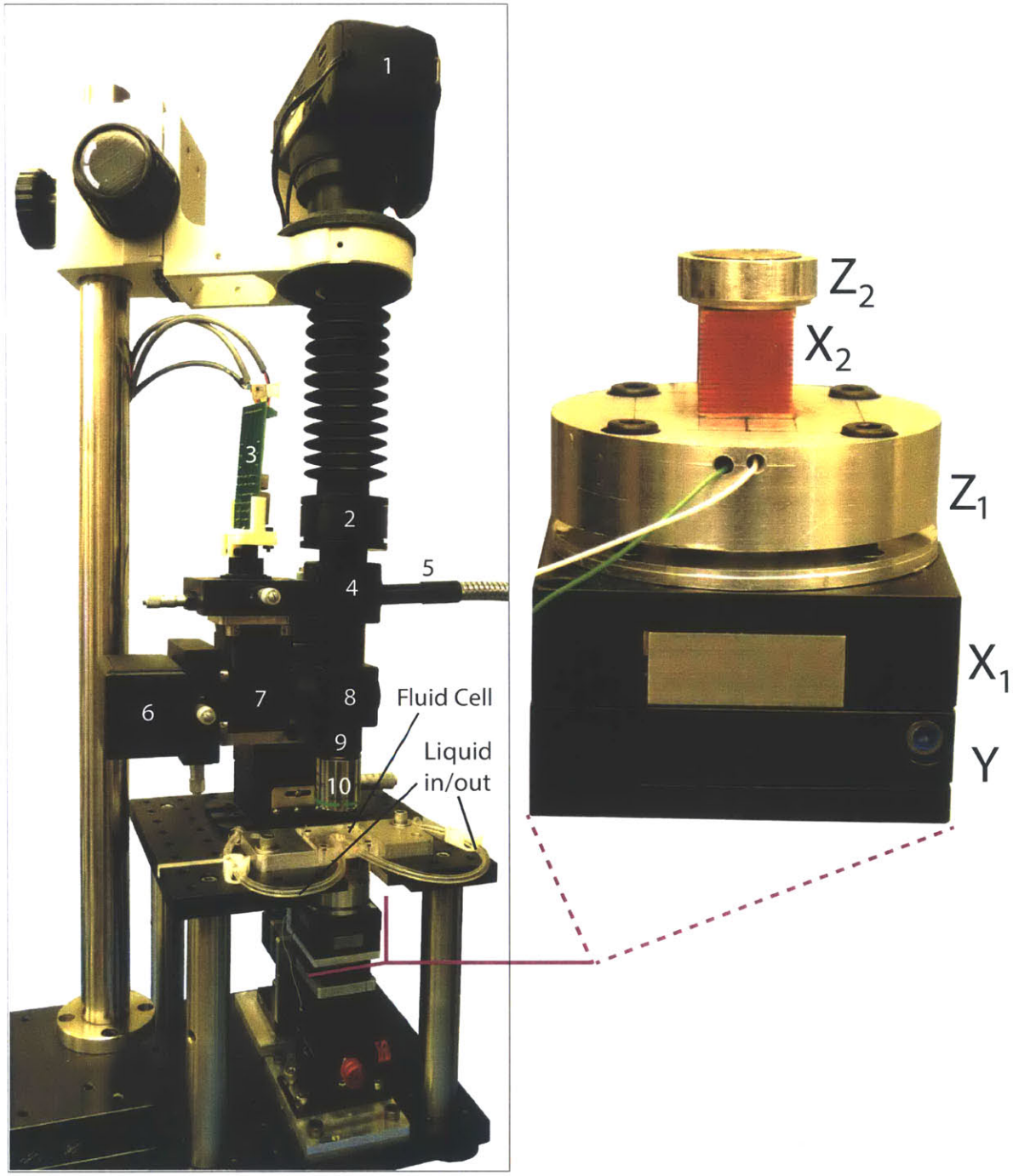

Figure 7-2: The AFM setup with a close-up view of the multi-actuated scanner. Various components are labeled/numbered similar to the schematic view of Fig. 7-3. The scanner is composed of a (from top to bottom) 1) fast/short-range out-of-plane actuator (Z_2), 2) fast/short-range lateral positioner (X_2) for raster scan, 3) slow/large-range out-of-plane actuator (Z_1), 4) slow/large-range lateral actuator (X_1) for raster scan, and 5) slow/large-range lateral actuator for frame up/down motion (Y).

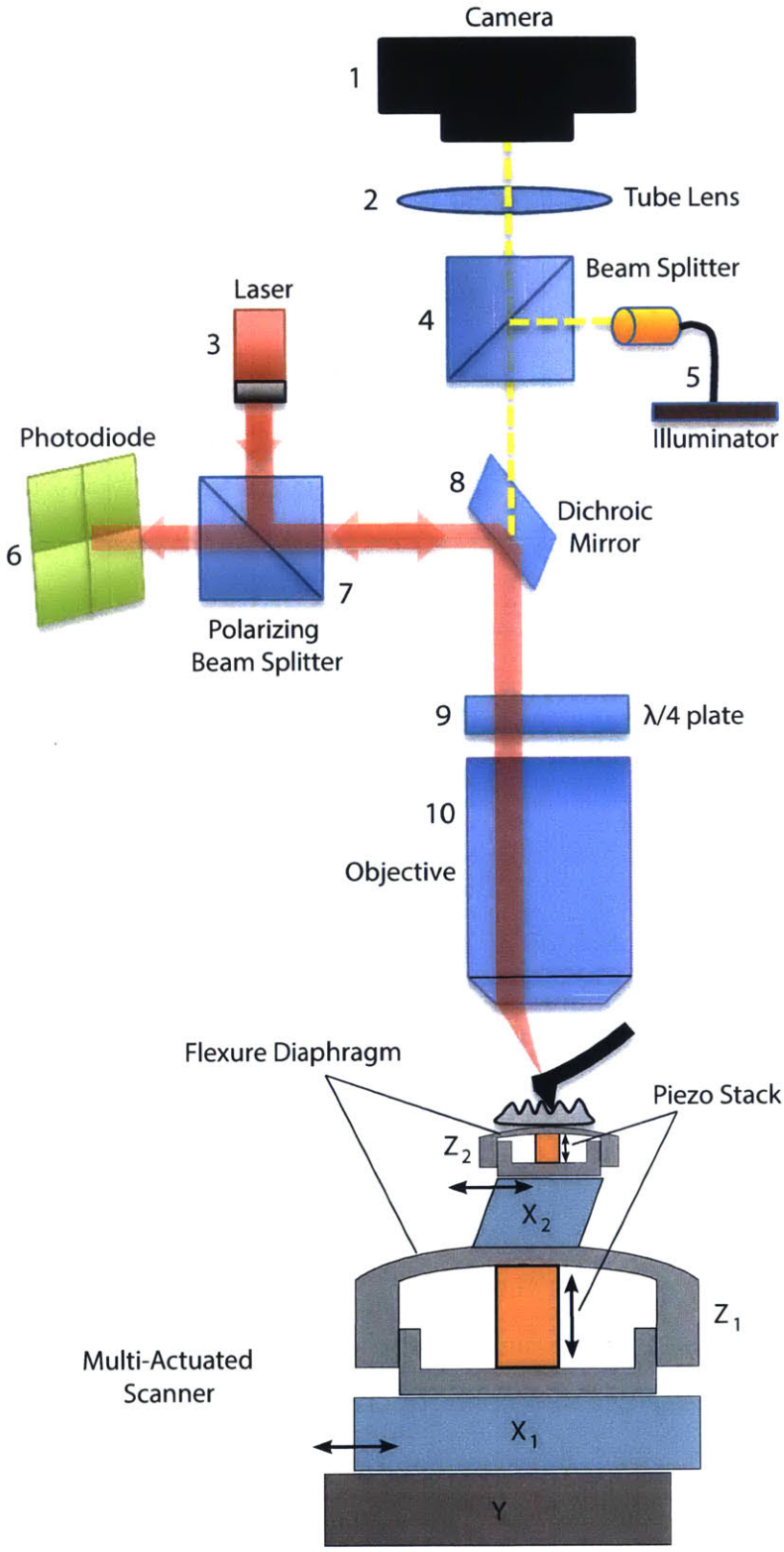

Figure 7-3: A schematic view of the designed AFM.

Table 7.1: Values associated with the components of different photodiode sub-circuits shown in Fig. 7-5 set for 1.3 MHz detection bandwidth.

C_1^{D}	0.1μF	$C_1^{\mathrm{S_1}}$	100 pF	$C_1^{\mathrm{S_2}}$	10 pF
C_1^{TI}	6.25 pF	C_2^{D}	47 pF	$C_2^{\mathrm{S_1}}$	0.1 μF
$C_2^{\mathrm{S_2}}$	0.1 μF	C_2^{TI}	0.1 μF	R_1^{D}	667 Ω
$R_1^{\mathrm{S_1}}$	2 kΩ	$R_1^{\mathrm{S_2}}$	2 kΩ	R_1^{TI}	20 kΩ
R_2^{D}	20 kΩ	$R_2^{\mathrm{S_1}}$	1 kΩ	$R_2^{\mathrm{S_2}}$	2 kΩ
R_3^{D}	6.67 kΩ	R_4^{D}	2 kΩ	-	-

7.1.2 Instrumentation

Photodiode Circuitry

A quad-cell Hamamatsu photodiode model S5980 is used to measure the laser beam deflection. Figure 7-4a demonstrates a block diagram of the photodiode circuitry. The output current of individual photodiode cells are fed to transimpedance stages. The voltages associated with the top two cells are then summed together through a summation stage to get $V_{\mathrm{u}} = V_1 + V_3$. A similar processing is applied to the voltages associated with the bottom two cells to get $V_{\mathrm{b}} = V_2 + V_4$. Another summation stage applied to V_{u} and V_{b} generates the overall sum signal. This signal is monitored to adjust the incident laser spot on the back of the cantilever and maximize the measured reflection. A difference stage also operates on the V_{u} and V_{b} to obtain the deflection signal $V_{\mathrm{def}} = V_{\mathrm{u}} - V_{\mathrm{b}}$. The difference signal represents cantilever deflection and is fed to the out-of-plane control loop. This signal is also captured by the data logging and plotting platform. Figure 7-5 shows the circuit arrangement for each stage. The associated component values are listed in Table 7.1.

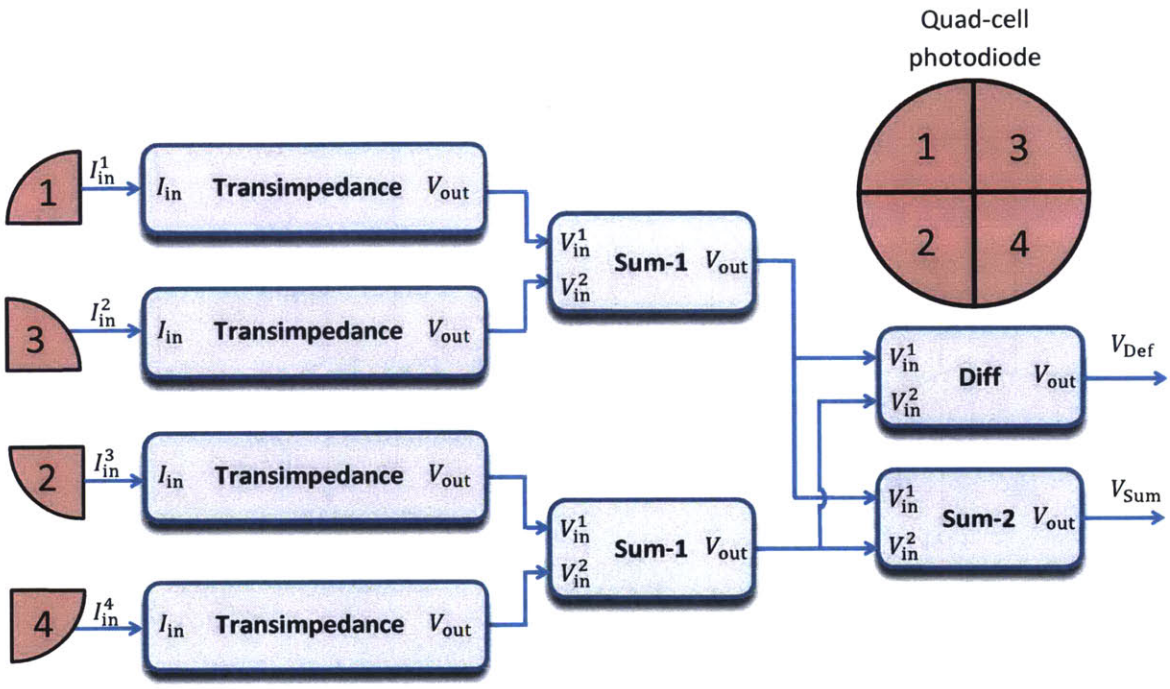

(a)

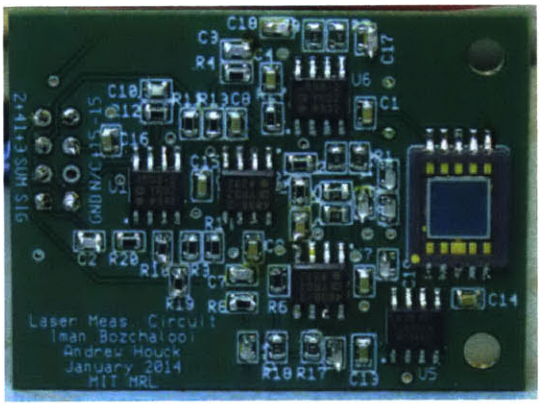

(b)

Figure 7-4: a) Simplified block diagram and b) a picture of the implemented photodiode circuitry.

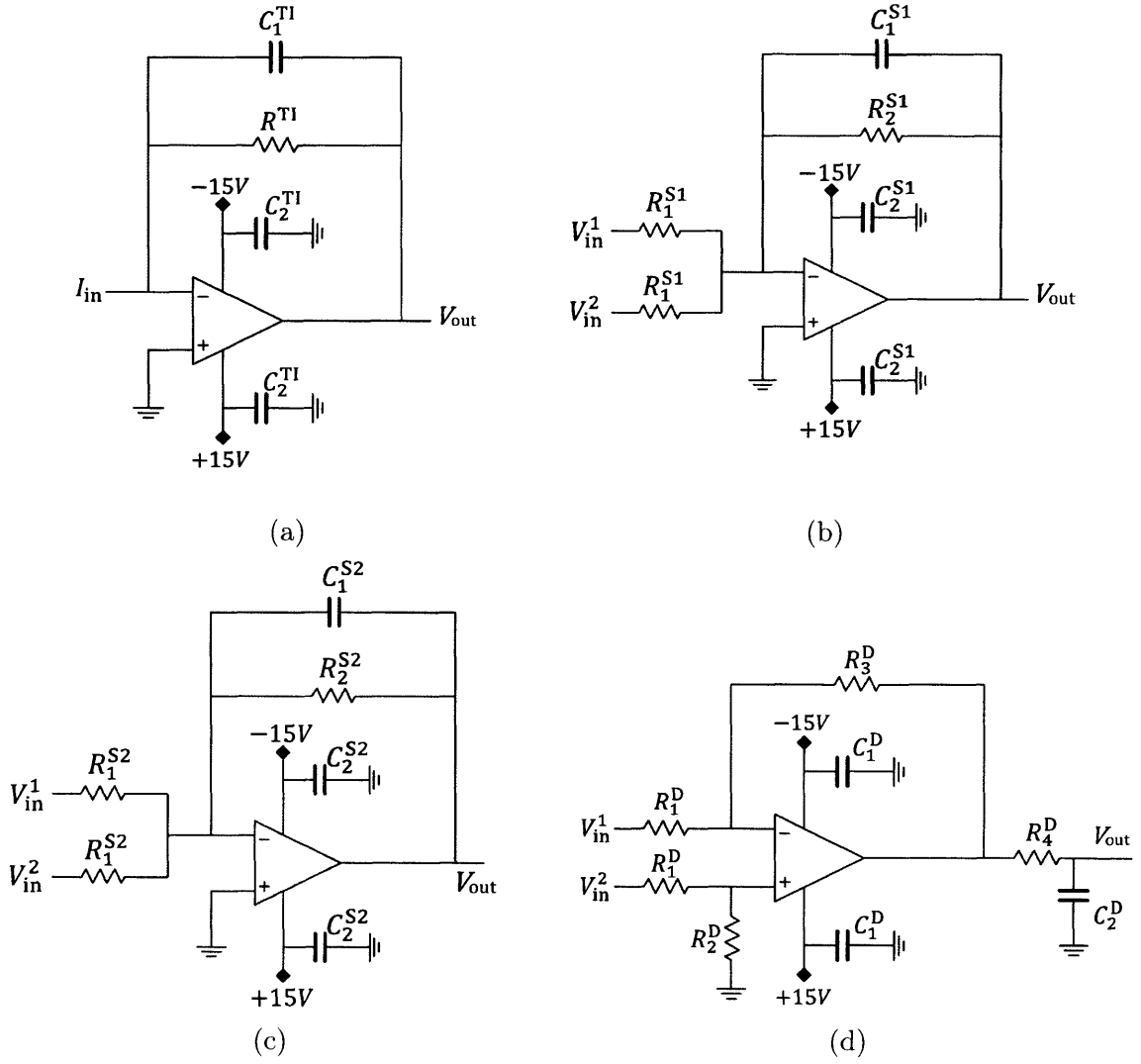

Figure 7-5: Schematic diagram of a) transimpedance, b) summation block #1, c) summation block #2, and d) difference circuitry associated with the block diagram of Fig. 7-4a.

Piezo Drivers

A piezo actuator behaves similar to a capacitive load. As such, it is important to ensure that not only the mechanical bandwidth of the actuator and the small signal bandwidth of the piezo driver meet the high-speed operation requirements, but also the combined driver-circuitry/piezo-actuator provides the necessary slew-rate. This should be taken into account in the design of the piezo drivers and the selection of the piezo actuators.

For an excitation voltage, $v(t)$ to a piezo actuator we can write:

$$I = C\frac{\mathrm{d}v}{\mathrm{d}t}$$

where I is the current drawn by the piezo actuator and C is its capacitance. As such, to accommodate this excitation signal the piezo driver should be able to provide the maximum current,

$$I_{\mathrm{r}} = C\frac{\mathrm{d}v}{\mathrm{d}t}|_{max} = C\sigma_r$$

where σ_r is the maximum slew rate imposed by the excitation signal $v(t)$. For a power amplifier with maximum current output, I_{m}, the maximum available slew rate, σ_{m} can be written as:

$$\sigma_{\mathrm{m}} = \frac{I_{\mathrm{m}}}{C}$$

To ensure that the piezo actuators do not experience any nonlinear behavior associated with the slew rate limitations, the following inequality should hold true at all times:

$$\sigma_{\mathrm{r}} \leq \sigma_{\mathrm{m}} \tag{7.1}$$

This should be taken into account in the design of the piezo drive circuitry.

The multi-actuated scanner presented in chapter 5 is composed of 5 positioners. The piezo actuator types incorporated into each positioner are listed in Table 7.2. This table also lists the capacitance, model number, and vendor of each piezo actuator. Based on these specifications and the requirement of Eq. (7.1) the piezo driver

Table 7.2: Piezos utilized in the positioners of multi-actuated scanner presented in chapter 5 and their capacitance.

Positioner	Piezo	Vendor	Capacitance
Z_2	PL022.30	PI	25 nF
Z_1	P-885.11	PI	0.7 μF
X_2	P-141.10	PI	60 nF
X_1	P-885.51	PI	1.5 μF
Y	P-885.51	PI	1.5 μF

circuitries are designed or selected.

Figures 7-6 and 7-7 show the schematic diagram of two types of piezo drivers designed and implemented here. The piezo driver implemented to drive X_1 and Y positioners, referred to as PZD1, is based on the design of Fig. 7-6. The associated component values leading to a 3.7 kHz bandwidth are listed in Table 7.3. A variant of the same design, PZD2, is used to drive positioner X_2 with the component values listed in Table 7.4 (9.4 kHz bandwidth). The design demonstrated in Fig. 7-7 with the components listed in Table 7.5, PZD3, has a much wider bandwidth (1.1 MHz 3dB bandwidth), designed to drive the fastest out-of-plane positioner Z_2. The output voltage range of this driver does not cover the full range of the Z_2 piezo actuator leading to approximately %75 of its maximum range. As such this driver is suitable for ultra high-speed applications with relaxed out-of-plane range requirements. This condition is frequently met in imaging biological samples. Figure 7-8 shows the PCB implementation along with a six channel piezo drive package that accommodates PZD1, PZD2 and PZD3 drivers. Additional details about the design of these circuitry and the utilized power amplifiers can be found in [81, 84, 82, 83]. In addition to

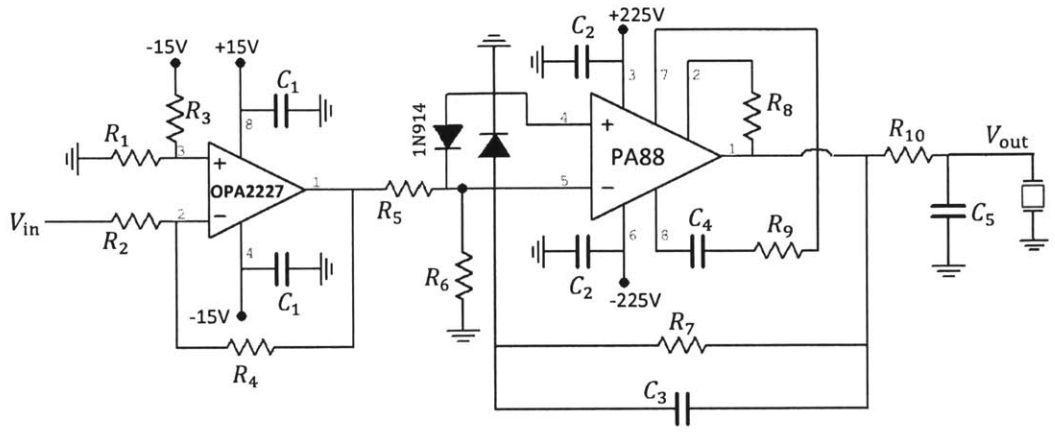

Figure 7-6: PZD1 and PZD2 Circuit schematics. Corresponding component values are listed in Tables 7.3 and 7.4 for PZD1 and PZD2, respectively.

the drivers PZD1, PZD2, and PZD3 a separate commercially available piezo driver (Techproject) is used to drive Z_1. When the full range of the Z_2 positioner is needed the high-speed output of the Techproject driver with 100 kHz bandwidth can replace PZD3. In this case however, the phase lag introduced by the Techproject (TP) driver limits the closed-loop topography tracking bandwidth.

For a triangular command signal with a peak to peak amplitude A and period T the required slew rate is given as:

$$\sigma_r = \frac{\mathrm{d}v}{\mathrm{d}t} = \frac{2A}{T}$$

As such, for an approximately known maximum lateral scan range and frequency the slew rate requirements can be calculated. However, for the out-of-plane piezos in addition to scan speed σ_r is also dependent on the sample surface topography. The slew rate requirements are more stringent for samples with high-spatial frequency and large-amplitude features. To give a sense on the ability of each piezo driver, σ_r can be calculated for a single harmonic excitation with a peak to peak amplitude A and period T. In this case we can write:

$$\sigma_r = \frac{\mathrm{d}v}{\mathrm{d}t}|_{\max} = \frac{\pi A}{T}$$

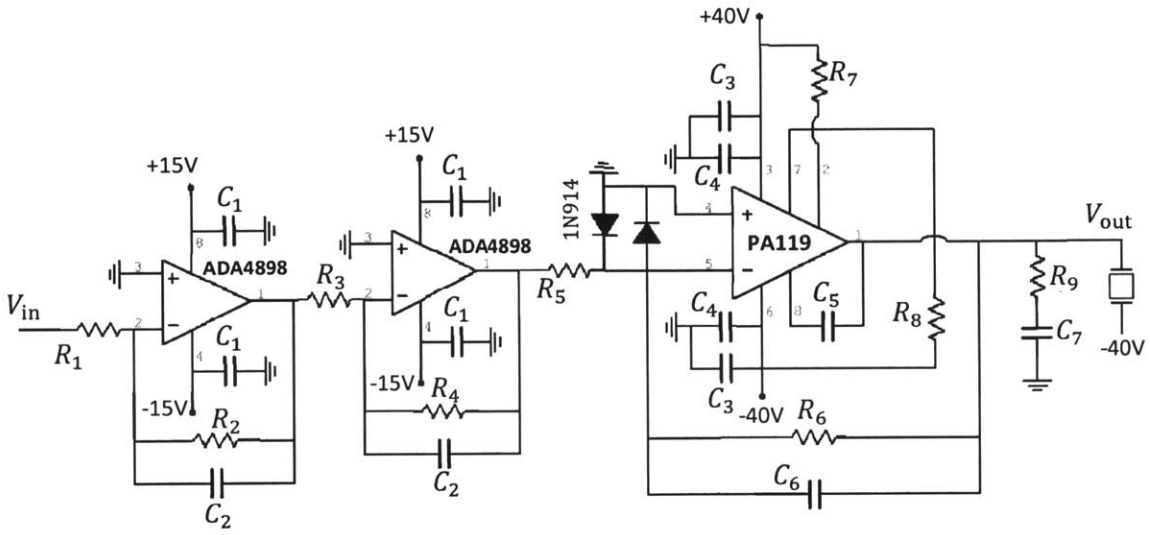

Figure 7-7: PZD3 Circuit schematics. Corresponding component values are listed in Table 7.5.

Table 7.3: Values associated with the components of PZD1

C_1	0.33μF	C_2	0.47 μF	C_3	750 pF
C_4	68 pF	C_5	33 nF	R_1	1 kΩ
R_2	20 kΩ	R_3	2.7 kΩ	R_4	20 kΩ
R_5	9.28 kΩ	R_6	3.32 kΩ	R_7	56 kΩ
R_8	10 Ω	R_9	100 Ω	R_{10}	500 Ω

Table 7.4: Values associated with the components of PZD2

C_1	0.33μF	C_2	0.47 μF	C_3	300 pF
C_4	68 pF	C_5	33 nF	R_1	short
R_2	20 kΩ	R_3	open	R_4	28 kΩ
R_5	3.6 kΩ	R_6	3.32 kΩ	R_7	56 kΩ
R_8	10 Ω	R_9	100 Ω	R_{10}	300 Ω

Table 7.5: Values associated with the components of PZD3

C_1	0.33μF	C_2	33 pF	C_3	0.22 μF	C_4	40 μF
C_5	220 pF	C_6	32 pF	C_7	0.51 μF	R_1	1 kΩ
R_2	1 kΩ	R_3	1 kΩ	R_4	1 kΩ	R_5	1 kΩ
R_6	3 kΩ	R_7	160 mΩ	R_8	160 mΩ	R_9	50 Ω

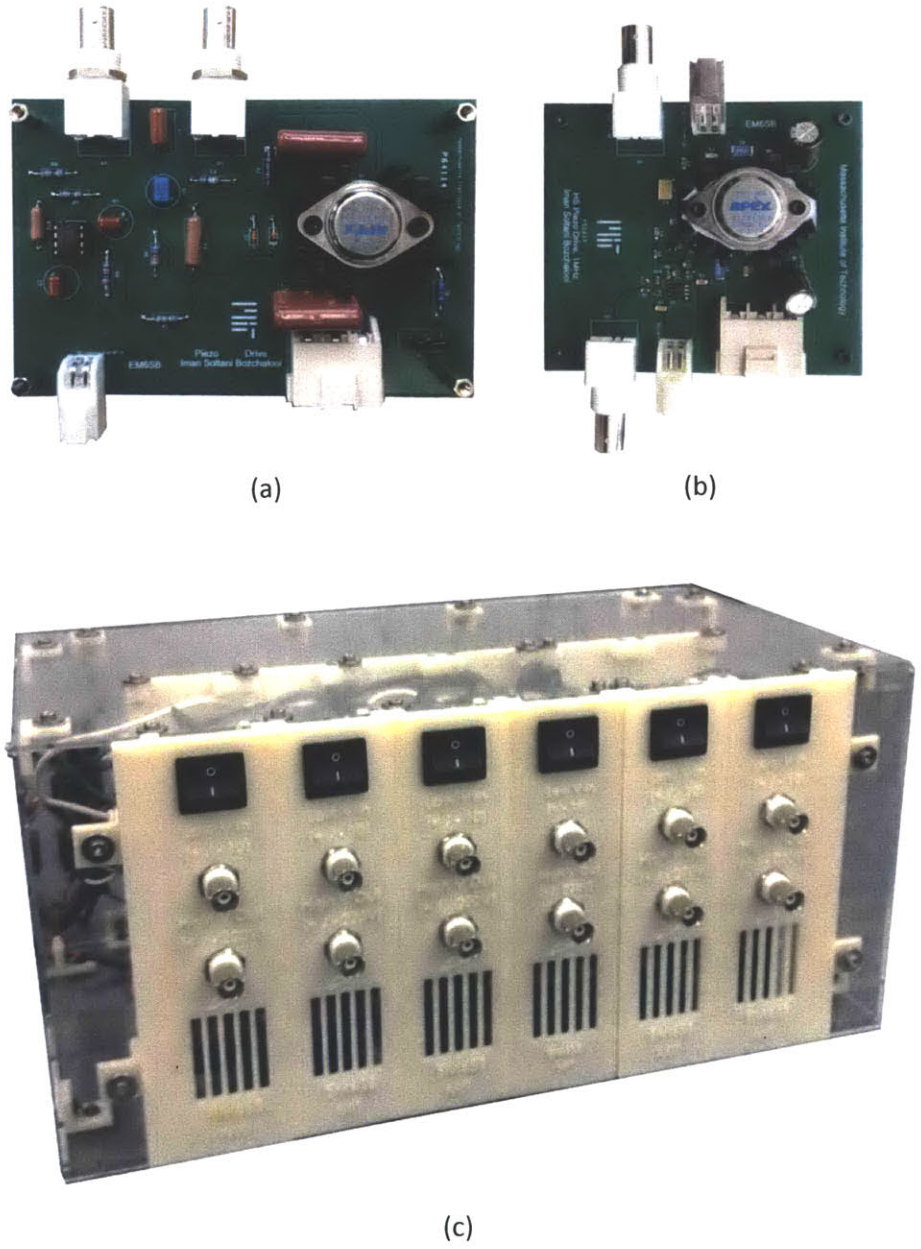

Figure 7-8: Piezo drivers: a) PZD1, PZD2, b) PZD3 and c) a six channel packaging of the drivers.

Table 7.6: Nano-positioners of the multi-actuated scanner, the associated driver, the available maximum stroke and mechanical bandwidth, and the maximum achievable drive frequency at the maximum stroke. For the out-of-plane piezos we assume a single harmonic excitation. TP refers to the Techproject piezo driver.

	Driver	Stroke, BW	Slew-Rate-Limited BW
Z_2	TP or PZD3	1 μm, 100 kHz	(1 μm, 850 kHz) or (0.5 μm, 1.06 MHz)
Z_1	TP	6 μm, 7 kHz	(6 μm, 30 kHz)
X_2	PZD2	10 μm, 7 kHz	(9 μm, 1.9 kHz)
X_1	PZD1	120 μm, 140 Hz	(120 μm, 277 Hz)
Y	PZD1	120 μm, 140 Hz	(120 μm, 277 Hz)

Table 7.6 lists the positioners, the associated piezo drivers, the available stroke and mechanical bandwidth for each positioner as well as the achievable drive frequency at the maximal range given the slew rate requirement of Eq. (7.1). In all the cases the achievable drive frequency is greater than the available mechanical bandwidth except for the lateral high-speed positioner X_2. However, one should note that a scan speed of 1.9 kHz at 9 μm leads to a very high tip speed (34.2 mm/s) that in most cases surpasses the capabilities of out-of-plane tracking. For a 3 μm scan range the acceptable scan frequency increases to 5.6 kHz.

7.1.3 Approach Mechanism

The part of the designed AFM that accommodate the scanner and the stepper motor is shown in Fig. 7-9. As shown, the multi-actuated scanner is placed on a linear stage (Newport, DS40-XYZ) with 14 mm lateral and 5 mm vertical displacement range. The lateral displacement of the stage enables manual change of the imaging site. The

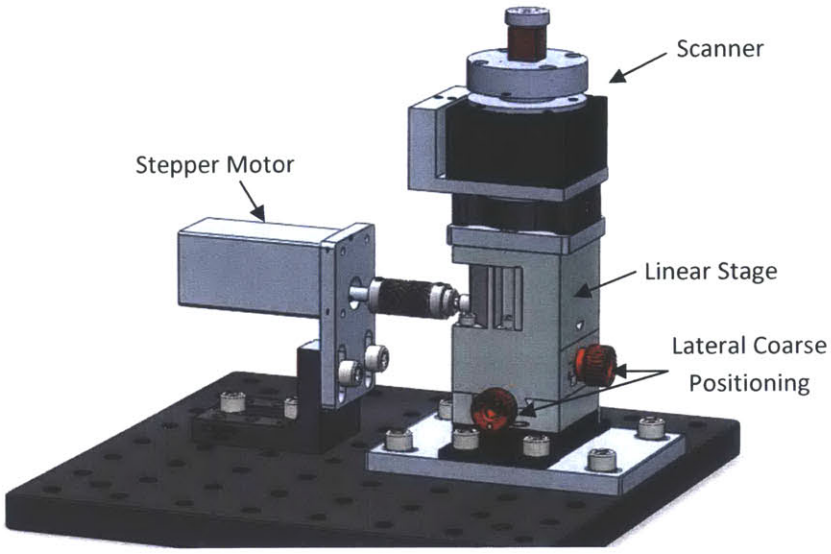

Figure 7-9: Schematics of the MIT-AFM approach mechanism.

out-of-plane motion is used to move the sample towards the probe for engagement. The drive screw of the Z axis of the linear stage (80 TPI) is connected to a stepper motor (Oriental Motor, PK223PB-SG36) with 200 steps per revolution through a reduction gearbox with 36:1 gear ratio resulting in 44 nm vertical displacement per step. The stepper motor is commanded through Labview via a NI PXI-7851 FPGA platform.

7.1.4 Control Hardware, Data Logging and Plotting

As discussed in chapter 5 two independent FPGA platforms are used to drive the lateral and out-of-plane actuators of the scanner. The out-of-plane actuators are driven by a National Instruments (NI) PXIe-7966R FlexRIO module with a NI 5781 baseband transceiver. The three lateral actuators are driven by a NI PXI-7851 FPGA module. Both FPGA modules are hosted by an NI PXIe-8135 chasis with 2.3 GHz core Windows controller. This controller captures the lateral position data along with the deflection and topography information to form real-time AFM images with a maximum of 20 MHz data throughput. This enables capture of high resolution images at high frame rate for real-time observation of nano-scale processes. Figure 7-10 shows a snapshot of the MIT-AFM setup.

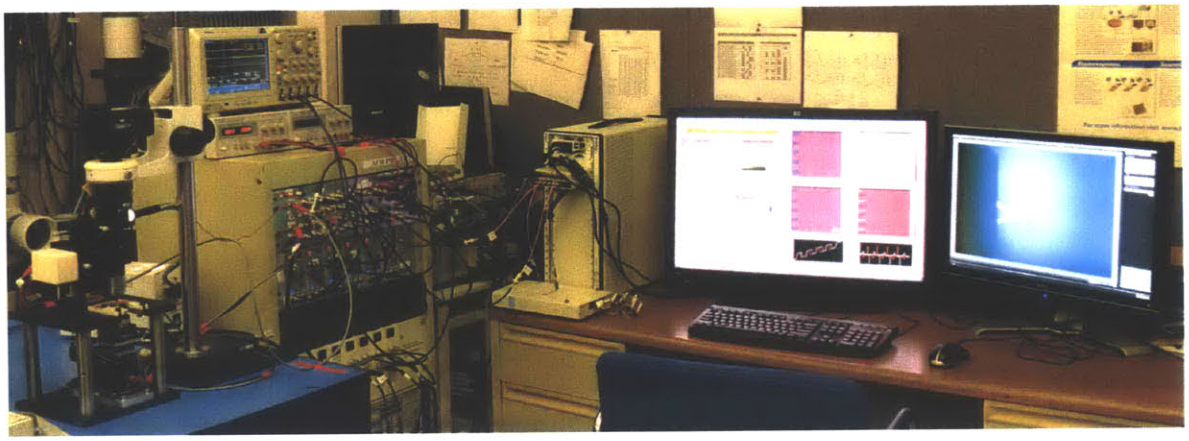

Figure 7-10: MIT-AFM full setup.

7.1.5 Probe Holder

The main application of the designed atomic force microscope is to observe dynamic nano-scale processes in real-time. Many of such processes take place in aqueous environment. This requires an easy to use liquid-cell/probe-holder. Figure 7-11 demonstrates schematics of the designed cantilever holder. The designed liquid cell features inlet and outlet for easy liquid exchange. It also accommodates different electrodes to initiate or stop an electrochemical reaction. To ensure that the focal distance of the laser focusing lens is not changed significantly, the part of the cell that is along the laser path is kept as thin as possible.

7.2 Study of Nano-Scale Processes using MIT-AFM

The designed atomic force microscope is used to study a chemical dissolution process and an electrochemical deposition/stripping process in real-time at the nano-scale. These experiments are described in the following.

7.2.1 Calcite Etching in Diluted Sulfuric Acid

We visualize the etching process of a freshly cleaved $\{10\bar{1}4\}$ calcite sample surface in a diluted solution of sulfuric acid in contact mode. A small cantilever (SCL-SensorTech) with fast dynamics and small spring constant (0.5 N/m) is used. The imaging starts

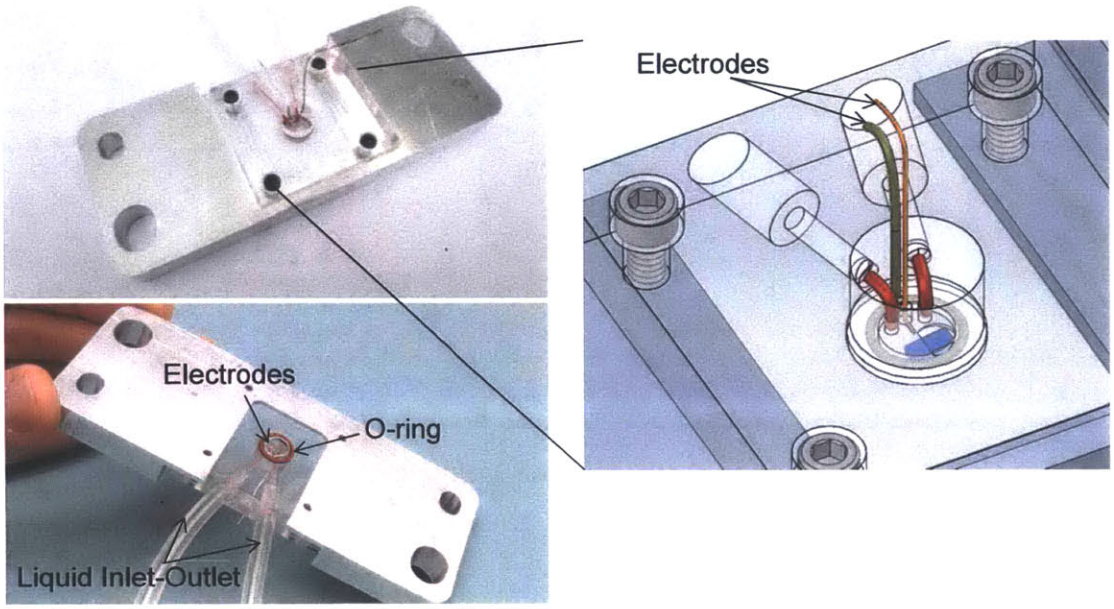

Figure 7-11: Probe holder/Electrochemical cell.

on the calcite sample in deionized water over a large scan area (70 μm $\times$ 70 μm) at 20 Hz scan rate (Fig. 7-12(a)). The calcite sample surface shows wide, flat terraces with step heights of a few nanometers. It also shows several shallow ($\sim$1 nm) and deeper ($\sim$10 nm) etch pits which are formed characteristically on calcite surface exposed to DI water [69]. The scan size is gradually decreased (to 42, 31.5, 21, 10.5, 6.3, and 3.1 μm range) while the scan speed is gradually increased (to 37 Hz, 50 Hz, 75 Hz, 135 Hz, 251 Hz and 512 Hz, respectively), keeping the tip speed near $\sim$3 mm/s. Figures 7-12 (b) and (c) show the 31.5 μm and 6.3 μm views of the sample selected from the zoom-in sequence. Imaging resolution is set to 256 lines per image and 2048 samples per line. The final 3.1 μm $\times$3.1 μm sample site is selected to reflect a moderate population of deep pits for the real-time observation of etching process in acid. Following the injection of 0.05M H_2SO_4 (pH $\approx$ 1.3), the surface morphology changes rapidly, showing layer-by-layer dissolution of calcite terraces through the merger of two or more pits or a pit and another step. The average height of the calcite terraces is measured as 16 $\pm$ 5 nm. The etching process is observed to be most active on the top calcite terrace leading to a retreat velocity of $\sim$254 nm/s. The time-laps of Fig. 7-12(d) shows the full dissolution of a step terrace during a

4-second time interval. The semi-rhombic shapes of the retreating steps reflect the rhombohedral symmetry of calcite crystals and approximately maintain a straight morphology along the moving steps during the dissolution. On top of each terrace, there are smaller steps with relatively small height (~3 nm) which are barely affected by the acid. Analysis of the time-lapse AFM images can also provide a relatively accurate estimate of calcite dissolution rate. AFM has been used in the past [105] to quantify the calcite dissolution process in pH>3.7 with an average step retreat velocity of a few nanometers per second. However, these experiments have not been extended to lower pH solutions where the step retreat velocities exceed 10 nm/s due to the slow operation speed of conventional AFMs. The following equation is used to estimate the calcite dissolution rate R (mol cm^{-2} s^{-1}) from an analysis of the time-lapse AFM images:

$$R = \frac{nD}{V_m T}$$

where n is the number of calcite terraces dissolved over the experiment interval T, D is the average thickness of the dissolving layers, and V_m is the molar volume of calcite (36.93 $cm^3 mol^{-1}$). The dissolution rate obtained based on the above equation is 9.98×10^{-9} mol cm^2 s^{-1}. The dissolution rate of calcite in HCl (pH of 1.7) has been measured through chemical analysis by Guidici [26] and is reported as 4×10^{-9} mol cm^{-2} s^{-1} which is in fair agreement with our estimation.

We repeat the experiment on a freshly cleaved $\{10\bar{1}4\}$ calcite sample. In this experiment the sample is exposed to acid right after initiation of the experiment to avoid formation of DI water induced pits. Figure 7-13 shows the first few topography images captured as the acid starts to attack the surface. These images demonstrate a few etched mono-layers as well as deeper pits [29]. These features are randomly distributed on the 3 μm by 3 μm scan area. Upon the merger of the neighboring pits the process again evolves into a layer by layer removal of calcite similar to that shown in Fig. 7-12d. The dissolution is influenced by the crystalline structure of calcite all along. Utilizing the large range of the multi-component scanner the imaging site is navigated over tens of microns of the sample surface to find an imaging site that clearly

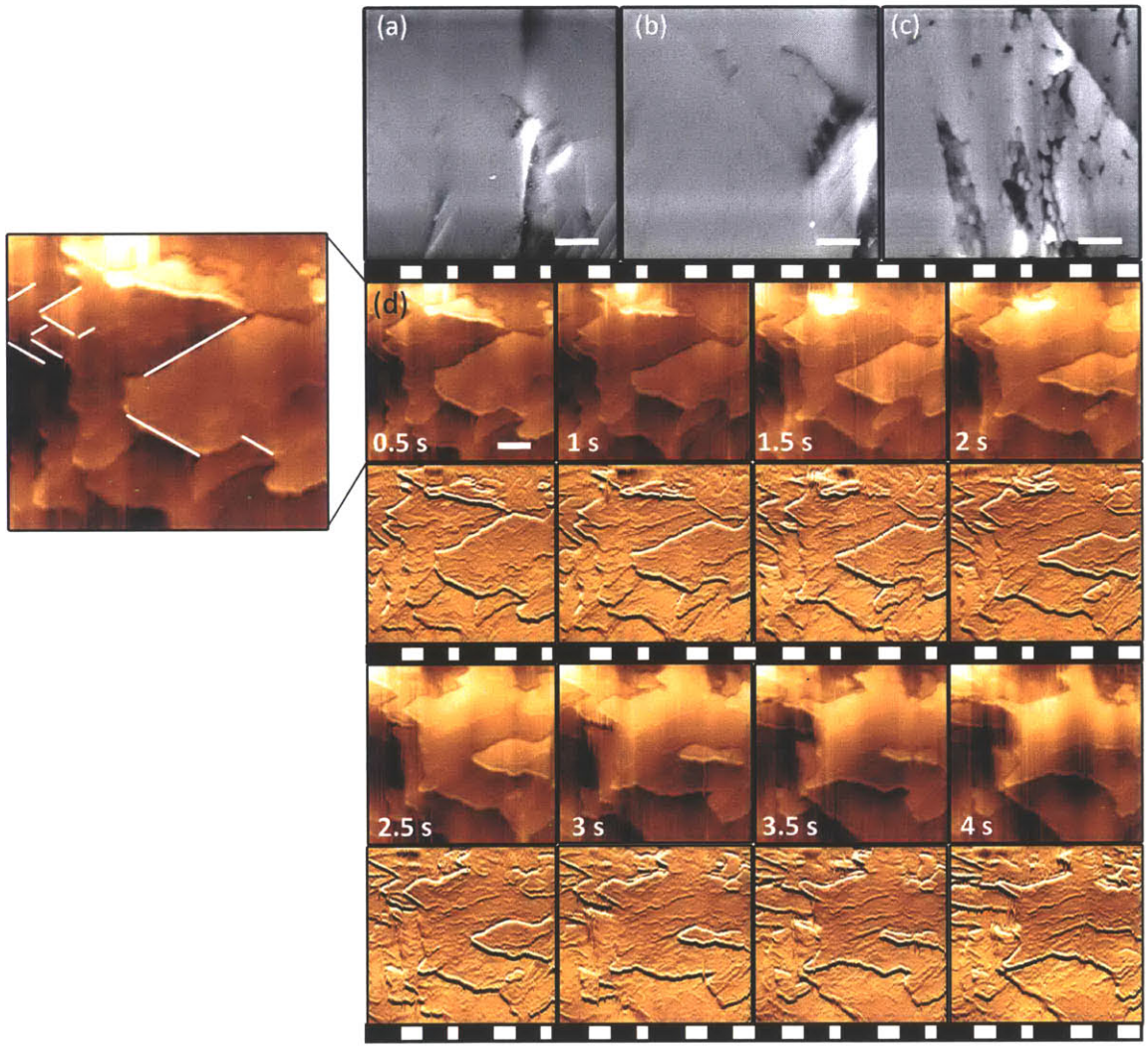

Figure 7-12: (a-c) AFM topography images of a calcite sample in deionized water starting from a 70 μm×70 μm view, and gradually zoomed into the area of interest. Scale bars are as follows: (a) 10 μm, (b) 4.5 μm, and (c) 900 nm, (d) Time-lapse images captured after acid injection (scale bar is 450 nm). Topography (top) and deflection (bottom) images are included in the movie stripes.

Figure 7-13: Topography images of freshly cleaved calcite right after exposition to diluted solution of sulfuric acid. Image resolution is set to 256 lines per image, and 2048 samples per line. The imaging range is 3 μm (scale bar is 500 nm).

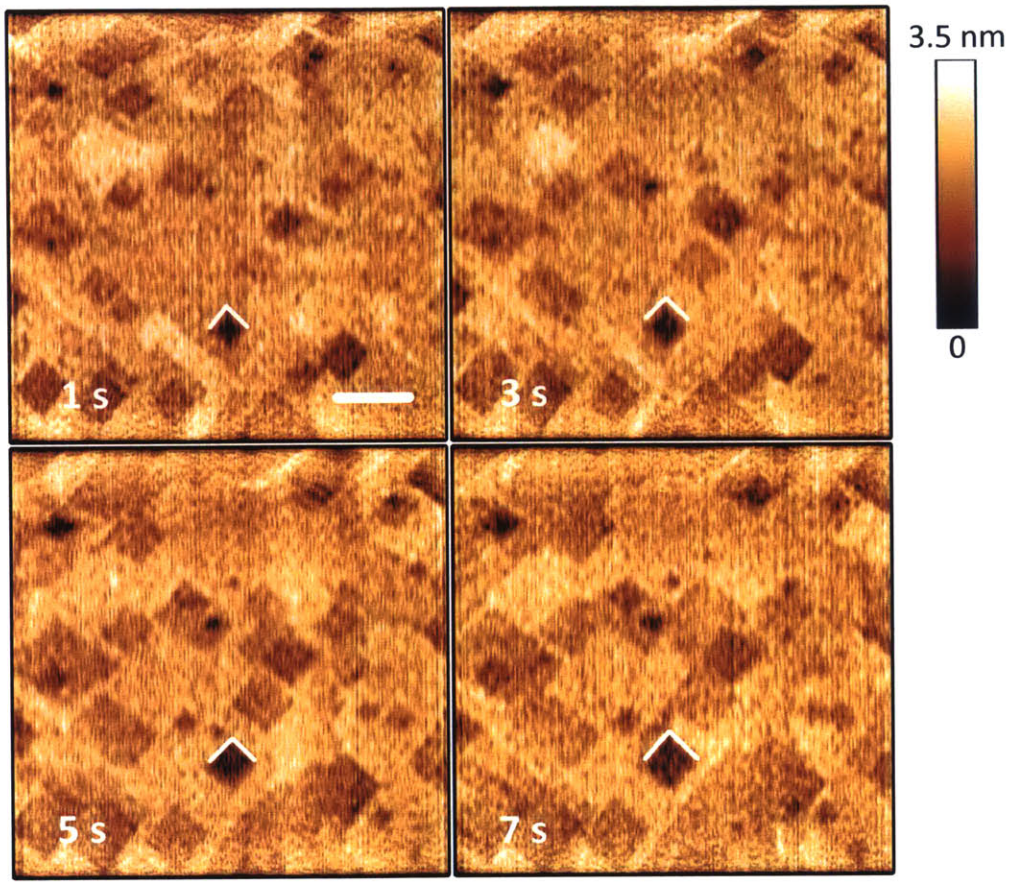

reflects initial formation and deepening of a pit. Figure 7-14 shows the corresponding topography images several minutes after the injection of the acid. This figure shows initiation and deepening of a new pit along the crystal lines.

The high speed imaging capability of the presented AFM is utilized for the study of calcite dissolution kinetics at low pH levels. The large range of the instrument helped us to assemble a more detailed perspective about the state and morphology of the sample over a significantly wider view prior to acid injection. This capability also enabled us to select the sample site of interest for real-time analysis. Other aspects of the device such as large sample stage and optical view to the sample contributed to the ease of use and flexibility of the instrument.

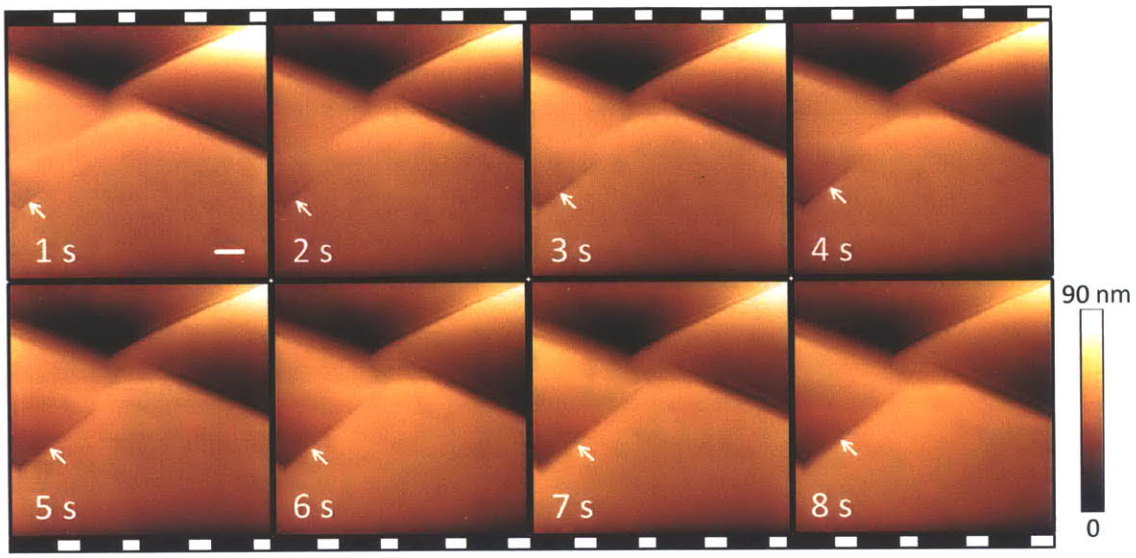

Figure 7-14: Topography images of a deep pit forming along the crystal lines. Imaging resoltuion is set to 256 lines per image and 2048 samples per line. Images are captured at 1 frame per second. The imaging range is 5 μm (scale bar is 500 nm).

7.2.2 Copper Deposition and Striping on Gold

The MIT-AFM setup is utilized to image the electrochemical process of copper deposition on gold at high-speed. A small cantilever (SCL-SensorTech) with a spring constant of 0.5 N/m is used to capture nucleation and growth of copper followed by its stripping on a gold substrate in contact mode at 256 Hz scan rate (1 frame/sec). Image resolution was set to 256 lines per image and 2048 samples per line. The cantilever-holder accommodates a platinum wire as a counter electrode and a copper wire as a reference electrode. The working electrode is a small piece of gold coated silicon wafer. Fresh 0.1mM copper sulfate ($CuSO_4$) solution in 0.1M sulfuric acid (H_2SO_4) is circulated through the inlet/outlet of the liquid cell to keep it fresh throughout the experiment. Figure 7-15 schematically demonstrates the arrangement of the AFM probe and the electrodes. The reference, counter and working electrodes are connected to a VersaStat4 (Stanford Research) potentiostat to control the electrochemical process. The potentiostat applies voltage pulses to the counter/working electrodes to initiate several periods of copper deposition that are followed by stripping. Figure 7-16 shows AFM images of copper deposition for a -150 mV applied

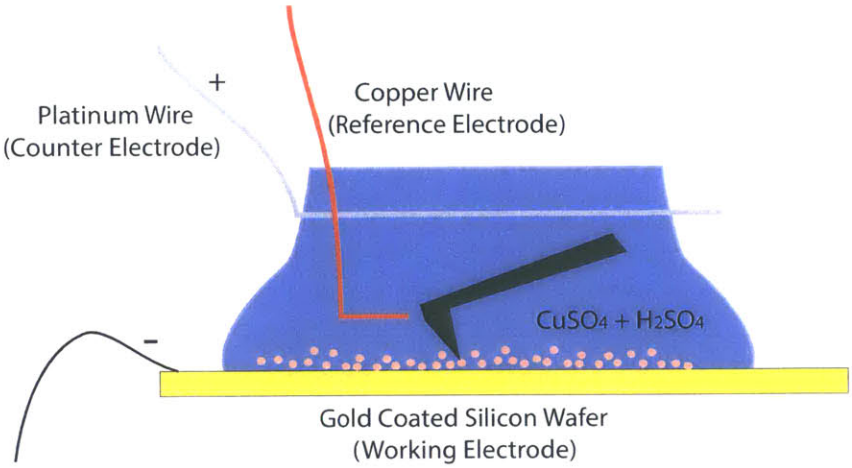

Figure 7-15: Arrangement of the AFM probe the reference, counter and working electrodes in the copper deposition/stripping experiment.

potential. Figures 7-16a and b show 3 μm topography images of the gold substrate at the initial and final states for a 16 sec deposition period. Part (c) of this figure demonstrates time-laps of the deposition process for an 8 second interval. The time-laps includes both the topography (top) and the deflection images (bottom). As observed in these images copper nucleation and growth takes place in an organized fashion on a lattice. The average horizontal distance between the columns of copper nucleate is measured to be 250 nm.

Figure 7-17 shows AFM images of the stripping process when the applied potential is changed to +100 mV. Parts (a) and (b) of the figure show the initial and final topography images for a 22 sec stripping period. Part (c) demonstrates the time-laps topography (top) and deflection (bottom) images of the stripping process for an 8 sec interval. At the start of stripping process, the electrical current measured by the potentiostat changed quickly from -0.5 mA (corresponding to deposition) to +1.6 mA (associated with stripping) reflecting a fast stripping rate. However, the measured current dropped to zero over a relatively short (15 sec) interval and the stripping process stopped. This is evident from the remnants of copper deposit seen in part (b) of the figure taken 22 seconds after the initiation of the stripping process.

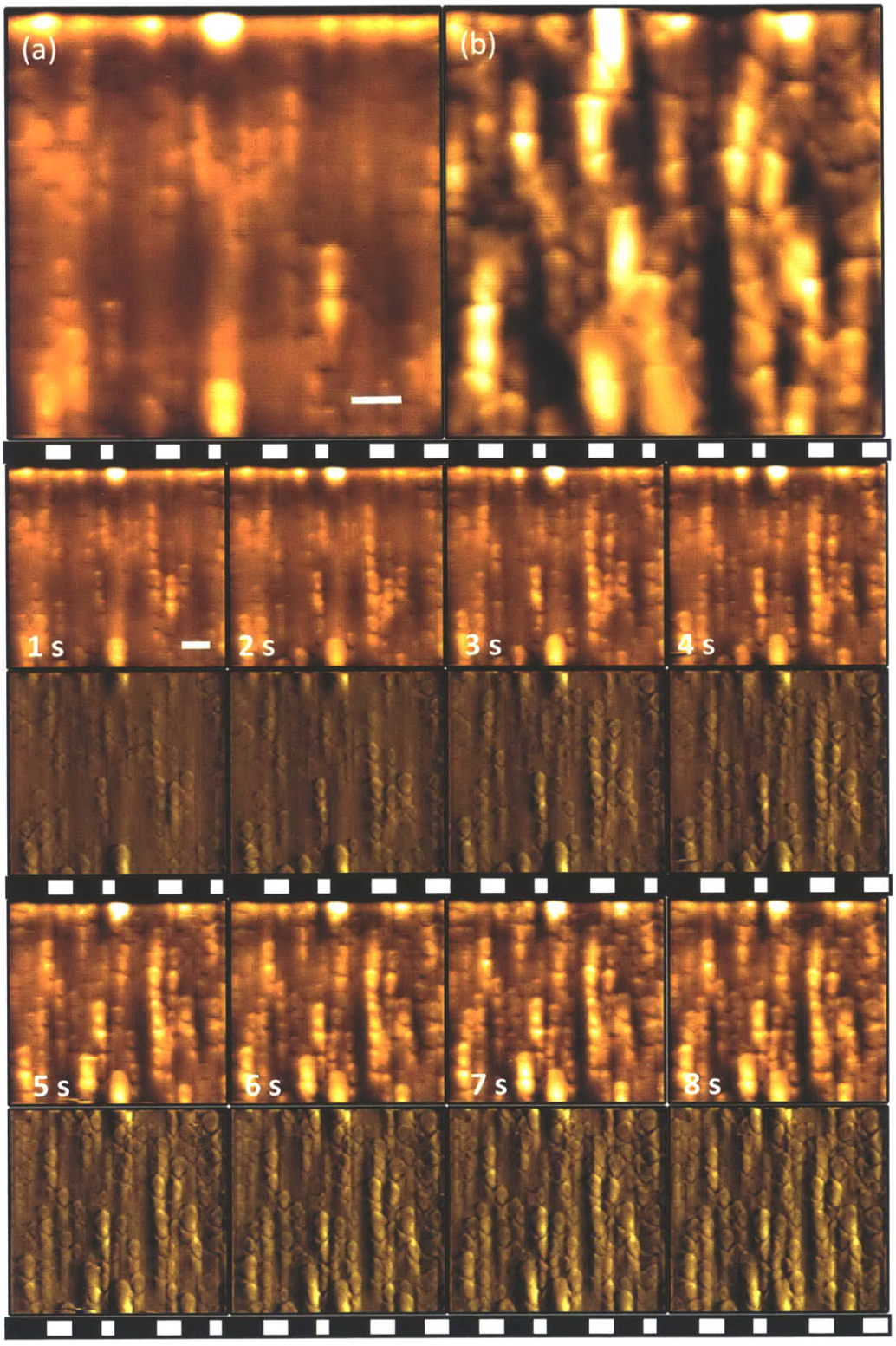

Figure 7-16: A 3 μm topography image of the gold substrate taken at a) the initial stages of deposition, b) after 16 seconds of continuous deposition at -150 mV applied potential, and c) a time-laps of the deposition process for an 8 sec interval including topography (top) and deflection (bottom) images. Scale bars are 300 nm.

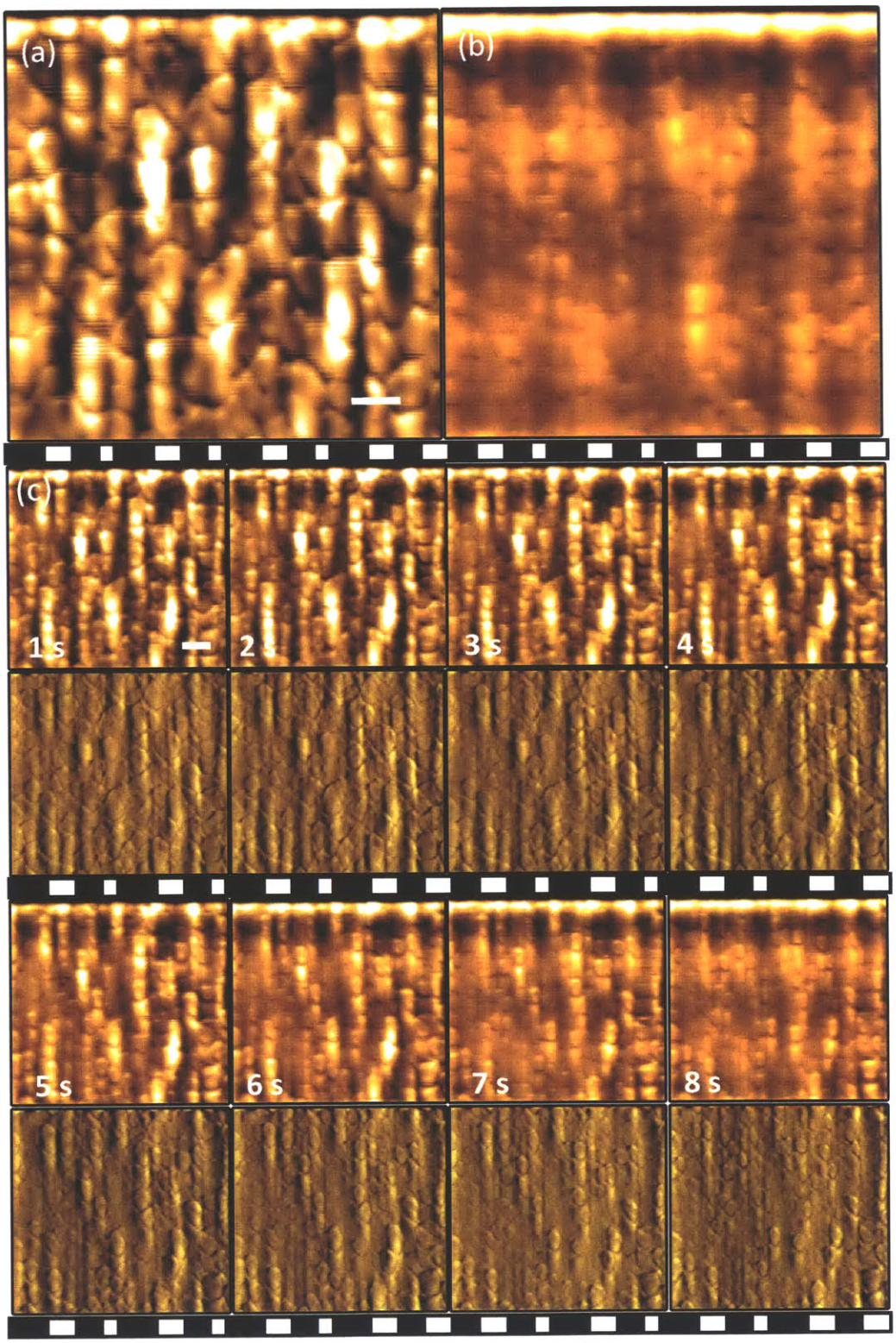

Figure 7-17: A 3 μm topography image of the gold substrate taken at a) the initial stage of stripping, b) after 22 seconds of continuous stripping at 100 mV applied potential, and c) a time-laps of the stripping process for an 8 sec interval including topography (top) and deflection (bottom) images. Scale bars are 300 nm.

7.3 Chapter Summary

In this chapter we build upon the earlier developments of this thesis work to make a novel high-speed and large-range atomic force microscope referred to as MIT-AFM. The components of the AFM including optical beam deflection setup, the photodiode circuitry, piezo drivers, approach mechanism, control hardware, data logging and plotting, cantilever holder/electrochemical cell are described.

The implemented atomic force microscope is then used to study chemical and electrochemical nano-scale processes. Etching of calcite in diluted sulfuric acid is visualized using this AFM. The fast retreat (~254 nm/s) of calcite terraces with an average thickness of 16 nm is captured. The morphology of dissolving layers is observed to be affected by the crystalline structure of calcite even at low pH levels. Furthermore, through the analysis of the time-lapse images the dissolution rate of calcite is found to be 9.98×10^{-9} mol cm^2 s^{-1}. The process of deposition and stripping of copper on gold is also studied in real-time. The nucleation, growth and stripping of copper is visualized.

The MIT-AFM combines high-speed imaging capability with lateral and out-of-plane scan ranges larger than any previously reported in an instrument of this type. Various practical features, such as simultaneous optical view of the sample and probe, a conveniently large sample stage, and compatibility with small cantilevers, further enhance its utility as a research tool. This design enables studies of various dynamic nanoscale processes in air and in aqueous environments.

Chapter 8

Conclusions and Suggestions for Future Work

8.1 Conclusions

This thesis presents the design, control and instrumentation techniques that enable high-speed and large-range atomic force microscopy. A multi-actuated AFM scanner is designed composed of 5 nano-positioners each with certain range and bandwidth characteristics. By combining the actuators of this scanner through properly designed controllers one can simultaneously achieve large-range and high-speed positioning. Although control design for redundantly actuated systems can be potentially very complex the controller design scheme proposed in this thesis is kept in the simplest form possible to enable easy update/fine-tuning of the control parameters and accommodate the variability of AFM dynamics. These controllers are designed directly based on the measured scanner response and without any intermediate modeling. Furthermore, the designed control structure is set auxiliary to a PID unit to benefit from the associated flexibility in an effective fashion. The resulting scanner and control design enabled high-speed positioning of the sample with 100 kHz out-of-plane and 7 kHz lateral positioning bandwidth. In addition, the implemented system maintained large-range scanning capability with 120 μm lateral and 6 μm out-of-plane positioning ranges. These range and speed characteristics, reported here for the first time,

simplify the application of the instrument on various types of samples and enable novel and exciting scientific experiments. The rest of AFM components such as the piezo drivers, photodiode circuitry, optical beam deflection setup, data-logging and plotting platforms are designed and implemented to meet the requirements of the high-speed operation. The resulting atomic force microscope setup also features 1) a 3.5 μm laser spot size compatible with small cantilevers, 2) a conveniently large (15 mm) sealed sample stage suitable for imaging in aqueous solutions and accommodating samples with different sizes, 3) a fully vertical engagement mechanism with 5 mm range accepting relatively thick samples, 4) an optical view to the sample and probe for site selection and laser adjustment, 5) incorporated system ID and control design platform for easy control update, and 6) a data-logging and plotting system with 20 MHz data throughput suitable for high resolution image acquisition at high-speed.

The designed atomic force microscope is tested in the study of nano-scale processes. In one experiment the fast dissolution of calcite crystals in a low ph solution of acid is visualized in realtime. It was shown that the etching process starts when acid attacks the surface to initiate very small pits or expand existing pits and then evolves into layer by layer dissolution of calcite along its crystalline lines. Based on the acquired AFM images and the measured thickness of the dissolving calcite layers the dissolution rate was estimated. In another experiment, the designed AFM was coupled to a potentiostat to study electrochemical processes at the nano-scale in real-time. Deposition and stripping of copper on a gold coated silicon substrate was then visualized.

The following list outlines major contributions of this thesis:

1. A high-speed and large-range atomic force microscope is designed and implemented capable of capturing high-speed images of nano-scale processes in air or in aqueous environments.

2. The control requirements of atomic force microscopes are studied and the conditions that warrant sufficient performance of PID controllers in high-speed imaging applications are investigated.

3. A direct data-based control design scheme is proposed that avoids any intermediate modeling and simplifies controller design/update. These controllers are designed auxiliary to a PID unit and ensure of its effective performance. This strategy helps to accommodate the variability of AFM dynamics.

4. The potentials of redundant actuation schemes in high-speed atomic force microscopy is investigated. A conventional active vibration suppression scheme known as counterbalancing is investigated and the corresponding limitations are demonstrated. The proposed control design scheme is then used to tackle these limitations. The resulting improvements are demonstrated on the dynamics as well as imaging performance of an existing AFM setup with incorporated counterbalancing piezo actuator in the scanner.

5. A general multi-actuation scheme is proposed for high-speed large-range atomic force microscopy. The proposed direct data-based control design strategy is tailored to the control of multi-actuated nano-positioners. The control strategy for the lateral and out-of-plane positioning directions are presented. Multi-actuation for high-speed large-range lateral positioning is proposed here for the first time.

6. The potential of the proposed multi-actuation scheme for the retroactive enhancement of conventional AFMs is demonstrated. A conventional AFM operating on a piezo tube is modified to accommodate an additional short-range and high-speed out-of-plane positioner. It is shown that upon the implementation of the proposed multi-actuation scheme, the out-of-plane tracking bandwidth of the conventional AFM can be improved by an order of magnitude. This improvement is also demonstrated on the imaging performance of the AFM.

7. A multi-actuated scanner composed of 5 nano-positioners is designed and implemented. The dynamic coupling between various components of the positioner is studied. It is shown that the dynamic coupling effect can be minimized upon proper arrangement of scanner components.

8. The Maxwell model parameter estimation is extended to utilize the full hysteresis cycle. In this approach one can reduce the vulnerability of the method to the deviations from the assumed physical model, noises and outliers in the measurements.

9. A nonlinear demodulation scheme based on the Teager Energy Operator is proposed for amplitude detection in tapping mode atomic force microscopy. This approach has a great potential for parallel sensing when utilizing probe arrays for high-speed large-range imaging. The digital and analog versions of this processing scheme are implemented and tested on the imaging performance of an AFM.

8.2 Suggestions for future work

8.2.1 Modular Large-Range and High-Speed AFM

The proposed multi-actuation scheme virtually removes any constraints on the scan range of atomic force microscopes. The arbitrary range of lorentz-force actuators or magnetically levitated positoners when combined with high-speed operation of piezo actuators can lead to very large-range scanners with high-speed positioning capability. This area has not been explored in the past and requires attention. However, in such systems the positioning precision can be rather limited. Incorporation of multiple position sensors with various range and resolution specification in such a multi-component system can significantly improve its performance. One potential research direction is then to effectively fuse the information provided by these sensors to build a high-precision positioning system with large range.

Furthermore, due to the variability of imaging experiments encountered in practice, the design of AFMs need to be relatively modular accommodating different types of imaging arrangements e.g. sample-scan vs probe-scan, or accept an exchange of scanner or optical components depending on the type of measurements. The atomic force microscope designed in this work features a certain level of modularity but needs

to be expanded in this respect. By actuating certain optical components, the designed AFM can potentially accept probe-scan measurements. In this form the AFM can be combined with inverted optical microscopes for the study of biological specimen. An area of great potential in this direction is the study of mechanotransduction properties of biological cells.

8.2.2 High Speed Jumping Mode Imaging

The dynamic limitations of a vibrating AFM probe in tapping mode imaging forms a major obstacle in achieving high-speed imaging performance in tapping mode. As discussed in chapter 6 this is caused by the slow response of the vibrating probe to topography changes on the sample surface. This is specially true for high Q-factor probes operating in air. This limitation however can be avoided if one does not excite the dynamics of the probe. In this approach one can move the whole AFM cantilever chip in the vertical direction to intermittently interact with the sample surface. This imaging mode here referred to as jumping-mode, would be similar to the motion observed in force volume measurements (force spectroscopy) where the probe tip comes in intermittent contact with the sample at different locations. As long as the frequency of the probe motion is well below the resonance frequency of the cantilever, unlike tapping mode imaging, one is not limited by the dynamics of the cantilever.

Another important advantage of this imaging approach is the possibility of coarse sampling when imaging over large ranges. In this form the probe can be set to jump over larger ranges before coming into contact with the sample. This feature enables one to form initial coarse/large views of the sample at high-speed and subsequently focus on the area of interest for high resolution image acquisition.

Furthermore, in this mode the dynamics of interaction between the probe and the sample on every contact can be studied to extract information about the mechanical properties of the sample. Researchers have tried in the past to utilize phase information of the tapping signal and estimate mechanical properties. However, the complex coupling between the topography variations, damping and elasticity properties of the

sample makes interpretation of the phase measurements very difficult. High-speed jumping mode imaging can potentially avoid these ambiguities and provide reliable estimates of the sample material properties. For this purpose non-linear parameter estimation techniques should be designed and coupled to the high-speed jumping mode imaging.

8.2.3 TEO for FM-AFM

In this thesis application of Teager Energy Operator in AM-AFM imaging is explored. TEO is capable of extracting frequency modulations as well [78, 11, 68] and hence is potentially useful in FM-AFM. However, this requires a variant implementations of TEO with simultaneous amplitude and frequency demodulations e.g. through energy separation algorithm [76]. This capability of TEO can be further explored.

8.2.4 Flexure-Based Multi-Actuated Nano-Positioner Design

The multi-actuated nano-positioner designed and implemented in this thesis is the first study of its kind. This is an exciting direction with great potential and can be further explored. Multi-actuated flexure based scanners can be designed to minimize the dynamic coupling between various actuators. Incorporation of sensors and fusion of the sensor measurements for improved positioning accuracy are other aspects of this methodology that are worth further investigation.

Appendix A

Fixed-Point Implementation of IIR Filters on FPGA Targets

The control techniques proposed in this thesis are all implemented on FPGA platforms. The flexibility of FPGAs makes them specially suitable for AFM applications where update of the control parameters are needed frequently. As is the case in this work, the controllers are often designed in floating point environments. When implemented on hardware however, the mathematical operations involved in digital filtering commonly take place in fixed point format. Hence, one needs to take proper measures to make sure that upon fixed point implementation the behavior of the given IIR filter does not change. In this appendix some useful concepts about the implementation of digital filters in a fixed point setting are discussed. It came to our attention that this information cannot be found in a unified learning package making the implementation time unnecessarily prolonged and the process a nuisance for the novice. As such, this appendix can also be used as a tutorial to speed up the learning course and may be a useful resource for research labs and engineers in the field.

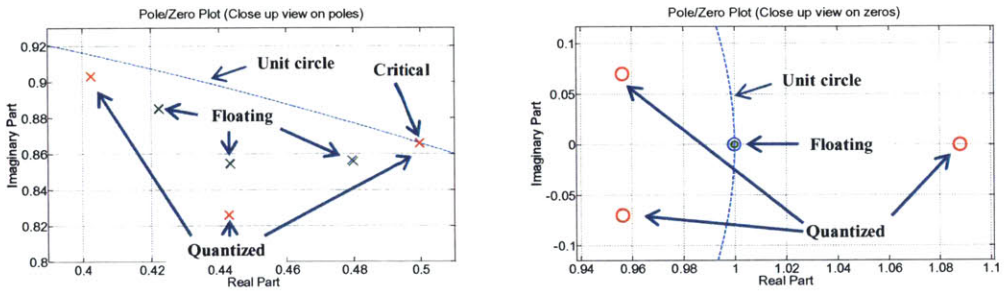

(a) (b)

Figure A-1: a) Poles with positive imaginary part in close up view, and b) zeros with positive real part for a 6th order Butterworth filter with a passband of 8.4 9 kHz, designed for a sampling rate of 50 kHz, Blue: for original floating point transfer function, Red: for quantized transfer function, Green: for second order decomposed and then quantized transfer functions.

A.1 Fixed Point Implementation of IIR Filters

An IIR filter can be presented in transfer function form as:

$$F(z) = \frac{b_0 + b_1 z^{-1} + \cdots + b_m z^{-m}}{1 - a_1 z^{-1} - \cdots - a_n z^{-n}} \tag{A.1}$$

where $b_{0\ldots m}$ and $a_{1\ldots n}$ denote the numerator and denominator coefficients respectively, and z^{-n} is a delay of order n. The concepts and definitions such as transfer function, delay, etc can be found in different sources e.g. [89]. The process of preparation of a given floating point discrete time transfer function (TF) for fixed point implementation includes the following steps:

A. Decomposition of the TF into second order sections

B. Selection of appropriate structure for each second order section (SOS)

C. Scaling of the individual second order sections

D. Sequential ordering of the scaled second order sections

E. Overall gain adjustment

These steps are discussed in the following.

A. Decomposition of the TF into second order sections

For fixed point implementation of IIR filters, the filter coefficients need to be quan-

tized. As a result, each IIR filter coefficient deviates slightly from its original value upon quantization. The cumulative effect of such deviations may be translated to significant behavioral changes of the filter i.e. changes in the pole-zero locations. This can be illustrated via an example. The effect of quantization on the location of poles and zeros is observed on a 6^{th} order Butterworth bandpass filter with a passband of 8.4-9 kHz, designed for a sampling rate of 50 kHz in floating point (using the filter design and analysis toolbox of MATLAB [79]). The coefficients of this filter are quantized into 12 bit numbers. The poles (with positive imaginary parts) and zeros (with positive real parts) for both the original floating (blue) and the quantized (red) filter are shown in complex plane in Figs. A-1(a) and (b), respectively. From these figures, significant shift in pole and zero locations is evident. In fact one pair of the complex conjugate poles are shifted very close to the unit circle (denoted by *Critical*) bringing the filter to the verge of instability. This effect is much less significant for lower order transfer functions [89, 62]. As such, decomposition of the filter to a cascade of low order second order sections (SOS) can be helpful in desensitizing the individual sections to coefficient quantization. The poles and zeros of the quantized, second order decomposed filter are superimposed on Figs. A-1(a) and 1(b) (green). The poles and zeros of the original floating point filter and the quantized/SOS-decomposed version can hardly be distinguished.

The main question in the SOS decomposition step is on how to pair the poles and zeros of the filter to form the SOS filter units. A heuristic approach is to pair each pole with the closest corresponding zero starting with more critical poles. The logic is to avoid considerable peaking of each section because a large peak in a formed second order section can lead to saturation. The effect of saturation will be evaluated in detail later. The steps for decomposing a filter into second order sections are summarized below:

A.1. Find the zeros and poles

The roots of the numerator and denominator form the set of zeros and poles of the given transfer function respectively.

A.2. Pair the poles

The next step is to form pairs of poles. Complex poles are already in pairs. Real poles can be paired based on their distance to the unit circle. Each real pole is paired with another real pole that is next closest to the unit circle. This approach aims to group real poles that similarly influence the frequency response. This process is started with the real-pole closest to the unit circle.

A.3. Pair the zeros

Similar to the previous step zeros are paired. Complex zeros are already in pairs. Each real zero is paired with another real zero that is next closest to the unit circle.

A.4 Find the distance of individual pole pairs to the unit circle

As the objective in pole/zero matching is to avoid peaking of a section, one needs to start the pole/zero matching process with the poles that are more critical i.e. closer to the unit circle. These poles lead to larger peaks and hence need to be restrained by the nearby zeros. To sort the pole pairs according to their importance, one needs to calculate the distance of each pole pair to the unit circle. The distance of a pole-pair to the unit-circle is defined here as the geometric mean of the distances of the two poles to the unit circle, i.e. for the pair (p_1, p_2), the distance D to the unit circle is defined as:

$$D_{PU} = \sqrt{(1 - |p_1|)(1 - |p_2|)}$$

The above equation represents a generalization of the distance of a single complex pole to the unit circle. For an odd order transfer function where a single real pole exists, the distance to unit circle for that pole is defined as:

$$D_{PU} = |(1 - |p_1|)|$$

A.5. Match pole-pairs with zero-pairs to form individual sections

To form the second order sections we need to match each pair of poles with the closest

pair of zeros. The distance between a pair of poles, (p_1, p_2), and a pair of zeros, (z_1, z_2) is defined as:

$$D_{PZ} = \sqrt{|p_1 - z_1||p_2 - z_2|}$$

where (p_1, p_2) and (z_1, z_2) are sorted such that z_1 is closest to p_1 i.e.

$$|p_1 - z_1| = min(|p_1 - z_1|, |p_2 - z_1|, |p_1 - z_2|, |p_2 - z_2|)$$

When the distance of a single real pole, p, to a single real zero, z, is considered, one can assume $p_1 = p_2 = p$ and $z_1 = z_2 = z$. When the distance of a single real zero, z, with a pair of poles, is considered, one can assume, $z_1 = z$ and $z_2 = 0$. A second order section can then be formed using the matched poles and zeros:

$$G_{sos} = \frac{(z - z_1)(z - z_2)}{(z - p_1)(z - p_2)} \tag{A.2}$$

B. Selection of appropriate structure for each second order section Following the decomposition of the given transfer function to second order sections (SOS) we need to assign an IIR structure to each section. The main IIR filter structures namely Direct Form I (DFI), Direct Form II (DFII), Transposed Direct Form I (TDFI) and Transposed Direct Form II (TDFII) are explained in detail in [89]. Each one of these structures provides a different pathway between the input and output of the SOS and consequently reflects a different behavior for quantization noise propagation and saturation. As such, selection of the proper structure for the implementation of individual second order IIR sections is guided by their saturation and quantization noise propagation performance. These two characteristics are incorporated into a selection index which directs the structure selection. In the following we discuss what we mean by the quantization noise propagation, and the saturation performance. We also explain how we are going to use these characteristics to select the appropriate structure for a given second order section filter.

B.1. Saturation Performance: Calculation of the scaling values for candidate

structures, DFI, DFII, TDFI and TDFII

To avoid saturation at various nodes of an IIR filter the SOS should be divided (scaled down) by the proper scaling value. Depending on the selected structure the required scaling constant is different. In general a smaller scaling factor is preferred as dividing the SOS by a large scaling value may adversely affect the signal to quantization noise ratio (SQNR). This point will be explained in more detail later. As such, the required scaling value for each candidate structure will be used as one criterion for structure selection. Here we will show the process of calculating the scaling value associated with each candidate structure. The actual scaling will be done later when an appropriate structure is selected for a given second order section. For saturation analysis we make the following assumptions:

1) We assume that in the implemented design, for an L bits quantized input signal to the filter, and L bits quantized filter coefficients, the flexibility of FPGA resources allow for the allocation of $2L$ bits to certain multipliers, adders and memory units. As explained later this makes sure that saturation can only happen at the summation nodes. As will be discussed in the next subsection this choice also significantly reduces the quantization noise variance.

2) We assume that the two's complement arithmetic (with natural overflow) is used at the summation nodes. In this case, at certain points where partial addition takes place, saturation is not problematic as long as the overall result is not saturated. To clarify this point, consider summation of three signed numbers with 3 bits word length and 1 bit integer length (Fig. A-2). The values can be any of [-1 -0.75 -0.5 ... 0.75] corresponding to [100 101 110 ... 011]. Now consider the summation of three values 0.5 (010), 0.75 (011) and -0.5 (110): 0.5 (010) + 0.75 (011) - 0.5 (110) = 0.75 (011). As shown in Fig. A-2 both the summations, 0.5 (010) + 0.75 (011) $\rightarrow$ -0.75 (101) and, -0.75 (101) - 0.5 (010) $\rightarrow$ 0.75 (011), are the results of natural overflow. However, the final result, 0.75, is the correct result of the summation. In other words, although saturation is happening in the intermediate summations, the final result is not saturated.

Given the above two points, in the following we look into saturation problem in

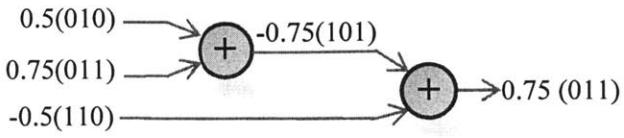

Figure A-2: Two's complement arithmetic with natural overflow is not vulnerable to inter-stage saturation, as long as the overall result falls into the available range.

DFI, DFII, TDFI and TDFII implementations of IIR filters.

- **Saturation analysis in DFII and TDFI**

Saturation analysis for DFII and TDFI structures are very similar. Consider the DFII filter structure of Fig. A-3(a). As one can see, nodes 2, 5, 7, 8 and 9 do not involve addition and hence saturation cannot take place at these nodes. Nodes 4 and 6 involve partial addition and hence with saturation behavior of the filter set to natural over flow, saturation at these nodes is not problematic (Fig. A-2). A similar argument applies to the TDFI structure of Fig. A-3(b). As such, for both structures saturation analysis should be focused on nodes 1 and 3. For saturation analysis we need the transfer functions from the input of the filter to the outputs of nodes 1 and 3. The transfer function from the input to the output of node 3 is the transfer function associated with the second order filter:

$$F_{\text{DFII/TDFI}}(z) = \frac{b_0 + b_1 z^{-1} + b_2 z^{-2}}{1 - a_1 z^{-1} - a_2 z^{-2}} \tag{A.3}$$

The transfer function from the input to the output of node 1 is associated only with the poles of the second order section:

$$F'_{\text{DFII/TDFI}}(z) = \frac{1}{1 - a_1 z^{-1} - a_2 z^{-2}} \tag{A.4}$$

These two transfer functions can be used for saturation analysis and hereafter are referred to as the saturation transfer functions. The filter coefficients, $[b_0, b_1, b_2]$ and $[a_1, a_2]$ are the numerator and denominator coefficients associated with the pole/zero

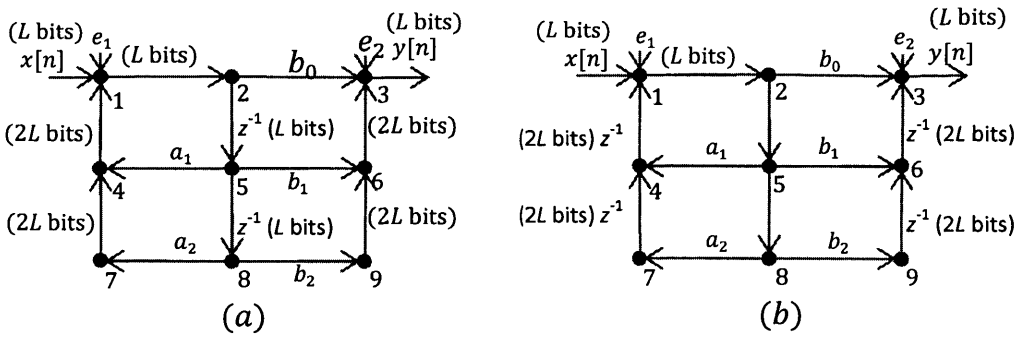

Figure A-3: Signal flow diagram of a second order filter structure in a) DFII and, b) TDFI, form. The filter coefficients and the input signal are quantized to L bits while $2L$ bits are allocated to certain paths.

matched second order sections obtained from Eq. (A.2) i.e.:

$$G(z) = \frac{B(z)}{A(z)} = \frac{b_0 + b_1 z^{-1} + b_2 z^{-2}}{1 - a_1 z^{-1} - a_2 z^{-2}} = \frac{(Z - Z_n)(Z - Z_m)}{(Z - P_k)(Z - P_l)}$$

where $[Z_n, Z_m], [P_k, P_l]$ are the pairs of poles and zeros. A similar approach can be applied to TDFII and DFI filter structures shown in Fig. A-4. Nodes 1, 3, 4, 6, 7, and 9 for both structures, do not include addition and hence are not of concern for saturation. Addition in nodes 5 and 8 are partial and can accommodate saturation without any harm to the filtering performance. The only remaining node for saturation analysis is node 2 or the output of the given SOS. Hence, the saturation transfer function in this case is the transfer function associated with the whole second order section:

$$F_{\text{TDFII/DFI}}(z) = \frac{b_0 + b_1 z^{-1} + b_2 z^{-2}}{1 - a_1 z^{-1} - a_2 z^{-2}} \tag{A.5}$$

As before, the coefficients of this transfer function are obtained by matching pairs of poles and zeros.

- **L^∞ norm analysis of saturation for scale calculation**

There are a few methods with various levels of conservatism [89] that suggest proper scaling to avoid saturation. However, a too conservative scaling strategy may de-

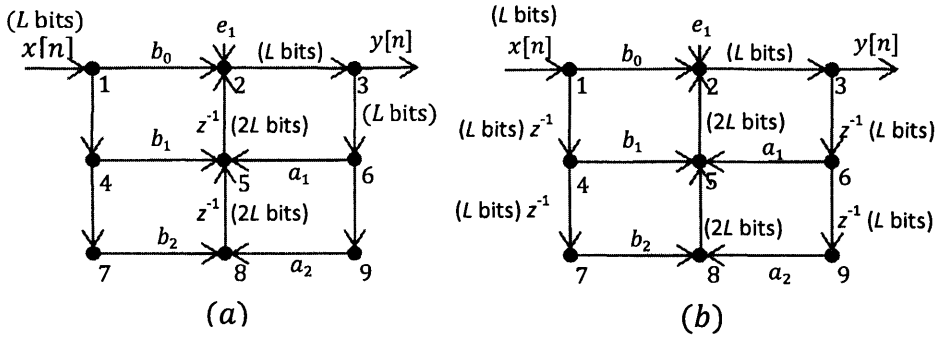

Figure A-4: Signal flow diagram of a second order filter structure in a) TDFII and, b) DFI, form. The filter coefficients and the input/output signals are quantized to L bits while $2L$ bits are allocated to certain paths.

teriorate the signal to quantization noise ratio (SQNR) at the output of the filter. Here we recommend a middling approach on the reliability and conservatism which is based on the L^∞ norm of the saturation transfer functions. The L^∞ norm of a given transfer function corresponds to the peak magnitude of the frequency response. For DFII or TDFI the saturation transfer functions are given by Eqs. (A.3) and (A.4). The scaling factor in this case is selected as the larger of the two L^∞ norms:

$$\mu_{\text{DFII/TDFI}} = max(||\frac{b_0 + b_1 z^{-1} + b_2 z^{-2}}{1 - a_1 z^{-1} - a_2 z^{-2}}||_\infty, ||\frac{1}{1 - a_1 z^{-1} - a_2 z^{-2}}||_\infty) \tag{A.6}$$

where $\mu_{\text{DFII/TDFI}}$ is the scaling factor for DFII and TDFI structures and $||\ ||_\infty$ denotes infinite norm. For TDFII and DFI structures the saturation transfer function is the SOS transfer function (Eq. (A.5)). As such, in this case we have:

$$\mu_{\text{TDFII/DFI}} = ||\frac{b_0 + b_1 z^{-1} + b_2 z^{-2}}{1 - a_1 z^{-1} - a_2 z^{-2}}||_\infty \tag{A.7}$$

B.2. Quantization noise performance: Calculation of quantization Noise Variance for candidate structures, DFI, DFII, TDFI and TDFII

Following the calculation of scaling values, we need to evaluate the quantization noise variance for each section. A combination of the quantization noise variances and the scaling values as explained later will help us select the appropriate IIR structure for a given second order section. To understand the quantization noise phenomenon and

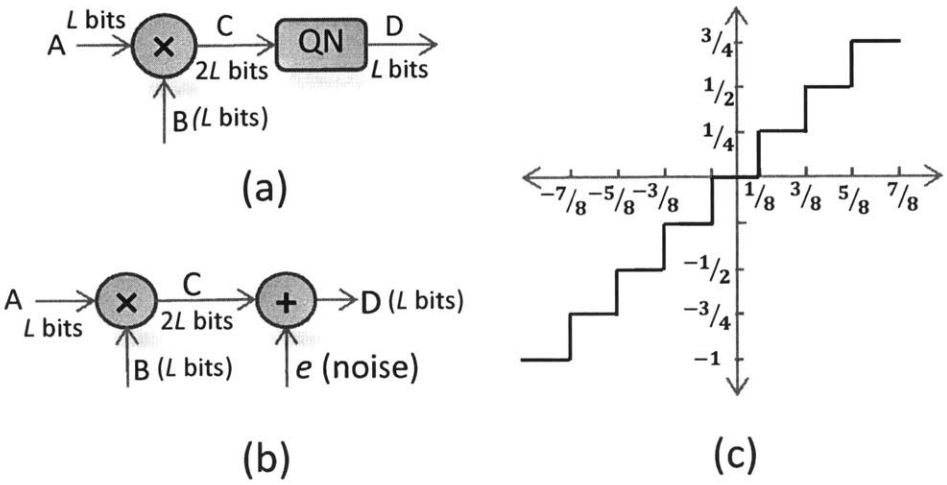

Figure A-5: a) Multiplication of two fixed point L-bits numbers with cascaded quantization (QN) to represent the result in L-bits instead of the required $2L$ bits format, b) additive noise model of the quantization effect, associated with part (a),and c) Quantization for L=3 bits [89].

its propagation, consider a simple example, where two fixed point L bits numbers, A and B, are multiplied (Fig. A-5(a)). Assume that the multiplicands, A and B, and the output result, D, in this simple multiplication structure (Fig. A-5(a)) are described in L bit fixed point format. However, the result of multiplication of two L-bits numbers contains a maximum of $2L$ bits. As such, we need an intermediate step to round the result down to the available L-bits format. To simplify the analysis we can approximately represent the effect of rounding as an additive noise (Fig.A-5(a)) [89]. The rounding effect for a signed number with $L = 3$ bits is illustrated schematically in Fig A-5(c).

For round-off it can be roughly assumed that the equivalent additive noise is white ($E\{e[n]e[m]\} = 0$, for $m \neq n$, where E denotes mathematical expectation) and has a uniform distribution over the quantization range $[\frac{-\Delta}{2}, \frac{\Delta}{2}]$ (with zero mean). For L bits fractional number over $[-1, 1]$, the length of the quantization grid is $\Delta = 2^{-(L-1)}$. One can show that the variance associated with such a noise is $\sigma^2 = \frac{\Delta^2}{12}$ [89, 49]. We base the analysis of round-off noise performance on the variance of the output noise. This is elaborated in the following subsections for various implementation structures. For such analysis we focus on second order IIR filters as a second order section (SOS)

filter constitutes the building block of the hardware implementation of an IIR filter with any order.

- **Propagation of Round-off noises in DFII and TDFI**

Figures A-6(a) and A-6(b) illustrate signal flow diagrams for second order DFII and TDFI filter structures respectively with the round-off effect represented as additive noises. As one can see from Figures A-6(c) and A-6(d), for both DFII and TDFI structures, such noises can be combined into two additive noises at the input and output of the filter. For both DFII and TDFI structures, the equivalent round-off noise at the input of the filter, e_I, is filtered by the whole second order transfer function. The additive output noise, e_o, is not affected by the filter. For the variances of e_I and e_o, and the variance of the resulting noise at the output of the filter we can write:

$$\sigma_I^2 = \frac{\Delta^2}{6}, \sigma_o^2 = \frac{\Delta^2}{4}$$

and,

$$\sigma^2_{f,\text{DFII/TDFI}} = \frac{\Delta^2}{6}[1/2 \int_{-\pi}^{\pi} |\frac{B'e^{j\omega}}{A(e^{j\omega})}|^2 d\omega] + \frac{\Delta^2}{4} \tag{A.8}$$

where σ_I^2 and σ_o^2 are the variances of the equivalent combined noises, e_I and e_o (Figs. A-6(c), A-6(d)), $\sigma^2_{f,DFII/TDFI}$ is the quantization noise variance observed at the output of the filter for DFII and TDFI structures, $\Delta^2 = 2^{-2(L-1)}$, $\frac{B'(z)}{A(z)}$ is the scaled transfer function where $B'(z) = \frac{B(z)}{\mu_{\text{STR}}}$ and $\frac{\frac{B(e^{j\omega})}{\mu_{\text{STR}}}}{A(e^{j\omega})} = \frac{B'(e^{j\omega})}{A(e^{j\omega})}$. The scaling factor μ_{STR} is calculated based on the candidate structures (STR can be any of DFII, TDFI) and according to either of the Eqs. (A.6) or (A.7).

- **Propagation of Round-off noises in TDFII and DFI**

Similar analysis can be done on the Transposed Direct Form II (TDFII) and the Direct Form I (DFI) structures. The round-off noise effects for both structures are shown in Figs. A-7(a) and A-7(b). The combined effect of the 5 round-off noise sources can be represented with a single additive noise of variance $\frac{5\Delta^2}{12}$, as shown in

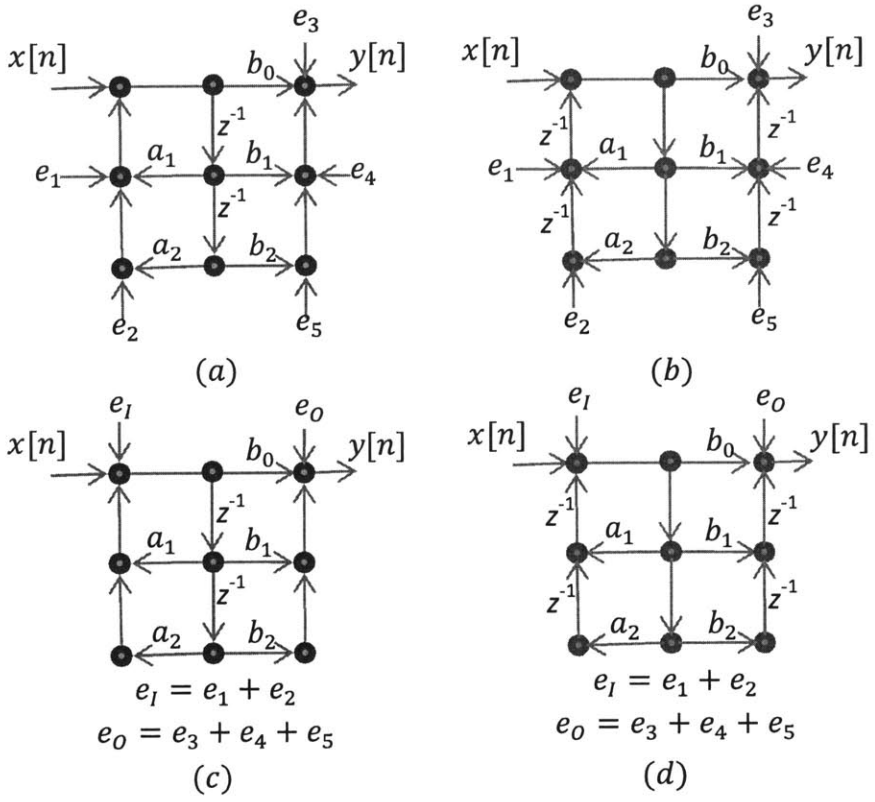

Figure A-6: Additive noise model of quantization effect in a) DFII, and b) TDFI format with L-bits fixed point processing. e_1, e_2, e_3, e_4 and e_5 are independent and identically distributed, parts c) and d) respectively show the equivalents of parts (a), and (b) with the noises combined.

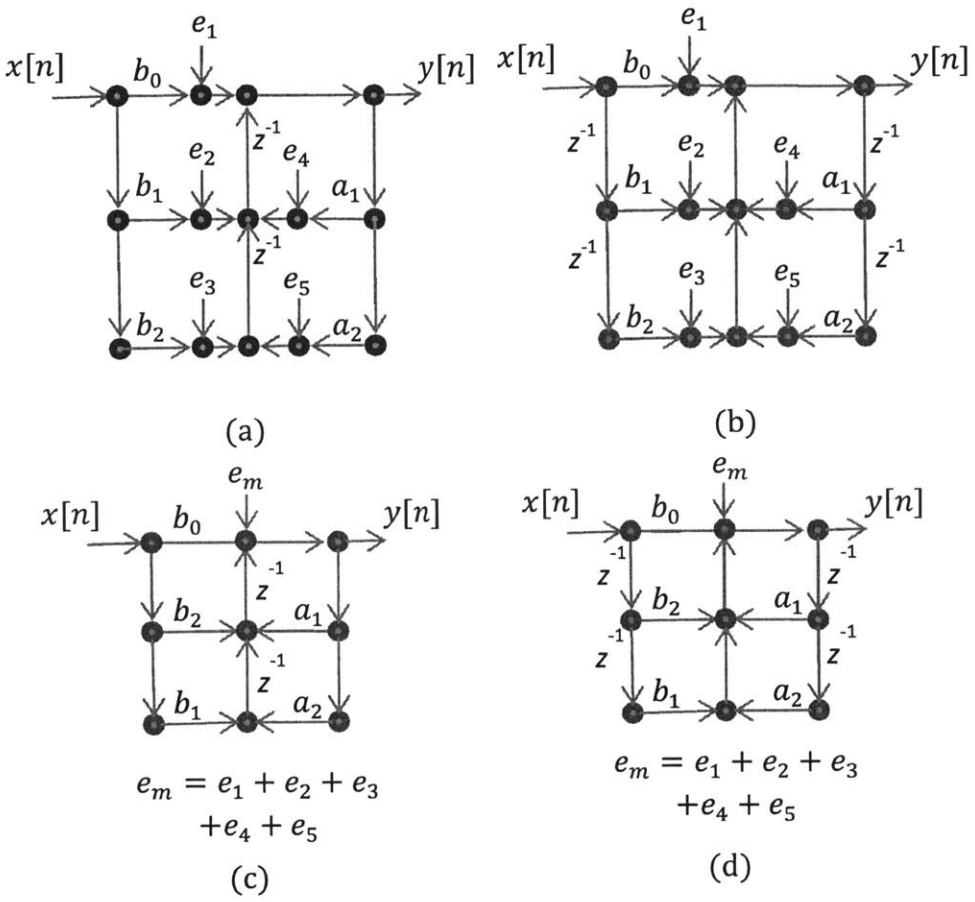

Figure A-7: Quantization noise model for a) TDFII and b) DFI structure of a second order filter. Parts c) , and d) respectively show equivalents of parts (a) and (b) with the quantization noises combined as a single noise source.

Figs. A-7(c) and A-7(d). As one can infer from both figures, the equivalent noise is processed only through the denominator (poles) of the transfer function. As such, for the variance of the round-off noise at the output of the filter we can write:

$$\sigma^2_{f,\text{TDFII/DFI}} = \frac{5\Delta^2}{12}[\frac{1}{2}\int_{-\pi}^{\pi}\frac{1}{|A(e^{j\omega})|^2}d\omega] \tag{A.9}$$

where $\frac{1}{A(e^{j\omega})}$ is the frequency response associated with the poles of the second order section. According to these results (Eqs. (A.9) and (A.8)), selection of the proper structure from the perspective of round-off noise propagation is dependent on the specific filter transfer function under consideration. In the above analysis we did not

take into account the $2L$ bits selection for certain paths proposed earlier (see Figs. A-3 and A-4). Consider the DFII and TDFI structures given in Figs. A-3(a) and (b). As shown in this figure, by selecting $2L$ bit for certain paths (in Fig. A-3 the bit length allocated to each path is denoted in brackets) the output propagation noise variance can be reduced significantly, leading to a variance of

$$\sigma^2_{f,\text{DFII/TDFI}} = \frac{\Delta^2}{12}[\frac{1}{2\pi}\int_{-\pi}^{\pi}|\frac{B'(e^{j\omega})}{A(e^{j\omega})}|^2 d\omega + 1] \tag{A.10}$$

, approximately half the variance given by Eq. (A.8). Similarly for TDFII and DFI, when taking into account the $2L$ bits selection for certain paths, round-off noise variance is reduced to a fifth of the original value and can be written as:

$$\sigma^2_{f,\text{TDFII/DFI}} = \frac{\Delta^2}{12}[\frac{1}{2\pi}\int_{-\pi}^{\pi}\frac{1}{|A(e^{j\omega})|^2} d\omega] \tag{A.11}$$

As such, the proposed bit length selection has important benefits on both saturation and noise performance of a given second order section.

The quantity of interest for IIR structure selection is the signal to quantization noise ratio (SQNR). For TDFII and DFI structures the round-off noise variance on the output of the filter is solely dependent on the poles of the filter and Δ. Hence, for a smaller scaling value (larger input signal), the SQNR is increased. As such, both the scaling strategy and the propagated quantization noise variance affect the output signal to quantization noise ratio. To select the proper filter structure one needs to take into account both the quantization noise variance corresponding to a given filter structure and also the applied scaling value. This point is further elaborated in the following.

B.3. Calculation of the selection index

Here we combine into a selection index, the saturation and the quantization noise performances of a given second order section for the structures discussed earlier. This index can guide the structure selection. The equations derived for the calculation of the scaling factor and the quantization noise variance for various structures, are summarized in Table A.1. For TDFII and DFI structures the quantization noise variance

Table A.1: Summary of the noise and saturation analysis results for DFI, TDFII, DFII and TDFI structures, $||\ ||_\infty$ denotes infinite norm.

Structure	Noise Variance	Scaling Factor to Avoid Saturation
DFI, TDFII	$\sigma^2_{f,\text{TDFII/DFI}} = \frac{\Delta^2}{12}[\frac{1}{2\pi}\int_{-\pi}^{\pi}\frac{1}{\lvert A(e^{j\omega})\rvert^2}d\omega]$	$\mu_{\text{TDFII/DFI}} = \lvert\lvert\frac{b_0+b_1z^{-1}+b_2z^{-2}}{1-a_1z^{-1}-a_2z^{-2}}\rvert\rvert_\infty$
TDFI, DFII	$\sigma^2_{f,\text{DFII/TDFI}} = \frac{\Delta^2}{12}[\frac{1}{2\pi}\int_{-\pi}^{\pi}\lvert\frac{B'(e^{j\omega})}{A(e^{j\omega})}\rvert^2 d\omega + 1]$	$\mu_{\text{DFII/TDFI}} = max(\lvert\lvert\frac{b_0+b_1z^{-1}+b_2z^{-2}}{1-a_1z^{-1}-a_2z^{-2}}\rvert\rvert_\infty, \lvert\lvert\frac{1}{1-a_1z^{-1}-a_2z^{-2}}\rvert\rvert_\infty)$

given by Eq. (A.11) is independent of the scaling factor. As such, upon scaling (dividing) with a factor of, $\mu_{\text{TDFII/DFI}}$, the signal to quantization noise ratio on the output of the same section will be reduced by a factor of $\mu^2_{\text{TDFII/DFI}}$. However, for DFII and TDFI structures (Eq. (A.10)), as the scaling value is applied to the numerator, both noise variance and signal power are reduced by the same factor, leaving the output signal to quantization noise ratio intact. With the above explanation and assuming that the described scaling strategy can successfully prevent saturation, a measure of comparison between the candidate structures is the following index, hereafter referred to as the selection index:

$$r_{\text{STR}} = \mu^2_{\text{STR}}\sigma^2_{f,\text{STR}}$$

where STR can be any of the structures DFI, DFII, TDFI, and TDFII. A structure with a smaller value of r is preferred. This index encapsulates the effects of the quantization noise variance and scaling on the overall SQNR of the section output.

B.4. Assignment of preferred structure to sections

As summarized in Table A.1 the equations used for the calculation of the quantization noise variance or the scaling factor are similar for the structures DFI and TDFII, also for DFII and TDFI. Bearing this point in mind and knowing that TDFII and DFII structures have reduced memory requirements, we use the selection index value to assign one of the DFII or TDFII structures to each section.

C. Scaling of the individual second order sections

Following the structure selection, the numerator of each section is divided by the scaling factor, μ_{STR} associated with the selected structure i.e. "STR = Selected Structure". The scaling value is already calculated based on the equations listed in Table A.1 as part of the structure selection process. We can then write:

$$G'(z) = \frac{G(z)}{\mu_{\text{STR}}} = \frac{\frac{b_0}{\mu_{\text{STR}}} + \frac{b_1}{\mu_{\text{STR}}} z^{-1} + \frac{b_2}{\mu_{\text{STR}}} z^{-2}}{1 - a_1 z^{-1} - a_2 z^{-2}}$$

where $G(z)$ is the transfer function associated with the second order section, and $G'(z)$ is the scaled version of $G(z)$.

D. Sequential ordering of the scaled second order sections

The second order sections that make up the original filter must be properly ordered. This ordering affects the intensity of the overall quantization noise observed at the output of the filter. For a filter, converted into M second order sections, there are $M!$ possibilities (permutations) for the arrangement of these sections. The logic behind the ordering procedure is described in what follows:

1) As explained earlier each second order section contributes to the intensity of round off noises. The noises associated with all the second order sections are filtered by the last section. As a result, it is reasonable to have sections with largest L^2 norm placed at the very beginning of the queue. With this logic ordering is done in a decreasing order of L^2 norm.

2) For a given second order section with a large scaling value, μ_{STR}, at the beginning of the queue, the signal amplitude is significantly reduced at the very early stages of filtering. This leads to lower overall signal to quantization noise ratio (SQNR). This point of view suggests arranging the second order sections in an increasing order of scaling value, μ_{STR}.

To incorporate both of the above points of view, an index referred to as the peakiness can be used to guide the ordering of second order sections. Peakiness index

is the square of the ratio of the scaling factor, to the L^2 norm of individual section transfer functions:

$$\gamma = \frac{\mu_{\text{STR}}^2}{||G'||_2^2} = \frac{\mu_{\text{STR}}^4}{||G||_2^2}$$

where G' and G are respectively the scaled and the original transfer functions associated with the given second order section. The sections are arranged in an increasing order of peakiness [49].

E. Overall Gain adjustment

The dynamics as well as the gain of the resulting fixed point implemented filter should match those of the original floating point filter. However, following the second order decomposition, and scaling, although all the poles and zeros of the resulting filter are the same as those of the original filter (similar dynamic behavior), the information regarding the gain (scaling) of the filter is lost. To compensate for this effect a final scaling stage with a factor of μ_f follows the last second order section. This final scaling aims to match the gain of the resulting filter to that of the original filter. Consider a filter decomposed to M second order sections. The poles, zeros and the section scaling values associated with each section are denoted as $p_{m1}, p_{m2}, z_{m1}, z_{m2}, \mu_{(m,\text{STR})}$ where m is the section number. The resulting decomposed and scaled sections followed by the final scaling stage form the overall filter given below:

$$\frac{(Z-z_{11})(Z-z_{12})}{\mu_{(1,\text{STR})}(Z-p_{11})(Z-p_{12})} \times \cdots \times \frac{(Z-z_{M1})(Z-z_{M1})}{\mu_{(M,\text{STR})}(Z-p_{M1})(Z-p_{M1})}\mu_f$$

where M is the total number of sections. We denote the gain of the original transfer function extracted upon second order decomposition as k. Then we can write:

$$\begin{aligned}\frac{(Z-z_{11})(Z-z_{12})}{\mu_{(1,\text{STR})}(Z-p_{11})(Z-p_{12})} \times \cdots \times \frac{(Z-z_{M1})(Z-z_{M1})}{\mu_{(M,\text{STR})}(Z-p_{M1})(Z-p_{M1})}\mu_f \\ = \frac{(Z-z_{11})(Z-z_{12})}{(Z-p_{11})(Z-p_{12}} \times \cdots \times \frac{(Z-z_{M1})(Z-z_{M1})}{(Z-p_{M1})(Z-p_{M1})} \times k\end{aligned}$$

As such, the final scaling value can be calculated as:

$$\mu_f = k \sum_{m=1}^{M} \mu_{(m,\mathrm{STR})}$$

Following the above steps, the quantized and second order decomposed filter is ready for hardware implementation. An account on the FPGA implementation of the second-order-decomposed and quantized IIR filters is given in the following section.

A.2 FPGA implementation of fixed point IIR filters

The processing of data on an FPGA takes place on discrete time steps [27, 97], referred to as clock cycles. On each clock cycle certain processing tasks may be fulfilled, while other subtasks may pass on intermediate values to the upcoming clock cycles for further processing. The timing structure of FPGA operation provides an additional degree of freedom for the programmer to best utilize the resources available. The applied FPGA programming methodology needs to meet a balance between speed of operation (throughput), delay (latency) and resource consumption. In this section we give a brief introduction to three major scenarios usually encountered in practice and the associated design structure, namely a) Brute Force (BF): can accommodate high throughput and minimal delay (hardware intensive, limited to low complexity processing), b) High Throughput Pipelined (HTP): is able to achieve high throughput at the cost of extra delay (hardware intensive), and c) Balanced Resource/Timing Pipelined (BRTP): achieves smaller delay, and reduced hardware usage but leading to reduced throughput. These are elaborated in what follows.

A. Brute force (BF) implementation

The objective of the brute force design is to achieve processing results at the maximum operation speed of the FPGA and with minimal delay. This is schematically illustrated in Fig. A-8. As the rotating arrow reaches the ADC, a raw sample is picked up, sent to the processing unit (here a 2^{nd} order filter as an example), and an already processed sample is sent out through DAC. The throughput is defined by the

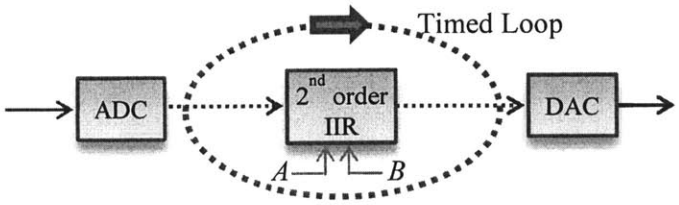

Figure A-8: A schematic illustration of brute force design on an FPGA. $A = [a_1, a_2]$, and $B = [b_0, b_1, b_2]$ are respectively the denominator and numerator coefficients (see Eq. (A.1)).

speed of rotation of the arrow (clock cycle) which is limited by the time required for the processing of a single sample, the FPGA clock period, or the minimum possible sampling time, whichever is longer.

The BF design is appealing as it can potentially meet both the throughput and delay requirements of the problem. However, it can only be used for relatively simple processing tasks. As the complexity of the processing unit increases the processing time grows and hence the processed sample cannot be available by the start of the next clock cycle. This forces the user to settle with a slower clock rate (lower throughput). Furthermore, in this approach the hardware resources are intensively utilized. For the example of second order IIR filter, five independent multipliers and four independent adders need to be used. This requirement increases for additional second order sections. This can easily surpass the limit on the available hardware resources for a relatively high order filter.

B. High Throughput Pipelined (HTP) implementation

The High Throughput-Pipelined (HTP) implementation can be applied when a) throughput is the main concern, b) hardware resources are abundant for the given processing task and c) processing delay is not problematic. For an N^{th} order IIR filter (assume N is even), the BF implementation, containing a cascaded series of $N/2$ second order sections, may not meet the throughput requirement. For the case where a decrease in the throughput cannot be afforded, but introducing a delay between input and output is not as problematic, one can apply a pipelined structure as shown in Fig. A-9(a). In this structure, several second order IIR units can work in parallel.

At the end of each clock cycle (when the rotating arrow reaches the ADC) individual second order sections (except the last one) pass on their outputs to memory. The stored values are then read into the following second order section in the next clock cycle. This structure can operate at the same clock rate as that of BF implementation for a single second order section (Fig. A-8). However, there will be a delay of $N/2$ clock cycles between the input and the output of the filter.

C. Balanced Resource/Timing Pipelined (BRTP) implementation

The Balanced Resource/Timing-Pipelined (BRTP) implementation uses the high operation frequency of FPGAs to reduce hardware usage. Current FPGAs usually can operate at very high frequencies (in the order of hundreds of MHz). Such a high sampling rate may not be available on the ADC periphery. In addition, for many applications the maximum required bandwidth is lower than the available FPGA clock rate. For these applications, the throughput requirement may be relaxed. The extra processing speed of FPGAs compared to the required data throughput can then be utilized for re-use of the hardware resources. This is shown in Fig. A-9(b) where the data handling/processing structure runs on two independent clock cycles. The outer cycle matches the sampling requirement (throughput) of the given task. The inner cycle on the other hand runs at the maximum processing speed provided by the FPGA which is higher than that of the outer cycle. As such, for every sample passed on to the FPGA, it is able to run several times (clock cycles) prior to the arrival of the next sample. This provides the possibility of re-using hardware resources. This approach is very appealing for high order IIR filtering applications where the requirements easily go beyond the hardware availability.

An N^{th} order IIR filter (assume N is even) can be implemented in BRTP form as long as the required sampling rate is smaller than the FPGA clock rate, f_{cc}, divided by $N/2$ i.e $f_s < \frac{f_{cc}}{N/2}$ (see Fig. A-9(b)). The only intricacy in this case is to update the coefficients of the core second order IIR filter for the active filtering stage and to store in memory the corresponding state of the filter (the delays) on every iteration. In this design one can simply adjust the order of the implemented filter in runtime by changing the number of times the inner loop re-iterates before sending a result out.

As the coefficients of the filter can also be easily loaded into the FPGA on runtime, the BRTP structure can be used as a variable order/coefficient IIR filter platform. This flexibility is very appealing in a research setting.

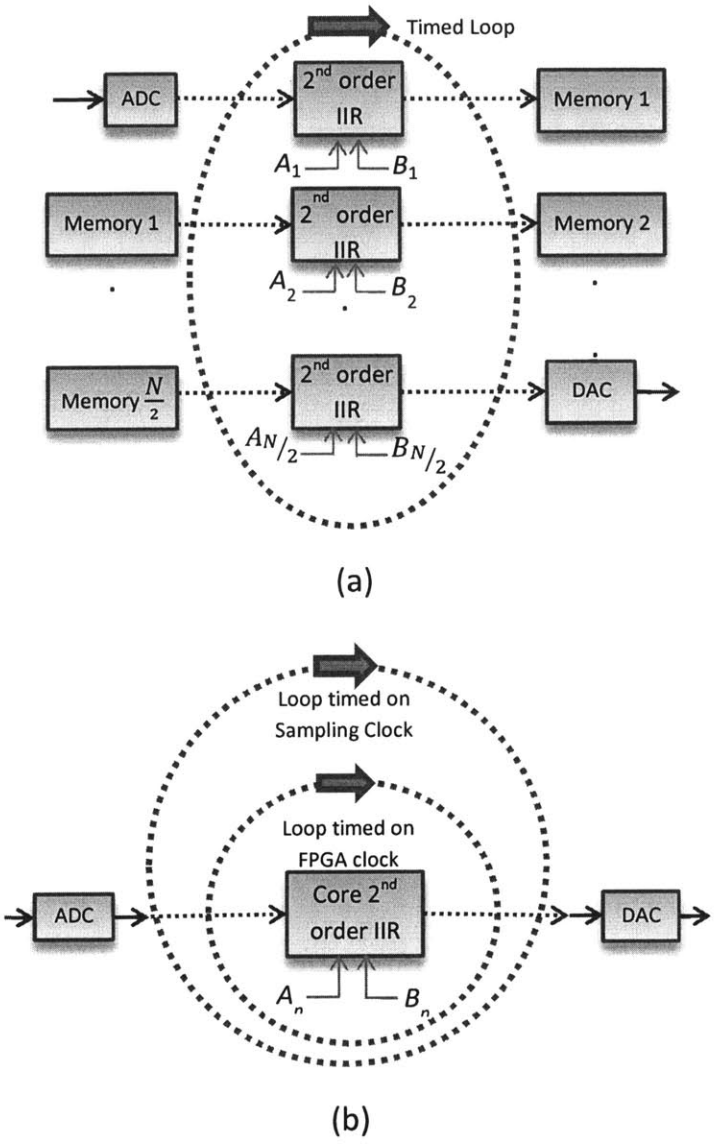

Figure A-9: a) High Throughput-Pipelined (HTP) implementation of an N^{th} order IIR filter for high throughput applications. The FPGA in this case can run at the same rate as that of the implementation of Fig. A-8, however there will be a delay of $N/2$ clock cycles between the input and output, and b) BRTP implementation with a second order core. n is the active filtering stage, $f_s < \frac{f_{cc}}{N/2}$ is the outer loop timing, f_{cc} is the timing for inner loop matching the maximum possible FPGA clock rate to run a 2nd order brute force IIR filter.

Bibliography

[1] D.Y. Abramovitch, S.B. Andersson, Lucy Y. Pao, and Georg Schitter. A tutorial on the mechanisms, dynamics, and control of atomic force microscopes. In *American Control Conference, 2007. ACC '07*, pages 3488–3502, July 2007.

[2] T. R. Albrecht, P. Grutter, D. Horne, and D. Rugar. Frequency modulation detection using high-q cantilevers for enhanced force microscope sensitivity. *Journal of Applied Physics*, 69(2):668–673, 1991.

[3] Toshio Ando, Noriyuki Kodera, Eisuke Takai, Daisuke Maruyama, Kiwamu Saito, and Akitoshi Toda. A high-speed atomic force microscope for studying biological macromolecules. *Proceedings of the National Academy of Sciences*, 98(22):12468–12472, 2001.

[4] Toshio Ando, Takayuki Uchihashi, Noriyuki Kodera, Daisuke Yamamoto, Atsushi Miyagi, Masaaki Taniguchi, and Hayato Yamashita. High-speed AFM and nano-visualization of biomolecular processes. *Pflugers Archiv - European Journal of Physiology*, 456(1):211–225, 2008.

[5] A. Bazaei, Yuen K. Yong, and S. O. Reza Moheimani. High-speed lissajous-scan atomic force microscopy: Scan pattern planning and control design issues. *Review of Scientific Instruments*, 83(6), 2012.

[6] D J Bell, T J Lu, N A Fleck, and S M Spearing. Mems actuators and sensors: observations on their performance and selection for purpose. *Journal of Micromechanics and Microengineering*, 15(7):S153, 2005.

[7] G. Binnig, C. F. Quate, and Ch. Gerber. Atomic force microscope. *Phys. Rev. Lett.*, 56:930–933, Mar 1986.

[8] G. Binnig and H. Rohrer. Scanning tunneling microscopy. *Surface Science*, 126(1-3):236–244, 1983.

[9] A. Bogner, G. Thollet, D. Basset, P.H. Jouneau, and C. Gauthier. Wet STEM: A new development in environmental SEM for imaging nano-objects included in a liquid phase. *Ultramicroscopy*, 104(3-4):290–301, 2005.

[10] I. S. Bozchalooi, K. Youcef-Toumi, D. J. Burns, and G. E. Fantner. Compensator design for improved counterbalancing in high speed atomic force microscopy. *Review of Scientific Instruments*, 82(11), 2011.

[11] I Soltani Bozchalooi and Ming Liang. Teager energy operator for multi-modulation extraction and its application for gearbox fault detection. *Smart Materials and Structures*, 19(7):075008, 2010.

[12] Christoph Braunsmann and Tilman E Schaffer. High-speed atomic force microscopy for large scan sizes using small cantilevers. *Nanotechnology*, 21(22):225705, 2010.

[13] James P. Buban, Quentin Ramasse, Bryant Gipson, Nigel D. Browning, and Stahlberg H. High-resolution low-dose scanning transmission electron microscopy. *Journal of Electron Microscopy*, 59(2):103–112, 2010.

[14] David Bullen, Xuefeng Wang, Jun Zou, Sung-Wook Chung, C.A. Mirkin, and Chang Liu. Design, fabrication, and characterization of thermally actuated probe arrays for dip pen nanolithography. *Microelectromechanical Systems, Journal of*, 13(4):594–602, Aug 2004.

[15] N A Burnham, O P Behrend, F Oulevey, G Gremaud, P-J Gallo, D Gourdon, E Dupas, A J Kulik, H M Pollock, and G A D Briggs. How does a tip tap? *Nanotechnology*, 8(2):67, 1997.

[16] Ignacio Casuso, Felix Rico, and Simon Scheuring. High-speed atomic force microscopy: Structure and dynamics of single proteins. *Current Opinion in Chemical Biology*, 15(5):704 – 709, 2011. Molecular Machines/Analytical Techniques.

[17] Ami Chand, Mario B. Viani, Tilman E. Schaffer, and Paul K. Hansma. Microfabricated small metal cantilevers with silicon tip for atomic force microscopy. *Microelectromechanical Systems, Journal of*, 9(1):112–116, March 2000.

[18] Guillaume T. Charras and Mike A. Horton. Single cell mechanotransduction and its modulation analyzed by atomic force microscope indentation. *Biophysical Journal*, 82(6):2970 – 2981, 2002.

[19] C. Julian Chen. Electromechanical deflections of piezoelectric tubes with quartered electrodes. *Applied Physics Letters*, 60(1), 1992.

[20] Chih-Lieh Chen, Jim-Wei Wu, Yi-Ting Lin, Yu-Ting Lo, and Li-Chen Fu. Sinusoidal trajectory for atomic force microscopy precision local scanning with auxiliary optical microscopy. In *Decision and Control (CDC), 2013 IEEE 52nd Annual Conference on*, pages 348–353, Dec 2013.

[21] Young-Man Choi, Jason J Gorman, Nicholas G Dagalakis, Seung Ho Yang, Yongsik Kim, and Jae Myung Yoo. A high-bandwidth electromagnetic mems motion stage for scanning applications. *Journal of Micromechanics and Microengineering*, 22(10):105012, 2012.

[22] Garrett M. Clayton, Szuchi Tien, Kam K. Leang, Qingze Zou, and Santosh Devasia. A review of feedforward control approaches in nanopositioning for high-speed SPM. *Journal of Dynamic Systems, Measurement, and Control*, 131(6):19, 2009.

[23] David C. Coffey and David S. Ginger. Patterning phase separation in polymer films with dip-pen nanolithography. *Journal of the American Chemical Society*, 127(13):4564–4565, 2005.

[24] A. Daniele, S. Salapaka, M.V. Salapaka, and M. Dahleh. Piezoelectric scanners for atomic force microscopes: design of lateral sensors, identification and control. In *American Control Conference, 1999. Proceedings of the 1999*, volume 1, pages 253–257 vol.1, 1999.

[25] G. D Danilatos. Foundations of environmental scanning electron microscopy. *Advances in Electornics and Electron Physics*, 71:109–250, 1988.

[26] Giovanni De Giudici. Surface control vs. diffusion control during calcite dissolution: Dependence of step-edge velocity upon solution pH. *American Mineralogist*, 87(10):1279–1285, 2002.

[27] Jean-Pierre Deschamps, Gustavo D. Sutter, and Enrique Canto. *Guide to FPGA Implementation of Arithmetic Functions*. Springer, New York, NY, 2012.

[28] Athene M. Donald. The use of environmental scanning electron microscopy for imaging wet and insulating materials. *Nature Materials*, 2:511–516, 2003.

[29] Owen W. Duckworth and Scot T. Martin. Dissolution rates and pit morphologies of rhombohedral carbonate minerals. *American Mineralogist*, 89(4):554–563, 2004.

[30] K. El Rifai, O. el Rifai, and K. Youcef-Toumi. On dual actuation in atomic force microscopes. In *American Control Conference, 2004. Proceedings of the 2004*, volume 4, pages 3128–3133 vol.4, June 2004.

[31] A.J. Fleming, B.J. Kenton, and K.K. Leang. Bridging the gap between conventional and video-speed scanning probe microscopes. *Ultramicroscopy*, 110(9):1205 – 1214, 2010.

[32] A.J. Fleming, B.J. Kenton, and K.K. Leang. Ultra-fast dual-stage vertical positioning for high performance SPMs. In *American Control Conference (ACC), 2010*, pages 4975–4980, June 2010.

[33] A.J. Fleming and K.K. Leang. Charge drives for scanning probe microscope positioning stages. *Ultramicroscopy*, 108(12):1551 – 1557, 2008.

[34] Andrew J. Fleming. Techniques and considerations for driving piezoelectric actuators at high-speed. In *in Proc. SPIE Smart Materials and Structures*, volume 6926, 2008.

[35] Andrew J. Fleming. High-speed vertical positioning for contact-mode atomic force microscopy. In *Advanced Intelligent Mechatronics, 2009. AIM 2009. IEEE/ASME International Conference on*, pages 522–527, July 2009.

[36] Andrew J. Fleming. Dual-stage vertical feedback for high-speed scanning probe microscopy. *Control Systems Technology, IEEE Transactions on*, 19(1):156–165, Jan 2011.

[37] Takeshi Fukuma and Suzanne P. Jarvis. Development of liquid-environment frequency modulation atomic force microscope with low noise deflection sensor for cantilevers of various dimensions. *Review of Scientific Instruments*, 77(4), 2006.

[38] Takeshi Fukuma, Masayuki Kimura, Kei Kobayashi, Kazumi Matsushige, and Hirofumi Yamada. Development of low noise cantilever deflection sensor for multienvironment frequency-modulation atomic force microscopy. *Review of Scientific Instruments*, 76(5), 2005.

[39] Ricardo Garcia and Ruben Perez. Dynamic atomic force microscopy methods. *Surface Science Reports*, 47(6-8):197–301, 2002.

[40] Ping Ge and Musa Jouaneh. Modeling hysteresis in piezoceramic actuators. *Precision Engineering*, 17(3):211 – 221, 1995.

[41] Franz J. Giessibl. Atomic resolution of the silicon (111)-(7x7) surface by atomic force microscopy. *Science*, 267(5194):68–71, 1995.

[42] Dariusz S. Golda. *Design of High-Speed, Meso-Scale Nanopositioners Driven by Electromagnetic Actuators.* PhD thesis, Massachusetts Institute of Technology, 2008.

[43] M. Goldfarb and N. Celanovic. A lumped parameter electromechanical model for describing the nonlinear behavior of piezoelectric actuators. *Journal of Dynamic Systems, Dynamics and Control*, 119(3):478–485, 1997.

[44] M. Goldfarb and N. Celanovic. Modeling piezoelectric stack actuators for control of micromanipulation. *Control Systems, IEEE*, 17(3):69–79, Jun 1997.

[45] Da-Wei Gu, Petko H. Petkov, and Mihail M. Konstantinov. *Robust Control Design with MATLAB.* Springer, 2nd edition edition, 2013.

[46] S. Hosaka, K. Etoh, A. Kikukawa, and H. Koyanagi. Megahertz silicon atomic force microscopy (AFM) cantilever and high-speed readout in AFM-based recording. *Journal of Vacuum Science and Technology B*, 18(1):94–99, 2000.

[47] Howell Larry L. Hubbard Neal B., Culpepper Martin L. Actuators for micropositioners and nanopositioners. *Applied Mechanics Review*, 59(6):324–334, 2006.

[48] J. E. Huber, N. A. Fleck, and M. F. Ashby. The selection of mechanical actuators based on performance indices. *Proceedings of the Royal Society of London A: Mathematical, Physical and Engineering Sciences*, 453(1965):2185–2205, 1997.

[49] L.B. Jackson. Roundoff-noise analysis for fixed-point digital filters realized in cascade or parallel form. *Audio and Electroacoustics, IEEE Transactions on*, 18(2):107–122, Jun 1970.

[50] Younkoo Jeong, G. R. Jayanth, and Chia-Hsiang Menq. Control of tip-to-sample distance in atomic force microscopy: A dual-actuator tip-motion control scheme. *Review of Scientific Instruments*, 78(9), 2007.

[51] N. de Jonge, D. B. Peckys, G. J. Kremers, and D. W. Piston. Electron microscopy of whole cells in liquid with nanometer resolution. *Proceedings of the National Academy of Sciences*, 106(7):2159–2164, 2009.

[52] J.F. Kaiser. Some useful properties of teager's energy operators. In *Acoustics, Speech, and Signal Processing, 1993. ICASSP-93., 1993 IEEE International Conference on*, volume 3, pages 149–152 vol.3, April 1993.

[53] Sergei V. Kalinin and Dawn A. Bonnell. Effect of phase transition on the surface potential of the BaTiO3 (100) surface by variable temperature scanning surface potential microscopy. *Journal of Applied Physics*, 87(8):3950–3957, 2000.

[54] S. Kasas, N. H. Thomson, B. L. Smith, P. K. Hansma, J. Miklossy, and H. G. Hansma. Biological applications of the AFM: From single molecules to organs. *International Journal of Imaging Systems and Technology*, 8(2):151–161, 1997.

[55] Brian J. Kenton, Andrew J. Fleming, and Kam K. Leang. Compact ultra-fast vertical nanopositioner for improving scanning probe microscope scan speed. *Review of Scientific Instruments*, 82(12), 2011.

[56] Young-Sik Kim, Hyo-Jin Nam, Seong-Moon Cho, Jae-Wan Hong, Dong-Chun Kim, and Jong U. Bu. PZT cantilever array integrated with piezoresistor sensor for high speed parallel operation of AFM. *Sensors and Actuators A: Physical*, 103(1-2):122–129, 2003. Micromechanics section of Sensors and Actuators, based on contributions revised from the Technical Digest of the 15th IEEE International conference on Micro Electro mechanical Systems (MEMS 2002).

[57] Noriyuki Kodera, Daisuke Yamamoto, Ryoki Ishikawa, and Toshio Ando. Video imaging of walking myosin V by high-speed atomic force microscopy. *Nature*, 468(7320):72–76, 2010.

[58] Noriyuki Kodera, Hayato Yamashita, and Toshio Ando. Active damping of the scanner for high-speed atomic force microscopy. *Review of Scientific Instruments*, 76(5), 2005.

[59] S. Kuiper and G. Schitter. Active damping of a piezoelectric tube scanner using self-sensing piezo actuation. *Mechatronics*, 20(6):656 – 665, 2010.

[60] S. Kuiper and G. Schitter. Model-based feedback controller design for dual actuated atomic force microscopy. *Mechatronics*, 22(3):327 – 337, 2012. Special Issue on Mechatronic Systems for Micro- and Nanoscale Applications.

[61] Schitter G. Kuiper S, Fleming AJ. Dual actuation for high speed atomic force microscopy. In *5th IFAC Symposium on Mechatronic Systems*, page 220, 2010.

[62] F. F. Kuo and J. F. Kaiser. *System Anlysis by Digital Computer*. Wiley, New York, NY, 1966.

[63] M.A. Lantz, H.E. Rothuizen, U. Drechsler, W. Haberle, and M. Despont. A vibration resistant nanopositioner for mobile parallel-probe storage applications. *Microelectromechanical Systems, Journal of*, 16(1):130–139, Feb 2007.

[64] K.K. Leang, Qingze Zou, and S. Devasia. Feedforward control of piezoactuators in atomic force microscope systems. *Control Systems, IEEE*, 29(1):70–82, Feb 2009.

[65] P.P Lehenkari, G.T Charras, A Nykanen, and M.A Horton. Adapting atomic force microscopy for cell biology. *Ultramicroscopy*, 82(1-4):289–295, 2000.

[66] Mo Li, H. X. Tang, and M. L. Roukes. Ultra-sensitive nems-based cantilevers for sensing, scanned probe and very high-frequency applications. *Nature Nanotechnology*, 2:114–120, 2007.

[67] Yang Li and John Bechhoefer. Feedforward control of a piezoelectric flexure stage for AFM. In *American Control Conference, 2008*, pages 2703–2709, June 2008.

[68] Ming Liang and I. Soltani Bozchalooi. An energy operator approach to joint application of amplitude and frequency-demodulations for bearing fault detection. *Mechanical Systems and Signal Processing*, 24(5):1473 – 1494, 2010. Special Issue: Operational Modal Analysis.

[69] Y. Liang and D.R. Baer. Anisotropic dissolution at the CaCO3—water interface. *Surface Science*, 373(2-3):275–287, 1997.

[70] L. Ljung. *System Identification: Theory for the user*. Prentice Hall, UpperSaddle River, NJ, 2nd edition edition, 1999.

[71] I A Mahmood and S O Reza Moheimani. Fast spiral-scan atomic force microscopy. *Nanotechnology*, 20(36):365503, 2009.

[72] I. A. Mahmood and S. O. Reza Moheimani. Making a commercial atomic force microscope more accurate and faster using positive position feedback control. *Review of Scientific Instruments*, 80(6), 2009.

[73] I.A. Mahmood and S.O.R. Moheimani. Spiral-scan atomic force microscopy: A constant linear velocity approach. In *Nanotechnology (IEEE-NANO), 2010 10th IEEE Conference on*, pages 115–120, Aug 2010.

[74] I.A. Mahmood, S.O.R. Moheimani, and B. Bhikkaji. A new scanning method for fast atomic force microscopy. *Nanotechnology, IEEE Transactions on*, 10(2):203–216, March 2011.

[75] H. J. Mamin, H. Birk, P. Wimmer, and D. Rugar. High-speed scanning tunneling microscopy: Principles and applications. *Journal of Applied Physics*, 75(1):161–168, 1994.

[76] P. Maragos, J.F. Kaiser, and T.F. Quatieri. On separating amplitude from frequency modulations using energy operators. In *Acoustics, Speech, and Signal Processing, 1992. ICASSP-92., 1992 IEEE International Conference on*, volume 2, pages 1–4 vol.2, Mar 1992.

[77] P. Maragos, J.F. Kaiser, and T.F. Quatieri. On amplitude and frequency demodulation using energy operators. *Signal Processing, IEEE Transactions on*, 41(4):1532–1550, Apr 1993.

[78] P. Maragos, T.F. Quatieri, and J.F. Kaiser. Speech nonlinearities, modulations, and energy operators. In *Acoustics, Speech, and Signal Processing, 1991. ICASSP-91., 1991 International Conference on*, pages 421–424 vol.1, Apr 1991.

[79] The MathWorks. *MATLAB R2014B user's manual.*

[80] R. Merkel, P. Nassoy, A. Leung, K. Ritchie, and E. Evans. Energy landscapes of receptor-ligand bonds explored with dynamic force spectroscopy. *Nature*, 397:50–53, 1999.

[81] Apex Microtechnology. *Driving Piezoelectric Actuators - AN44.* http://www.apexanalog.com, 2012.

[82] Apex Microtechnology. *High Voltage Power Operational Amplifiers - PA88, PA88a.* http://www.apexanalog.com, 2012.

[83] Apex Microtechnology. *Video Power Operational Amplifier - PA119CE, PA119CEA.* http://www.apexanalog.com, 2012.

[84] Apex Microtechnology. *Stability for Power Operational Amplifiers - AN19.* http://www.apexanalog.com, 2013.

[85] B. Mokaberi and Aristides A.G. Requicha. Compensation of scanner creep and hysteresis for AFM nanomanipulation. *Automation Science and Engineering, IEEE Transactions on*, 5(2):197–206, April 2008.

[86] Daniel J. Muller and Dufrene Yves F. Atomic force microscopy: a nanoscopic window on the cell surface. *Trends in Cell Biology*, 21(8):461–469, 2011.

[87] Hadi Tavakoli Nia, Iman S. Bozchalooi, Yang Li, Lin Han, Han-Hwa Hung, Eliot Frank, Kamal Youcef-Toumi, Christine Ortiz, and Alan Grodzinsky. High-bandwidth AFM-based rheology reveals that cartilage is most sensitive to high loading rates at early stages of impairment. *Biophysical Journal*, 104(7):1529 – 1537, 2013.

[88] Masahiro Ojima, Akira Arimoto, Naoki Chinone, Toshihiko Gotoh, and Kunio Aiki. Diode laser noise at video frequencies in optical videodisc players. *Applied Optics*, 25(9):1404–1410, 1986.

[89] Buck J R Oppenheim A V, Schafer R W. *Discrete-Time Signal Processing.* Prentice Hall, UpperSaddle River, NJ, 2nd edition edition, 1998.

[90] George T. Paloczi, Bettye L. Smith, Paul K. Hansma, Deron A. Walters, and Mark A. Wendman. Rapid imaging of calcite crystal growth using atomic force microscopy with small cantilevers. *Applied Physics Letters*, 73(12):1658–1660, 1998.

[91] R. Pearce and G.J. Vancso. Real-time imaging of melting and crystallization in poly(ethylene oxide) by atomic force microscopy. *Polymer*, 39(5):1237 – 1242, 1998.

[92] R. Penrose. On best approximate solutions of linear matrix equations. *Mathematical Proceedings of the Cambridge Philosophical Society*, 52:17–19, 1 1956.

[93] Alexandros Potamianos and Petros Maragos. A comparison of the energy operator and the hilbert transform approach to signal and speech demodulation. *Signal Processing*, 37(1):95 – 120, 1994.

[94] Irene Revenko, Francoise Sommer, Duc Tran Minh, Robert Garrone, and Jean-Marie Franc. Atomic force microscopy study of the collagen fibre structure. *Biology of the Cell*, 80(1):67 – 69, 1994.

[95] Matthias Rief, Filipp Oesterhelt, Berthold Heymann, and Hermann E. Gaub. Single molecule force spectroscopy on polysaccharides by atomic force microscopy. *Science*, 275(5304):1295–1297, 1997.

[96] E. Ruiz-Agudo, C.V. Putnis, C. Jimenez-Lopez, and C. Rodriguez-Navarro. An atomic force microscopy study of calcite dissolution in saline solutions: The role of magnesium ions. *Geochimica et Cosmochimica Acta*, 73(11):3201 – 3217, 2009.

[97] Ronald Sass and Andrew G. Schmidt. *Embedded Systems Design with Platform FPGAs: Principles and Practices.* Elsevier, New York, NY, 2010.

[98] G Schitter, F Allgower, and A Stemmer. A new control strategy for high-speed atomic force microscopy. *Nanotechnology*, 15(1):108, 2004.

[99] G. Schitter, P. Menold, H. F. Knapp, F. Allgower, and A. Stemmer. High performance feedback for fast scanning atomic force microscopes. *Review of Scientific Instruments*, 72(8):3320–3327, 2001.

[100] Georg Schitter, K.J. Astrom, Barry E. DeMartini, P.J. Thurner, K.L. Turner, and Paul K. Hansma. Design and modeling of a high-speed AFM-scanner. *Control Systems Technology, IEEE Transactions on*, 15(5):906–915, Sept 2007.

[101] Georg Schitter, W.F. Rijkee, and N. Phan. Dual actuation for high-bandwidth nanopositioning. In *Decision and Control, 2008. CDC 2008. 47th IEEE Conference on*, pages 5176–5181, Dec 2008.

[102] A. Sebastian, M.V. Salapaka, and Jason P. Cleveland. Robust control approach to atomic force microscopy. In *Decision and Control, 2003. Proceedings. 42nd IEEE Conference on*, volume 4, pages 3443–3444 vol.4, Dec 2003.

[103] Myung-Hwan Whangbo Sergei N. Magonov. *Surface Analysis with STM and AFM.* VCH, Weinheim, 1996.

[104] Takayuki Shibata, Kazuya Unno, Eiji Makino, and Shiro Shimada. Fabrication and characterization of diamond AFM probe integrated with PZT thin film sensor and actuator. *Sensors and Actuators A: Physical*, 114(2-3):398–405, 2004. Selected papers from Transducers 03.

[105] Ryoji Shiraki, PeterA. Rock, and WilliamH. Casey. Dissolution kinetics of calcite in 0.1 M NaCl solution at room temperature: An atomic force microscopic (AFM) study. *Aquatic Geochemistry*, 6(1):87–108, 2000.

[106] G. Song, Jinqiang Zhao, Xiaoqin Zhou, and J.A. De Abreu-Garcia. Tracking control of a piezoceramic actuator with hysteresis compensation using inverse preisach model. *Mechatronics, IEEE/ASME Transactions on*, 10(2):198–209, April 2005.

[107] Martin Stark, Clemens Moller, Daniel J. Muller, and Reinhard Guckenberger. From images to interactions: High-resolution phase imaging in tapping-mode atomic force microscopy. *Biophysical Journal*, 80(6):3009–3018, 2001.

[108] T. Sulchek, S. C. Minne, J. D. Adams, D. A. Fletcher, A. Atalar, C. F. Quate, and D. M. Adderton. Dual integrated actuators for extended range high speed atomic force microscopy. *Applied Physics Letters*, 75(11):1637–1639, 1999.

[109] Yuki Suzuki, Nobuaki Sakai, Aiko Yoshida, Yoshitsugu Uekusa, Akira Yagi, Yuka Imaoka, Shuichi Ito, Koichi Karaki, and Kunio Takeyasu. High-speed atomic force microscopy combined with inverted optical microscopy for studying cellular events. *Scientific Reports*, 3, 2013.

[110] Joel Therrien, Amir Dindar, and David Smith. AFM studies of nanoparticle deposition via electrospray ionization. *Microscopy Research and Technique*, 70(6):530–533, 2007.

[111] Szuchi Tien, Qingze Zou, and S. Devasia. Iterative control of dynamics-coupling-caused errors in piezoscanners during high-speed AFM operation. *Control Systems Technology, IEEE Transactions on*, 13(6):921–931, Nov 2005.

[112] Takayuki Uchihashi, Noriyuki Kodera, and Toshio Ando. Guide to video recording of structure dynamics and dynamic processes of proteins by high-speed atomic force microscopy. *Nature Protocols*, 7:1193–1206, 2012.

[113] S. Verma, H. Shakir, and W.-J. Kim. Novel electromagnetic actuation scheme for multiaxis nanopositioning. *Magnetics, IEEE Transactions on*, 42(8):2052–2062, Aug 2006.

[114] P. Vettiger, M. Despont, U. Drechsler, U. Durig, W. Haberle, M.I. Lutwyche, H.E. Rothuizen, R. Stutz, R. Widmer, and G.K. Binnig. The "millipede"-more than thousand tips for future AFM storage. *IBM Journal of Research and Development*, 44(3):323–340, May 2000.

[115] M. B. Viani, T. E. Schaffer, G. T. Paloczi, L. I. Pietrasanta, B. L. Smith, J. B. Thompson, M. Richter, M. Rief, H. E. Gaub, K. W. Plaxco, A. N. Cleland, H. G. Hansma, and P. K. Hansma. Fast imaging and fast force spectroscopy of single biopolymers with a new atomic force microscope designed for small cantilevers. *Review of Scientific Instruments*, 70(11), 1999.

[116] Mario B. Viani, Tilman E. Schaffer, Ami Chand, Matthias Rief, Hermann E. Gaub, and Paul K. Hansma. Small cantilevers for force spectroscopy of single molecules. *Journal of Applied Physics*, 86(4):2258–2262, 1999.

[117] Sachin P. Wadikhaye, Yuen Kuan Yong, and S. O. Reza Moheimani. A serial-kinematic nanopositioner for high-speed atomic force microscopy. *Review of Scientific Instruments*, 85(10), 2014.

[118] D. A. Walters, J. P. Cleveland, N. H. Thomson, P. K. Hansma, M. A. Wendman, G. Gurley, and V. Elings. Short cantilevers for atomic force microscopy. *Review of Scientific Instruments*, 67(10), 1996.

[119] Deron A. Walters, Mario Viani, George T. Paloczi, Tilman E. Schaeffer, Jason P. Cleveland, Mark A. Wendman, Gus Gurley, Virgil B. Elings, and Paul K. Hansma. Atomic force microscopy using small cantilevers. *Proc. SPIE*, 3009:43–47, 1997.

[120] Yan Yan, Ying Wu, Qingze Zou, and Chanmin Su. An integrated approach to piezoactuator positioning in high-speed atomic force microscope imaging. *Review of Scientific Instruments*, 79(7), 2008.

[121] Y. K. Yong, S. O. R. Moheimani, B. J. Kenton, and K. K. Leang. Invited review article: High-speed flexure-guided nanopositioning: Mechanical design and control issues. *Review of Scientific Instruments*, 83(12), 2012.

[122] Y K Yong, S O R Moheimani, and I R Petersen. High-speed cycloid-scan atomic force microscopy. *Nanotechnology*, 21(36):365503, 2010.

[123] Y.K. Yong and S.O.R. Mohemani. Design of an inertially counterbalanced z -nanopositioner for high-speed atomic force microscopy. *Nanotechnology, IEEE Transactions on*, 12(2):137–145, March 2013.

[124] Yuen K. Yong, Bilal Ahmed, and S. O. Reza Moheimani. Atomic force microscopy with a 12-electrode piezoelectric tube scanner. *Review of Scientific Instruments*, 81(3), 2010.

[125] Q. Zhong, D. Inniss, K. Kjoller, and V.B. Elings. Fractured polymer/silica fiber surface studied by tapping mode atomic force microscopy. *Surface Science Letters*, 290(1-2):L688–L692, 1993.

[126] Q. Zou, K. K. Leang, E. Sadoun, M. J. Reed, and S. Devasia. Control issues in high-speed AFM for biological applications: Collagen imaging example. *Asian Journal of Control*, 6(2):164–178, 2004.

[127] Qingze Zou and S. Devasia. Preview-based optimal inversion for output tracking: application to scanning tunneling microscopy. *Control Systems Technology, IEEE Transactions on*, 12(3):375–386, May 2004.

[128] M. Zupan, M.F. Ashby, and N.A. Fleck. Actuator classification and selection - the development of a database. *Advanced Engineering Materials*, 4(12):933–940, 2002.